

**Mathematical Modelling of Cell
Aggregation in Liver Tissue
Engineering**

by

John Edward F. Green, M. A.

Thesis submitted to the University of Nottingham for the
Degree of Doctor of Philosophy,
September 2006

Acknowledgements

I would like to thank my supervisors, Professor H. M. Byrne and Dr S. L. Waters, for their encouragement and guidance throughout my time at Nottingham. I will always be grateful for their support, insight, patience and helpfulness. In addition, I would like to thank Professor K. M. Shakesheff, Dr R. N. Bhandari and Mr R. J. Thomas of the Tissue Engineering Group for useful discussions of the biological aspects of liver tissue engineering. I also wish to express my gratitude to Professor L. Edelstein-Keshet of the University of British Columbia for taking an interest in my research and allowing me the opportunity to visit her in Vancouver, where the work which eventually became Chapter 5 was initiated.

Special thanks are due to my parents, for their continued kindness and support. I would also like to acknowledge all my friends in the department who have made my time here so enjoyable, and have helped me in numerous ways.

Finally, I wish gratefully to acknowledge the financial support of the BBSRC, which provided funding for this work through a research studentship, and the Royal Commission for the Exhibition of 1851, whose Special Award allowed me to visit the University of British Columbia.

Contents

1	Introduction	1
1.1	Tissue engineering	2
1.2	The Liver	4
1.3	Liver cell culture <i>in vitro</i>	7
1.4	Theoretical approaches to tissue formation	11
1.5	Mathematical models	14
1.5.1	Individual-based versus continuum models	14
1.5.2	<i>Dictyostelium</i> aggregation and the Keller-Segel model	16
1.5.3	Mechanochemical models	17
1.5.4	Non-local models	19
1.5.5	Multiphase models	21
1.5.6	Continuum descriptions of biological materials	23
1.6	Thesis overview	25
2	A one-dimensional two-phase model of hepatocyte aggregation <i>in vitro</i>	28
2.1	Introduction	28
2.2	Model formulation	30
2.2.1	Constitutive relations	32
2.2.2	Initial and boundary conditions	35
2.2.3	Model reduction	36
2.2.4	Parameters	37
2.2.5	Nondimensionalisation	38

2.3	Linear stability analysis	39
2.4	Long-time behaviour	42
2.5	Numerical simulations	44
2.5.1	Numerical methods	44
2.5.2	Numerical results	45
2.6	Discussion	50
3	Modelling of chemotactic cell aggregation <i>in vitro</i>. Part I:	
	Model derivation and thin film limits	55
3.1	Introduction	55
3.2	Review of mathematical modelling of thin films	57
3.3	Model formulation	60
3.3.1	Preamble	60
3.3.2	Extracellular matrix model	62
3.3.3	Cell culture model	64
3.3.4	Chemoattractant concentration	69
3.3.5	Nondimensionalisation	70
3.4	Chemoattractant concentration: rapid diffusion limit	76
3.5	Extensional regime	77
3.5.1	Summary of governing equations	83
3.6	Lubrication regime	85
3.6.1	ECM equations	86
3.6.2	Cell and culture medium equations	88
3.6.3	Summary of governing equations	90
3.7	Discussion	92
4	Modelling of chemotactic cell aggregation <i>in vitro</i>. Part II:	
	Analysis and numerical simulations	96
4.1	Introduction	96
4.2	Linear stability analysis	97
4.2.1	Extensional regime	97

4.2.2	Lubrication regime	100
4.3	Numerical simulations - Extensional regime	104
4.3.1	Numerical methods	104
4.3.2	Numerical results	105
4.4	Numerical simulations - Lubrication regime	113
4.4.1	Numerical methods	113
4.4.2	Numerical results	113
4.5	Discussion	118
5	Non-local models for the interactions of hepatocytes and stel-	
	late cells	125
5.1	Introduction	125
5.2	Review of non-local modelling framework	130
5.2.1	Relation to individual-based models	131
5.3	Model formulation	133
5.3.1	Modelling aims	133
5.3.2	Governing equations	134
5.4	Hypothesis 1: Hepatocyte-stellate interactions through chemo-	
	taxis	136
5.4.1	Boundary and initial conditions	138
5.4.2	Nondimensionalisation	139
5.5	Hypothesis 2: Hepatocyte-stellate interactions through direct	
	physical contact	140
5.5.1	Nondimensionalisation	142
5.6	Linear stability analysis	143
5.6.1	Model 1: Chemotaxis	145
5.6.2	Model 2: Physical contact	149
5.7	Numerical simulations	151
5.7.1	Numerical methods	151
5.7.2	Model 1	152

5.7.3	Model 2	157
5.8	Discussion	162
6	Discussion	168
A	Diffusion in a multiphase mixture	175
A.1	Basic notions	175
A.2	Reaction-diffusion equation for a solute in an mixture	176
B	ECM equations in the extensional regime	179
B.1	ECM equations	179
C	Numerical schemes for the thin-film models	182
C.1	Extensional regime	182
C.2	Lubrication regime	184
D	Travelling wave solutions of the two-species non-local model	186
	References	189

Abstract

A promising method for growing functional liver tissue *in vitro* involves culturing hepatocytes as spheroidal cell aggregates. In this thesis, we develop mathematical models of cell aggregation, and use them to determine how hepatocytes' interactions with the extracellular matrix (ECM) on which they are seeded, and with stellate cells, affect the process.

Chapters 2-4 focus on the effect that cell-ECM coupling has on the aggregation process. We use a novel formulation that couples a mechanical model for the ECM with a two-phase model for the cell-culture region. A combination of linear stability analysis and numerical simulations are used to identify parameter regimes in which aggregation occurs, and investigate the effect of changing key parameters. In Chapter 2, we assume a one-dimensional geometry, whereas in Chapters 3 and 4, the slender two-dimensional geometry is exploited to obtain two alternative one-dimensional models in which the mechanisms dominating aggregation are chemotaxis and surface tension.

In Chapter 5, we focus on interactions between hepatocytes and stellates, neglecting the role of the ECM. We develop new non-local models to investigate the relative contributions of hepatocyte-hepatocyte and hepatocyte-stellate interactions in controlling spheroid formation. Comparison with experimental results suggests that the hepatocyte-stellate interaction is the stronger, in which case a 1:1 seeding ratio of hepatocytes to stellates is likely to be optimal for promoting swift aggregate formation.

Chapter 1

Introduction

The possibility of growing tissues in the laboratory for use in clinical applications is an area of intense biological research interest. As the largest and most complex organ in humans, the liver has been the focus of much of this effort. In this thesis, we develop and analyse mathematical models for the aggregation of liver cells *in vitro*. These models are motivated by the need to understand better the formation of multicellular spheroids, which appears to hold the key to engineering viable, functional liver tissue in the laboratory. In this chapter, we review existing literature (biological and theoretical) that is relevant to problem. We begin by introducing the relatively new science of tissue engineering, and discussing the general challenges faced by researchers aiming to grow functional tissues *in vitro*. We then discuss the structure and function of the liver, and the particular issues connected with culturing liver cells in the laboratory. Theoretical frameworks which have been proposed to explain the ways in which tissues are formed (both *in vitro* and *in vivo*) are then reviewed. Finally, we consider existing mathematical models, and modelling approaches, on which we shall build in this thesis.

1.1 Tissue engineering

Tissue engineering might be caricatured as the ‘science of spare parts’ [100]; its aim is to grow functional tissues and organs to replace those which have become defective through age, trauma or disease. Described in this way, we can see tissue engineering as a logical extension to current transplant therapies, motivated by a lack of donors and the difficulties caused by immunosuppressive treatment.

One approach, termed ‘*in vivo* tissue engineering’ [138] involves introducing a microporous, biodegradable scaffold into the damaged tissue; healthy cells will then migrate into the scaffold and proliferate. The scaffold is gradually degraded, leaving behind regenerated tissue. However, this technique presents formidable challenges such as engineering biomaterials with appropriate properties for the scaffold, integrating the scaffold with the surrounding tissue *in vivo*, and stimulating cell colonisation of the implant. At present, more attention is focused on growing new tissue *in vitro* [117]. A small sample of healthy cells is harvested (ideally from the patient in question, so as to avoid rejection of the engineered tissue) and cultured in the laboratory. Various techniques are then applied to the cells to expand their number, and trigger differentiation (specialisation to a particular function) [114]. These cells may then be seeded into a scaffold, which can provide biomechanical support and structural cues for the growth of the new tissue [117]. The scaffold in turn may be placed in a bioreactor, which uses fluid flow to provide appropriate mechanical forces to aid growth and differentiation, and to help to provide an adequate supply of nutrients (see below). Finally, the engineered tissue is re-implanted into the patient, replacing the defective tissue whilst avoiding the problems of rejection inherent in current organ transplant techniques.

Whilst the concept may sound simple, tissue engineering poses numerous

practical challenges. For example, harvesting healthy cells from the subject can be problematic, as there may only be a small number of suitable cells available. Furthermore, their removal may result in morbidity at the donor site, and the cells thus obtained may have only a limited ability to proliferate and undergo differentiation [104]. One way around these difficulties, which is the subject of increasing research interest, is to use relevant precursor cells, multipotent stem cells or similar, stem-like cells for tissue regeneration [80,104,109]. These cell types appear to have excellent capacity for proliferation in culture, and can differentiate to perform multiple different functions under defined culture conditions.

Another problem arises from the fact that cells cultured under traditional monolayer techniques frequently undergo phenotypic and functional dedifferentiation [9,67,104,114]. It appears that nearly all cell functions are influenced by cell-cell and cell-extracellular matrix (ECM) interactions. As a result, the search for appropriate biomaterials has received a new impetus [43,54]. These materials may consist of biologically derived components found in the ECM *in vivo* (e.g. collagen), or artificial substrates (often polymers) such as polylactic acid (PLA). To encourage successful tissue growth, tissue engineering scaffolds may also incorporate chemicals, which are released in a controlled manner over time, mimicking the release of growth factors *in vivo* [133].

A variety of different culture techniques have been developed to overcome some of the difficulties associated with tissue engineering. Cell culture within scaffolds has already been mentioned, and it has been reported that three-dimensional cultures exhibit improved cell functionality [55,107], as they recapitulate, at least to some extent, the architecture of the tissue *in vivo*. Bioreactor culture systems are also frequently employed to modulate the properties of the engineered tissue [68,129]. The stagnant environment experienced by cells grown in conventional culture vessels means that, over time, the supply of

nutrients can become depleted, and harmful waste products accumulate, leading to a loss of function [67]. Perfusion culture systems allow for the constant supply of fresh culture medium, whilst metabolised medium is drained off, thus helping to ensure a constant environment for the cells. A refinement of the technique allows for media of differing compositions to be supplied to the upper and lower portions of the tissue; this allows tissue engineers to mimic the nutrient gradients often found across tissues *in vivo*, which are thought to be important mediators of cell function [4, 67].

Mechanical forces also have an important effect on the development of tissue [22], and other types of bioreactor have been developed with this in mind. One example is the Rotary Cell Culture System (RCCS), which was designed to protect tissues during space flight [102]; cells within this culture system experience very low shear forces. By contrast, cells cultured in mixed flasks experience much greater shear, but the turbulent flow of the medium enhances the uptake of nutrients [129]. However, for some cell types, particularly bone and cartilage, culture in a stress free environment can have a negative impact on the mechanical properties of the engineered tissue. To overcome this problem, recently new types of bioreactor have been developed which attempt to induce appropriate stresses in the cultured cells *e.g.* using magnetic forces [18, 42].

1.2 The Liver

Weighing approximately 1.5 kg, the liver is the largest, and most metabolically complex, organ in humans. It receives oxygenated blood from the hepatic artery, and also blood from the gut (via the hepatic portal vein), which facilitates the processing of the nutrients and removal of toxic byproducts from food digestion. The liver controls carbohydrate and lipid metabolism, regula-

tion of the blood glucose level (by storing excess glucose as glycogen, which is converted back into glucose when required) and also stores many vitamins and minerals. In addition, it performs an essential role in the metabolism of many types of drugs. Other important functions include the secretion of bile (to aid digestion of fats), production of blood coagulation factors and conversion of ammonia to urea. Unsurprisingly, given that the liver is estimated to have around 500 different functions, at present there is no artificial organ or medical device which is capable of replacing it. Some systems have been designed which remove blood toxins accumulated during liver failure by *e.g.* haemodialysis, haemofiltration and plasma exchange, but these have so far shown disappointing results in terms of patient survival [48]. Thus, the only treatment currently available for serious, end-stage liver disease is organ transplantation.

In vivo, under non-pathological conditions, the majority of liver tissue (around 80 % [69]) is composed of hepatocytes. These are epithelial cells which form the liver's basic functional units [108] and are arranged in lobules (see Fig. 1.1). Blood, from branches of the hepatic artery and hepatic portal vein, flows through the sinusoids between the plates of hepatocytes, towards the terminal hepatic venule, which eventually rejoins the hepatic vein. The endothelial cells lining the sinusoids differ from the vascular endothelium elsewhere in the body in that they lack a basement membrane and contain numerous fenestrae. These features give the hepatocytes ready access to the nutrients and macromolecules in plasma, which is essential for them to carry out many of their functions. The bile canaliculi are formed by grooves on the contact surfaces of adjacent plates of hepatocytes. Bile produced in these tiny channels flows into the interlobular bile ducts, which connect with the gall bladder; this in turn drains into the intestines, where the bile is used in the digestion of fats.

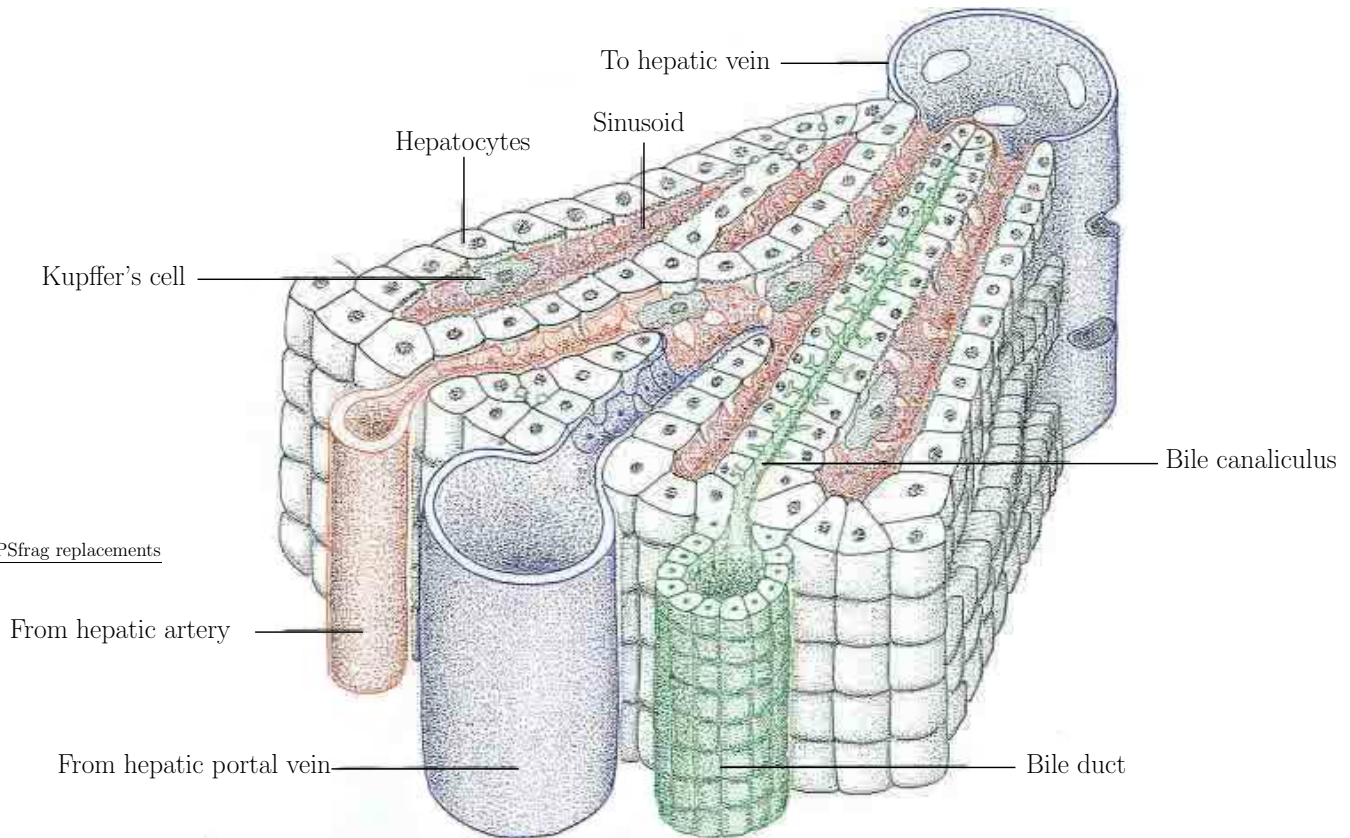


FIGURE 1.1: A liver lobule (image adapted from www.biologymad.com).

In addition to hepatocytes and endothelial cells, the liver also contains Kupffer's cells, pit cells and stellate cells (also known as Ito cells). Kupffer's cells, found in the sinusoids, are tissue macrophages whose major functions are phagocytosis of foreign particles and removal of noxious substances, whilst pit cells form part of the lining of the sinusoid and are large granular lymphocytes, which function as natural killer cells [137]. Stellate cells are perisinusoidal cells which surround hepatocytes with long processes. They store vitamin A, secrete a number of growth factors, and produce ECM proteins [66]. In the event of liver injury, they become activated and highly proliferative, secreting large amounts of collagen, which contributes to liver fibrosis.

Under normal conditions, the proliferation rate of hepatocytes is low (the

liver is replaced by standard tissue renewal about once a year, [139]) but their capacity for regeneration after liver injury is considerable [66]. The reconstitution of the entire organ after partial hepatectomy (surgical removal of up to 70% of the liver) occurs within around two weeks [139]. The factors which orchestrate and control this process are currently an area of active experimental research. Hepatocyte growth factor (HGF) and epidermal growth factor (EGF) are known to provoke hepatocyte proliferation, whilst many other growth factors appear to have some role to play [66, 106]. Tissue engineers aspire to harness this amazing regenerative capacity to produce functional liver tissue *in vitro*, and hence the effects of many of these chemicals on cultured hepatocytes are currently under study [56].

1.3 Liver cell culture *in vitro*

Diseases of the liver, including hepatitis and cirrhosis, were the cause of around 46,000 deaths in the USA in 1998 [19], and at present there are few successful treatments for such conditions apart from organ transplant. Whilst waiting lists for transplants continue to lengthen, the level of organ donation has remained static [83], so interest has logically turned in recent years towards the development of liver support devices. Passive systems to remove blood toxins accumulated during liver failure have shown disappointing results in terms of patient survival, and so attention has focused on cell-based liver assistance devices [48]. The engineering of liver tissue for such devices, for drug testing and, potentially, for transplantation, has stimulated new interest in understanding the interactions amongst the various cell populations in the liver, and amongst the cells, growth factors and ECM.

Hepatocytes cultured *in vitro* often form a monolayer; grown in this way, the cells have a tendency to de-differentiate (lose their ability to function nor-

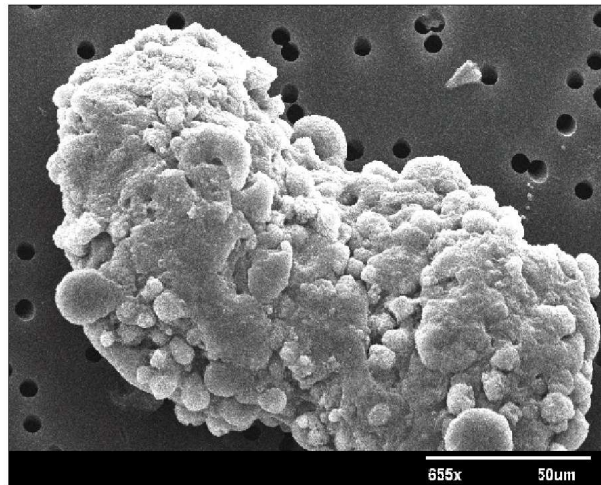


FIGURE 1.2: Scanning electron micrograph of a multicellular liver spheroid (courtesy of L. Riccalton-Banks, Tissue Engineering Group, University of Nottingham)

mally) within hours, and to die after a few days [9,101]. Various techniques have been developed in an attempt to overcome this problem, including co-culture with other types of cell, culture on polymer scaffolds and the use of growth factors and cytokines [9]. Some of these techniques result in the hepatocytes forming multi-cellular spheroids (see Fig. 1.2). The migratory behaviour of hepatocytes which leads to aggregation is described in detail in [96]. This study found that only around 6 % of observed cells exhibited ‘classical single-cell locomotion’, defined as occurring when a cell translates at least one body length, without contacting another cell. More frequently, cells exhibited membrane extension, and these extensions often led to direct cell-cell coupling, giving rise to the formation of a growing aggregate. Translation of the coupled cells was not quantified in this study; however, many of the cells were observed to translate more than one body length after cell-cell contact had occurred.

On suitable substrates, the cell clusters reorganise themselves into multicellular spheroids, which then detach from the surface (see Fig. 1.3). The arrangement of the cells in spheroids appears to mimic, in some respects, that

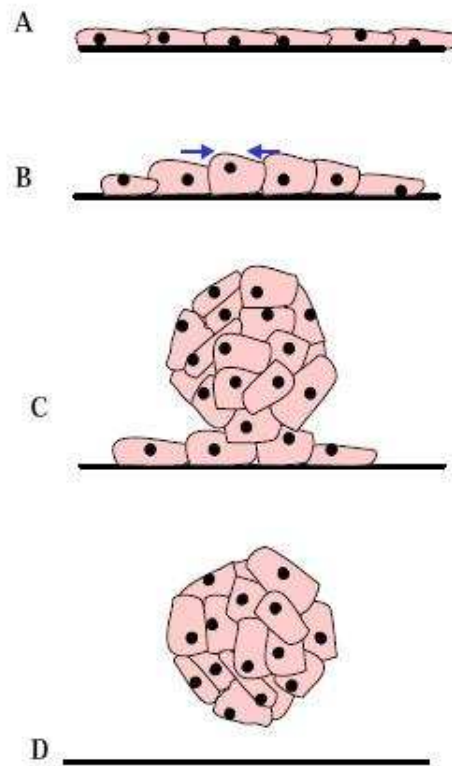


FIGURE 1.3: Schematic representation of the process of spheroid formation (from [102]). (A) Cell clusters form on the surface of the substrate. (B) Clusters begin to contract (arrows indicate direction of contraction). (C) Cell contact with the surface decreases at the centre of the aggregate and a three-dimensional structure is formed. (D) The spheroid detaches from the surface.

seen *in vivo* - for example, channels resembling bile canaliculi are seen [2]. Spheroid culture also results in prolonged expression of liver-specific functions (commonly measured by albumin production [102]) and hepatocyte viability [103].

A common procedure for culturing hepatocytes as spheroids involves seeding the freshly isolated cells in culture wells coated with ECM and bathed in a culture medium, which supplies them with nutrients such as oxygen. This is

the method of culture on which we concentrate in this thesis. Hepatocytes are anchorage-dependent cells [9, 108], and their interactions with the ECM are believed to be of great importance, both *in vivo* [8] and *in vitro*. Significantly, experiments have shown that the kind of ECM used affects the morphology of the cells, the likelihood of aggregation, and the ability of the cells to sustain liver specific functions [70, 97]. Tissue engineers employ a wide variety of types of ECM. Often these are artificial substrates such as tissue culture plastic (TCP) or polylactic acid (PLA). However, unlike the ECM *in vivo*, such substrates lack specific recognition groups for cells. Matrix proteins such as fibronectin can be employed to modify such surfaces, and provide a more favourable environment for attachment (see [134, Ch. 5]). Another approach is to culture the cells on natural ECM components, such as Matrigel or in a collagen sandwich [103]. In addition to cell-ECM interactions, cell-cell contacts appear to play a significant role, and studies have shown that spheroid formation is inhibited if the initial cell plating density is either too high or too low [93, 94]. Cell-cell interactions are also important in maintaining the viability and functionality of the hepatocytes [71].

The role of chemical signalling in spheroid formation is another area of considerable interest. Potentially, aggregation may be due to a chemotactic response, as experimental studies have found that artificially stimulating the hepatocytes with HGF (hepatocyte growth factor) and EGF (epidermal growth factor) promotes aggregation [110, 113]. We develop and investigate mathematical models based on this hypothesis in Chapters 3 and 4. Evidence for chemical signalling between hepatocytes *in vitro* is provided by studies showing that adding hepatocyte conditioned medium (*i.e.* medium which has already been used in a hepatocyte culture system) to freshly isolated cells also promotes aggregation [37].

The role of stellate cells in the aggregation process is an area of active

research. Experimental results show that aggregation is initiated more quickly when stellates are added to the cultured hepatocytes, but the reason for this is not clear [102]. Cell-cell contacts may be significant, as the stellates extend long processes, contacting multiple hepatocytes [118]. However, enhanced chemical signalling may also explain this effect, as *in vivo* the stellates are important producers of HGF [32, 106]. Both hypotheses are investigated in more detail in Chapter 5.

In this section, we have focused on the culture of liver cells as spheroids in culture wells where the culture medium is not agitated (as in a bioreactor). The models developed in this thesis are all based on this method of static culture, and concentrate on the early stages of spheroid formation, during which the cells aggregate to form clusters. This is because we believe it is important to try to understand this simple system, before moving on to more complex cases. However, it is by no means the only way of culturing hepatocytes - some groups are investigating the efficacy of using porous scaffolds (*e.g.* [28]), whilst others have constructed elaborate bioreactor systems [95]. Mathematical modelling of these alternative types of culture system (applied to other cell types) is currently an area of active research (see *e.g.* [59, 131] and references therein).

1.4 Theoretical approaches to tissue formation

At present, we still do not completely understand the processes by which tissues are assembled in the body [22], and we are thus a long way away from being able to harness and manipulate these processes in order to fabricate functional tissues *in vitro*. Morphogenesis is the term used to describe that part of embryology concerned with the development of pattern and form [76]; *i.e.* the processes of cell proliferation, migration and differentiation which eventually give rise to the different tissues, organs and body parts. In this section,

we shall review some of the main hypotheses put forward to explain various aspects of morphogenesis, and discuss their relevance in the field of tissue engineering.

Some of the most influential ideas about the mechanisms of morphogenesis were presented in Turing's famous paper of 1952 [124]. He considered the reaction and diffusion of two chemical species, referred to as 'morphogens', and showed that the uniform steady state of the governing equations may be unstable. This instability can give rise to spatial patterning. Turing assumed that cells can 'read off' this pattern by changing their behaviour according to the local concentration of the two morphogens. For example, cells may express a dark pigment when the concentration of morphogen X is greater than that of Y , and remain unpigmented otherwise; this could explain the formation of simple animal coat markings [76].

Turing's theory is attractively simple, and was mathematically novel in that the instability is driven by diffusion, usually considered a stabilising influence. The ideas have stimulated a great deal of research, with extensions taking into account the effects of domain geometry, domain growth and boundary conditions to name but a few [76]. Whilst in some cases (*e.g.* animal coat patterns) the theory appears to reproduce observations very accurately, its most significant weakness is that, to date, very few morphogens have been identified in real organisms [76]. This has been a great obstacle to the theory's general acceptance as an explanation for pattern formation in morphogenesis, and as a result, a number of rival hypotheses have emerged.

One of the most influential alternatives to Turing's theory is the so-called 'Differential Adhesion Hypothesis' (DAH), also known as the Steinberg hypothesis. This was inspired by observations of the behaviour of two initially dissociated populations of different cells. Depending upon the two cell types

involved, a particular final configuration of the populations would be seen; the two cell types might intermix, one cell population might completely, or incompletely, surround the other, or the two populations may remain separate. Steinberg adopted a thermodynamic type approach to this problem [112]. He postulated the collection of dissociated cells had a ‘free energy’; this could be reduced by the formation of adhesions between individual cells. He labelled the two cell types A and B , and showed, using simple mathematics, that the final configuration observed would depend on the relative strengths of the $A - A$, $A - B$ and $B - B$ adhesions.

A satisfying feature of this theory was the fact that it could be used to make predictions (*e.g.* if type A cells surround type B , and type B cells surround type C , then A should surround C), and these predictions agreed with experimental results [112]. Indeed, a large volume of subsequent research is in support of the DAH, and its ideas can be extended to deal with cell-ECM interactions [6]. However, it does notably fail to explain why homologous adhesions (*i.e.* those between cells of the same type) are, with a few exceptions, established more quickly than heterologous ones, even when the DAH predicts (from the final configuration of the cells) that the latter should be stronger. Another weakness is the fact that the DAH can only generate a small number of configurations, which do not include tubules and epithelial structures; however, a modified version of the hypothesis, in which cells have multiple domains of differing adhesiveness appears to overcome this problem [6].

The two hypotheses outlined above consider the effect of diffusible chemicals and cell-cell and cell-ECM adhesions separately. The mechanochemical theory of Murray and co-workers [76–78] attempts to unite a number of different processes within a single framework. The main tenet of the theory is that tissue formation is a dynamic process in which cell proliferation, and cell-cell and cell-ECM adhesions interact with environmental cues to produce cell

movements which give rise to pattern formation. Particular consideration is given to cell migration along concentration gradients of diffusible or bound chemicals (termed chemotaxis and haptotaxis respectively), but other possible influences are also discussed, including applied electrical fields (galvanotaxis). This approach underpins the models developed in the later chapters of this thesis. Due not least to the greater number of effects included, the mechanochemical theory appears to have greater scope for generating different types of pattern than those previously mentioned. Mathematical models based on these ideas have been extensively studied in connection with a wide variety of systems, including limb-bud formation, wound healing and cancer [85, 116, 123]; however, we shall postpone discussion of such work until the next section.

1.5 Mathematical models

Originally published in 1917, D'Arcy Thompson's 'On Growth and Form' [121] is one of the earliest, and certainly one of the most influential, works detailing the insights into the natural world that can be gained by the application of mathematical ideas. However, despite a few notable contributions during the intervening period, such as that of Turing, mathematical biology is a relatively new field, with most of the literature being less than 30 years old. In this section, the aim is to introduce some of the more influential mathematical models which have been proposed in connection with pattern formation in biological systems, and to discuss some of the general issues with which the modeller must be concerned.

1.5.1 Individual-based versus continuum models

In considering biological systems made up of interacting individuals, be they cells or entire organisms, the modeller must make a fundamental choice of

approach; whether to seek to determine the trajectory in space and time of each individual making up the system, or to forgo such a detailed description and focus on collective behaviour, by formulating equations for the density of individuals. The latter description is termed a continuum approach, and until recently, most models in mathematical biology have been continuum models. The advantage of the continuum approach is that it gives rise to a model which comprises a system of partial differential equations (PDEs); this allows us to apply a vast range of mathematical techniques from PDE theory in the analysis of the model, and we can often construct analytical or asymptotic, as well as fully numerical, solutions to the governing equations. However, the challenge then remains in relating solutions of the continuum model to experimental data, which may be presented in terms of discrete individuals.

Models which allow us to follow the trajectory of each individual are termed Lagrangian, and clearly give very detailed information about the evolution of the biological system. However, this type of model can be difficult to analyse, especially when large numbers of individuals are present. A recent example of a Lagrangian model, representing swarming behaviour, is presented in [74]; under suitable assumptions concerning the interaction forces between individuals (namely, that these be of gradient type), analytical results can be obtained from the model, via consideration of a Lyapounov function. In general though, analytical insights may not be available, and individual-based models often rely heavily on numerical simulations. A particularly simple type of individual-based computational models is termed a cellular automaton [30]. These numerical simulations are discrete in time, space and state, with a set of rules governing the interactions between individuals. As the computing power available to modellers continues to increase, individual-based models are becoming more common.

1.5.2 *Dictyostelium* aggregation and the Keller-Segel model

One of the best known examples of cell aggregation behaviour occurs in the slime-mould *Dictyostelium discoideum*. In this organism, aggregation is driven by chemotaxis - *i.e.* the migration of cells up spatial gradients of a chemical, in this case cAMP. It is in connection with work on this species that Keller and Segel's widely-used model of chemotaxis, was derived [51, 52]. The model consists of two equations, an evolution equation for the cell density, n , with movement due to random motion and chemotaxis, and a reaction diffusion equation for the chemoattractant (cAMP) concentration, c

$$\frac{\partial n}{\partial t} = \nabla \cdot (\mu \nabla n) - \nabla \cdot (\chi n \nabla c) + f(n, c), \quad (1.5.1)$$

$$\frac{\partial c}{\partial t} = \nabla \cdot (D \nabla c) + g(n, c). \quad (1.5.2)$$

Here, the constants μ and χ are the random motility and chemotactic sensitivity coefficients for the cells, D is the diffusion coefficient of the chemoattractant and the functions f and g describe the production and degradation of the cells and chemoattractant respectively. In many cases, the diffusion of the chemoattractant will be rapid compared to the timescale of aggregation, in which case the LHS of equation (1.5.2) can be set to zero. For simple choices of g , the solution of the resulting equation can then be obtained in terms of n using Green's functions, as in *e.g.* [63].

The Keller-Segel model has found many applications in other biological situations. Numerous extensions to this basic model have been considered, including various non-constant forms for the cell motility parameters μ and χ , and different types of cell birth/death and chemical production/degradation terms; an excellent summary of these studies is given in [63]. However, an unfortunate feature of the Keller-Segel model is the fact that solutions for the cell density may become arbitrarily large [86], which is clearly unrealistic; as a result, further modifications have been proposed, to include effects such as

space limitation, to eliminate this feature [89].

A second strand of research has concentrated on validating continuum models by relating the behaviour of individual cells to the population level equations. Two types of cell movement are commonly assumed in deriving continuum equations in this way. The mathematically simpler of the two is known as a ‘space jump’ process, and considers cellular motion as a series of discrete jumps in space [86, 89]. However, it has been noticed through observations of bacteria, that they tend to move in straight lines, before suddenly stopping and reorienting themselves, a phenomenon known as ‘run and tumble’. The assumption of this type of motion is described as a ‘velocity jump’ process. Under either set of assumptions, it is possible in appropriate limits to recover population-level equations similar to the Keller-Segel model [89, 92].

We should also note some more recent work on *dictyostelium* aggregation, which has taken a different approach from that of Keller and Segel. In [90, 91], an individual-based computational approach to cell aggregation and collective movement of the resulting aggregate are discussed. The model produces good agreement with experimental results, and may also be conveniently visualised as animations, in a way which makes it easy to understand for non-mathematicians. Collective movement of the cell aggregates is also discussed in [126], where the cells are modelled as a viscous fluid, similar to the approach taken in some multiphase models of tumour growth (*e.g.* [12]) which are discussed in §1.5.5. The type of model developed in [126] has also been extended to describe cell sorting within aggregates [125].

1.5.3 Mechanochemical models

We have discussed in §1.4 how mechanochemical theory relates the formation of pattern in biological tissues to interactions between the cells and their envi-

ronment. The aim of this section is to illustrate the mathematical formulation of the theory, through a simple example. In [78], the interactions between a single population of cells of density $n(\mathbf{x}, t)$ and the ECM are considered. The ECM has density $\rho(\mathbf{x}, t)$, and its displacement vector is denoted by $\mathbf{u}(\mathbf{x}, t)$. Conservation of cells leads to a general equation of the form

$$\frac{\partial n}{\partial t} = -\nabla \cdot \mathbf{J} + M, \quad (1.5.3)$$

where \mathbf{J} is the cell flux and M is the cell proliferation rate.

The flux of cells \mathbf{J} is prescribed in terms of the cell and ECM densities, and the ECM displacement, the aim being to represent a number of factors known to influence cell movement, such as random dispersal, haptotaxis (movements along gradients of a bound chemical) and so forth. When cell proliferation is negligible, equation (1.5.3) is frequently assumed to take the form

$$\frac{\partial n}{\partial t} = \underbrace{D_1 \nabla^2 n - D_2 \nabla^4 n}_{\text{dispersal}} - \underbrace{\nabla \cdot (\alpha n \nabla \rho)}_{\text{haptotaxis}} - \underbrace{\nabla \cdot \left(n \frac{\partial \mathbf{u}}{\partial t} \right)}_{\text{advection}}. \quad (1.5.4)$$

The first term on the RHS represents random cell dispersion due to Fickian diffusion, as in the Keller-Segel model. However, when cell density is high, the cells may also be able to sense the *local average* cell density, and this effect is represented by the biharmonic term. (The two dispersal coefficient (D_1 and D_2) are generally assumed constant for simplicity.) The remaining terms model haptotaxis (with haptotactic sensitivity α) and advection of the cells due to ECM displacement. Additional effects, such as chemotaxis, may also be incorporated, by the addition of appropriate terms.

Conservation of mass for the ECM leads to the following equation

$$\frac{\partial \rho}{\partial t} + \nabla \cdot \left(\rho \frac{\partial \mathbf{u}}{\partial t} \right) = 0, \quad (1.5.5)$$

where we have assumed that matrix production by the cells is negligible and the displacements of the ECM are small, so its velocity is approximately $\frac{\partial \mathbf{u}}{\partial t}$. An

evolution equation for \mathbf{u} , the ECM displacement, is generated by considering the momentum balance on the system (neglecting inertial effects, and assuming no external forces act on the cells). This gives

$$\nabla \cdot (\boldsymbol{\sigma}_{ECM} + \boldsymbol{\sigma}_{cell}) + \rho \mathbf{F} = 0, \quad (1.5.6)$$

where $\boldsymbol{\sigma}_{ECM}$ and $\boldsymbol{\sigma}_{cell}$ are the stress tensors for the two phases and \mathbf{F} represents the external forces exerted on the ECM (per unit matrix density). Constitutive relations specifying the stress tensors for the cells and extracellular matrix are hence required; however, it is not necessary to specify the nature of the interaction forces between the cells and ECM. This is because the cell flux is prescribed in terms of n , ρ and \mathbf{u} , rather than being derived from a momentum balance (as is the case for most multiphase models - see §1.5.5). The model then consists of equations (1.5.4)-(1.5.6), together with the constitutive relations and suitable boundary conditions. These are investigated using a combination of linear stability analysis, weakly non-linear analysis and numerical simulations [64, 76]. We note that the exact form of the constitutive relations specified can have an effect on the stability behaviour of the model, as is shown in [14].

As was previously remarked, mechanochemical models offer enormous scope for generating many different types of patterns, through many different types of effect. Even a very simple case, in which cell birth and death are neglected and cells move only by advection with the ECM, has been shown to support rolls and hexagons as stable patterns in 2D [64]. This richness of behaviour suggests that they will provide a fruitful area for further study in the future.

1.5.4 Non-local models

The models discussed in the preceding sections involve systems of differential equations which describe the evolution of a variety of biological species

in terms of the values of those quantities and their derivatives at a particular point in time and space. However, the underlying biology may often lead us to want to include dependence on the values of the variables at other points in space. (For example, in Chapter 5 we discuss how hepatocytes may be pulled toward nearby stellate cells by their tentacle-like processes; the movement of an hepatocyte thus depends on the presence of stellates in a neighbourhood surrounding it.) We would term these models non-local. Note that we use this term to mean a model where the non-local dependence occurs explicitly in the governing equations (*e.g.* [73]). Such a model may be recovered from the Keller-Segel model under suitable assumptions (as we explain below), but in its original form, we would not term the Keller-Segel model non-local. The aim of this section is to describe non-local models in greater detail, discussing their advantages and disadvantages, and their connection with other models.

There are numerous biological situations in which non-local effects are likely to be important. In a swarm or similar grouping, organisms are likely to use visual, auditory or other cues to orient themselves, implying a long-range interaction [72,73]. In cell biology, the phenomenon of contact inhibition of cell motion suggests that short-range physical contacts between cells give rise to changes in cell velocity [72]. These non-local interactions may be introduced into mathematical models via integral terms, so that the model (in a one-dimensional Cartesian geometry) typically has the following form

$$\frac{\partial n}{\partial t} + \frac{\partial}{\partial x} \left(n \int_D K(x - \xi) n(\xi, t) d\xi \right) = D_n \frac{\partial^2 n}{\partial x^2}, \quad (1.5.7)$$

where K is the kernel function which represents the non-local interactions, and we have neglected birth and death (see also [73]). Naturally, the appropriate form for the kernel will vary depending on the situation being modelled. In [73] the authors show how, in the context of swarming behaviour, an odd kernel induces organisms at the edges of the swarm to move towards its centre (*i.e.* the swarm becomes more dense). An even kernel results in collective motion of the swarm.

In mathematical ecology, models similar to those above may be used to describe the distribution of a population of organisms, with the non-local terms representing competition for food resources. Additional terms may be included to represent the effects of grouping, and competition for space [40]. For certain cases in which the kernel is even, travelling wave solutions of the ecological model may be found [10, 40]. Similarly, travelling band solutions for a particular case of a swarming model are found in [73]. However, in general we should note that the problem with non-local models is that it is much more difficult to make any analytical progress [72]. One obvious method might be to try to expand the solution as a Taylor series, assuming that the higher order terms are negligible and hence reducing the integro-differential equation to a PDE. Unfortunately, this does not always give an accurate approximation [72, 73]. Nevertheless, there are mathematical advantages in using a non-local treatment when considering aggregation phenomena, as in some cases local models may give rise to a backward heat-type equation, which is ill-posed [16].

Finally, we should remark that one of the most natural ways for non-local models to arise is as a limiting case of a larger system of local model equations. If we take a one-dimensional version of the standard Keller-Segel model (1.5.1) and (1.5.2), with $g(n, c) = a^2(n - c)$, and assume that $\mu \ll D$, so we can set $\frac{\partial c}{\partial t} = 0$, we find a Green's function solution (on an infinite domain)

$$c = \frac{1}{2} \int_{-\infty}^{\infty} e^{-a|x-\xi|} n(\xi) d\xi. \quad (1.5.8)$$

Upon substituting this solution into equation (1.5.1), we obtain an integro-differential equation, as shown in [63].

1.5.5 Multiphase models

In a biological context, it is frequently necessary to consider the interactions amongst several different types of materials; common examples are cells

and extracellular water [12, 15], ECM [47, 62] and other cell populations *e.g.* macrophages [87]. These different materials are often referred to as different phases, and multiphase models which use the theory of mixtures have recently emerged as a way of treating such situations. It is not our intention to enter into a detailed discussion of the derivation of the governing equations here (this is given in [25–27]), but rather to discuss the general issues which arise from this approach.

The multiphase approach arrives at a macroscopic model of the behaviour of the various phases through the averaging of the exact equations of motion (*i.e.* mass and momentum conservation). The details of the average used are not of great importance; volume and ensemble averages are frequently employed [26] (see also Appendix A for an example of the volume averaging approach applied to a reaction-diffusion equation). The resulting momentum equations then contain terms which represent the effects of interphase drag and interfacial forces. We must specify the form of these terms via a constitutive relation [27, 65]. Although the resulting system of equations may be nonlinear, it nonetheless represents a significant simplification. Were we to use the exact formulation, we would have to take into account the fact that the interfaces between different phases represent free boundaries, the position of which must be determined as part of the solution. The averaging procedure ‘smears out’ the interfaces, essentially by allowing more than one phase to occupy a particular point and thus avoids this complication.

One of the differences between multiphase models and the others discussed in this section is the need to specify not only constitutive relations for the mechanical properties for each of the phases, but also to postulate the form of the interaction forces between them. At present, relatively simple forms for these interactions are usually employed *e.g.* drag-type terms [12, 15]. However, establishing more physically realistic constitutive relations for biological

materials is an area of intense research interest, as we shall see below.

1.5.6 Continuum descriptions of biological materials

The mechanical response of a material to an applied force depends on its internal composition, and is described by the stress tensor. A complete and accurate description would include the effects of small-scale structures within the material on its behaviour - *e.g.* the deformation of a tissue depends upon the behaviour of each of the different cells types of which it is composed, the extracellular matrix, and the ways in which these components adhere to each other. However, because in a biological context such details are often prohibitively complex there has been a tendency instead to rely on a phenomenological description, in the form of a constitutive relation for the stress tensor, which provides a reasonably accurate representation of the material's overall behaviour under the particular conditions of interest [46].

In situations where we are not concerned with phenomena on sub-cellular lengthscales, a single cell is often represented as a fluid-filled 'bag' [128]. In many cases, the fluid is assumed to be Newtonian. However, a more accurate treatment might assume the fluid is viscoplastic (only able to flow when the stress exceeds a certain threshold) and may also include the nucleus as a separate material (viscous, elastic and viscoelastic nuclei have been assumed by different authors [82, 128]). An alternative approach has been to consider the cell as a viscoelastic body [41]. More recently, the contents of the cell have been modelled as a two-phase mixture of viscous and inviscid fluid, the viscous component representing the actin network, which is essential to cell migration, whilst the inviscid part represents the surrounding solution [84].

Researchers have also begun to look at ways of including microscale effects when moving from a single cell to multicellular or tissue-level description. Mixture theory, as discussed above, provides one possible mathematical frame-

work, and has been used in the description of tumours [12,17], and engineered cartilage tissue, which consists of cells seeded in an artificial scaffold [59]. Another possible approach is to use homogenisation theory [128]. This assumes that the macroscopic material of interest (*e.g.* the tissue) consists of a periodic array of a large number of much smaller units, usually referred to as ‘cells’ (though they do not necessarily have to correspond to single biological cells, but rather, they are the basic units of which the material is made up). The key assumption is that the ratio of the microscopic ‘cell’ lengthscale to the macroscopic ‘tissue’ lengthscale, ϵ , is extremely small, as this permits the use of a multiple scales expansion for the spatial gradients in the relevant governing equations. The dependent variables are then likewise expanded as power series in the small parameter ϵ , and perturbation solutions sought in the usual way.

We illustrate the procedure by giving a simple example of a biological application of the technique from Chapter 7 of Keener and Sneyd [50]. It concerns the diffusion of a chemical signal through a line of N cells (where $N \gg 1$) separated by gap junctions. We assume that the chemical concentration u obeys

$$\frac{\partial u}{\partial t} = \frac{\partial}{\partial x} \left(\frac{1}{R(\frac{x}{\epsilon})} \frac{\partial u}{\partial x} \right), \quad (1.5.9)$$

where $\epsilon = 1/N$ is the ratio of the lengthscale of a single unit (cell plus gap junction) to the lengthscale of the tissue. The resistance R thus varies over the short lengthscale. We then introduce two independent spatial variables $y = x$ and $z = x/\epsilon$, in terms of which equation (1.5.9) becomes

$$\frac{\partial u}{\partial t} = \left(\frac{\partial}{\partial y} + \frac{1}{\epsilon} \frac{\partial}{\partial z} \right) \left(\frac{1}{R(z)} \left(\frac{\partial u}{\partial y} + \frac{1}{\epsilon} \frac{\partial u}{\partial z} \right) \right). \quad (1.5.10)$$

We expand the solution as

$$u(x, t) = u_0(y, t) + \epsilon u_1(y, z, t) + \epsilon^2 u_2(y, z, t) + \dots \quad (1.5.11)$$

and thus obtain equations for u_0 , u_1 and u_2 from equation (1.5.10). After some

manipulation, we can eliminate u_1 and u_2 , and obtain the following for u_0

$$\frac{\partial u_0}{\partial t} = D_e \frac{\partial^2 u_0}{\partial y^2}, \quad (1.5.12)$$

where $D_e = 1/\bar{R}$ and \bar{R} is the resistance averaged over a unit - *i.e.*

$$\bar{R} = \int_0^1 R(z) dz. \quad (1.5.13)$$

The result of homogenisation is thus a macroscopic equation (or set of equations) which contain information about the microstructure through the values of the coefficients. The mass and momentum conservation equations for an elastic solid containing fluid-filled pores were derived using this method by Burrige and Keller [13]. These results were exploited, and extended to the case of a viscoelastic solid, by Owen and Lewis in a model of the mechanics of lung tissue (where the ‘cells’ were the alveoli) [88]. However, the assumption of the periodicity of the material on the microscale limits the usefulness of the technique, as, for example, situations in which the arrangements of cells change over time cannot be accommodated.

1.6 Thesis overview

As we have seen, the formation of spheroidal liver cell aggregates appears to hold the key to growing functional liver tissue which will remain viable for prolonged periods, *in vitro*. In this thesis, we concern ourselves only with the initial stages of spheroid formation, in which cell clusters are formed on the surface of the culture well, rather than on the subsequent reorganisation of the cells into a spheroid, which is followed by detachment from the surface. Our aim is then to use mathematical models to understand the dynamics of cell aggregation, and in particular, the roles of cell-ECM adhesion, chemical cues which regulate cell movement (chemotaxis) and cell-cell interactions in co-culture.

In Chapter 2, we focus on the question of how cell-ECM adhesion affects the aggregation process. We derive a new model for cell aggregation, based on the principles of the mechanochemical theory, but employing a multiphase modelling framework as described in §1.5.5. The two-phase approach allows us to couple the motion of the cells with that of the culture medium in which they are grown, the two phases being treated as viscous and inviscid fluids respectively. In an extension of previous multiphase models (*e.g.* [12]), cell movement is also coupled to the deformations of the ECM (which coats the base of the culture well) which is assumed to be a Voigt viscoelastic material. In order to render the model tractable, an idealised one-dimensional slab geometry is assumed, and we neglect any chemical signals which might affect cell movement, instead prescribing the forces generated by the cells as a function of cell density. We use linear stability analysis to determine the parameter regimes in which we can expect to observe aggregation. Numerical simulations are then employed to determine the effect of varying certain key parameters. We find that the cell seeding density and degree of cell-ECM adhesion are the most important factors influencing aggregation.

In Chapter 3, the two-phase model developed in Chapter 2 is extended and refined. Cell movement is taken to depend upon the concentration of a chemoattractant in the surrounding culture medium, and a two-dimensional geometry - representing a section through the culture well - is assumed. This extends the earlier two-phase model of chemotaxis by Byrne and Owen [16], who consider a one-dimensional geometry and neglected cell viscosity and cell-ECM adhesion. Following King and Oliver [53], we then consider the limit in which the depth of the layer containing the cells is small compared to its length. We find there are two scaling regimes (which, borrowing terminology from fluid mechanics, we call ‘extensional’ and ‘lubrication’) in which the two-dimensional governing equations may be reduced to one-dimensional form. The reduced models are investigated using a combination of linear sta-

bility analysis and numerical simulations in Chapter 4. In both regimes, we find that the cell seeding density determines the number of aggregates formed, and the rate of aggregation. In the extensional regime, cell-ECM adhesion has little effect on cell behaviour, whilst in the lubrication regime, increased cell adhesion reduces the rate of aggregation. As in Chapter 2, the mechanical properties of the ECM have negligible effect on the formation of aggregates.

The interactions of hepatocytes and hepatic stellate cells in co-culture are considered in Chapter 5. Here, we adopt a different modelling framework, based on the non-local approach described in §1.5.4. Earlier work by Mogilner and Edelstein-Keshet [73], who considered a swarm consisting of a single species, is extended to the case of two interacting populations. We formulate two models, based on alternative experimental hypotheses about how these two cell types affect each other. The first is that the interaction occurs via chemical signals; the second, based on time-lapse video taken during co-culture, is that the stellates put out long tentacle-like protrusions which, when they contact hepatocytes, physically pull the cells into an aggregate. The models neglect interactions between the cells and the ECM and culture medium, in order to focus on the cell-cell interactions, and once again, assume an idealised one-dimensional geometry. For both hypotheses, if the hepatocyte-stellate interaction is stronger than the hepatocyte-hepatocyte interaction, we observe the formation of aggregates in which both cell types are evenly distributed. Conversely, if the hepatocyte-hepatocyte interaction is the stronger, stellates are relegated to the edges of the aggregates. Comparison with experimental results suggests that the hepatocyte-stellate attraction is strongest in practice, in which case our model results suggest aggregation may occur most swiftly when the cell types are seeded in a 1:1 ratio.

The thesis concludes in Chapter 6, where we summarise our main results, and offer suggestions for further work.

Chapter 2

A one-dimensional two-phase model of hepatocyte aggregation *in vitro*

2.1 Introduction

As described in the previous chapter, when seeded onto suitable substrates and cultured under appropriate conditions, hepatocytes form cell clusters or aggregates, which eventually reorganise themselves into spheroids. In this chapter, we develop a simple mathematical model of hepatocyte aggregation. Our aim is to use the insights gained from our model to suggest ways in which tissue engineers may be able to improve their culture technique in order to speed up aggregation. We use a multiphase framework, similar to that adopted by Beward *et al.* [12], which allows us to couple the motion of the cells and the culture medium in which they are grown. However, our model extends this work by coupling the movement of the cells with the deformations of a layer of ECM which occupies the base of the culture well. Our model is thus similar to

the mechanochemical models of Murray and co-workers described in Chapter 1. However, instead of prescribing the cell flux as in equation (1.5.4), we derive it from a momentum balance.

Previous modelling work on this problem appears limited. Glicklis *et al.* [39] assumed the diameter of individual spheroids undergoes logistic growth, and determined the values of the relevant parameters by fitting to experimental data. They then used this solution to determine the rate of albumin production. To the best of our knowledge, ours is the first mechanical model of the aggregation process. We consider hepatocytes plated onto a layer of ECM and bathed in culture medium (see Fig. 2.1). In formulating our model, we shall make two important assumptions. Firstly, we do not explicitly include the effects of chemotaxis. Although this is a potential mechanism for hepatocyte aggregation, for simplicity we omit consideration of chemical factors in this chapter. Instead we relate the forces generated by the cells directly to the cell volume fraction. This allows us to concentrate on the effect of cell-ECM adhesion on aggregate formation. Secondly, we assume that the cells are well nourished and hence neglect nutrient transport. We remark that, in the absence of a complete set of data for hepatocytes, some of our modelling assumptions are speculative, so we do not attempt to recreate the full complexity of the biological system. Our aim instead is to gain insight into the dynamics of the aggregation process and provide a starting point for further experimental research by suggesting which variables may have the most significant effect.

The remainder of this chapter is structured as follows. In §2.2, we derive mass and momentum balances for the cellular and culture medium phases (hereafter referred to collectively as the cell culture region) and the ECM. In §2.2.1, we close the model by introducing constitutive laws for the mechanical properties of the cells, culture medium and ECM. Interaction forces are also specified as drag-type terms, being proportional to the difference in velocity

of the two phases in question. Suitable boundary and initial conditions are specified in §2.2.2 and the model reduced to a system of four coupled PDEs in §2.2.3. In §2.3 we consider the linear stability of the spatially uniform steady state solution of the reduced model, to determine the parameter regimes in which we can expect to observe aggregation. This is followed by consideration of the long-time behaviour of the model in §2.4. Numerical simulations are presented in §2.5. The chapter concludes in §2.6 with a discussion of our main results, and suggestions for future work.

2.2 Model formulation

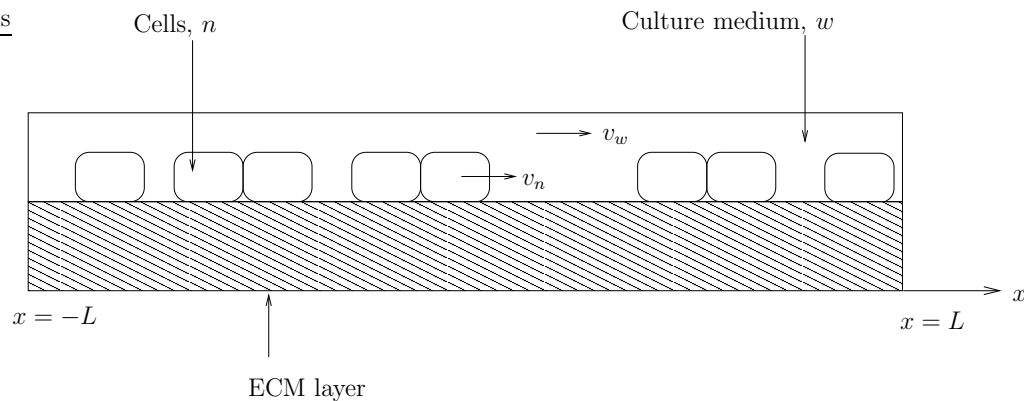


FIGURE 2.1: Definition sketch

For simplicity, an idealised one-dimensional slab geometry is adopted. We take the culture well to occupy the region $-L \leq x \leq L$, and assume that its upper and lower boundaries are impermeable, so no cells or culture medium can enter or leave. We denote the local volume fractions of the cells and culture medium by $n(x, t)$ and $w(x, t)$ respectively and their horizontal velocities by $v_n(x, t)$ and $v_w(x, t)$. We assume there are no voids, so

$$n + w = 1. \tag{2.2.1}$$

As cells consist predominantly of water, we assume both phases have an equal, constant density and without loss of generality exclude this (non-zero) common factor from the mass balance equations. We assume that the proliferation and death rates of hepatocytes are negligible on the timescales of interest, and thus obtain the following mass conservation equation for the cells and culture medium respectively

$$\frac{\partial n}{\partial t} + \frac{\partial}{\partial x}(nv_n) = 0, \quad (2.2.2a)$$

$$\frac{\partial w}{\partial t} + \frac{\partial}{\partial x}(wv_w) = 0. \quad (2.2.2b)$$

We let σ_n and σ_w be the Cauchy stresses in the cells and culture medium respectively. Neglecting inertial effects, the momentum balance in each phase is given by

$$\frac{\partial}{\partial x}(n\sigma_n) + F_n = 0, \quad (2.2.3a)$$

$$\frac{\partial}{\partial x}(w\sigma_w) + F_w = 0, \quad (2.2.3b)$$

where F_n and F_w represent the net sources of momentum in each phase, the precise forms of which will be discussed in §2.2.1.

The ECM density and displacement are given by $\rho(x, t)$ and $s(x, t)$ respectively. Mass conservation for the ECM gives the following equation

$$\frac{\partial \rho}{\partial t} + \frac{\partial}{\partial x}(\rho v_E) = 0, \quad (2.2.4)$$

where v_E is the ECM velocity. For simplicity, we consider only small ECM displacements, so that the application of linear theory is valid, and $v_E \approx \partial s / \partial t$. (We remark that this small displacement approximation is consistent with the numerical results of §2.5, for the parameter values considered.)

The Cauchy stress in the ECM is denoted by σ_ρ ; we again neglect inertial effects, so that the ECM momentum balance is

$$\frac{\partial \sigma_\rho}{\partial x} + F_\rho = 0, \quad (2.2.5)$$

where F_ρ is the force acting on the ECM due to interactions with the cell culture region.

2.2.1 Constitutive relations

We now introduce constitutive laws for the physical properties of each material, and specify the interaction forces between them.

We model the culture medium as a fluid, the viscosity of which is negligible on the macroscopic scale. Hence

$$\sigma_w = -p, \tag{2.2.6}$$

where p is the fluid pressure.

We model the cells as an incompressible viscous fluid with constant viscosity μ_n . The viscous effects are intended to capture the tendency of cells to align and match their velocities with the local average cell velocity [7]. In the context of liver cell aggregation, the viscous term represents the way hepatocytes migrate as coupled pairs or groups [96]. Obviously, cells differ from viscous fluids in that they are able to generate forces in response to cues from their environment, such as variations in the local cell density. We assume these forces manifest themselves in the cellular phase as an additional pressure term, Σ_n , and following Breward *et al.* [12] we write

$$\sigma_n = -p - \Sigma_n + 2\mu_n \frac{\partial v_n}{\partial x}. \tag{2.2.7}$$

Note that we have assumed that the pressures in the cells and culture medium are the same, and hence p is as in equation (2.2.6).

In general, the function Σ_n may depend upon such factors as ECM density or the concentration of a diffusible chemical [16]. However, for simplicity we

follow [12] by writing

$$\Sigma_n = \Gamma_1 \frac{(n - n^*)}{(1 - n)^2} H(n - n_{min}), \quad (2.2.8)$$

where H is the Heaviside function. When $\Sigma'_n(n) < 0$ (*i.e.* for $n_{min} < n < 2n^* - 1$), this term tends to drive cells up gradients of n , and hence represents a tendency for cells to aggregate at low densities. For $1 > n > 2n^* - 1$, $\Sigma'_n(n) > 0$ which corresponds to cell diffusion at high cell density. However, these are local phenomena, and if the cells are too sparsely populated (*i.e.* if $n < n_{min}$ for some constant n_{min}) they will experience no cell-cell interactions. For simplicity, we fix $n_{min} = 0$. Following Breward *et al.*, we term the constant $n^* \in (0, 1)$ in equation (2.2.8) the cells' *close-packing* density and Γ_1 is the tension constant which describes the strength of the cell-generated forces. A graph of $\Sigma_n(n)$ is plotted in Fig. 2.2.

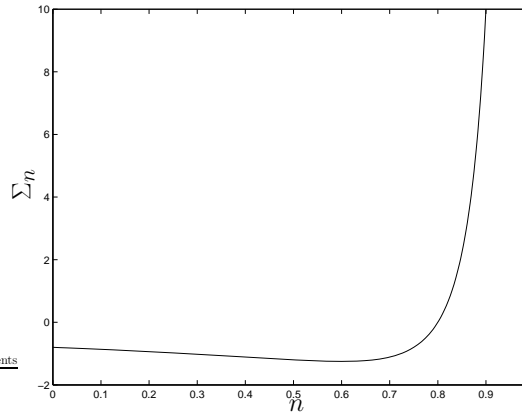


FIGURE 2.2: Σ_n against n ($n^*=0.8$, $\Gamma_1 = 1$, $n_{min} = 0$).

We believe the form chosen for Σ_n is consistent with the type of interactions required to form aggregates of bounded cell density. However, in the absence of experimental validation, other choices with the same qualitative behaviour could be considered.

We model the ECM as an isotropic, viscoelastic material, which forms a base layer over which the cells move (see Fig. 2.1). It should be noted that, in

general, mechanochemical models are sensitive to the particular constitutive laws adopted [14]. However, in the absence of appropriate experimental data, we use the Voigt model of viscoelasticity (see *e.g.* [41]) to describe the mechanical properties of the ECM. This model exhibits viscous behaviour over short timescales, and elastic behaviour at long times. Accordingly, the stress and displacement in the ECM are related by

$$\sigma_\rho = \frac{\partial}{\partial x} \left(\mu_E \frac{\partial s}{\partial t} + E' s \right), \quad (2.2.9)$$

where μ_E and E' are the viscous and elastic constants for the material. (In fact, μ_E is the sum of the bulk and shear viscosities of the material, and E' is related to the Young's modulus E and Poisson ratio ν via: $E' = E(1-2\nu)(1-\nu)/(1+\nu)$ [76]).

Turning to the momentum source terms, F_n and F_w in equations (2.2.3). We assume that the culture medium and the ECM exert drag forces on the cells (and *vice versa*), but neglect any drag between the ECM and the culture medium (as the latter has negligible viscosity). Our choice of cell-ECM interaction term differs from that used in [76], where a 'tethering' force proportional to the ECM displacement, s is postulated. We denote the drag coefficients between the cells and culture medium and cells and ECM by k_{nw} and $k_{n\rho}$ respectively. Following [12] these are specified as

$$k_{nw} = k_1 n w, \quad k_{n\rho} = k_2 n \rho, \quad (2.2.10)$$

(where k_1, k_2 are non-negative constants). Consequently, there is no drag if either of the two species is not present. While other empirically determined forms for the drag coefficients may be more physically realistic (*e.g.* the Carman-Kozeny relation described in [35]), the form we have adopted has the virtue of simplicity.

Combining the information above, we thus have

$$F_n = -k_{n\rho}(n, \rho) \left(v_n - \frac{\partial s}{\partial t} \right) - k_{nw}(n)(v_n - v_w) + p \frac{\partial n}{\partial x}, \quad (2.2.11)$$

$$F_w = -k_{nw}(n)(v_w - v_n) + p \frac{\partial w}{\partial x}. \quad (2.2.12)$$

$$F_\rho = k_2 n \rho \left(v_n - \frac{\partial s}{\partial t} \right). \quad (2.2.13)$$

We remark that the last term in equations (2.2.11) and (2.2.12) represents the contribution of interfacial forces (see [26, 27] for a detailed derivation).

2.2.2 Initial and boundary conditions

Our model now comprises equations (2.2.2)-(2.2.5), together with the constitutive relations (2.2.6)-(2.2.13). We close the model by specifying appropriate boundary and initial conditions. The initial distribution of cells is given by

$$n(x, 0) = n_0(x). \quad (2.2.14)$$

We assume that the solution is symmetric about the origin, so that we may restrict attention to $0 \leq x \leq L$ and impose

$$v_n(0, t) = v_w(0, t) = 0. \quad (2.2.15)$$

We also impose a no-flux boundary condition at the edge of the domain

$$v_n(L, t) = 0. \quad (2.2.16)$$

We assume that initially there is a uniform layer of undeformed ECM with constant density ρ_0 , and, hence, we impose

$$\rho(x, 0) = \rho_0, \quad s(x, 0) = 0. \quad (2.2.17)$$

Finally, we assume that the ECM is attached at the ends of the culture well, so that

$$s(0, t) = s(L, t) = 0. \quad (2.2.18)$$

2.2.3 Model reduction

We now show how we may reduce the model to a coupled system of four PDEs for n , ρ , v_n and s . This allows us to focus on the four physical quantities which are most relevant to tissue engineers. Although we eliminate the variables w , v_w and p , these quantities may be determined, if required, from the reduced model (see below).

Given (2.2.10) and the definitions of σ_n , σ_w , F_n , F_w and F_ρ from §2.2.1, the momentum balance equations (2.2.3) become

$$\frac{\partial}{\partial x} \left(2\mu_n n \frac{\partial v_n}{\partial x} - n \Sigma_n \right) - n \frac{\partial p}{\partial x} - k_2 n \rho \left(v_n - \frac{\partial s}{\partial t} \right) - k_1 n w (v_n - v_w) = 0, \quad (2.2.19)$$

$$w \frac{\partial p}{\partial x} + k_1 n w (v_w - v_n) = 0, \quad (2.2.20)$$

$$\frac{\partial^2}{\partial x^2} \left(\mu_E \frac{\partial s}{\partial t} + E' s \right) + k_2 n \rho \left(v_n - \frac{\partial s}{\partial t} \right) = 0. \quad (2.2.21)$$

Summing equations (2.2.2) leads to the incompressibility relation

$$\frac{\partial}{\partial x} (n v_n + w v_w) = 0, \quad (2.2.22)$$

which, following integration and imposition of (2.2.15), yields

$$v_w = \frac{-n v_n}{w}, \quad (2.2.23)$$

(assuming $w \neq 0$). If we use (2.2.23) to eliminate v_w and (2.2.1) to eliminate $w = 1 - n$ then (2.2.20) gives

$$\frac{\partial p}{\partial x} = \frac{k_1 n}{(1 - n)} v_n. \quad (2.2.24)$$

Using (2.2.24) in equation (2.2.19) gives

$$\frac{k_1 n}{(1 - n)} v_n + k_2 n \rho \left(v_n - \frac{\partial s}{\partial t} \right) + \frac{\partial}{\partial x} (n \Sigma_n) - 2\mu_n \frac{\partial}{\partial x} \left(n \frac{\partial v_n}{\partial x} \right) = 0. \quad (2.2.25)$$

The reduced model thus comprises equations (2.2.2a), (2.2.4), (2.2.21) and (2.2.25) for n , ρ , s and v_n respectively, together with the boundary and initial conditions specified by equation (2.2.14), the first of (2.2.15), and (2.2.16)-(2.2.18).

2.2.4 Parameters

To gain quantitative insight from our model, we require parameter estimates. A representative lengthscale for a liver cell spheroid is $\lambda \sim 200 \mu m$ (see Figure 1.2); we assume this to be a reasonable estimate for the lengthscale over which aggregation occurs. By comparison, the half-length of the culture well, L , is large $\sim 1 cm$. *In vitro* the timescale, T^* , over which aggregation occurs is about one day [102]. The close-packing density of the cells, n^* , is thought to be about 0.75 (or slightly greater for liver tissue) [95]; we shall henceforth set $n^* = 0.8$.

The types of ECM commonly used in liver tissue engineering include collagen gels and PLA (see Chapter 1); for the former, $\mu_E \sim 10^5 kgm^{-1}s^{-1}$ and $E' \sim 10^0 - 10^1 Pa$ [127], whilst for the latter, $\mu_E \sim 10^5 - 10^8 kgm^{-1}s^{-1}$ and $E' \sim 10^6 - 10^9 Pa$ [20, 43, 81]. We shall thus consider a range of values for these parameters in the model. The values of the cell viscosity μ_n , cell-culture medium drag constant k_1 and the initial ECM density ρ_0 have not been measured for the experimental system considered here. Hence, we turn to the literature to obtain estimated parameters from similar experiments. The resulting parameter estimates, together with supporting references, are summarised in Table 2.1.

At present, values for the cell-ECM drag constant, k_2 , and the tension constant Γ_1 cannot be determined from the literature and so must be estimated. We assume that $k_2 \geq k_1$, since on some substrates, *e.g.* tissue culture plastic (TCP), cells adhere sufficiently strongly almost to eliminate cell aggregation [102]. We take $2\mu_n/\Gamma_1$ to give a timescale for aggregation in the absence of drag effects (*i.e.* we set $T^* \sim 2\mu_n/\Gamma_1$), and use this to estimate Γ_1 . Given $T^* \sim 10^5 s$ and using the range for μ_n stated in Table 2.1, we predict $O(10^{-1}) < \Gamma_1 < O(10)$.

Parameter	Symbol	Units	Value	Source
Spheroid diameter	λ	m	10^{-4}	estimated from Fig. 1.2 ^a
Domain half-length	L	m	10^{-2}	[102]
Cell close-packing density	n^*	none	0.8	[95]
Aggregation timescale	T^*	s	10^5	estimated from [102]
ECM density	ρ_0	kg m ⁻³	0.5-8	[81] and refs. therein
Cell-water drag ^b	k_1	kg m ⁻³ s ⁻¹	10^7 - 10^{11}	[62, 115]
Cell viscosity ^c	μ_n	kg m ⁻¹ s ⁻¹	10^4 - 10^6	[33, 62]

^a image provided by L. Riccalton-Banks, Tissue Engineering Group, University of Nottingham.

^b measurements in [115] relate to hepatoma.

^c measurements in [33] are for spherical aggregates of embryonic chick liver cells

TABLE 2.1: Summary of dimensional parameter estimates and the corresponding references

2.2.5 Nondimensionalisation

We non-dimensionalise the governing equations as follows, using tildes to denote dimensionless quantities

$$\tilde{x} = \frac{x}{\lambda}, \quad \tilde{t} = \frac{t}{T}, \quad \tilde{\rho} = \frac{\rho}{\rho_0}, \quad \tilde{v}_n = \frac{v_n T}{\lambda}, \quad \tilde{s} = \frac{s}{\lambda}. \quad (2.2.26)$$

Here T is a general timescale, representing the period over which the culture well is being observed. Since we are primarily interested in the aggregation process, we generally set $T = T^*$ (except in §2.4, where we rescale T to determine the long-time behaviour of the model).

The dimensionless equations are then (dropping tildes for convenience)

$$\frac{\partial n}{\partial t} + \frac{\partial}{\partial x} (nv_n) = 0, \quad (2.2.27)$$

$$\frac{\partial \rho}{\partial t} + \frac{\partial}{\partial x} \left(\rho \frac{\partial s}{\partial t} \right) = 0, \quad (2.2.28)$$

$$\frac{\hat{k}_1 n}{(1-n)} v_n + \hat{k}_2 n \rho \left(v_n - \frac{\partial s}{\partial t} \right) + \tau_1 \frac{\partial}{\partial x} \left(\frac{n(n-n^*)}{(1-n)^2} \right) - \frac{\partial}{\partial x} \left(n \frac{\partial v_n}{\partial x} \right) = 0, \quad (2.2.29)$$

$$-\hat{k}_2 n \rho \left(v_n - \frac{\partial s}{\partial t} \right) = \hat{\mu}_E \frac{\partial^2}{\partial x^2} \left(\frac{\partial s}{\partial t} + \tau_2 s \right), \quad (2.2.30)$$

where

$$\hat{k}_1 = \frac{k_1 \lambda^2}{2\mu_n}, \quad \hat{k}_2 = \frac{k_2 \lambda^2 \rho_0}{2\mu_n}, \quad \tau_1 = \frac{\Gamma_1 T}{2\mu_n}, \quad \hat{\mu}_E = \frac{\mu_E}{2\mu_n}, \quad \tau_2 = \frac{E' T}{\mu_E}, \quad \epsilon = \frac{\lambda}{L}. \quad (2.2.31)$$

The physical interpretation of the dimensionless parameters is as follows: \hat{k}_1 and \hat{k}_2 are the ratios of cell-culture medium and cell-ECM drag to viscous forces; τ_1 is the ratio of the observation timescale to the aggregation timescale; $\hat{\mu}_E$ is the ratio of the ECM and cell viscosities; and τ_2 is the ratio of the observation timescale to the ECM relaxation time, $T_R = \mu_E/E'$ (*i.e.* T_R is the time taken for an initially applied deformation of the ECM to decrease by a factor e^{-1} in the absence of external forces).

The initial conditions are now applied to the large domain $[0, \epsilon^{-1}]$; given the lengthscales stated in §2.2.4, $\epsilon^{-1} \approx 50$. The boundary conditions for v_n and s at $x = 0$ now become

$$v_n(0, t) = v_n(\epsilon^{-1}, t) = 0, \quad (2.2.32)$$

$$s(0, t) = s(\epsilon^{-1}, t) = 0. \quad (2.2.33)$$

2.3 Linear stability analysis

Equations (2.2.27)-(2.2.30) have a spatially homogeneous steady state solution $n = n_0$ (where $0 < n_0 < 1$ is a constant), $\rho = 1$, $v_n = 0$ and $s = 0$. This steady

state approximates the conditions immediately after the liver cells have been seeded in the culture wells. We now perform a linear stability analysis [63] of this steady state to determine the parameter ranges in which aggregation might occur.

We consider small amplitude perturbations to the steady state of the following form (where it is to be understood that the real part is implied)

$$n \sim n_0 + \hat{n}e^{iqx+\omega t}, \quad \rho \sim 1 + \hat{\rho}e^{iqx+\omega t}, \quad v_n \sim \hat{v}_n e^{iqx+\omega t}, \quad s \sim \hat{s}e^{iqx+\omega t}. \quad (2.3.1)$$

Here, q is the wavenumber, $\omega = \omega(q)$ is the growth rate of the perturbation and $|\hat{n}|$, $|\hat{\rho}|$, $|\hat{v}_n|$ and $|\hat{s}| \ll 1$. We remark that the no-flux boundary conditions impose the constraint $q = m\pi\epsilon$, where m is an integer.

If there exists a pair $(q, \omega(q))$ for which $\Re(\omega) > 0$, then the steady state is linearly unstable; if $\Re(\omega) < 0$ for all q , then the spatially uniform steady state is linearly stable with respect to perturbations of the form (2.3.1). We expect aggregation to occur in parameter regimes in which the steady state is linearly unstable.

We substitute the above forms (2.3.1) into equations (2.2.27)-(2.2.30) and linearise to obtain

$$\omega \hat{n} + iq n_0 \hat{v}_n = 0, \quad (2.3.2)$$

$$\omega (\hat{\rho} + iq \hat{s}) = 0, \quad (2.3.3)$$

$$\frac{\hat{k}_1 n_0}{(1 - n_0)} \hat{v}_n + \hat{k}_2 n_0 (\hat{v}_n - \omega \hat{s}) + iq \frac{\tau_1 \hat{n} \beta(n_0)}{(1 - n_0)^3} + q^2 \hat{v}_n n_0 = 0, \quad (2.3.4)$$

$$\hat{k}_2 n_0 (\hat{v}_n - \omega \hat{s}) = q^2 \hat{\mu}_E \hat{s} (\omega + \tau_2), \quad (2.3.5)$$

where $\beta(n_0) = 2n_0 - n^*(1 + n_0)$.

For a non-trivial solution, it is straightforward to show that $\omega = \omega(q^2)$ satisfies

$$A(q^2)\omega^2 + B(q^2)\omega + C(q^2) = 0, \quad (2.3.6)$$

where

$$A = \hat{k}_2 n_0 \left(\frac{\hat{k}_1}{(1-n_0)} + q^2 \right) + q^2 \hat{\mu}_E \left(\frac{\hat{k}_1}{(1-n_0)} + \hat{k}_2 + q^2 \right), \quad (2.3.7)$$

$$B = q^2 \hat{\mu}_E \tau_2 \left(\frac{\hat{k}_1}{(1-n_0)} + q^2 \right) + q^2 \tau_1 \beta(n_0) \frac{(\hat{k}_2 n_0 + q^2 \hat{\mu}_E)}{(1-n_0)^3}, \quad (2.3.8)$$

$$C = \frac{q^4 \tau_1 \tau_2 \hat{\mu}_E \beta(n_0)}{(1-n_0)^3}. \quad (2.3.9)$$

Since all model parameters, except β , are positive; we deduce that $A > 0$ and hence that the behaviour depends upon the signs of B and C . When $B > 0$ and $C > 0$ both roots have negative real part, and the system is linearly stable to perturbations of the form (2.3.1). This situation arises when $\beta(n_0) > 0$, *i.e.* when the cells are seeded at a density higher than a critical density, $n_c = n^*/(2 - n^*)$. We remark that the case $B < 0 < C$ cannot occur since the latter condition requires $\beta(n_0) > 0$, whereas the former requires $\beta(n_0) < 0$. The other possibility, where both roots are real and of opposite sign, occurs when $\beta(n_0) < 0$. We note that equation (2.3.6) has no purely imaginary roots.

The above analysis shows that the stability of the system depends only on the initial cell seeding density. If $\beta(n_0) > 0$, (*i.e.* $n_0 > n_c = n^*/(2 - n^*)$) then the cell-cell interaction force is repulsive and so the uniform steady state is stable. When $\beta(n_0) < 0$ (*i.e.* $n_0 < n_c$) the cells achieve their preferred density by redistributing themselves over the domain. We note from equation (2.3.6) that ω is bounded (but may be positive) as $q \rightarrow \infty$, since the highest power of q is the same in A , B and C . As a result a large number of modes grow at almost equal rates. In order to determine which modes are observed in practice, nonlinear effects need to be considered. This is undertaken via numerical simulations in §2.5. First, however, we investigate the long-time behaviour of the model, as this gives some qualitative insights into the ultimate distribution

of the cells.

2.4 Long-time behaviour

We consider the long-time behaviour of the model, by adopting the timescale $T = \delta^{-1}T^*$ (where $\delta \ll 1$). Equations (2.2.27) and (2.2.28) are unchanged under this rescaling, whilst at leading order (2.2.29) and (2.2.30) give

$$\frac{\partial}{\partial x} \left(\frac{n(n - n^*)}{(1 - n)^2} \right) = 0, \quad (2.4.1)$$

$$\frac{\partial^2 s}{\partial x^2} = 0, \quad (2.4.2)$$

where we have assumed $\hat{k}_1, \hat{k}_2 \sim O(1)$ and $T_R \sim O(T^*)$. Hence, at long times, the movement of the cells and the displacement of the ECM are independent. The only solution of equation (2.4.2) which satisfies $s = 0$ at $x = 0, 1/\epsilon$ is $s \equiv 0$; thus at long times, the ECM returns to its undeformed configuration, and has uniform density (by equation (2.2.28)).

We observe from (2.4.1) that two types of behaviour are possible at long times. We may have

$$n = N(t), \quad (2.4.3)$$

in which case equation (2.2.27) can be integrated, subject to $v_n = 0$ at $x = 0, 1/\epsilon$, to give $v_n \equiv 0$ and hence n is constant. However, as we have seen in §2.3, the spatially uniform state is unstable for $n < n_c$, so we would not expect to observe this solution if at any time $n < n_c$ anywhere in the domain.

The second possibility is that n is piecewise constant, taking the values 0 and n^* in different regions. This corresponds to having aggregates, within which the cells achieve their close-packing density, alternating with regions devoid

of cells. This solution satisfies equation (2.4.1), since then throughout the domain

$$\frac{n(n - n^*)}{(1 - n)^2} = 0. \quad (2.4.4)$$

In regions in which $n = 0$, v_n is undefined, whilst in regions where $n = n^*$ equation (2.2.27) implies v_n is a function of time only. If the region includes the edges of the domain, then $v_n = 0$ by the boundary conditions; otherwise, it is necessary to assume that the long-time solution is steady (which is consistent with the numerical simulations in §2.5).

Since the role of cell-ECM adhesion is of particular interest, we also briefly consider the long-time behaviour in the limit of large \hat{k}_2 . We write $\hat{k}_2 = \hat{k}_2^*/\delta$, in which case, equations (2.2.29) and (2.2.30) become

$$\hat{k}_2^* n \rho \left(v_n - \frac{\partial s}{\partial t} \right) + \tau_1 \frac{\partial}{\partial x} \left(\frac{n(n - n^*)}{(1 - n)^2} \right) = 0, \quad (2.4.5)$$

$$-\hat{k}_2^* n \rho \left(v_n - \frac{\partial s}{\partial t} \right) = \hat{\mu}_E \tau_2 \frac{\partial^2 s}{\partial x^2} \quad (2.4.6)$$

Combining equations (2.4.5) and (2.2.27) gives the following nonlinear diffusion equation for n

$$\frac{\partial n}{\partial t} + \frac{\partial}{\partial x} \left(\frac{1}{\hat{k}_2 \rho} \left(\frac{\partial s}{\partial t} - \tau_1 \frac{\partial}{\partial x} \left(\frac{n(n - n^*)}{(1 - n)^2} \right) \right) \right) = 0. \quad (2.4.7)$$

We note that v_n now includes a term representing advection of the cells with the ECM as it is deformed. The form of this term is similar to that prescribed by [76], though we have derived it here from a momentum balance. We also note that equation (2.4.7) is ill-posed when $n < n_c = n^*/2 - n^*$; this would suggest the formation of localised regions of high or low cell density [84]. This is indeed what is seen numerically, with the formation of extremely small ‘aggregates’ (see §2.5.2, especially Fig. 2.8). (We remark that, although the above equation is ill-posed, retention of a small viscous term in the full system renders it well-posed.)

The type of solution described in this section, in which shocks form, is similar to those described in [17] for a two-phase model of tumour growth (in which the cell viscosity is neglected), or in [136] for the one-dimensional Cahn-Hilliard equation. In the latter case, a similarity solution for the time-dependent problem is found in which the small interfacial energy term uniquely determines the position of the shocks. Whilst the above analysis provides useful qualitative information on the long-time behaviour of our model, it crucially does not tell us the positions at which the solution ‘jumps’, and hence the number of aggregates we can expect to observe. This will depend on the initial conditions, and the evolution of the model over $O(1)$ timescales, and must hence be investigated numerically. This is undertaken in the following section.

2.5 Numerical simulations

2.5.1 Numerical methods

The governing equations were discretised using finite difference methods, and simulations were performed in MATLAB as follows. Firstly, we solve equations (2.2.29) and (2.2.30) for v_n and $\partial s/\partial t$ by matrix inversion, using the initial conditions for n , ρ and s . These solutions are then used to calculate n and ρ (from equations (2.2.27) and (2.2.28)) at the next timestep using an explicit first-order upwinding scheme [75]. The code verifies that the Courant-Freidrichs-Lewy (CFL) condition (a necessary condition for the convergence of the finite difference approximation [75]) is satisfied at each grid point. We found it convenient to include a small stabilising diffusion term on the RHS of equation (2.2.27) (with diffusion coefficient 10^{-4}), as this reduces the number of grid-points required to obtain satisfactorily smooth solutions. This means an additional numerical boundary condition, $\partial n/\partial x = 0$ at $x = 1/\epsilon$, must be imposed. (This did not affect the qualitative behaviour of the solutions, as expected, given the length of the domain.) The solution for s is then updated,

using the calculated value of $\partial s/\partial t$. We then use the solutions for n , ρ and s to obtain v_n , $\partial s/\partial t$ at the new timestep and repeat the process as required.

As a check on the accuracy of the numerical method, mass conservation of cells was verified at each timestep. We used a spatial step size $\Delta x = 1/800$ for the simulations presented in this section; this gave a 0.7% error in the mass at $t = 20$ for the parameter values in Fig. 2.3. Repeating the simulations with $\Delta x = 1/1600$ reduced the error to 0.5%, although there was no discernible change in the results. The error in mass conservation at the final time point was less than 2% for all the simulations presented below. For convenience, the domain was truncated to $0 \leq x \leq 10$ (numerical experiments with longer domains (*e.g.* $0 \leq x \leq 50$) gave the same qualitative results; results not presented).

2.5.2 Numerical results

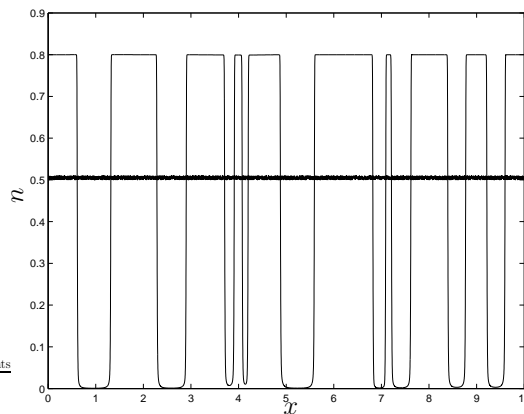


FIGURE 2.3: Numerical solution for cell volume fraction, n , at times $t = 0$ (line close to $n = 0.5$) and $t = 10$ ($\hat{k}_1 = \hat{k}_2 = \tau_1 = \hat{\mu}_E = \tau_2 = 1$).

Unless otherwise stated we fix $\hat{k}_1 = \hat{k}_2 = \tau_1 = \hat{\mu}_E = \tau_2 = 1$, which is reasonable given the ranges suggested in §2.2.4. We impose initial conditions where the value of $n(x, 0)$ at each gridpoint is uniformly distributed on $[0.50, 0.51]$.

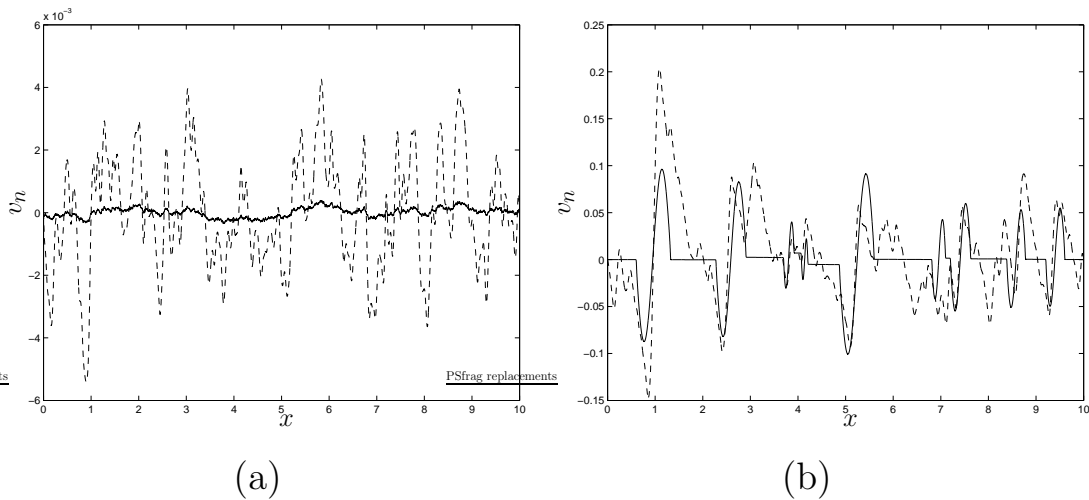


FIGURE 2.4: Numerical solution for cell velocity, v_n at: (a) $t = 2$ (solid) and $t = 4$ (dashed); (b) $t = 6$ (dashed) and $t = 10$ (solid). Parameter values as for Fig. 2.3.

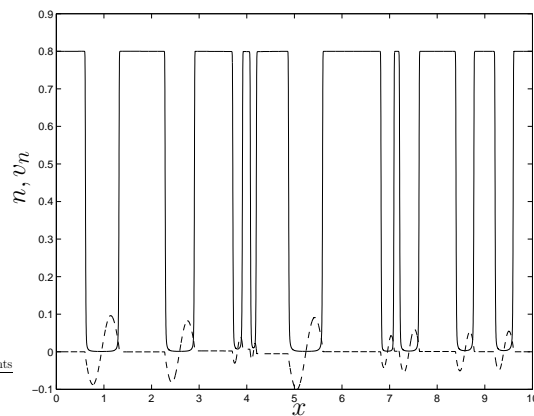


FIGURE 2.5: Numerical solution for n (solid) and v_n (dashed) at $t = 10$. Parameter values as for Fig. 2.3.

The corresponding numerical simulations show the formation of aggregates which have sharply defined edges, and uniform cell density (equal to $n^* = 0.8$) on the interior (Fig. 2.3).

In the early stages of aggregation, cell movement is slow (Fig. 2.4a shows $v_n \sim O(10^{-3})$ for $0 \leq t \leq 4$). Thereafter, the cell velocity increases and

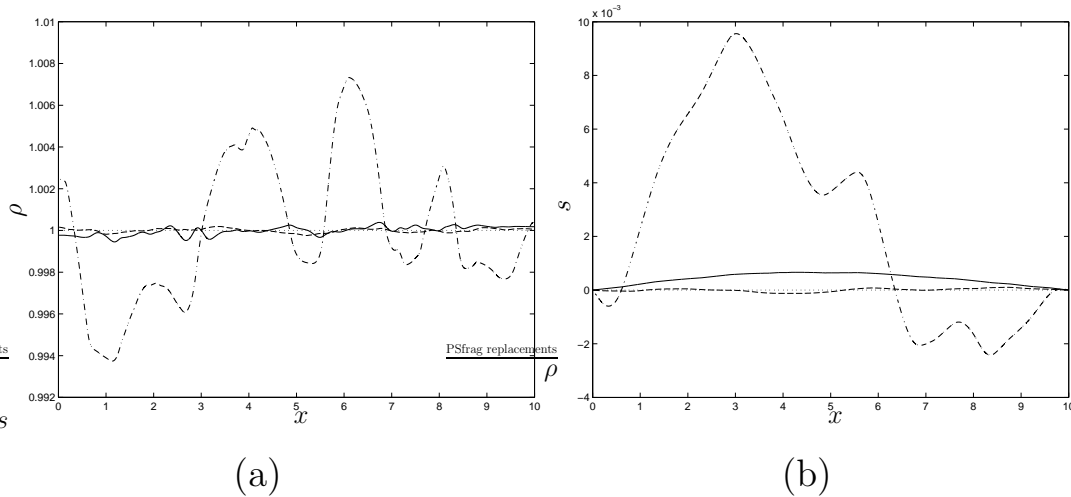


FIGURE 2.6: (a) Numerical solution for ECM density, ρ , at $t = 0$ (dotted), $t = 4$ (dashed), $t = 10$ (dot-dashed) and $t = 20$ (solid). (b) Numerical solution for ECM deformation, s , at $t = 0$ (dotted), $t = 4$ (dashed), $t = 10$ (dot-dashed) and $t = 20$ (solid). Parameter values as for Fig. 2.3.

aggregation proceeds relatively quickly (see Fig. 2.4b). After $t = 10$, there is little noticeable change in n , and we observe that $v_n = 0$ within aggregates (see Fig. 2.5), whilst elsewhere it is non-zero, with the few remaining cells moving towards their nearest cluster. The ECM density is redistributed as the cells move over its surface (see Fig. 2.6a), but at later times, when aggregation is essentially complete, elastic forces begin to act and deformation of the ECM decreases (see Fig. 2.6b) until its distribution becomes approximately uniform once again.

We now investigate the effect of varying key model parameters on the behaviour of the system, and thus suggest ways in which experimentalists may optimise their culture technique. The parameters over which tissue engineers have most control include the initial cell seeding density, represented by $n(x, 0)$; the physical properties of the ECM, represented by μ_E and τ_2 ; the strength of cell-ECM adhesion \hat{k}_2 , which can be changed, for example, by surface modification of the substrate with various proteins, and the degree of drag between

the cells and the culture medium \hat{k}_1 , which will depend on the viscosity of the culture medium.

Reducing the cell seeding density (so $n(x, 0)$ is distributed on $[0.30, 0.31]$) leads to the formation of slightly smaller aggregates, but does not otherwise affect the qualitative behaviour (compare Figs. 2.3 and 2.7). If we increase the cell seeding density above $n_c = 2/3$ (for $n^* = 0.8$), so the initial condition is uniformly distributed on $[0.7, 0.71]$, the cells distribute themselves uniformly throughout the culture well, as predicted by the linear stability analysis (results not shown).

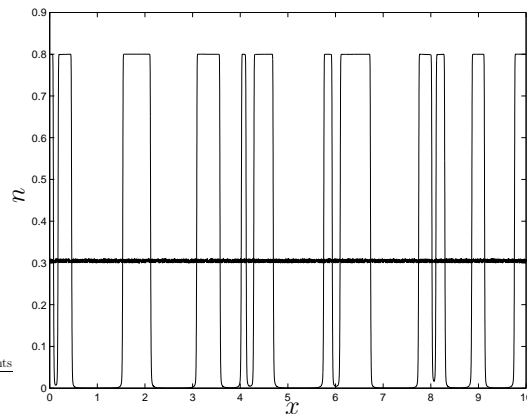


FIGURE 2.7: Numerical solution for n at $t = 0$ and $t = 10$. Reduced cell seeding density leads to the formation of smaller aggregates. Parameter values as for Fig. 2.3.

Repeated simulations suggest that altering the ECM properties (by changing the parameters μ_E and τ_2 whilst holding the other parameters fixed) does not affect the qualitative nature of the cells' aggregation (results not presented). We do, however, see a change in ECM behaviour, with deformation almost eliminated for stiff substrates (large μ_E, τ_2), whilst reducing these parameters leads to increased deformation.

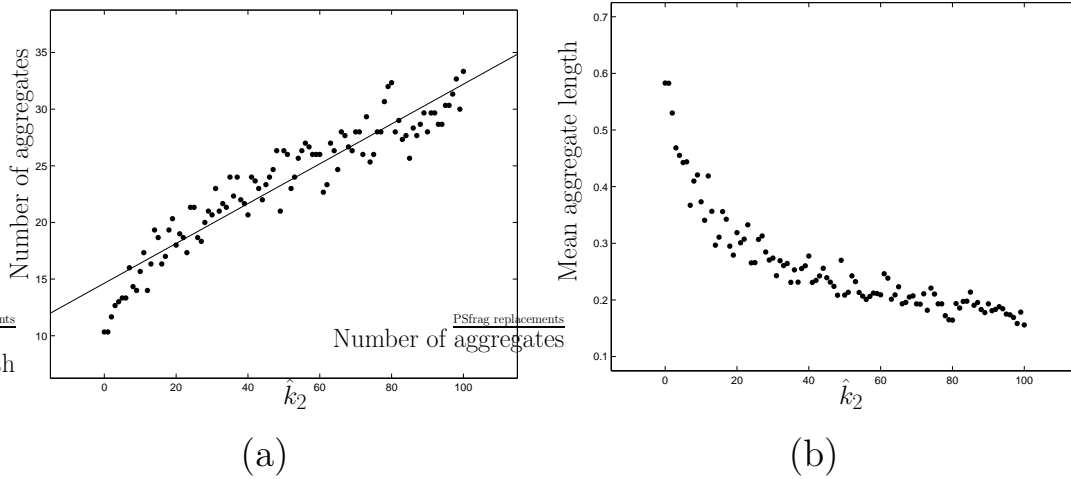


FIGURE 2.8: (a) Effect of increasing \hat{k}_2 on number of aggregates formed. (Best fit line is given by $y = 0.18\hat{k}_2 + 14.63$.) (b) Effect of increasing \hat{k}_2 on mean length of aggregates formed. Parameter values: $\hat{k}_1 = \tau_1 = \hat{\mu}_E = \tau_2 = 1$.

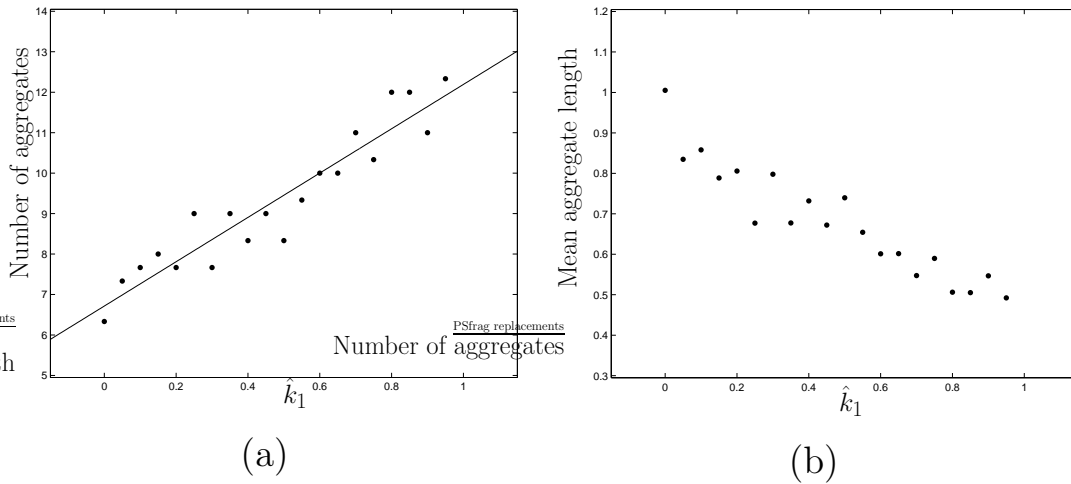


FIGURE 2.9: (a) Effect of increasing \hat{k}_1 on number of aggregates formed. (Best fit line is given by: $y = 5.48\hat{k}_1 + 6.71$.) (b) Effect of increasing \hat{k}_1 on mean length of aggregates formed. Parameter values: $\hat{k}_2 = \tau_1 = \hat{\mu}_E = \tau_2 = 1$.

Varying the cell-ECM drag parameter \hat{k}_2 has a more dramatic effect on cell aggregation than varying the ECM parameters. In particular, increasing \hat{k}_2 increases the number of aggregates formed, but they are correspondingly of

smaller size. We quantify this effect in Fig. 2.8 where we plot the number and mean length of cellular aggregates at $t = 10$ for different values of \hat{k}_2 . Here, an aggregate is defined to be a continuous region throughout which $n > 0.79$. The simulation is run three times for identically-distributed initial conditions, and an average is then taken. It appears that increasing cell-ECM adhesion reduces the cells' mobility, thereby leading to smaller aggregates. At extremely large values of \hat{k}_2 (e.g. $\hat{k}_2 = 10000$), cell movement is almost completely eliminated (results not presented). Increasing the cell-culture medium drag parameter, \hat{k}_1 , has a similar effect on the number and size of aggregates formed (see Fig. 2.9). (Where we have taken $\hat{k}_2 = \tau_1 = \hat{\mu}_E = \tau_2 = 1$, and used values of \hat{k}_1 between 0 and 1, the upper limit being suggested by the parameter values given in §2.2.4.)

2.6 Discussion

In this chapter we have used a multiphase approach to develop a new model of liver cell aggregation *in vitro*. The model extends previous work by Breward *et al.* [12] to include coupling between the cells and a deformable substrate, and may also be viewed as an alternative formulation of the mechanochemical theory of Murray and co-workers [76] using a multiphase framework.

Our simulations show the formation of 'aggregates' with clearly defined outer boundaries, and uniform cell density in the interior. This is consistent with the long-time behaviour predicted in §2.4, and in qualitative agreement with images of aggregates cultured *in vitro* [101]. Our most significant result is that strong cell-ECM adhesion inhibits the formation of large-scale aggregates. For extremely strong cell-ECM adhesion, the cells are effectively immobilised, and remain in their initial configuration. At more moderate adhesion strengths, they undergo short-range movements, and our simulations show the formation of small aggregates. (Note that, if the size of these aggregates ap-

proaches that of a single cell, the validity of using a continuum model becomes an issue.) Our results agree with experimental findings reported in [96], that strong cell-substrate adhesion inhibits migration, and are consistent with the hypothesis that aggregates do not form when cell-ECM adhesions are stronger than cell contractile forces. When cell-ECM adhesion is extremely strong, we found cell movement was almost completely eliminated, which reproduces the experimental findings of [102] for cells seeded on TCP (tissue culture plastic). On the basis of these results we predict that reducing the strength of cell-substrate adhesion may promote the formation of large aggregates. In practice, this can be achieved by surface modification of the substrate as described earlier. However, our model does not account for the fact that some degree of cell-substrate adhesion may be necessary for cell locomotion, which would make the elimination of this effect undesirable.

Our results also suggest that the cell seeding density may be important. In section §2.3, we showed that if the cells are seeded too densely (*i.e.* $n > n_c$), then aggregation will not occur. To our knowledge, this phenomenon has not been reported of hepatocytes in the experimental literature; this may be because, in practice, it is difficult to achieve a sufficiently high cell seeding density. However, Peshwa *et al.* [93] report that, at high hepatocyte seeding densities, multilayers rather than spheroidal aggregates are formed. Our numerical results also suggest that reducing the cell seeding density leads to the formation of smaller aggregates. This agrees with experimental results reported by Tong *et al.* [122].

In our model, the physical properties of the ECM (*i.e.* its viscosity and elastic modulus) do not have a significant effect on cell aggregation. However, this may be because we have assumed that the strength of cell-ECM adhesion (characterised by the drag coefficient $k_{n\rho}$) is independent of the ECM properties (characterised by μ_E and E'). Evidence already exists that some cell

types form weaker adhesions to compliant substrates [41], suggesting a more complex relation between the physical properties of the ECM and the strength of cell-ECM adhesion than has been assumed in this chapter. We could extend our model by replacing the $k_{n\rho}$ with a more complex function involving μ_E and E' . However, although the current experimental literature contains a number of studies of spheroid formation on a variety of substrates, the mechanical properties of the substrates are not well characterised. We would suggest that further experimental investigation of the impact of the material properties of the substrate on cell adhesion may prove fruitful, and might allow us to postulate an improved functional form for $k_{n\rho}$. Furthermore, our use of a drag term to model cell adhesion is also an idealisation of the biological situation. An alternative approach has been taken by Preziosi and Astanin [98], who, when modelling the formation of capillaries, distinguished between a ‘viscous’ cell-ECM interaction force (equivalent to our cell-ECM drag term) and an ‘elastic’ force, which acts if the cells have had sufficient time to anchor to the ECM (or alternatively, if cells are moving sufficiently slowly), and is proportional to their relative displacement. We also remark that the motility of hepatocytes may depend on ECM properties, as other cell types such as fibroblasts are known to be able to sense and respond to the stiffness of the substrate on which they are seeded [23, 61]. A recent model of cell crawling [120] suggests that cells move with maximum speed on rigid substrates: on compliant materials the ECM may deform preferentially relative to the cell, retarding cell motion. We could incorporate these effect by making the function Σ_n dependent upon ρ and the ECM properties.

Perhaps the most natural extension of our model would be to formulate it in a more realistic geometry *i.e.* two or three dimensions. One obvious deficiency of this 1D model is the fact that the cell-ECM drag force acts throughout the region occupied by the cells and culture medium, when it would be more realistic for it to act as a traction at the cell-ECM interface. Furthermore,

although we have not considered chemical signalling explicitly, aggregation is almost certainly influenced by chemical factors. For example, when hepatocyte conditioned medium (culture medium in which hepatocytes have previously been grown) is added to freshly isolated cells, their rate of aggregation increases [37]. This suggests that the hepatocytes produce a chemical signal which enhances their motility. Moreover, hepatocytes are known to respond chemotactically to hepatocyte growth factor (HGF) and epidermal growth factor (EGF) *in vitro* [113]. Extending our model to investigate the impact of chemical signalling on cell aggregation would require us to augment our system of equations with an equation describing the evolution of the concentration of the chemical species of interest, and incorporate dependence upon the chemical concentration into the function Σ_n . An example of such a model has recently been described by Byrne and Owen [16]. We pursue these extensions in the following chapter, where we develop a two-dimensional model for cell aggregation, incorporating chemotaxis.

As it is known that the stability properties of standard mechanochemical models are influenced by the constitutive relations adopted for the ECM [14], it would be interesting to determine if this is also true of our two-phase model. This would entail introducing different constitutive laws for the ECM in §2.2.1, and repeating the linear stability analysis of §2.3. Alternatively, by extending our model to allow for multiple cell populations, we could investigate the impact of cellular heterogeneity on the rate of aggregation and the size of aggregates formed. Recent experimental research has looked at the effect of coculturing hepatocytes with other cell types, such as hepatic stellate cells [101], fibroblasts [9] and pancreatic islet cells [58]. Under such conditions, spheroids appear to form more quickly, and may also be larger than those which arise in hepatocyte-only cultures. These cell types could be included as additional phases within the multiphase framework. It would be interesting to compare the results of such modelling with those obtained using the non-local models

in Chapter 5.

Chapter 3

Modelling of chemotactic cell aggregation *in vitro*. Part I: Model derivation and thin film limits

3.1 Introduction

In Chapter 2, we derived a simple, one-dimensional model for the aggregation of liver cells *in vitro*. Aggregation was driven by intercellular forces modelled through a prescribed function (Σ_n) of the cell volume fraction n . We did not consider explicitly the possibility that chemical signalling between the cells was responsible for aggregation. Experiments have shown that when hepatocyte conditioned medium (culture medium in which hepatocytes have previously been grown) is added to freshly isolated hepatocytes, their rate of aggregation is increased [37]. This suggests that the hepatocytes express some chemical signal which affects their motility. It has previously been observed that

hepatocytes respond chemotactically to hepatocyte growth factor (HGF) and epidermal growth factor (EGF) *in vitro* [113]; however these do not appear to be produced by hepatocytes themselves *in vivo* [32]. *In vitro* behaviour may be different, as a recent study found evidence of increased HGF production in spheroids containing hepatocytes co-cultured with stellate cells [119] (although we note that stellate cells are also known to produce HGF [111]). In this chapter, we postulate the existence of a generic chemoattractant produced by the hepatocytes *in vitro*, and show that this provides a possible explanation for their aggregation.

A second departure from the modelling approach of Chapter 2, is that we consider a two-dimensional geometry, representing a vertical section through the culture well. We assume that the inverse aspect ratio of the problem (the ratio of typical vertical to horizontal lengthscales) is small. We then exploit the geometry by making a thin-film approximation, which in two particular scaling regimes (both corresponding to strong chemotaxis, but with differing assumptions made about the magnitude of the pressure in the culture medium, the extent of cell-ECM adhesion, cell-culture medium drag and surface tension) allows us to simplify the governing equations to a one-dimensional form. These equations are compared with the model developed in the previous chapter, and are investigated both analytically and numerically in Chapter 4.

This chapter is organised as follows. In §3.2, we survey existing mathematical models of the dynamics of thin films. As the literature is extensive, we confine our attention to a small number of papers of particular relevance to the model developed here. Our two-dimensional model is developed in §3.3, where we introduce equations for the dynamics of the ECM, cells, culture medium and chemoattractant. Assuming that the Péclet number (ratio of advection to diffusion) for the chemoattractant is small, we exploit the thin geometry of the problem in §3.4 to obtain a one-dimensional equation gov-

erning the leading-order distribution of chemoattractant. We then consider two scaling regimes which, borrowing terminology from fluid mechanics, we term ‘extensional’ (§3.5) and ‘lubrication’ (§3.6). In both cases, when the thin film limit is taken the governing equations for the ECM and the cells reduce to one-dimensional form. This chapter concludes with a discussion of the two reduced models and their relationship to the one-dimensional model developed in Chapter 2. In Chapter 4, we investigate the two reduced models using a combination of linear stability analysis and numerical simulations.

3.2 Review of mathematical modelling of thin films

Mathematical modelling of thin films is an area of intense research activity in fluid mechanics, particularly in relation to coating flows in industrial problems [79]. Frequently, the films consist of incompressible Newtonian fluid, and hence their dynamics are governed by the Navier-Stokes and continuity equations. Such a case was considered by Howell [44, 45], who used systematic asymptotic methods to derive the leading-order equations describing the behaviour of a two-dimensional sheet of viscous fluid.

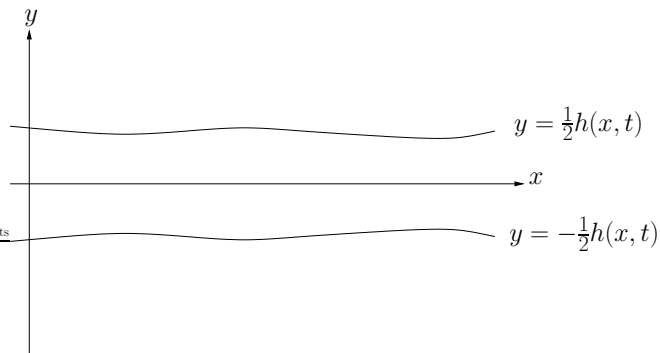


FIGURE 3.1: Geometry of the two-dimensional fluid sheet

The geometry of the situation considered by Howell is displayed in Fig. 3.1. Inertial effects and surface tension are taken to be negligible, and the sheet is assumed nearly flat with two, stress-free, free boundaries at $y = \pm \frac{1}{2}h(x, t)$ (the sheet's centreline can, without loss of generality, be taken to lie at $y = 0$). The governing equations are the two-dimensional Stokes equations, which, together with appropriate boundary and initial conditions, are expanded in powers of the small parameter ϵ^2 (where ϵ is the inverse aspect ratio of the sheet - *i.e.* the ratio of the sheet's vertical and horizontal lengthscales). The Trouton model, which consists of the following hyperbolic system for the leading-order film thickness, h_0 and axial velocity, u_0 , is then obtained

$$\frac{\partial h_0}{\partial t} + \frac{\partial}{\partial x} (u_0 h_0) = 0, \tag{3.2.1a}$$

$$\frac{\partial}{\partial x} \left(4h_0 \frac{\partial u_0}{\partial x} \right) = 0. \tag{3.2.1b}$$

The factor of 4 in equation (3.2.1b) is known as the Trouton ratio, and is dependent on the geometry of the problem (*e.g.* the corresponding value is 3 for an axisymmetric fibre).

We remark that in this case, the axial velocity u_0 depends only on x and t at leading order; flows of this type are termed extensional, in contrast to the usual 'lubrication' limit for a thin film of viscous fluid, where the presence of a no-slip condition on at least one boundary leads to a velocity profile which is parabolic in y (the depth co-ordinate) [79]. The Trouton model is adequate for studying the behaviour of a sheet under tension, but breaks down when the ends of the sheet are pushed together, as 'buckling' will then occur, and the assumption that the sheet is nearly flat is violated. The model (3.2.1) may, however, be extended to encompass cases where surface tension or inertial effects are significant [45], as well as to three-dimensional geometries, including those in which both bending and stretching of the sheet occur [45, 99].

Another much-studied situation is the surface tension-dominated flow of

a thin fluid film over a solid surface [79]. This gives rise to a fourth-order nonlinear parabolic equation of the form

$$\frac{\partial h}{\partial t} + \frac{\partial}{\partial x} \left(C \frac{h^3}{3} \frac{\partial^3 h}{\partial x^3} + f \left(h, \frac{\partial h}{\partial x}, \frac{\partial^2 h}{\partial x^2} \right) \right) = 0, \quad (3.2.2)$$

where C is the inverse capillary number (ratio of surface tension to viscous forces), and the function f includes terms due to gravity, inclination of the surface, and so on. The related ‘generalised lubrication equation’

$$\frac{\partial h}{\partial t} + \frac{\partial}{\partial x} \left(h^n \frac{\partial^3 h}{\partial x^3} \right) = 0, \quad (3.2.3)$$

has been the subject of many analytical studies [79]. Equation (3.2.3) is a nonlinear parabolic equation. It is degenerate, as the coefficient of the highest derivative tends to zero as $h \rightarrow 0$. The case $n = 3$ is obviously of greatest relevance to surface tension-driven flows. Analysis of equation (3.2.3) has involved performing linear stability analysis, and constructing travelling wave and similarity solutions [79].

In a biological context, thin film models have been developed to describe a number of situations. Recent examples include work by Weekley [132], who studied the transport of particles in the lungs, treating the mucus lining of the airway as a viscous sheet, and Franks and King [36] who investigated a thin-film model of tumour growth, treating the cells and extracellular water as a Stokes fluid.

Both of the models (3.2.1) and (3.2.2) have recently been generalised by King and Oliver to the case of a fluid mixture, consisting of viscous and inviscid components [53]. The theory is applied as a ‘minimal model’ for cell motion, with additional biological detail being introduced in another paper [84]. In both cases, the cell is assumed well-spread (and hence thin). The cell interior is treated as a mixture of viscous, polymerised actin and an inviscid solution, enveloped by a membrane under tension. Actin is postulated to polymerise

(or depolymerise) at the contact line (where the cell edge meets the substrate), hence conversion of mass between the two phases occurs there. In [53], it is assumed that the mass transfer rate between the two phases depends only on the velocity of the contact line. It is then shown, using asymptotic analysis in the limit corresponding to strong cell-substrate adhesion, that a novel class of multi-valued contact line laws arise. Qualitative analysis of these laws reveals a variety of possible behaviours, including ‘pulsation’ (periodic expansion and contraction of the cell), in addition to steady cell translocation.

3.3 Model formulation

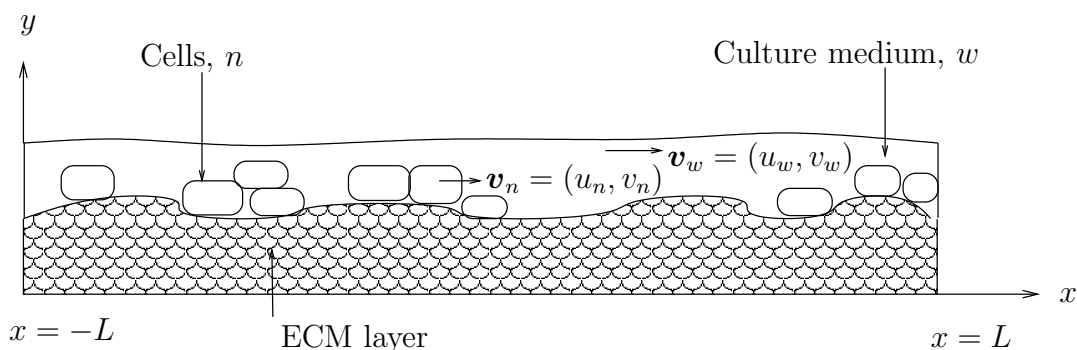


FIGURE 3.2: Simplified representation of a vertical slice through a culture well.

3.3.1 Preamble

We consider a system consisting of a population of a single type of cells (hepatocytes), plated onto a thin layer of ECM and bathed in culture medium, a simplified representation of which is presented in Fig. 3.2. As in Chapter 2, we adopt a continuum modelling approach in which the cells and culture medium are treated as a two-phase fluid mixture. A definition sketch is given in Fig. 3.3. A two-dimensional Cartesian coordinate system $\mathbf{x} = (x, y)$ is employed, with t used to denote time. The culture well is taken to occupy the

region $-L \leq x \leq L$, the lower part of which ($0 \leq y \leq g(x, t)$) contains a thin layer of ECM. Cells and culture medium occupy the region $g(x, t) < y \leq h(x, t)$ (thus the boundaries $y = g(x, t)$ and $y = h(x, t)$ delineate the region in which the volume fraction of cells, n , is non-zero). The region $y > h$ is assumed to be empty space. The impermeable interfaces between the cell-fluid mixture and ECM, and the cell-fluid mixture and free space are free boundaries, which must be determined as part of the solution.

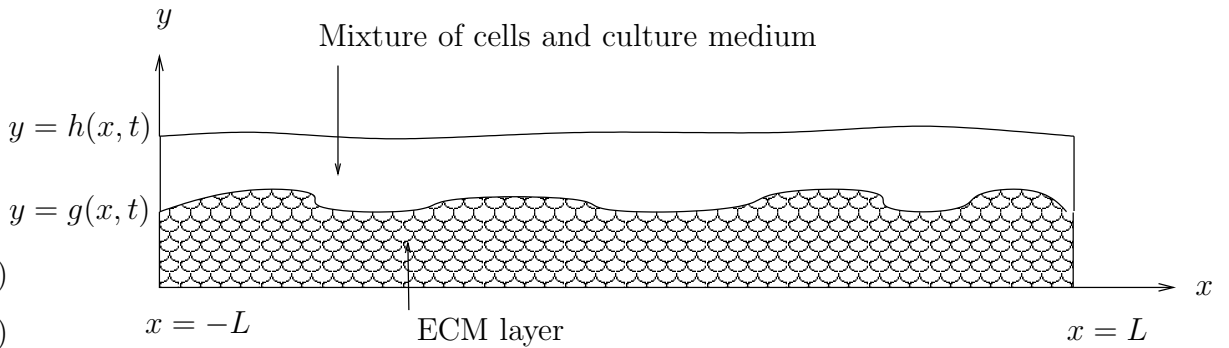


FIGURE 3.3: Definition sketch.

In addition to the dependent variables specified in Fig. 3.3 we introduce a generic hepatocyte-derived chemoattractant, and denote its concentration per unit volume of culture medium by $c(\mathbf{x}, t)$. We assume that all cells are well nourished, as under co-culture conditions at least, the number of viable cells remains approximately constant for up to ten days [9]; it thus appears that nutrient availability is unlikely to be limiting during aggregation.

The formulation of the model falls naturally into two parts: in §3.3.2, we derive equations describing the behaviour of the ECM, whilst equations for the cells and culture medium are stated in §3.3.3. Deformation of the ECM is coupled to the movement of the cells via boundary conditions on the upper surface of the ECM. The governing equation for the chemoattractant concentration is derived in §3.3.4 and the complete model rendered dimensionless in

§3.3.5.

3.3.2 Extracellular matrix model

We model the ECM as an isotropic, viscoelastic material, which forms a base layer to which the cells may adhere (see Fig. 3.3). In previous studies [78, 85, 123], the ECM has been treated as a Voigt viscoelastic solid. It should be noted that, in general, mechanochemical models are sensitive to the particular constitutive laws adopted [14]. However, given a lack of experimental data on the behaviour of the ECM considered here, we also use the Voigt constitutive law, as in Chapter 2.

The ECM density and displacement vector are denoted by $\rho(\mathbf{x}, t)$ and $\mathbf{U}(\mathbf{x}, t)$ respectively. We assume that ECM displacements are small, so that we can apply linear theory. Then, neglecting inertial effects, and assuming no body forces act within the ECM, the momentum balance equation is

$$\nabla \cdot \boldsymbol{\sigma}_\rho = \mathbf{0}, \quad (3.3.1)$$

where $\boldsymbol{\sigma}_\rho$ is the stress tensor for the ECM. The stress-strain relation is given by [76]

$$\boldsymbol{\sigma}_\rho = 2\mu_1 \frac{\partial \boldsymbol{\epsilon}}{\partial t} + \mu_2 \frac{\partial \Theta}{\partial t} \mathbf{I} + E'(2\boldsymbol{\epsilon} + \nu' \Theta \mathbf{I}), \quad (3.3.2)$$

where

$$\Theta = \nabla \cdot \mathbf{U}, \quad \boldsymbol{\epsilon} = \frac{1}{2} (\nabla \mathbf{U} + \nabla \mathbf{U}^T), \quad E' = \frac{E}{1 + \nu}, \quad \nu' = \frac{\nu}{1 - 2\nu}. \quad (3.3.3)$$

In (3.3.2) μ_1 and μ_2 are the shear and bulk viscosities, and E' and ν' are related to the Young's modulus E and Poisson ratio ν as indicated above. Thus, Θ represents the dilation of the material, and $\boldsymbol{\epsilon}$ the elastic strain tensor .

For simplicity, we assume that the ECM is incompressible, with density ρ_0 . We let the velocity of the ECM be \mathbf{v}_E , and since we have made the linear

approximation, $\mathbf{v}_E \approx \frac{\partial \mathbf{U}}{\partial t}$. Writing $\mathbf{U} = (U, V)$, conservation of mass gives

$$\frac{\partial U}{\partial x} + \frac{\partial V}{\partial y} = 0, \quad (3.3.4)$$

(*i.e.* zero dilation of the material). In this incompressible limit, the Poisson ratio $\nu \rightarrow \frac{1}{2}$. However, the product $E'\nu'\Theta$ remains finite, and is associated with a pressure, P_E , such that $E'\nu'\Theta \rightarrow -P_E$ as $\nu' \rightarrow \infty$ (see Ch. 9 of [29]).

Applying equations (3.3.2) and (3.3.4), equations (3.3.1) yield the following momentum balances in the x and y directions respectively

$$-\frac{\partial P_E}{\partial x} + \frac{\partial^2}{\partial x^2} \left(\mu_1 \frac{\partial U}{\partial t} + E'U \right) + \frac{\partial^2}{\partial y^2} \left(\mu_1 \frac{\partial U}{\partial t} + E'U \right) = 0, \quad (3.3.5)$$

$$-\frac{\partial P_E}{\partial y} + \frac{\partial^2}{\partial x^2} \left(\mu_1 \frac{\partial V}{\partial t} + E'V \right) + \frac{\partial^2}{\partial y^2} \left(\mu_1 \frac{\partial V}{\partial t} + E'V \right) = 0. \quad (3.3.6)$$

Equations (3.3.4)-(3.3.6) specify the dependent variables in the ECM (U , V and P_E), and are closed by imposing the following boundary and initial conditions

$$\mathbf{U}(x, y, 0) = 0, \quad (3.3.7)$$

$$\mathbf{U}(x, 0, t) = 0, \quad (3.3.8)$$

$$\mathbf{U}(0, y, t) = \mathbf{U}(L, y, t) = 0, \quad (3.3.9)$$

$$\hat{\mathbf{n}} \cdot (\boldsymbol{\sigma}_\rho \cdot \hat{\mathbf{n}})|_{y=g} = \hat{\mathbf{n}} \cdot (\boldsymbol{\sigma} \cdot \hat{\mathbf{n}})|_{y=g}, \quad (3.3.10)$$

$$\hat{\mathbf{t}} \cdot (\boldsymbol{\sigma}_\rho \cdot \hat{\mathbf{n}})|_{y=g} = \hat{\mathbf{t}} \cdot (\boldsymbol{\sigma} \cdot \hat{\mathbf{n}})|_{y=g}, \quad (3.3.11)$$

where $\boldsymbol{\sigma}$ is the stress tensor for the mixture of cells and culture medium (see equation (3.3.23)), and $\hat{\mathbf{n}}$ and $\hat{\mathbf{t}}$ are the unit normal and tangent vectors to the surface of the ECM, given by

$$\hat{\mathbf{n}} = \frac{1}{\sqrt{1 + \left(\frac{\partial g}{\partial x}\right)^2}} \left(-\frac{\partial g}{\partial x}, 1 \right), \quad \hat{\mathbf{t}} = \frac{1}{\sqrt{1 + \left(\frac{\partial g}{\partial x}\right)^2}} \left(1, \frac{\partial g}{\partial x} \right). \quad (3.3.12)$$

The physical interpretations of these boundary and initial conditions are as follows. We assume that initially, there is no displacement of the ECM (3.3.7), and that the ECM layer is anchored to the bottom and sides of the

culture well, so that there is no ECM displacement on $y = 0$ and $x = 0, L$ (see equations (3.3.8) and (3.3.9)). Equations (3.3.10) and (3.3.11) represent continuity of normal and tangential stress respectively at the interface between the ECM and the cell and culture medium mixture.

Finally, the kinematic condition at the interface between the ECM and the cells and culture medium gives

$$\frac{\partial V}{\partial t} = \frac{\partial g}{\partial t} + \frac{\partial U}{\partial t} \frac{\partial g}{\partial x} \quad \text{on } y = g. \quad (3.3.13)$$

This equation is used to determine g , given U and V , and is subject to the condition that the interface is initially flat - *i.e.*

$$g(x, 0) = g_i, \quad (\text{constant}). \quad (3.3.14)$$

3.3.3 Cell culture model

Mass balance

We denote the local volume fractions of the cells and culture medium by $n(\mathbf{x}, t)$ and $w(\mathbf{x}, t)$ respectively and their velocities by $\mathbf{v}_n(\mathbf{x}, t) = (u_n, v_n)$ and $\mathbf{v}_w(\mathbf{x}, t) = (u_w, v_w)$. We assume there are no voids, so

$$n + w = 1. \quad (3.3.15)$$

As cells consist predominantly of water, we assume both phases have an equal, constant density: we can then exclude this common factor from the mass balance equations. As in Chapter 2, we assume that the proliferation and death rates of the hepatocytes are negligible (see also comment in §3.3.1), and thus obtain the following mass conservation equation for the cells and culture medium respectively

$$\frac{\partial n}{\partial t} + \frac{\partial}{\partial x}(nu_n) + \frac{\partial}{\partial y}(nv_n) = 0, \quad (3.3.16)$$

$$\frac{\partial w}{\partial t} + \frac{\partial}{\partial x}(wu_w) + \frac{\partial}{\partial y}(wv_w) = 0. \quad (3.3.17)$$

We impose the following kinematic boundary conditions on the interfaces $y = g, h$

$$v_n = \frac{\partial g}{\partial t} + u_n \frac{\partial g}{\partial x}, \quad v_w = \frac{\partial g}{\partial t} + u_w \frac{\partial g}{\partial x}, \quad \text{on } y = g, \quad (3.3.18)$$

$$v_n = \frac{\partial h}{\partial t} + u_n \frac{\partial h}{\partial x}, \quad v_w = \frac{\partial h}{\partial t} + u_w \frac{\partial h}{\partial x}, \quad \text{on } y = h, \quad (3.3.19)$$

and state that cells and culture medium which begin on the free boundaries remain upon them. Note that conditions (3.3.13) and (3.3.18) imply continuity of normal velocity at the interface $y = g$.

As in the previous section, the following initial and boundary conditions are imposed on h

$$h(x, 0) = g_i + h_i, \quad (\text{constant}) \quad (3.3.20)$$

$$\left. \frac{\partial h}{\partial x} \right|_{x=0} = 0, \quad (3.3.21)$$

i.e. the interface is initially flat, and h is symmetric about $x = 0$.

Momentum balance

We assume that inertial effects may be neglected and, hence, that the momentum balance for each phase is given by

$$\nabla \cdot (n\boldsymbol{\sigma}_n) + \mathbf{F}_n = 0, \quad \nabla \cdot (w\boldsymbol{\sigma}_w) + \mathbf{F}_w = 0, \quad (3.3.22)$$

where $\boldsymbol{\sigma}_n$ and $\boldsymbol{\sigma}_w$ are the stress tensors for the cells and culture medium respectively, and \mathbf{F}_n and \mathbf{F}_w represent the net sources of momentum in each phase. We assume that $\mathbf{F}_n = -\mathbf{F}_w$.

For subsequent convenience, we now introduce the stress tensor for the cell-culture medium mixture, given by

$$\boldsymbol{\sigma} = n\boldsymbol{\sigma}_n + w\boldsymbol{\sigma}_w, \quad (3.3.23)$$

and thus the overall momentum balance for the mixture is

$$\nabla \cdot \boldsymbol{\sigma} = \mathbf{0}. \quad (3.3.24)$$

Constitutive relations

We model the culture medium as a fluid, the viscosity of which is negligible compared to that of the cells. Hence

$$\boldsymbol{\sigma}_w = -p\mathbf{I}, \tag{3.3.25}$$

where p is the fluid pressure and \mathbf{I} the identity tensor.

As in Chapter 2, we model the cells as an incompressible fluid, with constant viscosity μ_n . Cells differ from ordinary viscous fluids, however, in that they are assumed to be able to generate forces in response to cues from their environment, such as variations in the local cell density or chemical concentrations. We assume these forces manifest themselves in the form of an additional pressure, Σ_n , in the cellular phase. We thus write

$$\boldsymbol{\sigma}_n = -(p + \Sigma_n(n, c))\mathbf{I} + \mu_n(\nabla\mathbf{v}_n + \nabla\mathbf{v}_n^T), \tag{3.3.26}$$

where we have assumed that the pressures in the cells and culture medium are equal, so p is as in equation (3.3.25). We remark that (3.3.26) generalises to two or three dimensions the constitutive law adopted in Chapter 2. However, we note that Σ_n may now also depend upon c (the concentration of chemoattractant in the culture medium), as well as n .

For simplicity, we shall assume that Σ_n depends only upon the concentration of the chemoattractant in the water phase, c , though at present there is no experimental verification that this is the case. Likewise, there is no widely accepted functional form for the relationship between c and the stress generated by the cells, other than the fact that as we expect cells to move up chemoattractant gradients, Σ_n should be a decreasing function of c . On that basis, we adopt the following simple linear form for Σ_n

$$\Sigma_n = \Gamma_1(1 - \tau c)H(c_{max} - c), \tag{3.3.27}$$

where Γ_1 gives a measure of the strength of the forces generated by the cells, and τ describes the cells' sensitivity to the chemoattractant. The factor $H(c_{max} - c)$ (where H is the Heaviside function) switches off chemotaxis when the chemical concentration exceeds the upper bound c_{max} . We might interpret this biologically as the cells' chemoreceptors being 'swamped' when $c > c_{max}$, leaving the cell unable to determine the direction in which it should move. (Note that we have assumed that cells are sensitive to low levels of chemoattractant, since we have not imposed a lower threshold which c must exceed for the cells to detect it.) The constraint $c_{max} < 1/\tau$ prevents ill-posedness (which would occur for $\Sigma_n < 0$) in the thin film limits of the model with which we shall subsequently be concerned (see §3.5.1).

We remark that alternative functional forms for Σ_n were adopted in [16], of exponential and rational type, which included a constant term representing a 'background potential'. However, the basic assumption (that Σ_n is a decreasing function of the concentration of the chemoattractant in water) was retained.

We assume that the culture medium exerts a drag force on the cells, and let the drag coefficient be k_{nw} . We hence write

$$\mathbf{F}_n = -k_{nw}(\mathbf{v}_n - \mathbf{v}_w) + p\nabla n, \quad (3.3.28)$$

$$\mathbf{F}_w = -k_{nw}(\mathbf{v}_w - \mathbf{v}_n) + p\nabla w, \quad (3.3.29)$$

noting that the last term in equations (3.3.28) and (3.3.29) represents the contribution of interfacial forces (see [26, 27] for a detailed derivation).

As in the previous chapter, we specify the drag coefficient, k_{nw} as follows

$$k_{nw} = k_1 n w, \quad (3.3.30)$$

(where k_1 is a non-negative constant) so there is no drag if either of the two phases is not present. While other, empirically determined, forms for the drag

coefficient may be more physically realistic (*e.g.* the Carman-Kozeny relation described in [35]), the form we have adopted has the virtue of greater simplicity.

Adopting these constitutive relations, equation (3.3.24) gives the following momentum balances for the two-phase mixture in the x and y -directions respectively

$$\frac{\partial}{\partial x} \left(-p - n\Sigma_n + 2\mu_n n \frac{\partial u_n}{\partial x} \right) + \mu_n \frac{\partial}{\partial y} \left(n \frac{\partial u_n}{\partial y} + n \frac{\partial v_n}{\partial x} \right) = 0, \quad (3.3.31)$$

$$\frac{\partial}{\partial y} \left(-p - n\Sigma_n + 2\mu_n n \frac{\partial v_n}{\partial y} \right) + \mu_n \frac{\partial}{\partial x} \left(n \frac{\partial u_n}{\partial y} + n \frac{\partial v_n}{\partial x} \right) = 0. \quad (3.3.32)$$

Similarly, from equations (3.3.22) and (3.3.29), we now have the following for the culture medium

$$\frac{\partial}{\partial x} (-wp) - k_1 n w (u_w - u_n) + p \frac{\partial w}{\partial x} = 0, \quad (3.3.33)$$

$$\frac{\partial}{\partial y} (-wp) - k_1 n w (v_w - v_n) + p \frac{\partial w}{\partial y} = 0. \quad (3.3.34)$$

These equations are subject to the following boundary and initial conditions. At $t = 0$ we must specify the distribution of the cells (which automatically specifies the distribution of the culture medium via $w = 1 - n$). We restrict our attention to initial conditions for which n is independent of y (this is required for consistency in the thin film limits we shall consider later). We thus set

$$n(x, y, 0) = n_i(x). \quad (3.3.35)$$

At $x = 0, L$ we assume there is zero flux of cells and culture medium out of the domain, which gives

$$u_n(0, y, t) = u_w(0, y, t) = u_n(L, y, t) = u_w(L, y, t) = 0. \quad (3.3.36)$$

Cell aggregates have a measurable surface tension, due to the fact that cell-cell adhesion within the aggregate means that the pressure within it need not equal that in the surrounding culture medium. In fact, the aggregate surface tension has recently been shown to be proportional to the level of expression

of cadherin (a cell adhesion molecule) [34]. The normal stress condition at $y = h$ is thus given by

$$\hat{\mathbf{n}} \cdot (\boldsymbol{\sigma} \cdot \hat{\mathbf{n}})|_{y=h} = -\gamma_c \Upsilon(n) \nabla \cdot \hat{\mathbf{n}}. \quad (3.3.37)$$

The term on the RHS represents surface tension with coefficient $\gamma_c \Upsilon(n)$, where γ_c is a typical value of the surface tension and $\Upsilon(n)$ is a dimensionless function. The dependence of Υ on n in our model is essential, as in the absence of cells, there is no distinction between the regions $g < y \leq h$ and $y > h$, and thus $\Upsilon(0) = 0$. (Note that, within the two-phase mixture, we have already accounted for the fact that the pressures in the cells and culture medium differ.)

In the tangential direction, we assume there is no stress at $y = h$ which gives

$$\hat{\mathbf{t}} \cdot (\boldsymbol{\sigma} \cdot \hat{\mathbf{n}})|_{y=h} = 0, \quad (3.3.38)$$

whilst at $y = g$ cell-ECM adhesion results in drag, with coefficient $k_2 n \rho_0$

$$\hat{\mathbf{t}} \cdot (\boldsymbol{\sigma} \cdot \hat{\mathbf{n}})|_{y=g} = k_2 n \rho_0 \left(\mathbf{v}_n - \frac{\partial \mathbf{U}}{\partial t} \right) \cdot \hat{\mathbf{t}}. \quad (3.3.39)$$

In addition we have the kinematic conditions at $y = g, h$, (3.3.18) and (3.3.19), and the stress conditions at the cell-ECM interface, $y = g$, (3.3.10) and (3.3.11).

3.3.4 Chemoattractant concentration

We assume that the chemoattractant disperses through the culture medium by a combination of advection and diffusion, with diffusion coefficient D . Its distribution thus evolves according to the following reaction-advection-diffusion equation

$$\frac{\partial}{\partial t}(cw) + \nabla \cdot (cw \mathbf{v}_w) = D \nabla \cdot (w \nabla c) + P(n, c) - S(n, c), \quad (3.3.40)$$

where $P(n, c)$ represents production of chemoattractant by the cells, and $S(n, c)$ is the rate at which the chemical decays and is consumed. (A detailed derivation of this equation, using the volume averaging technique, is given in Appendix A.)

We assume that the chemoattractant is produced by the cells at a rate α_0 , and then released into the culture medium. The source term P is thus assumed to be proportional to the product of the volume fractions of the two phases, since there must be contact between them in order for the chemical to enter the culture medium. Natural decay of the chemoattractant is assumed to occur at a rate α_1 , and (as in a number of other models [63]) we neglect the amount consumed by the cells when sensing concentrations, so

$$P(n, c) = \alpha_0 n(1 - n), \quad S(n, c) = \alpha_1(1 - n)c, \quad (3.3.41)$$

where we have used the fact that $w = 1 - n$. We remark that the factor of $1 - n$ in S arises as a result of the volume averaging process (see Appendix A).

Equation (3.3.40) will be subject to an initial condition for the distribution of chemoattractant - *i.e.*

$$c(x, y, 0) = c_i(x, y), \quad (3.3.42)$$

and no-flux conditions at the boundaries

$$cwu_w - Dw \frac{\partial c}{\partial x} = 0 \quad \text{at } x = 0, L, \quad (3.3.43)$$

$$\hat{\mathbf{n}} \cdot (cw\mathbf{v}_w - Dw\nabla c) = 0 \quad \text{at } y = g, h. \quad (3.3.44)$$

3.3.5 Nondimensionalisation

We now nondimensionalise the governing equations, initial and boundary conditions, making the additional assumption that the depth of the cell culture layer is of the same order as that of the ECM.

We denote dimensionless variables by tildes, and nondimensionalise the independent variables as follows

$$\tilde{x} = \frac{x}{\lambda}, \quad \tilde{y} = \frac{y}{g_i}, \quad \tilde{t} = \frac{t}{T}, \quad (3.3.45)$$

where g_i is the depth of the undisturbed ECM layer, λ is the lengthscale of an aggregate, and T is the timescale of interest (*i.e.* the aggregation timescale), the latter two of which will be determined subsequently.

In the ECM, we nondimensionalise the dependent variables U , V , P_E and g as follows

$$\tilde{U} = \frac{U}{\kappa\lambda}, \quad \tilde{V} = \frac{V}{\kappa g_i}, \quad \tilde{P} = \frac{P_E T}{\kappa\mu_n}, \quad \tilde{g} = \frac{g}{g_i}, \quad (3.3.46)$$

where κ is the ratio of the ECM deformation lengthscale to that of an aggregate (which is to be determined) and the scaling for P_E has been chosen to match with the pressure in the overlying two-phase mixture, as a result of continuity of normal stress at the interface. In the cell culture layer, we set

$$\tilde{u}_n = \frac{u_n T}{\lambda}, \quad \tilde{v}_n = \frac{v_n T}{g_i}, \quad \tilde{u}_w = \frac{u_w T}{\lambda}, \quad \tilde{v}_w = \frac{v_w T}{g_i}, \quad \tilde{h} = \frac{h}{g_i}. \quad (3.3.47)$$

Governing equations for the extracellular matrix

The dimensionless form of equation (3.3.4) is unchanged, whilst the momentum equations (3.3.5) and (3.3.6) now become (dropping tildes)

$$-\eta^2 \hat{\mu}_n \frac{\partial P}{\partial x} + \eta^2 \frac{\partial^2}{\partial x^2} \left(\frac{\partial U}{\partial t} + \hat{E}U \right) + \frac{\partial^2}{\partial y^2} \left(\frac{\partial U}{\partial t} + \hat{E}U \right) = 0, \quad (3.3.48)$$

$$-\hat{\mu}_n \frac{\partial P}{\partial y} + \frac{\partial^2}{\partial y^2} \left(\frac{\partial V}{\partial t} + \hat{E}V \right) + \eta^2 \frac{\partial^2}{\partial x^2} \left(\frac{\partial V}{\partial t} + \hat{E}V \right) = 0, \quad (3.3.49)$$

where we have introduced the following dimensionless parameters

$$\eta = \frac{g_i}{\lambda}, \quad \hat{\mu}_n = \frac{\mu_n}{\mu_1}, \quad \hat{E} = \frac{E'T}{\mu_1}. \quad (3.3.50)$$

Physically, η is the inverse aspect ratio, $\hat{\mu}_n$ is the ratio of the viscosities of the cells and ECM, and \hat{E} the ratio of the timescale of interest to the ECM

relaxation timescale.

The dimensionless forms of equations (3.3.7) and (3.3.8) are unchanged. The boundary conditions (3.3.9) become

$$\mathbf{U}(0, y, t) = \mathbf{U}(1/\epsilon, y, t) = 0, \quad (3.3.51)$$

where $\epsilon = \lambda/L$, the ratio of the aggregate lengthscale to that of the culture well, is observed to be small.

We now introduce the dimensionless version of the stress tensor $\boldsymbol{\sigma}_\rho$, which is scaled with $\kappa\mu_1/T$

$$\boldsymbol{\sigma}_\rho = -\hat{\mu}_n P\mathbf{I} + \frac{\partial \boldsymbol{\epsilon}}{\partial t} + \hat{E}\boldsymbol{\epsilon}, \quad (3.3.52)$$

where

$$\boldsymbol{\epsilon} = \begin{pmatrix} 2\frac{\partial U}{\partial x} & \frac{1}{\eta}\frac{\partial U}{\partial y} + \eta\frac{\partial V}{\partial x} \\ \frac{1}{\eta}\frac{\partial U}{\partial y} + \eta\frac{\partial V}{\partial x} & 2\frac{\partial V}{\partial y} \end{pmatrix}. \quad (3.3.53)$$

The continuity of normal stress condition, (3.3.10) becomes

$$\hat{\mathbf{n}} \cdot (\boldsymbol{\sigma}_\rho \cdot \hat{\mathbf{n}})|_{y=g} = \frac{\hat{\mu}_n}{\kappa} \hat{\mathbf{n}} \cdot (\boldsymbol{\sigma} \cdot \hat{\mathbf{n}})|_{y=g}, \quad (3.3.54)$$

whilst the nondimensional tangential stress condition (3.3.11) gives

$$\hat{\mathbf{t}} \cdot (\boldsymbol{\sigma}_\rho \cdot \hat{\mathbf{n}})|_{y=g} = \frac{\hat{\mu}_n}{\kappa} \hat{\mathbf{t}} \cdot (\boldsymbol{\sigma} \cdot \hat{\mathbf{n}})|_{y=g}. \quad (3.3.55)$$

Here, $\boldsymbol{\sigma}$ is the dimensionless stress tensor for the cell and culture medium mixture (scaled with μ_n/T). We note that choosing $\hat{\mu}_n/\kappa = 1$ sets the ratio of the deformation and aggregate lengthscales; thus, when the ECM is very viscous compared to the cells, we expect deformations to be small.

The unit normal and tangent vectors to the surface $y = g$ are given by

$$\hat{\mathbf{n}} = \frac{1}{\sqrt{1 + \eta^2 \left(\frac{\partial g}{\partial x}\right)^2}} \left(-\eta \frac{\partial g}{\partial x}, 1 \right), \quad \hat{\mathbf{t}} = \frac{1}{\sqrt{1 + \eta^2 \left(\frac{\partial g}{\partial x}\right)^2}} \left(1, \eta \frac{\partial g}{\partial x} \right). \quad (3.3.56)$$

The dimensionless form of the kinematic boundary condition (3.3.13) is

$$\kappa \frac{\partial V}{\partial t} = \frac{\partial g}{\partial t} + \kappa \frac{\partial U}{\partial t} \frac{\partial g}{\partial x}, \quad (3.3.57)$$

and is subject to the initial condition

$$g(x, 0) = 1. \quad (3.3.58)$$

Governing equations for the cells and culture medium

Following nondimensionalisation, the forms of the mass conservation equations for the cells and the culture medium, (3.3.16) and (3.3.17) and the kinematic conditions (3.3.18) and (3.3.19) remain unchanged. We now introduce $p_T = p + n\Sigma_n$ which appears as the ‘total’ pressure in $\boldsymbol{\sigma}$ (the stress tensor for the two phase mixture), and the following scalings

$$\tilde{p}_T = \frac{p_T T}{\mu_n}, \quad \tilde{\Sigma}_n = \frac{\Sigma_n}{\Gamma_1}. \quad (3.3.59)$$

Scaling the chemoattractant concentration with $\alpha_0 \lambda^2 / D$ (see below for details), we thus see from equation (3.3.27) that the nondimensional form of Σ_n is

$$\tilde{\Sigma}_n = (1 - \hat{\tau} \tilde{c}) H(\hat{c}_{max} - \tilde{c}), \quad (3.3.60)$$

where $\hat{\tau} = \tau \alpha_0 \lambda^2 / D$ and $\hat{c}_{max} = c_{max} D / \alpha_0 \lambda^2$, with the constraint becoming $\hat{c}_{max} < 1 / \hat{\tau}$.

The nondimensional versions of equations (3.3.31) and (3.3.32) are then

$$-\frac{\partial p_T}{\partial x} + 2 \frac{\partial}{\partial x} \left(n \frac{\partial u_n}{\partial x} \right) + \frac{\partial}{\partial y} \left(n \frac{\partial v_n}{\partial x} \right) + \eta^{-2} \frac{\partial}{\partial y} \left(n \frac{\partial u_n}{\partial y} \right) = 0, \quad (3.3.61)$$

$$-\frac{\partial p_T}{\partial y} + 2 \frac{\partial}{\partial y} \left(n \frac{\partial v_n}{\partial y} \right) + \frac{\partial}{\partial x} \left(n \frac{\partial u_n}{\partial y} \right) + \eta^2 \frac{\partial}{\partial x} \left(n \frac{\partial v_n}{\partial x} \right) = 0, \quad (3.3.62)$$

while equations (3.3.33) and (3.3.34) become

$$-\frac{\partial p_T}{\partial x} + \hat{\Gamma}_1 \frac{\partial}{\partial x} (n \Sigma_n) - \hat{k}_1 n (u_w - u_n) = 0, \quad (3.3.63)$$

$$\eta^{-2} \left(-\frac{\partial p_T}{\partial y} + \hat{\Gamma}_1 \frac{\partial}{\partial y} (n \Sigma_n) \right) - \hat{k}_1 n (v_w - v_n) = 0. \quad (3.3.64)$$

The dimensionless parameters $\hat{\Gamma}_1$ and \hat{k}_1 represent respectively the relative strengths of chemotaxis and cell-culture medium drag compared to viscous effects, such that

$$\hat{\Gamma}_1 = \frac{\Gamma_1 T}{\mu_n}, \quad \hat{k}_1 = \frac{k_1 \lambda^2}{\mu_n}. \quad (3.3.65)$$

We now specify the dimensionless boundary and initial conditions. Continuity of normal stress at $y = g$ then gives

$$\frac{\hat{\mu}_n}{\kappa} \hat{\mathbf{n}} \cdot (\boldsymbol{\sigma} \cdot \hat{\mathbf{n}})|_{y=g} = \hat{\mathbf{n}} \cdot (\boldsymbol{\sigma}_\rho \cdot \hat{\mathbf{n}})|_{y=g}, \quad (3.3.66)$$

where

$$\boldsymbol{\sigma} = p_T \mathbf{I} + n \mathbf{e}, \quad (3.3.67)$$

and

$$\mathbf{e} = \begin{pmatrix} 2 \frac{\partial u_n}{\partial x} & \eta^{-1} \frac{\partial u_n}{\partial y} + \eta \frac{\partial v_n}{\partial x} \\ \eta^{-1} \frac{\partial u_n}{\partial y} + \eta \frac{\partial v_n}{\partial x} & 2 \frac{\partial v_n}{\partial y} \end{pmatrix}. \quad (3.3.68)$$

Continuity of tangential stress at $y = g$, combined with the cell-ECM adhesion condition (3.3.39), gives

$$\hat{\mathbf{t}} \cdot (\boldsymbol{\sigma} \cdot \hat{\mathbf{n}})|_{y=g} = \frac{\kappa}{\hat{\mu}_n} \hat{\mathbf{t}} \cdot (\boldsymbol{\sigma}_\rho \cdot \hat{\mathbf{n}})|_{y=g} \quad (3.3.69)$$

$$= \frac{\hat{k}_2 n}{\eta} \left(\mathbf{v}_n - \kappa \frac{\partial \mathbf{U}}{\partial t} \right) \cdot \hat{\mathbf{t}}|_{y=g}, \quad (3.3.70)$$

where $\hat{k}_2 = k_2 \rho_0 g_i / \mu_n$ is the ratio of cell-ECM drag to cell viscosity.

At $y = h$, the normal and tangential stress conditions are, respectively

$$\hat{\mathbf{n}} \cdot (\boldsymbol{\sigma} \cdot \hat{\mathbf{n}}|_{y=h}) = -C \Upsilon(n) \frac{\partial}{\partial x} \left(\frac{1}{\sqrt{1 + \eta^2 \frac{\partial h^2}{\partial x}}} \frac{\partial h}{\partial x} \right). \quad (3.3.71)$$

where C is the inverse capillary number given by $C = \gamma_c \eta T / \mu_n \lambda$, and

$$\hat{\mathbf{t}} \cdot (\boldsymbol{\sigma} \cdot \hat{\mathbf{n}}|_{y=h}) = 0. \quad (3.3.72)$$

The unit normal and tangent to $y = h$ are given by

$$\hat{\mathbf{n}} = \frac{1}{\sqrt{1 + \eta^2 \left(\frac{\partial h}{\partial x} \right)^2}} \left(-\eta \frac{\partial h}{\partial x}, 1 \right), \quad \hat{\mathbf{t}} = \frac{1}{\sqrt{1 + \eta^2 \left(\frac{\partial h}{\partial x} \right)^2}} \left(1, \eta \frac{\partial h}{\partial x} \right). \quad (3.3.73)$$

These are supplemented by the rescaled no-flux boundary conditions on $x = 0, 1/\epsilon$

$$u_n(0, y, t) = u_n(1/\epsilon, y, t) = u_w(1/\epsilon, y, t) = 0. \quad (3.3.74)$$

The initial condition for n becomes

$$n(x, y, 0) = n_i(x), \quad 0 \leq x \leq 1/\epsilon, \quad g \leq y \leq h. \quad (3.3.75)$$

Governing equation for the chemoattractant

In (3.3.40) we scale c with $\alpha_0 \lambda^2 / D$, which gives an estimate of the amount of chemoattractant produced on the timescale for diffusion, $T_{\text{diff}} = \lambda^2 / D$. In nondimensional variables, the governing equation is then

$$\mathcal{P} \left[\frac{\partial}{\partial t}(cw) + \frac{\partial}{\partial x}(c w u_w) + \frac{\partial}{\partial y}(c w v_w) \right] = \frac{\partial}{\partial x} \left(w \frac{\partial c}{\partial x} \right) + \eta^{-2} \frac{\partial}{\partial y} \left(w \frac{\partial c}{\partial y} \right) + n w - \alpha c w, \quad (3.3.76)$$

where $\mathcal{P} = \lambda^2 / DT$ is the Péclet number (ratio of diffusive and advective timescales), and $\alpha = \alpha_1 \lambda^2 / D$ is the dimensionless decay rate of the chemical.

The dimensionless boundary and initial conditions are

$$c(x, y, 0) = c_i(x, y), \quad (3.3.77)$$

$$\mathcal{P} c w u_w - w \frac{\partial c}{\partial x} = 0 \quad \text{at } x = 0, \frac{1}{\epsilon}, \quad (3.3.78)$$

$$\hat{\mathbf{n}} \cdot (\mathcal{P} c w \mathbf{v}_w - w \nabla c) = 0 \quad \text{at } y = g, h. \quad (3.3.79)$$

We have now developed our two-dimensional model of cell aggregation *in vitro*. In the early stages of the process, the cell clusters remain well spread on the surface of the ECM (see Chapter 1), so the inverse aspect ratio of the aggregates η will be small. (Note that this assumption is violated during the later stages, when the clusters contract and detach from the ECM to form spheroids.) Following King and Oliver [53], in the remainder of this chapter, we exploit the thin geometry of the problem to reduce our two dimensional model to a simpler, one-dimensional form. We begin in §3.4 by considering the evolution of the chemoattractant concentration .

3.4 Chemoattractant concentration: rapid diffusion limit

We consider the limit in which diffusion of the chemoattractant occurs almost instantaneously, compared to the timescale for cell movement *i.e.* the Péclet number, $\mathcal{P} \ll 1$. Formally setting $\mathcal{P} = 0$ in equation (3.3.76), we obtain the following

$$\frac{\partial}{\partial x} \left(w \frac{\partial c}{\partial x} \right) + \eta^{-2} \frac{\partial}{\partial y} \left(w \frac{\partial c}{\partial y} \right) + nw - \alpha cw = 0. \quad (3.4.1)$$

Note that an initial condition for c is no longer required. We exploit the thin geometry of the problem, by assuming $\eta = g_i/\lambda \ll 1$ and seeking a regular power series expansion for c in terms of the small parameter η^2

$$c = c_0 + \eta^2 c_1 + \dots \quad (3.4.2)$$

At $O(\eta^{-2})$ we thus have

$$\frac{\partial}{\partial y} \left(w_0 \frac{\partial c_0}{\partial y} \right) = 0 \Rightarrow w_0 \frac{\partial c_0}{\partial y} = f(x, t), \quad (3.4.3)$$

where $w_0 = 1 - n_0$ is the leading order solution for w and $f(x, t)$ is a function to be determined by imposing the boundary conditions. At leading order, equation (3.3.79) gives

$$w_0 \frac{\partial c_0}{\partial y} = 0 \quad \text{at } y = g_0, h_0. \quad (3.4.4)$$

Hence applying this condition at either g_0 or h_0 implies that $f(x, t) \equiv 0$. We thus find that c_0 depends only on x and t (since c is the concentration of the chemoattractant in water, it is not defined for $w = 0$).

At next order we have

$$\frac{\partial}{\partial x} \left(w_0 \frac{\partial c_0}{\partial x} \right) + \frac{\partial}{\partial y} \left(w_0 \frac{\partial c_1}{\partial y} \right) + n_0 w_0 - \alpha c_0 w_0 = 0. \quad (3.4.5)$$

The boundary conditions (3.3.79) become, at this order

$$w_0 \frac{\partial c_1}{\partial y} - w_0 \frac{\partial g_0}{\partial x} \frac{\partial c_0}{\partial x} = 0, \quad \text{on } y = g_0 \quad (3.4.6)$$

$$w_0 \frac{\partial c_1}{\partial y} - w_0 \frac{\partial h_0}{\partial x} \frac{\partial c_0}{\partial x} = 0, \quad \text{on } y = h_0 \quad (3.4.7)$$

Integrating equation (3.4.5) with respect to y between $y = g_0$ and $y = h_0$ and applying boundary conditions (3.4.6) and (3.4.7), we obtain

$$\frac{1}{h_0 - g_0} \frac{\partial}{\partial x} \left((h_0 - g_0) \overline{w_0} \frac{\partial c_0}{\partial x} \right) + \overline{(w_0 n_0)} - \alpha \overline{w_0} c_0 = 0, \quad (3.4.8)$$

where depth averages are denoted by overbars so that

$$\overline{F}(x, t) = \frac{1}{(h_0 - g_0)} \int_{g_0}^{h_0} F(x, y, t) dy. \quad (3.4.9)$$

Hence, in this section, we have reduced the two dimensional, time-dependent equation (3.3.76) to a much simpler one dimensional, quasi-steady formulation (3.4.8), subject to the boundary conditions (3.3.78).

3.5 Extensional regime

In this section, we continue to exploit the fact that $\eta = g_i/\lambda \ll 1$ to simplify the equations for the ECM, cells and culture medium developed in §3.3.5. By introducing new scalings for the additional pressure or ‘chemotaxis’ term, Σ_n , and the cell-culture medium drag \hat{k}_1 , we reduce our two-dimensional model to a one-dimensional system. In the particular regime studied in this section, we find that the horizontal cell velocity, u_n , is independent of y . Borrowing terminology from fluid dynamics [45], we therefore refer to this as the ‘extensional regime’.

We consider a regime in which the scaling for the total pressure in the two-phase mixture (p_T) is as in §3.3.5; however, Σ_n is assumed to be large so that

$$\hat{\Gamma}_1 = \eta^{-2} \hat{\Gamma}_1^*, \quad (3.5.1)$$

(stars denote rescaled quantities). Thus the forces generated by the cells in response to the chemoattractant are assumed large, whilst the overall mixture

pressure is assumed $O(1)$ (the latter being equivalent to the scaling adopted by Howell in the one-phase case [45]). We also rescale the coefficient of drag between cells and culture medium as follows:

$$\hat{k}_1 = \eta^{-2} \hat{k}_1^*, \quad (3.5.2)$$

so there is strong coupling between the movement of the cells and the culture medium; this allows us to obtain a non-trivial relationship between Σ_n , u_n and u_w in equation (3.5.4) below. Finally, we rescale the cell-ECM drag parameter \hat{k}_2 to be $O(\eta^2)$ - *i.e.*

$$\hat{k}_2 = \eta^2 \hat{k}_2^*, \quad (3.5.3)$$

so cell adhesion to the ECM is weak. This scaling is introduced, as for $\hat{k}_2 \sim O(1)$ we find that we have a trivial situation in which $u_n \equiv 0$ at leading order (see Appendix B). In this regime, there is no ECM deformation at leading order, so the cell-ECM interface is fixed at $y = g_i \equiv 1$.

The mass conservation equations (3.3.16) and (3.3.17) are unchanged as a result of the rescalings above. However, the momentum equations and dynamic boundary conditions for the cells and culture medium are modified as set out below.

Following the rescalings, equations (3.3.63), (3.3.64), (3.3.61) and (3.3.62) become

$$-\eta^2 \frac{\partial p_T}{\partial x} + \hat{\Gamma}_1^* \frac{\partial}{\partial x} (n \Sigma_n) - \hat{k}_1^* n (u_w - u_n) = 0, \quad (3.5.4)$$

$$-\eta^2 \frac{\partial p_T}{\partial y} + \hat{\Gamma}_1^* \frac{\partial}{\partial y} (n \Sigma_n) - \eta^2 \hat{k}_1^* n (v_w - v_n) = 0, \quad (3.5.5)$$

$$-\eta^2 \frac{\partial p_T}{\partial x} + 2\eta^2 \frac{\partial}{\partial x} \left(n \frac{\partial u_n}{\partial x} \right) + \eta^2 \frac{\partial}{\partial y} \left(n \frac{\partial v_n}{\partial x} \right) + \frac{\partial}{\partial y} \left(n \frac{\partial u_n}{\partial y} \right) = 0, \quad (3.5.6)$$

$$-\frac{\partial p_T}{\partial y} + 2 \frac{\partial}{\partial y} \left(n \frac{\partial v_n}{\partial y} \right) + \frac{\partial}{\partial x} \left(n \frac{\partial u_n}{\partial y} \right) + \eta^2 \frac{\partial}{\partial x} \left(n \frac{\partial v_n}{\partial x} \right) = 0. \quad (3.5.7)$$

Henceforth we shall drop the stars when referring to rescaled parameters.

We seek solutions of the governing equations in the form of regular power series expansions in the small parameter η^2 so that

$$n = n_0 + \eta^2 n_1 + \dots,$$

with similar expressions for p_T , u_n , v_n and h .

The leading order boundary conditions become

$$v_{n0} = \frac{\partial g_0}{\partial t} + u_{n0} \frac{\partial g_0}{\partial x}, \quad v_{w0} = \frac{\partial g_0}{\partial t} + u_{w0} \frac{\partial g_0}{\partial x} \quad \text{on } y = g_0, \quad (3.5.8)$$

$$v_{n0} = \frac{\partial h_0}{\partial t} + u_{n0} \frac{\partial h_0}{\partial x}, \quad v_{w0} = \frac{\partial h_0}{\partial t} + u_{w0} \frac{\partial h_0}{\partial x} \quad \text{on } y = h_0, \quad (3.5.9)$$

$$n_0 \frac{\partial u_{n0}}{\partial y} = 0 \quad \text{on } y = 1, h_0, \quad (3.5.10)$$

$$-p_{T0} + 2n_0 \frac{\partial v_{n0}}{\partial y} = C\Upsilon(n_0) \frac{\partial^2 h_0}{\partial x^2} + n_0 \frac{\partial h_0}{\partial x} \frac{\partial u_{n0}}{\partial y} \quad \text{on } y = h_0. \quad (3.5.11)$$

Note that we have omitted the continuity of normal stress boundary condition at $y = g_0$. This condition is used to determine the leading-order pressure P_0 in the ECM, but since this does not produce an $O(1)$ deformation of the ECM it is omitted here and instead appears in Appendix B. Our aim in the remainder of this section is to manipulate the rescaled equations (subject to the boundary conditions above) to obtain an equivalent one-dimensional model.

At leading order equation (3.5.5) supplies

$$\frac{\partial}{\partial y}(n_0 \Sigma_{n0}) = 0 \quad \Rightarrow \quad n_0 = n_0(x, t), \quad (3.5.12)$$

since $n\Sigma_n$ is a function of n and c , and we have shown in §3.4 that, at leading order, c is independent of y . The leading order balance in equation (3.5.6) then gives

$$\frac{\partial}{\partial y} \left(n_0 \frac{\partial u_{n0}}{\partial y} \right) = 0. \quad (3.5.13)$$

Integrating with respect to y and imposing the zero tangential stress boundary condition on either $y = 1$ or $y = h_0$ (3.5.10) yields

$$n_0 \frac{\partial u_{n0}}{\partial y} = 0 \quad \Rightarrow \quad u_{n0} = u_{n0}(x, t), \quad (3.5.14)$$

assuming, for a non-trivial solution, that $n_0 \neq 0$.

Having established that n_0 and u_{n0} are independent of y , we proceed as follows. Firstly, we obtain an equation for u_{n0} by integration of equation (3.5.6), considered at $O(\eta^2)$. We then determine p_{T0} , v_{n0} and u_{w0} in terms of n_0 , u_{n0} and h_0 using equations (3.3.16), (3.5.4) and (3.5.7) and associated boundary conditions. (We find it is not necessary to solve for v_{w0} .) By integrating equations (3.3.16) and (3.3.17) between $y = 1$ and $y = h_0$, we obtain equations for n_0 and h_0 , and complete our derivation of the reduced model.

To obtain an equation for u_{n0} , it is necessary to consider equation (3.5.6) at $O(\eta^2)$. This gives the following

$$-\frac{\partial p_{T0}}{\partial x} + 2\frac{\partial}{\partial x} \left(n_0 \frac{\partial u_{n0}}{\partial x} \right) + \frac{\partial}{\partial y} \left(n_0 \frac{\partial v_{n0}}{\partial x} \right) + \frac{\partial}{\partial y} \left(n_0 \frac{\partial u_{n1}}{\partial y} \right) = 0. \quad (3.5.15)$$

Integrating equation (3.5.15) between $y = g_0 \equiv 1$ and $y = h_0$ yields

$$-\int_1^{h_0} \frac{\partial p_{T0}}{\partial x} dy + 2(h_0 - 1) \frac{\partial}{\partial x} \left(n_0 \frac{\partial u_{n0}}{\partial x} \right) = - \left[n_0 \frac{\partial u_{n1}}{\partial y} + n_0 \frac{\partial v_{n0}}{\partial x} \right]_{y=1}^{y=h_0}. \quad (3.5.16)$$

We note that at $O(\eta^2)$ the tangential stress boundary conditions at $y = 1, h_0$ (3.5.10) give

$$n_0 \frac{\partial u_{n1}}{\partial y} + n_0 \frac{\partial v_{n0}}{\partial x} + 2n_0 \frac{\partial v_{n0}}{\partial y} \frac{\partial h_0}{\partial x} - 2n_0 \frac{\partial u_{n0}}{\partial x} \frac{\partial h_0}{\partial x} = 0, \quad \text{on } y = h_0 \quad (3.5.17)$$

$$n_0 \frac{\partial u_{n1}}{\partial y} + n_0 \frac{\partial v_{n0}}{\partial x} = \hat{k}_2 n_0 u_{n0} \quad \text{on } y = 1, \quad (3.5.18)$$

so that

$$-\left[n_0 \frac{\partial u_{n1}}{\partial y} + n_0 \frac{\partial v_{n0}}{\partial x} \right]_1^{h_0} = 2n_0 \frac{\partial v_{n0}}{\partial y} \frac{\partial h_0}{\partial x} - 2n_0 \frac{\partial u_{n0}}{\partial x} \frac{\partial h_0}{\partial x} + \hat{k}_2 n_0 u_{n0}. \quad (3.5.19)$$

We thus obtain the following equation for the leading-order cell velocity

$$-\int_1^{h_0} \frac{\partial p_{T0}}{\partial x} dy + 2(h_0 - 1) \frac{\partial}{\partial x} \left(n_0 \frac{\partial u_{n0}}{\partial x} \right) = 2n_0 \frac{\partial v_{n0}}{\partial y} \frac{\partial h_0}{\partial x} - 2n_0 \frac{\partial u_{n0}}{\partial x} \frac{\partial h_0}{\partial x} + \hat{k}_2 n_0 u_{n0}. \quad (3.5.20)$$

Using Leibniz integral rule, we can re-write the above as

$$-\frac{\partial}{\partial x} \int_1^{h_0} p_{T0} dy + 2 \frac{\partial}{\partial x} \left(n_0 (h_0 - 1) \frac{\partial u_{n0}}{\partial x} \right) = -p_{T0} \Big|_{y=h_0} \frac{\partial h_0}{\partial x} + 2n_0 \frac{\partial v_{n0}}{\partial y} \frac{\partial h_0}{\partial x} + \hat{k}_2 n_0 u_{n0}. \quad (3.5.21)$$

To eliminate the p_{T0} term in equation (3.5.20), we now consider equation (3.5.7) at leading order. We note that since $u_{n0} = u_{n0}(x, t)$, the leading order term involving $\partial u_n / \partial y$ in (3.5.7) vanishes, to give

$$-\frac{\partial p_{T0}}{\partial y} + 2 \frac{\partial}{\partial y} \left(n_0 \frac{\partial v_{n0}}{\partial y} \right) = 0. \quad (3.5.22)$$

Integrating equation (3.5.22), and imposing the normal stress boundary condition at $y = h_0$ (3.5.11) gives

$$-p_{T0} + 2n_0 \frac{\partial v_{n0}}{\partial y} = C\Upsilon(n_0) \frac{\partial^2 h_0}{\partial x^2}, \quad (3.5.23)$$

since u_{n0} is independent of y . This expression can be used to eliminate the first two terms on the RHS of equation (3.5.21). However, in order to eliminate the p_{T0} term from the LHS of equation (3.5.21), we return to the conservation of mass equation (3.3.16), which gives

$$\frac{\partial}{\partial y} (n_0 v_{n0}) = - \left(\frac{\partial n_0}{\partial t} + \frac{\partial}{\partial x} (n_0 u_{n0}) \right). \quad (3.5.24)$$

Since the RHS is a function of x and t only, we can simply integrate to determine $n_0 v_{n0}$ as a function of n_0 and u_{n0} . We impose the kinematic boundary condition on $y = 1$ to obtain the following

$$v_{n0} = - \frac{(y-1)}{n_0} \left(\frac{\partial n_0}{\partial t} + \frac{\partial}{\partial x} (n_0 u_{n0}) \right). \quad (3.5.25)$$

Equation (3.5.23) then gives, at leading order

$$p_{T0} = -2 \left(\frac{\partial n_0}{\partial t} + \frac{\partial}{\partial x} (n_0 u_{n0}) \right) - C\Upsilon(n_0) \frac{\partial^2 h_0}{\partial x^2}. \quad (3.5.26)$$

Since we have now established that p_{T0} is independent of y , the integral in equation (3.5.21) can be performed, giving the following equation for u_{n0} in terms of n_0 and h_0

$$2 \frac{\partial}{\partial x} \left[(h_0 - 1) \left(\frac{\partial n_0}{\partial t} + u_{n0} \frac{\partial n_0}{\partial x} + 2n_0 \frac{\partial u_{n0}}{\partial x} \right) \right] + (h_0 - 1) \frac{\partial}{\partial x} \left(C\Upsilon(n_0) \frac{\partial^2 h_0}{\partial x^2} \right) = \hat{k}_2 n_0 u_{n0}. \quad (3.5.27)$$

We derive equations for n_0 and h_0 as follows. Integrating equation (3.3.16) between $y = 1$ and $y = h_0$ yields

$$\frac{\partial}{\partial t}[n_0(h_0 - 1)] + \frac{\partial}{\partial x}[n_0 u_{n0}(h_0 - 1)] = 0. \quad (3.5.28)$$

We remark that this equation can also be derived by setting $y = h_0$ on the RHS of equation (3.5.25), and using the kinematic boundary condition (3.5.9) to eliminate v_{n0} . This provides a simple check on the consistency of our formulation.

Similarly, integration of equation (3.3.17) between $y = 1$ and $y = h_0$ gives

$$\frac{\partial}{\partial t}[w_0(h_0 - 1)] + \frac{\partial}{\partial x}[w_0 u_{w0}(h_0 - 1)] = 0. \quad (3.5.29)$$

We eliminate w_0 in equation (3.5.29) above using the no voids condition, and then by taking linear combinations of equations (3.5.28) and (3.5.29) we obtain the following evolution equations for n_0 and h_0

$$\frac{\partial}{\partial t}(h_0 - 1) + \frac{\partial}{\partial x}[(h_0 - 1)(n_0 u_{n0} + (1 - n_0)u_{w0})] = 0, \quad (3.5.30)$$

$$\frac{\partial n_0}{\partial t} + u_{n0} \frac{\partial n_0}{\partial x} - \frac{n_0}{(h_0 - 1)} \frac{\partial}{\partial x}[(h_0 - 1)(1 - n_0)(u_{w0} - u_{n0})] = 0, \quad (3.5.31)$$

wherein, from equation (3.5.4),

$$u_{w0} = u_{n0} + \frac{\hat{\Gamma}_1}{\hat{k}_1 n_0} \frac{\partial}{\partial x}(n_0 \Sigma_{n0}). \quad (3.5.32)$$

In this regime, since there is no ECM deformation at leading order, the model simplifies greatly; we no longer need to solve for P , U , V or g , and the values of the dimensionless parameters $\hat{\mu}_n$ and \hat{E} , which are related to the ECM's mechanical properties, are not required. Using a thin-film approximation, we have reduced our two-dimensional model for the cells and culture medium to a one-dimensional problem at leading order. The reduced model consists of three coupled partial differential equations for n_0 , u_{n0} and h_0 , supplemented by equation (3.4.8) for the chemoattractant and associated boundary conditions.

3.5.1 Summary of governing equations

For clarity, we now summarise the reduced model which, in this case, consists of four coupled PDEs for n_0 , u_{n_0} , h_0 and c_0 .

The leading-order volume fraction of cells, n_0 is given by

$$\frac{\partial n_0}{\partial t} + u_{n_0} \frac{\partial n_0}{\partial x} - \frac{\hat{\Gamma}_1 n_0}{\hat{k}_1 (h_0 - 1)} \frac{\partial}{\partial x} \left[\frac{(h_0 - 1)(1 - n_0)}{n_0} \frac{\partial}{\partial x} (n_0 \Sigma_{n_0}) \right] = 0, \quad (3.5.33)$$

where we have substituted for u_{w_0} using equation (3.5.32).

Eliminating $\partial n_0 / \partial t$ between equations (3.5.33) and equation (3.5.27) we deduce that u_{n_0} satisfies

$$\begin{aligned} 2 \frac{\partial}{\partial x} \left[(h_0 - 1) \left(2n_0 \frac{\partial u_{n_0}}{\partial x} + \frac{\hat{\Gamma}_1 n_0}{\hat{k}_1 (h_0 - 1)} \frac{\partial}{\partial x} \left[\frac{(h_0 - 1)(1 - n_0)}{n_0} \frac{\partial}{\partial x} (n_0 \Sigma_{n_0}) \right] \right) \right] \\ = \hat{k}_2 n_0 u_{n_0} - (h_0 - 1) \frac{\partial}{\partial x} \left(C \Upsilon(n_0) \frac{\partial^2 h_0}{\partial x^2} \right). \end{aligned} \quad (3.5.34)$$

The evolution of h_0 is then governed by

$$\frac{\partial}{\partial t} (h_0 - 1) + \frac{\partial}{\partial x} \left[(h_0 - 1) \left(u_{n_0} + \frac{\hat{\Gamma}_1 (1 - n_0)}{\hat{k}_1 n_0} \frac{\partial}{\partial x} (n_0 \Sigma_{n_0}) \right) \right] = 0. \quad (3.5.35)$$

Finally, the chemoattractant concentration evolves as follows

$$\frac{1}{h_0 - 1} \frac{\partial}{\partial x} \left((h_0 - 1)(1 - n_0) \frac{\partial c_0}{\partial x} \right) + n_0(1 - n_0) - \alpha(1 - n_0)c_0 = 0, \quad (3.5.36)$$

where we have dropped the overbars which appeared in equation (3.4.8), as n_0 is independent of y in this scaling regime.

In summary, our reduced model comprises equations (3.5.33)-(3.5.36), which contain the dimensionless parameters $\hat{\Gamma}_1 / \hat{k}_1$, \hat{k}_2 , C , α , $\hat{\tau}$ and \hat{c}_{max} (the latter two arising in our chosen form for Σ_n). They are solved subject to the following boundary and initial conditions

$$n_0(x, 0) = n_i(x), \quad (3.5.37)$$

$$\frac{\partial n_0}{\partial x} = 0 \quad \text{at } x = 0, 1/\epsilon, \tag{3.5.38}$$

$$u_{n_0} = 0 \quad \text{at } x = 0, 1/\epsilon, \tag{3.5.39}$$

$$h_0(x, 0) = 1 + h_i, \tag{3.5.40}$$

$$\frac{\partial c_0}{\partial x} = 0 \quad \text{at } x = 0, 1/\epsilon. \tag{3.5.41}$$

A notable feature of equations (3.5.33)-(3.5.35) is that the parameters $\hat{\Gamma}_1$ and \hat{k}_1 appear only in the combination $\hat{\Gamma}_1/\hat{k}_1 = \Gamma_1 T/k_1 \lambda^2$. Further, if we fix $\hat{\Gamma}_1/\hat{k}_1 = \alpha = 1$ then we are effectively selecting the time and length scales of interest (T and λ) on the basis of chemotactic cell movement.

Before continuing, we pause to point out a number of features of our reduced model. We note that equations (3.5.33), (3.5.34) and (3.5.35) are the one-dimensional analogues of those presented in Appendix 1 of [53] (where a underlying 3D model is reduced to 2D form by use of the thin film approximation). Furthermore, in the limit where $n_0 \rightarrow 1$, $\hat{\Gamma}_1$, \hat{k}_2 and $C \rightarrow 0$ (corresponding to a one phase model without chemotaxis, and where surface tension and ECM adhesion effects are negligible), equations (3.5.34) and (3.5.35) reduce to the Trouton model (3.2.1). We also note that equations (3.5.28) and (3.5.29) are the analogues of (2.2.2a) and (2.2.2b), representing conservation of cells and culture medium within the mixture layer. In the limit where $C = 0$, the viscous and cell-ECM drag terms in equation (3.5.34) take the same form as in equation (2.2.29) (provided ECM deformation is negligible in the latter). However, there is no correspondence between the Σ_n and \hat{k}_1 terms in the two models, due to the fact that the thin film model assumes the Σ_n term to be large.

We remark that the term in equation (3.5.33) involving Σ_{n_0} may be split into ‘diffusive’ and ‘chemotactic’ components via:

$$\frac{\partial}{\partial x}(n_0 \Sigma_{n_0}) = \frac{\partial}{\partial n_0}(n_0 \Sigma_{n_0}) \frac{\partial n_0}{\partial x} + n_0 \frac{\partial \Sigma_{n_0}}{\partial c_0} \frac{\partial c_0}{\partial x}. \tag{3.5.42}$$

From this decomposition it is clear that we require $\partial/\partial n_0(n_0\Sigma_{n_0}) > 0$; otherwise equation (3.5.33) becomes the backward heat equation. Since we have assumed that $\Sigma_{n_0} = \Sigma_{n_0}(c_0)$, this condition reduces to $\Sigma_{n_0} > 0$. We also remark that the condition that $\partial\Sigma_{n_0}/\partial c_0 < 0$ (required so that c acts as a chemoattractant) implies that diffusion is reduced as c_0 increases, since the effective diffusion coefficient depends on Σ_{n_0} , which is a decreasing function of c_0 . The biological significance of this fact is discussed in §3.7. Furthermore, the appearance of Σ_{n_0} in the evolution equation for n_0 (contrast equation (2.2.2a)) means that the approach we adopted in Chapter 2 (where we neglected the chemoattractant and specified Σ_n in terms of n) cannot be adopted here, as the model would then be ill posed in the case of aggregation.

Another interesting feature of equation (3.5.33) is that we observe there are two mechanisms by which the cell volume fraction n_0 can change. The most obvious is by cell migration (represented by the u_{n_0} term), but n_0 may also change due to movement of the culture medium, since cell-culture medium drag gives rise to the Σ_{n_0} term in equation (3.5.33) (see equation (3.5.32) above).

3.6 Lubrication regime

In this section, we consider an alternative thin film reduction of our model. We retain the scalings of §3.5 for the additional pressure or ‘chemotaxis’ term, Σ_n , and the cell-culture medium drag, \hat{k}_1 , but now assume that the mixture pressure and surface tension are large, as is conventional in lubrication theory [79]. Specifically, the dimensionless governing equations of §3.3.5 are rescaled in the following manner

$$p_T = \eta^{-2}p_T^*, \quad \Gamma_1^* = \eta^{-2}\Gamma_1^*, \quad P = \eta^{-2}P^*, \quad C = \eta^{-2}C^*, \quad (3.6.1)$$

where the stars denote rescaled quantities. These scalings imply that both the pressure generated in response to the chemoattractant (Σ_n) and the overall pressure in the two-phase mixture of cells and culture medium (p_T) are large. This, in turn, means that surface tension effects (C) must be stronger to accommodate the larger pressure jump between the mixture and free space, and that the pressure in the underlying ECM layer (P) must also be large, in order to guarantee continuity of normal stress.

In the ensuing analysis, we drop the stars for notational convenience.

3.6.1 ECM equations

As in §3.5, we expand the dependent variables as power series in the small parameter $\eta^2 \ll 1$, and thence reduce the governing equations to one-dimensional form at leading order. By making a suitable ansatz for the horizontal displacements of the ECM, we are able to solve for U_0 , V_0 , P_0 and g_0 in terms of quantities associated with the cells and culture medium (n_0 , u_{n0} and p_{T0}) and two new functions $\phi(x, t)$ and $\psi(x, t)$, equations for which are derived here.

The leading-order version of equation (3.3.49) gives

$$\frac{\partial P_0}{\partial y} = 0 \Rightarrow P_0 = P_0(x, t). \tag{3.6.2}$$

To determine P_0 , we impose the normal stress boundary condition on $y = g_0$ (3.3.54), which gives:

$$\kappa P_0 = p_{T0}. \tag{3.6.3}$$

In the x -direction, the leading order balance in (3.3.48) is now

$$\frac{\partial^2}{\partial y^2} \left(\frac{\partial U_0}{\partial t} + \hat{E}U_0 \right) = \hat{\mu}_n \frac{\partial P_0}{\partial x}. \tag{3.6.4}$$

We seek a solution of the form

$$U_0(x, y, t) = y\phi(x, t) + y^2\psi(x, t), \tag{3.6.5}$$

which automatically satisfies the zero-displacement boundary condition on $y = 0$. We note that the condition $U(x, y, 0) = 0$ implies that $\phi(x, 0) = \psi(x, 0) = 0$. Equation (3.6.4) then gives

$$\frac{\partial \psi}{\partial t} + \hat{E}\psi = \frac{\hat{\mu}_n}{2} \frac{\partial P_0}{\partial x} = \frac{\hat{\mu}_n}{2\kappa} \frac{\partial p_{T0}}{\partial x}. \quad (3.6.6)$$

Imposition of the tangential stress boundary condition on $y = g_0$ (3.3.55) then gives an equation for ϕ

$$\frac{\partial \phi}{\partial t} + \hat{E}\phi = \frac{\hat{\mu}_n \hat{k}_2 n_0}{\kappa} \left(u_{n0}|_{y=g_0} - \kappa g_0 \frac{\partial \phi}{\partial t} - \kappa g_0^2 \frac{\partial \psi}{\partial t} \right) - 2\kappa g_0 \left(\frac{\partial \psi}{\partial t} + \hat{E}\psi \right). \quad (3.6.7)$$

The leading order vertical displacement V_0 is now determined from the ECM incompressibility condition (3.3.4) as

$$V_0 = -y^2 \left(\frac{1}{2} \frac{\partial \phi}{\partial x} + \frac{y}{3} \frac{\partial \psi}{\partial x} \right), \quad (3.6.8)$$

where we have applied $V_0|_{y=0} = 0$.

Imposing the kinematic condition on $y = g_0$ (3.3.57) yields the following equation for the position of the interface, g_0

$$\frac{\partial g_0}{\partial t} + \kappa \frac{\partial}{\partial x} \left(\frac{g_0^2}{2} \frac{\partial \phi}{\partial t} + \frac{g_0^3}{3} \frac{\partial \psi}{\partial t} \right) = 0. \quad (3.6.9)$$

In contrast to the extensional flow regime, in this case coupling of the cells and ECM is non-trivial. By introducing the two new functions $\phi(x, t)$ and $\psi(x, t)$, and making a thin film approximation, we have reduced the leading-order problem for the ECM displacements U_0 and V_0 to one-dimensional form. A 1D partial differential equation for the interface position g_0 (3.6.9) has also been derived and the pressure P_0 specified in terms of the pressure in the mixture of cells and culture medium, p_{T0} . The functions $\psi(x, t)$ and $\phi(x, t)$ are determined by equations (3.6.6) and (3.6.7) and depend on variables associated with the cells and culture medium (p_{T0} and u_{n0}), which will be determined in the next section. The two-dimensional ECM model has thus been reduced to three coupled one-dimensional equations - namely (3.6.6), (3.6.7) and (3.6.9).

3.6.2 Cell and culture medium equations

In this section, we determine the leading-order solution of the 2D model for the mixture of cells and culture medium, using the same approach as in §3.5. Following the rescalings presented in equation (3.6.1), the momentum equations for the culture medium, (3.3.33) and (3.3.34), become

$$-\frac{\partial p_T}{\partial x} + \hat{\Gamma}_1 \frac{\partial}{\partial x}(n\Sigma_n) - \hat{k}_1 n(u_w - u_n) = 0, \quad (3.6.10)$$

$$-\frac{\partial p_T}{\partial y} + \hat{\Gamma}_1 \frac{\partial}{\partial y}(n\Sigma_n) - \eta^2 \hat{k}_1 n(v_w - v_n) = 0, \quad (3.6.11)$$

whilst those for the two-phase mixture, (3.3.31) and (3.3.32), give

$$-\frac{\partial p_T}{\partial x} + 2\eta^2 \frac{\partial}{\partial x} \left(n \frac{\partial u_n}{\partial x} \right) + \eta^2 \frac{\partial}{\partial y} \left(n \frac{\partial v_n}{\partial x} \right) + \frac{\partial}{\partial y} \left(n \frac{\partial u_n}{\partial y} \right) = 0, \quad (3.6.12)$$

$$-\frac{\partial p_T}{\partial y} + 2\eta^2 \frac{\partial}{\partial y} \left(n \frac{\partial v_n}{\partial y} \right) + \eta^2 \frac{\partial}{\partial x} \left(n \frac{\partial u_n}{\partial y} \right) + \eta^4 \frac{\partial}{\partial x} \left(n \frac{\partial v_n}{\partial x} \right) = 0. \quad (3.6.13)$$

As in §3.5, we expand the dependent variables in powers of the small parameter η^2 . At leading order the boundary conditions are as follows

$$\kappa P_0 = p_{T0} \quad \text{on } y = g_0, \quad (3.6.14)$$

$$n_0 \frac{\partial u_{n0}}{\partial y} = \hat{k}_2 n_0 \left(u_{n0} - \kappa \frac{\partial U_0}{\partial t} \right) \quad \text{on } y = g_0, \quad (3.6.15)$$

$$v_{n0} = \frac{\partial g_0}{\partial t} + u_{n0} \frac{\partial g_0}{\partial x}, \quad v_{w0} = \frac{\partial g_0}{\partial t} + u_{w0} \frac{\partial g_0}{\partial x} \quad \text{on } y = g_0 \quad (3.6.16)$$

$$v_{n0} = \frac{\partial h_0}{\partial t} + u_{n0} \frac{\partial h_0}{\partial x}, \quad v_{w0} = \frac{\partial h_0}{\partial t} + u_{w0} \frac{\partial h_0}{\partial x} \quad \text{on } y = h_0 \quad (3.6.17)$$

$$n_0 \frac{\partial u_{n0}}{\partial y} = 0 \quad \text{on } y = h_0, \quad (3.6.18)$$

$$-p_{T0} = C\Upsilon(n_0) \frac{\partial^2 h_0}{\partial x^2} \quad \text{on } y = h_0. \quad (3.6.19)$$

At leading order equation (3.6.13) supplies

$$\frac{\partial p_{T0}}{\partial y} = 0 \quad \Rightarrow \quad p_{T0} = -C\Upsilon(n_0) \frac{\partial^2 h_0}{\partial x^2}, \quad (3.6.20)$$

where we have applied the normal stress boundary condition (3.6.19).

As in §3.5, equation (3.6.11) gives

$$\frac{\partial}{\partial y}(n_0 \Sigma_{n_0}) = 0 \Rightarrow n_0 = n_0(x, t). \quad (3.6.21)$$

Integration of equation (3.6.12) thus yields

$$u_{n_0} = \kappa g_0 \frac{\partial \phi}{\partial t} + \kappa g_0^2 \frac{\partial \psi}{\partial t} + \frac{C}{2n_0} \left(\frac{2(h_0 - g_0)}{\hat{k}_2} + (h_0 - g_0)^2 - (h_0 - y)^2 \right) \frac{\partial}{\partial x} \left(\Upsilon(n_0) \frac{\partial^2 h_0}{\partial x^2} \right), \quad (3.6.22)$$

where we have substituted for p_{T_0} from equation (3.6.20), for $\frac{\partial U_0}{\partial t}|_{y=g_0}$ from equation (3.6.5) and applied conditions (3.6.18) and (3.6.15).

In order to obtain equations for n_0 and h_0 , we integrate equations (3.3.16) and (3.3.17) between $y = g_0$ and $y = h_0$ and apply the kinematic boundary conditions (3.6.16)-(3.6.17), to get

$$\frac{\partial}{\partial t}[n_0(h_0 - g_0)] + \frac{\partial}{\partial x}[n_0(h_0 - g_0)\bar{u}_{n_0}] = 0, \quad (3.6.23)$$

$$\frac{\partial}{\partial t}[w_0(h_0 - g_0)] + \frac{\partial}{\partial x}[w_0(h_0 - g_0)\bar{u}_{w_0}] = 0, \quad (3.6.24)$$

where, as in §3.4, we have defined

$$\bar{F} = \frac{1}{(h_0 - g_0)} \int_{g_0}^{h_0} F dy. \quad (3.6.25)$$

From equation (3.6.22) we hence obtain

$$\bar{u}_{n_0} = \kappa g_0 \frac{\partial \phi}{\partial t} + \kappa g_0^2 \frac{\partial \psi}{\partial t} + \frac{C(h_0 - g_0)}{n_0} \left(\frac{1}{\hat{k}_2} + \frac{(h_0 - g_0)}{3} \right) \frac{\partial}{\partial x} \left(\Upsilon(n_0) \frac{\partial^2 h_0}{\partial x^2} \right). \quad (3.6.26)$$

Equation (3.6.10) gives

$$u_{w_0} = u_{n_0} + \frac{1}{\hat{k}_1 n_0} \frac{\partial}{\partial x} \left[\hat{\Gamma}_1 n_0 \Sigma_{n_0} + C \Upsilon(n_0) \frac{\partial^2 h_0}{\partial x^2} \right], \quad (3.6.27)$$

and thus

$$\bar{u}_{w_0} = \bar{u}_{n_0} + \frac{1}{\hat{k}_1 n_0} \frac{\partial}{\partial x} \left[\hat{\Gamma}_1 n_0 \Sigma_{n_0} + C \Upsilon(n_0) \frac{\partial^2 h_0}{\partial x^2} \right]. \quad (3.6.28)$$

By taking linear combinations of equations (3.6.23) and (3.6.24) we arrive at the following system of equations for h_0 and n_0 which are similar to those

presented in [53]

$$\frac{\partial(h_0 - g_0)}{\partial t} + \frac{\partial}{\partial x} ((h_0 - g_0)(n_0 \bar{u}_{n_0} + (1 - n_0) \bar{u}_{w_0})) = 0, \quad (3.6.29)$$

$$\frac{\partial n_0}{\partial t} + \bar{u}_{n_0} \frac{\partial n_0}{\partial x} + \frac{n_0}{(h_0 - g_0)} \frac{\partial}{\partial x} ((1 - n_0)(h_0 - g_0)(\bar{u}_{n_0} - \bar{u}_{w_0})) = 0. \quad (3.6.30)$$

In this section, we began with partial differential equations for the physical variables n , u_n , u_w , v_n , v_w , p_T and h . Using the thin-film approximation, we have reduced the system to two PDEs for n_0 and h_0 (the leading-order expression for h and n). All other variables have been specified in terms of h_0 and n_0 , and quantities associated with the ECM (ϕ , ψ and g_0).

3.6.3 Summary of governing equations

For clarity, we now summarise the governing equations, boundary and initial conditions for the reduced model. In this regime, the coupling between the cells and the ECM is non-trivial. The horizontal deformation of the ECM is determined by the relation $U(x, y, t) = y(\phi(x, t) + \psi(x, t))$ with the two functions ϕ and ψ , given by

$$\frac{\partial \phi}{\partial t} + \hat{E}\phi = \frac{\hat{\mu}_n C}{\kappa} h_0 \frac{\partial}{\partial x} \left(\Upsilon(n_0) \frac{\partial^2 h_0}{\partial x^2} \right), \quad (3.6.31)$$

$$\frac{\partial \psi}{\partial t} + \hat{E}\psi = -\frac{\hat{\mu}_n C}{2\kappa} \frac{\partial}{\partial x} \left(\Upsilon(n_0) \frac{\partial^2 h_0}{\partial x^2} \right). \quad (3.6.32)$$

Equations (3.6.31) and (3.6.32) are subject to the initial condition $\phi = \psi = 0$ at $t = 0$, which guarantees that the initial displacement of the ECM is zero.

The leading-order volume fraction of the cells is given by

$$\begin{aligned} & \frac{\partial n_0}{\partial t} + \bar{u}_{n_0} \frac{\partial n_0}{\partial x} \\ & - \frac{n}{\hat{k}_1(h_0 - g_0)} \frac{\partial}{\partial x} \left[\frac{(1 - n_0)(h_0 - g_0)}{n_0} \frac{\partial}{\partial x} \left(\hat{\Gamma}_1 n_0 \Sigma_{n_0} + C \Upsilon(n_0) \frac{\partial^2 h_0}{\partial x^2} \right) \right] = 0, \end{aligned} \quad (3.6.33)$$

which is similar to its equivalent in the extensional regime (equation (3.5.33)), except for the inclusion of the surface tension term. Hence the comments regarding Σ_n and the possibility of ill-posedness also apply here.

The positions of the interfaces, g_0 and h_0 obey

$$\frac{\partial g_0}{\partial t} + \kappa \frac{\partial}{\partial x} \left(\frac{g_0^2}{2} \frac{\partial \phi}{\partial t} + \frac{g_0^3}{3} \frac{\partial \psi}{\partial t} \right) = 0, \quad (3.6.34)$$

$$\frac{\partial(h_0 - g_0)}{\partial t} + \frac{\partial}{\partial x} \left((h_0 - g_0)(\bar{u}_{n_0} + \frac{(1 - n_0)}{\hat{k}_1 n_0} \frac{\partial}{\partial x} \left[\hat{\Gamma}_1 n_0 \Sigma_{n_0} + C \Upsilon(n_0) \frac{\partial^2 h_0}{\partial x^2} \right]) \right) = 0, \quad (3.6.35)$$

where the depth-averaged, leading-order horizontal velocity of the cells is given by

$$\bar{u}_{n_0} = \kappa g_0 \frac{\partial \phi}{\partial t} + \kappa g_0^2 \frac{\partial \psi}{\partial t} + \frac{C(h_0 - g_0)}{n_0} \left(\frac{1}{\hat{k}_2} + \frac{(h_0 - g_0)}{3} \right) \frac{\partial}{\partial x} \left(\Upsilon(n_0) \frac{\partial^2 h_0}{\partial x^2} \right). \quad (3.6.36)$$

In the case of h_0 , we once again note the close correspondence between equations (3.6.35) and (3.5.35), with the exception of the surface tension term in the former. However, as there is now non-zero deformation of the ECM, we have coupling between g_0 and h_0 .

Finally, the chemoattractant concentration satisfies

$$\frac{1}{(h_0 - g_0)} \frac{\partial}{\partial x} \left((1 - n_0)(h_0 - g_0) \frac{\partial c_0}{\partial x} \right) + n_0(1 - n_0) - \alpha(1 - n_0)c_0 = 0, \quad (3.6.37)$$

where we have dropped the overbars which appeared in equation (3.4.8), as n_0 is independent of y in this scaling regime.

Our reduced model comprises equations (3.6.31)-(3.6.37), which contain the dimensionless parameters $\hat{\mu}_n$, \hat{E} , $\hat{\Gamma}_1$, \hat{k}_1 , \hat{k}_2 , C , α , $\hat{\tau}$ and \hat{c}_{max} (the latter two arising in our chosen form for Σ_n). Initial conditions for equations for (3.6.31) and (3.6.32) have already been stated, whilst equations (3.6.33)-(3.6.37) are subject to the following boundary and initial conditions

$$n_0(x, 0) = n_i(x), \quad (3.6.38)$$

$$\frac{\partial n_0}{\partial x} = 0 \quad \text{at } x = 0, 1/\epsilon, \quad (3.6.39)$$

$$\frac{\partial}{\partial x} \left(\Upsilon(n_0) \frac{\partial^2 h_0}{\partial x^2} \right) = 0 \quad \text{at } x = 0, 1/\epsilon, \quad (3.6.40)$$

$$g_0(x, 0) = 1, \quad (3.6.41)$$

$$h_0(x, 0) = 1 + h_i, \quad (3.6.42)$$

$$\frac{\partial h_0}{\partial x} = 0 \quad \text{at } x = 0, 1/\epsilon, \quad (3.6.43)$$

$$\frac{\partial c_0}{\partial x} = 0 \quad \text{at } x = 0, 1/\epsilon. \quad (3.6.44)$$

We remark that we can recover the thin film equation (3.2.2) of [79] in the limit $\hat{\mu}_n = 0$, $n = 1$, $\hat{\Gamma}_1 = 0$ and $\hat{k}_2 \rightarrow \infty$. The condition on $\hat{\mu}_n$ implies that the ECM is effectively rigid; equations (3.6.32) and (3.6.31) give $\phi = \psi = 0$ on applying the initial condition, and hence $g \equiv 1$ by equation (3.6.34). The remaining conditions correspond to the limit of a one-phase model with no chemotaxis and a no-slip boundary condition on $y = g \equiv 1$. Equation (3.6.36) then becomes

$$\bar{u}_n = \frac{C(h_0 - 1)^2}{3} \frac{\partial^3 h_0}{\partial x^3}, \quad (3.6.45)$$

where we have assumed, without loss of generality, that $\Upsilon(1) = 1$. Substituting this into equation (3.6.35), we obtain (3.2.2) with $f \equiv 0$ (as we have neglected gravity and other effects).

3.7 Discussion

In this chapter, we have generalised the two-phase model of cell aggregation introduced in the previous chapter by adopting a two-dimensional Cartesian geometry (representing a vertical slice through the culture well), and including the effect of a chemoattractant produced by the cells. Our model thus extends previous work by Byrne and Owen [16], who also developed a two-phase cell aggregation model, but considered only the one-dimensional case, and neglected the viscosity of the cells and their interaction with the underlying substrate. We identified two scaling regimes (termed ‘extensional’ and

‘lubrication’) in which we could exploit the thin geometry of the problem to reduce the governing equations to a one-dimensional form. In the use of thin film approximations, our model most closely resembles that derived by King and Oliver [53], who used a mixture theory framework to model cell migration on a rigid surface. Although the applications are rather different, the resulting models are similar, and our work might thus be extended to examine the migration of a single cell on a deformable substrate. An important application of such work would be to quantify the relationship between the migration behaviour of the cell and the mechanical properties of the substrate, as experimental studies have demonstrated that average cell speeds are lower on more compliant substrates [120].

One noteworthy feature of the multiphase approach to modelling chemotaxis is the fact that the random motility and chemotaxis coefficients - which are usually represented via independent constants in the Keller-Segel model - are related, both deriving from the Σ_n term [16]. Given the restrictions $\Sigma_n > 0$, $\partial\Sigma_n/\partial c < 0$ (which are required to ensure well-posedness of the model, and that c acts as a chemoattractant), it is then apparent from equations (3.5.33) and (3.6.33) that random cell motility must decline as c increases. Although it may appear biologically plausible that at low chemical concentrations cells move mainly at random, whilst at higher levels of chemoattractant directed movement comes to dominate, at present there is no evidence of this being true for hepatocytes. However, recent research by Lin *et al.* involving neutrophils shows that their diffusion coefficient initially increases and then decreases, as the concentration of a chemoattractant (interleukin 8 or IL-8) increases [60]. In addition, this paper also suggests that ‘the effective chemotaxis is possibly strongly influenced by the mean IL-8 concentration of the stable linear gradient’. These results imply a relationship between c and the motility coefficients, and given appropriate experimental data could be fitted to the function Σ_n . An alternative approach would be to use a version of the Keller-Segel model with

non-constant coefficients (as has been proposed, for example, in [24] where the chemotaxis coefficient depends linearly on the cell density). This would also require validation against experiment for each combination of cell type and chemical.

In contrast with the 1D model in Chapter 2, for the thin film geometry considered here it is not possible to ignore the existence of the chemoattractant (and specify Σ_n as a function of n alone); doing so would result in a model that is ill-posed in the case of aggregation. Another difference is the role of cell-culture medium drag in the models. In the 1D model, even in the absence of cell-culture medium drag ($\hat{k}_1 \rightarrow 0$), mass conservation requires that culture medium move to fill any void left by migrating cells, and so the two velocities are always coupled. In the thin film model, however, in the absence of drag there would be no coupling between the cells and culture medium - cell movement need only result in a movement of the interface h . This fact is particularly obvious in the extensional regime, where $\hat{\Gamma}_1$ and \hat{k}_1 appear only as the combination $\hat{\Gamma}_1/\hat{k}_1$, whereas in the model of Chapter 2, the equivalent parameters appear independently.

In the extensional regime, we found that ECM deformations can be neglected (providing a considerable simplification of the model), and significant cell-ECM adhesion inhibits cell movement. This is in qualitative agreement with the results of the previous chapter, and with experimental evidence. When cell-ECM adhesion is weaker ($\hat{k}_2 \sim O(\eta^2)$) cell movement is possible, and at leading order the cell velocity is given by equation (3.5.34). However, we note from equation (3.5.33) that even if we ignore cell migration (u_{n0}), the local volume fraction of cells, n_0 , can change due to movement of the culture medium. This is discussed further in Chapter 4.

In the lubrication regime, coupling between cell movement and ECM defor-

mation is non-trivial. Further surface tension at $y = h_0$ plays a more important role than in the extensional regime, since it determines u_{n0} and thus also drives the ECM deformations. Comparing the two regimes we noted a close correspondence between equations (3.5.33) and (3.6.33), and (3.5.35) and (3.6.35) - the correspondence being exact in the limit $C \rightarrow 0$, $g_0 \rightarrow 1$. However, the velocity equations, (3.5.34) and (3.6.36), obviously differ significantly as a result of the differing balances between surface tension, chemotactic and viscous effects. Both regimes are investigated using a combination of linear stability analysis and numerical simulations in the following chapter.

The reduced thin-film models we have developed in this chapter represent significant simplifications of the original system of two-dimensional equations. An improvement would be to extend our model to three spatial dimensions and once again use the thin-film approximation to reduce the governing equations to two-dimensional form, as in [53, 84]. We suspect that the latter refinement would be necessary before any detailed comparison between the model predictions and experimental results could be made. Furthermore, we would need to use the fully two-dimensional version of our model (or a three-dimensional extension of it) if we wished to consider the later stages of spheroid formation in which the cells begin to detach from the surface of the ECM, as in that case our assumption that n is independent of y is clearly violated. Our investigations of the simpler, one-dimensional thin-film models in the following chapter can thus be seen as providing a starting point for future work.

Chapter 4

Modelling of chemotactic cell aggregation *in vitro*. Part II: Analysis and numerical simulations

4.1 Introduction

In the previous chapter, we presented a new model for the chemotactic aggregation of cells seeded onto a viscoelastic substrate. We considered two scaling regimes (which we termed extensional and lubrication), and exploited the thin geometry of the problem to reduce our original two-dimensional system of governing equations to one-dimensional systems at leading order. Two-phase, thin-film models similar to ours have previously been derived by King and Oliver [53] (see also [84]), who used them to study the motility of individual cells on a rigid substrate. They investigated their models using a combination of linear stability analysis and asymptotic methods, revealing a number

of possible behaviours of the model (see §3.2 for details). However, due to a number of differences in the details of the modelling (*e.g.* King and Oliver include mass exchange between the two phases at the contact line) their results are not relevant to our models. To the best of our knowledge, numerical simulations of such two-phase thin film models have not yet been presented in the literature, most existing work on models similar to ours having focused on the case of a one-dimensional geometry (*e.g.* [16]).

In this chapter, we aim to investigate the behaviour of the two thin-film models in greater detail. We begin in §4.2 by performing a linear stability analysis of each model, in order to determine the parameter regimes in which we might expect to observe aggregation. We then present numerical simulations in §4.3 – 4.4. The chapter concludes with a discussion of our main findings, and suggestions for further future work.

4.2 Linear stability analysis

In this section, we perform a linear stability analysis of the two thin-film models derived in Chapter 3, in order to determine the regimes in which we may expect to observe aggregation. As, in this chapter, we are concerned only with the reduced models, whose governing equations are given in §3.5.1 and §3.6.3 we shall henceforth, for the sake of clarity, drop the zero-subscript when referring to the dependent variables n_0 , h_0 *etc.*.

4.2.1 Extensional regime

In this regime, the governing equations are

$$\frac{\partial n}{\partial t} + u_n \frac{\partial n}{\partial x} - \frac{\hat{\Gamma}_1 n}{\hat{k}_1 (h-1)} \frac{\partial}{\partial x} \left[\frac{(h-1)(1-n)}{n} \frac{\partial}{\partial x} (n \Sigma_n) \right] = 0, \quad (4.2.1)$$

$$2\frac{\partial}{\partial x} \left[(h-1) \left(2n\frac{\partial u_n}{\partial x} + \frac{\hat{\Gamma}_1 n}{\hat{k}_1(h-1)} \frac{\partial}{\partial x} \left[\frac{(h-1)(1-n)}{n} \frac{\partial}{\partial x} (n\Sigma_n) \right] \right) \right] = \hat{k}_2 n u_n - (h-1) \frac{\partial}{\partial x} \left(C\Upsilon(n) \frac{\partial^2 h}{\partial x^2} \right), \quad (4.2.2)$$

$$\frac{\partial}{\partial t} (h-1) + \frac{\partial}{\partial x} \left[(h-1) \left(u_n + \frac{\hat{\Gamma}_1(1-n)}{\hat{k}_1 n} \frac{\partial}{\partial x} (n\Sigma_n) \right) \right] = 0, \quad (4.2.3)$$

$$\frac{1}{h-1} \frac{\partial}{\partial x} \left((h-1)(1-n) \frac{\partial c}{\partial x} \right) + n(1-n) - \alpha(1-n)c = 0. \quad (4.2.4)$$

These are solved subject to the following boundary and initial conditions

$$n(x, 0) = n_i(x), \quad (4.2.5)$$

$$\frac{\partial n}{\partial x} = 0 \quad \text{at } x = 0, 1/\epsilon, \quad (4.2.6)$$

$$u_n = 0 \quad \text{at } x = 0, 1/\epsilon, \quad (4.2.7)$$

$$h(x, 0) = 1 + h_i, \quad (4.2.8)$$

$$\frac{\partial c}{\partial x} = 0 \quad \text{at } x = 0, 1/\epsilon. \quad (4.2.9)$$

We consider the spatially homogeneous steady state of equations (4.2.1)-(4.2.4), given by $h = 1 + h_s$, $n = n_s$, $u_n = 0$ and $c = c_s = n_s/\alpha$ (where the final constraint applies because c_s must satisfy equation (4.2.4)). We then introduce small amplitude perturbations of the following form

$$n \sim n_s + \hat{n}e^{iqx+\omega t}, \quad u_n \sim \hat{u}_n e^{iqx+\omega t}, \quad (4.2.10a)$$

$$h \sim 1 + h_s + \hat{h}e^{iqx+\omega t}, \quad c \sim c_s + \hat{c}e^{iqx+\omega t}. \quad (4.2.10b)$$

where q is the wavenumber, ω is the growth rate of the perturbation and $|\hat{h}|$, $|\hat{n}|$, $|\hat{u}_n|$, $|\hat{c}| \ll 1$.

Substituting (4.2.10) into equations (4.2.1)-(4.2.4) and linearising, we obtain the following

$$\omega \hat{n} + \frac{q^2 \hat{\Gamma}_1 (1-n_s)}{\hat{k}_1} (\beta_1 \hat{n} + \beta_2 \hat{c}) = 0, \quad (4.2.11)$$

$$-4q^2 h_s n_s \hat{u}_n - 2iq^3 \frac{\hat{\Gamma}_1 h_s}{\hat{k}_1} (1 - n_s) (\beta_1 \hat{n} + \beta_2 \hat{c}) = \hat{k}_2 n_s \hat{u}_n + iq^3 h_s C \Upsilon(n_s) \hat{h}, \quad (4.2.12)$$

$$\omega \hat{h} + iq h_s \hat{u}_n - \frac{q^2 h_s \hat{\Gamma}_1 (1 - n_s)}{\hat{k}_1 n_s} (\beta_1 \hat{n} + \beta_2 \hat{c}) = 0, \quad (4.2.13)$$

$$\hat{n} - (\alpha + q^2) \hat{c} = 0, \quad (4.2.14)$$

where $\beta_1 = \frac{\partial}{\partial n}(n\Sigma_n)|_{n=n_s, c=c_s}$ and $\beta_2 = \frac{\partial}{\partial c}(n\Sigma_n)|_{n=n_s, c=c_s}$. Note that we assumed only that the combination $n\Sigma_n$ depends upon n and c - we have not yet made any assumption about the functional form of Σ_n .

We then observe that a dispersion relation for $\omega = \omega(q^2)$ may be obtained from equations (4.2.11) and (4.2.14), since they contain only \hat{n} and \hat{c} . (Equations (4.2.12) and (4.2.13) can then be used to determine \hat{u}_n and \hat{h} in terms of \hat{n} .) This gives

$$\omega + \frac{q^2 \hat{\Gamma}_1 (1 - n_s)}{\hat{k}_1} \left(\beta_1 + \frac{\beta_2}{(\alpha + q^2)} \right) = 0. \quad (4.2.15)$$

A necessary condition for instability to occur is thus

$$\beta_1 + \beta_2/\alpha < 0. \quad (4.2.16)$$

For the simple linear choice of Σ_n proposed in equation (3.3.27), this reduces to the constraint

$$\frac{\alpha}{\hat{\tau}} > n_s > \frac{\alpha}{2\hat{\tau}}. \quad (4.2.17)$$

(Note that the upper bound comes from the constraint that $c_s = n_s/\alpha < \hat{c}_{max} < 1/\hat{\tau}$.) We also require $\beta_1 > 0$, to avoid ill-posedness. In contrast with the 1D model of Chapter 2, n_s must now exceed a lower bound for instability to occur. We interpret the instability condition (4.2.17) as follows. For aggregation to occur, the cell density must be sufficient to produce a concentration of chemoattractant high enough that chemotaxis dominates random cell movement. However, if the cell density is too high, the chemoattractant level will be too high ($c > \hat{c}_{max}$), the cells receptors will be swamped and aggregation

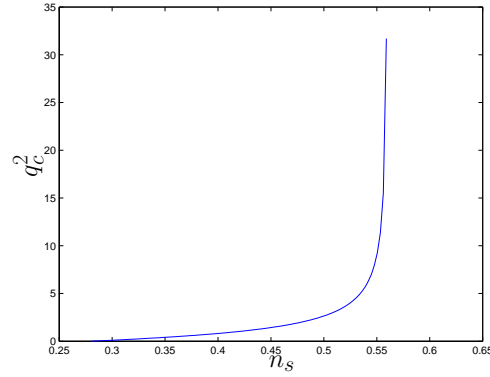


FIGURE 4.1: Plot of the square of the most unstable wavenumber, q_c^2 for given seeding density n_s ($\alpha = 1.4$, $\hat{\tau} = 2.5$, $\hat{c}_{max} = 1/\hat{\tau}$)

will not occur.

From equation (4.2.15) it is clear that if (4.2.16) is satisfied, the range of unstable wavenumbers must be finite (since the β_2 term vanishes as $q \rightarrow \infty$). Hence, we can determine the wavenumbers q_c with the highest growth rates as being the roots of $\partial\omega/\partial q = 0$, which gives

$$q_c^2 = -\alpha \pm \sqrt{\frac{-\alpha\beta_2}{\beta_1}}. \quad (4.2.18)$$

Note that $q_c^2 > 0$ provided the instability criterion (4.2.16) is fulfilled. A graph of q_c^2 is plotted in Fig. 4.1. The domain size constrains the wavenumbers which can be selected: they must be multiples of $\pi\epsilon$ in order to obey the boundary conditions. In practice we would expect to observe the mode q for which $|q - q_c|$ is smallest.

4.2.2 Lubrication regime

In this regime, the governing equations are

$$\frac{\partial\phi}{\partial t} + \hat{E}\phi = \hat{\mu}_n Ch \frac{\partial}{\partial x} \left(\Upsilon(n) \frac{\partial^2 h}{\partial x^2} \right), \quad (4.2.19)$$

$$\frac{\partial \psi}{\partial t} + \hat{E}\psi = -\frac{1}{2}\hat{\mu}_n C \frac{\partial}{\partial x} \left(\Upsilon(n) \frac{\partial^2 h}{\partial x^2} \right), \quad (4.2.20)$$

$$\begin{aligned} & \frac{\partial n}{\partial t} + \bar{u}_n \frac{\partial n}{\partial x} \\ & - \frac{n}{\hat{k}_1(h-g)} \frac{\partial}{\partial x} \left[\frac{(1-n)(h-g)}{n} \frac{\partial}{\partial x} \left(\hat{\Gamma}_1 n \Sigma_n + C \Upsilon(n) \frac{\partial^2 h}{\partial x^2} \right) \right] = 0, \end{aligned} \quad (4.2.21)$$

$$\frac{\partial g}{\partial t} + \frac{\partial}{\partial x} \left(\frac{g^2}{2} \frac{\partial \phi}{\partial t} + \frac{g^3}{3} \frac{\partial \psi}{\partial t} \right) = 0, \quad (4.2.22)$$

$$\frac{\partial(h-g)}{\partial t} + \frac{\partial}{\partial x} \left((h-g)(\bar{u}_n + \frac{(1-n)}{\hat{k}_1 n} \frac{\partial}{\partial x} \left[\hat{\Gamma}_1 n \Sigma_n + C \Upsilon(n) \frac{\partial^2 h}{\partial x^2} \right]) \right) = 0, \quad (4.2.23)$$

$$\bar{u}_n = g \frac{\partial \phi}{\partial t} + g^2 \frac{\partial \psi}{\partial t} + \frac{C(h-g)}{n} \left(\frac{1}{\hat{k}_2} + \frac{(h-g)}{3} \right) \frac{\partial}{\partial x} \left(\Upsilon(n) \frac{\partial^2 h}{\partial x^2} \right), \quad (4.2.24)$$

$$\frac{1}{(h-g)} \frac{\partial}{\partial x} \left((1-n)(h-g) \frac{\partial c}{\partial x} \right) + n(1-n) - \alpha(1-n)c = 0, \quad (4.2.25)$$

which are solved subject to the following boundary and initial conditions

$$n(x, 0) = n_i(x), \quad (4.2.26)$$

$$\frac{\partial n}{\partial x} = 0 \quad \text{at } x = 0, 1/\epsilon, \quad (4.2.27)$$

$$\frac{\partial}{\partial x} \left(\Upsilon(n) \frac{\partial^2 h}{\partial x^2} \right) = 0 \quad \text{at } x = 0, 1/\epsilon, \quad (4.2.28)$$

$$g(x, 0) = 1, \quad (4.2.29)$$

$$h(x, 0) = 1 + h_i, \quad (4.2.30)$$

$$\frac{\partial h}{\partial x} = 0 \quad \text{at } x = 0, 1/\epsilon, \quad (4.2.31)$$

$$\frac{\partial c}{\partial x} = 0 \quad \text{at } x = 0, 1/\epsilon. \quad (4.2.32)$$

Note that throughout this chapter, we have set $\kappa = 1$ (where κ is the ratio of the ECM deformation lengthscale to that of an aggregate).

We now consider the spatially homogeneous steady states of equations (4.2.19)-(4.2.25), given by $n = n_s$, $\phi = \psi = 0$, $g = g_i = 1$, $h = 1 + h_s$ and

$c = c_s = n_s/\alpha$. Small amplitude perturbations of the following form are then introduced

$$\phi \sim \hat{\phi}e^{iqx+\omega t}, \quad \psi \sim \hat{\psi}e^{iqx+\omega t}, \quad (4.2.33a)$$

$$g \sim 1 + \hat{g}e^{iqx+\omega t}, \quad h \sim 1 + h_s + \hat{h}e^{iqx+\omega t}, \quad (4.2.33b)$$

$$n \sim n_s + \hat{n}e^{iqx+\omega t}, \quad u_n \sim \hat{u}_ne^{iqx+\omega t}, \quad c \sim c_s + \hat{c}e^{iqx+\omega t}. \quad (4.2.33c)$$

where q is the wavenumber, ω is the growth rate of the perturbation and $|\hat{\phi}|, |\hat{\psi}|, |\hat{g}|, |\hat{h}|, |\hat{n}|, |\hat{u}_n|, |\hat{c}| \ll 1$.

Substituting (4.2.33) into equations (4.2.19)-(4.2.25) and linearising, we obtain the following

$$(\omega + \hat{E})\hat{\phi} = -iq^3\hat{\mu}_n C\Upsilon(n_s)(1 + h_s)\hat{h}, \quad (4.2.34)$$

$$(\omega + \hat{E})\hat{\psi} = \frac{iq^3\hat{\mu}_n\Upsilon(n)}{2}\hat{h}, \quad (4.2.35)$$

$$\omega\hat{n} + \frac{q^2(1 - n_s)}{\hat{k}_1} \left[\hat{\Gamma}_1(\beta_1\hat{n} + \beta_2\hat{c}) - q^2 C\Upsilon(n_s)\hat{h} \right] = 0, \quad (4.2.36)$$

$$\hat{g} + iq \left(\frac{\hat{\phi}}{2} + \frac{\hat{\psi}}{3} \right) = 0, \quad (4.2.37)$$

$$\omega(\hat{h} - \hat{g}) + iq^2 h_s \left[\hat{u}_n + iq \frac{(1 - n_s)}{\hat{k}_1 n_s} \left(\hat{\Gamma}_1(\beta_1\hat{n} + \beta_2\hat{c}) - q^2 C\Upsilon(n)\hat{h} \right) \right] = 0, \quad (4.2.38)$$

$$\hat{u}_n = \omega(\hat{\phi} + \hat{\psi}) - \frac{iq^3 C\Upsilon(n_s)h_s}{n_s} \left(\frac{1}{\hat{k}_2} + \frac{h_s}{3} \right) \hat{h} \quad (4.2.39)$$

$$\hat{n} - (\alpha + q^2)\hat{c} = 0, \quad (4.2.40)$$

where $\beta_1 = \frac{\partial}{\partial n}(n\Sigma_n)|_{n=n_s, c=c_s}$ and $\beta_2 = \frac{\partial}{\partial c}(n\Sigma_n)|_{n=n_s, c=c_s}$, and we have taken $n\Sigma_n$ to be a general function of n and c .

Eliminating the perturbation amplitudes between equations (4.2.34)-(4.2.40), we obtain a dispersion relation which is a cubic in ω , and takes the form

$$\omega^3 + B\omega^2 + C\omega + D = 0, \quad (4.2.41)$$

where

$$\begin{aligned}
 B = \hat{E} + \frac{q^2 \hat{\Gamma}_1 (1 - n_s)}{\hat{k}_1} \left(\beta_1 + \frac{\beta_2}{\alpha + q^2} \right) + q^4 \hat{\mu}_n C \Upsilon(n_s) \left(h_s^2 + h_s + \frac{1}{3} \right) \\
 + \frac{q^4 h_s^2 C \Upsilon(n_s)}{n_s} \left(\frac{1}{\hat{k}_2} + \frac{h_s}{3} \right) + \frac{q^4 h_s (1 - n_s) C \Upsilon(n_s)}{\hat{k}_1 n_s} \quad (4.2.42)
 \end{aligned}$$

$$\begin{aligned}
 C = \frac{q^2 \hat{\Gamma}_1 \hat{E} (1 - n_s)}{\hat{k}_1} \left(\beta_1 + \frac{\beta_2}{\alpha + q^2} \right) + \frac{q^4 \hat{E} h_s (1 - n_s) C \Upsilon(n_s)}{\hat{k}_1 n_s} \\
 + \frac{q^6 (1 - n_s) \hat{\mu}_n \hat{\Gamma}_1 C \Upsilon(n_s)}{\hat{k}_1} \left(h_s^2 + h_s + \frac{1}{3} \right) \left(\beta_1 + \frac{\beta_2}{\alpha + q^2} \right) \\
 + \frac{q^6 h_s^2 (1 - n_s) \hat{\Gamma}_1 C \Upsilon(n_s)}{\hat{k}_1 n_s} \left(\frac{1}{\hat{k}_2} + \frac{h_s}{3} \right) \left(\beta_1 + \frac{\beta_2}{\alpha + q^2} \right) \\
 + \frac{q^4 h_s^2 C \Upsilon(n_s) \hat{E}}{n_s} \left(\frac{1}{\hat{k}_2} + \frac{h_s}{3} \right) \quad (4.2.43)
 \end{aligned}$$

$$D = \frac{q^6 h_s^2 (1 - n_s) C \Upsilon(n_s) \hat{\Gamma}_1 \hat{E}}{\hat{k}_1 n_s} \left(\beta_1 + \frac{\beta_2}{\alpha + q^2} \right) \left(\frac{1}{\hat{k}_2} + \frac{h_s}{3} \right). \quad (4.2.44)$$

In order to analyse the cubic dispersion relation, we shall need to make use of the following fact: the roots, $\omega_1, \omega_2, \omega_3$ of equation (4.2.41) satisfy the following

$$\omega_1 + \omega_2 + \omega_3 = -B, \quad (4.2.45)$$

$$\omega_1 \omega_2 \omega_3 = -D, \quad (4.2.46)$$

$$\omega_1 \omega_2 + \omega_2 \omega_3 + \omega_1 \omega_3 = C. \quad (4.2.47)$$

The system can only be linearly stable if all three roots of equation (4.2.41) have negative real part. A necessary and sufficient condition for stability is thus that B, C and D are simultaneously positive. Thus instability can occur in each of the following cases: (i) $D < 0$; (ii) $B < 0 < D$; (iii) $B, C < 0 < D$. However, since all the parameters which appear in equations (4.2.42)-(4.2.44) are assumed positive, except for β_2 , we note that only (i) can arise in practice (since if $D > 0$, then $B, C > 0$).

In order to have $D < 0$, we require

$$\beta_1 + \frac{\beta_2}{\alpha + q^2} < 0, \tag{4.2.48}$$

and hence a sufficient condition for instability to occur is (4.2.16). The same comments thus apply as for the extensional regime.

4.3 Numerical simulations - Extensional regime

4.3.1 Numerical methods

The governing equations (4.2.1)-(4.2.4) were solved in MATLAB, using a semi-implicit method, details of which are given in Appendix C. Upwind differencing was used for the advection terms in equations(3.5.33) and (3.5.35), and the code verifies that the Courant-Freidrichs-Lewy (CFL) condition (a necessary condition for the convergence of the finite difference approximation [75]) is satisfied at each grid point. The scheme is thus only first-order accurate.

The initial conditions for n and h are used to determine the solutions for c and u_n at $t = 0$ using equations (3.5.34) and (3.5.36). We then update n and h using equations (3.5.33) and (3.5.35), and the values of c and u_n we have just obtained. The process is repeated until the desired end time is reached. For the sake of numerical convenience, the code incorporates an additional small diffusion term (with coefficient 10^{-4}) on the RHS of equation (3.5.35), and the additional boundary conditions $\partial h/\partial x = 0$ are imposed at $x = 0, 1/\epsilon$.

The code was validated by comparing the growth rates of small sinusoidal perturbations to the uniform steady state obtained by running the numerical simulations to short times ($t_{end} < 0.1$) with those obtained from the linear

stability analysis; good agreement was obtained for a range of parameter values (results not shown). An additional check on the solution is provided by verifying that mass is conserved at each time point. This is the case (to within a 3% tolerance) for all of the simulations presented here.

Unless stated otherwise, the simulations shown below use 1001 grid points and timestep $\Delta t = 10^{-4}$. Increasing the number of grid points N to 2001 resulted in a reduction in the mass conservation error by approximately half (as would be expected) in simulations run up to $t = 1$, but there was no change in the qualitative behaviour of the solutions (*i.e.* a similar number of aggregates with similar densities were formed). In common with the previous chapter, we have taken $\epsilon = 0.1$ here; simulations using longer domains reveal no qualitative differences in the results. Throughout, we take $c_{max} = 1/\tau$.

4.3.2 Numerical results

For the growth rate of the instability to be large, we observe from equation (4.2.15) that we require β_2 to be as large in magnitude as possible, and hence τ/α should be large. However, this would tend to give rather a low upper bound on n_s (see equation (4.2.17)), which although not a problem in itself, would mean we were less likely to observe the aggregation behaviour in which we are interested. As a compromise, we take $\alpha = 1.4$ and $\tau = 2.5$ in the following simulations (unless otherwise stated), which gives a growth rate $\omega \approx 1/5$ for $n_s = 0.5$, $\hat{\Gamma}_1/\hat{k}_1 = 1$ and $q = 1$ (note from equation (4.2.17) that we require $0.28 < n_s < 0.56$ for instability to occur). For these values of α , τ we have $q_c^2 \approx 1.6$, and so we would expect to observe three aggregates in our domain length of 10 units (corresponding to the permissible wavenumber of 0.5π).

We begin by setting $\hat{\Gamma}_1/\hat{k}_1 = \hat{k}_2 = 1$ and neglect the effects of surface tension by setting $C = 0$. We take the value of $n(x, 0)$ at each grid point

to be normally distributed with mean 0.5 and standard deviation 0.01. The derivative of n is thus not properly defined. However, diffusive effects will tend to give a smooth n after the code has run for a few timesteps. We set $n(0, t) = n(\Delta x, t)$ and $n(1/\epsilon - \Delta x, t) = n(1/\epsilon, t)$ so the boundary condition (4.2.6) is satisfied at first order, and the condition $\partial h/\partial x = 0$ is imposed in the same way. Initially, we take $h(x, 0) = 2$.

Figure 4.2 shows the development over time of three aggregates, in line with the prediction of the linear stability analysis. The simulation is run until $t = 26$, when we see that in the centre of the aggregate on the extreme right, the cell volume fraction approaches unity - *i.e.* the cells reach their maximum possible packing density. Since c , the concentration of chemoattractant in the culture medium, is not defined where $n = 1$, it is not possible to continue the simulation to longer times without more careful consideration of the chemical distribution in this region. (This is left for future work.) Figure 4.2 also shows the corresponding evolution of the height of the cell and culture medium layer, h . From being flat initially, it bulges to become higher between the developing clusters, as the aggregating cells force out the culture medium; correspondingly, h decreases within the developing aggregates. (We note that the derivative of h is quite large close to the boundary, which we believe to be an artifact of the numerical scheme.)

In the regions between aggregates, the chemoattractant concentration in the culture medium c , decreases throughout the period of the simulation; as the cells aggregate, there is reduced production of chemoattractant in these regions. Within the developing aggregates, c initially rises (since there are more cells in those regions to produce the chemical), but begins to fall at later times. This is because we assumed the production of chemoattractant to depend on the product $n(1 - n)$ - hence production falls in regions devoid of culture medium (see Figure 4.3). The cell velocity u_n at three time points is

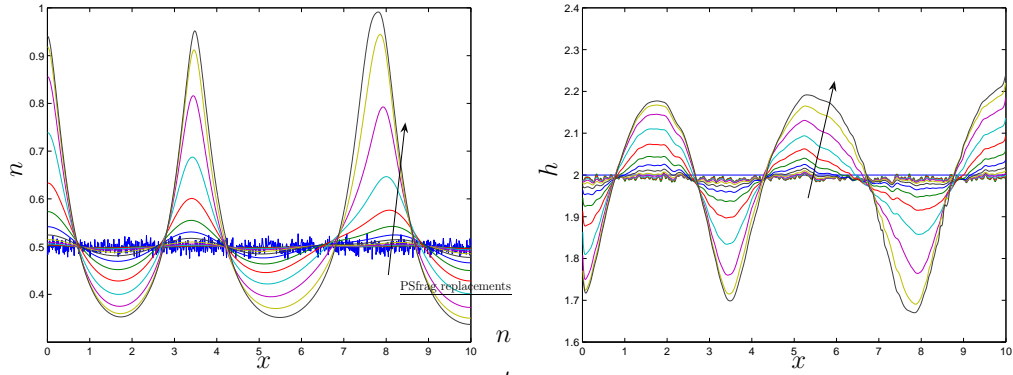


FIGURE 4.2: Numerical solution for n (left) and h (right). Results displayed at intervals of 2 time units from $t = 0$ to $t = 26$ - arrow indicates increasing time. Parameter values $\hat{\Gamma}_1/\hat{k}_1 = \hat{k}_2 = 1, C = 0$

also plotted in Figure 4.3. At early times, there is little cell movement, but u_n then increases as the cells migrate towards the developing aggregates. At later times, when the aggregates are more clearly formed, u_n again decreases.

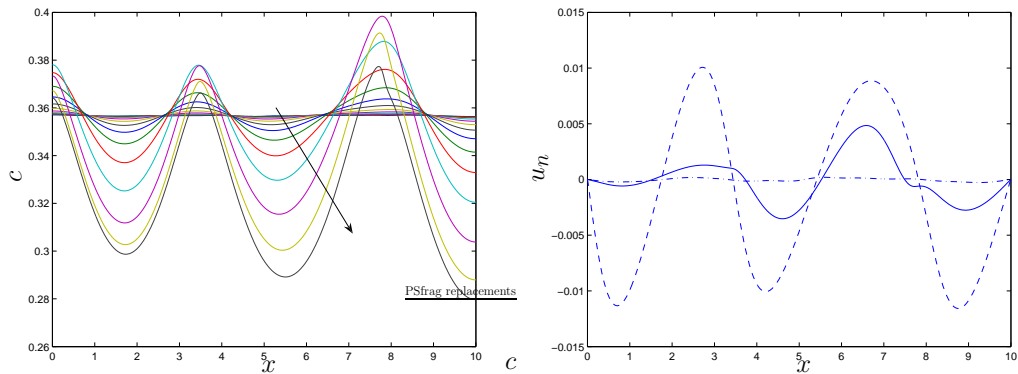


FIGURE 4.3: Left: numerical solution for c at $t = 0, 2, \dots, 26$ - arrow indicates increasing time. Right: numerical solution for u_n at $t = 2$ (dash-dot), $t = 18$ (dash) and $t = 26$ (solid). Parameter values as for Fig. 4.2

The simulation was repeated for a smooth initial condition, which con-

tained a range of modes. Specifically, we set

$$n(x, 0) = 0.5 + 0.002 [\cos(0.2\pi x) + \cos(0.3\pi x) + \cos(0.5\pi x) + \cos(0.6\pi x) + \cos(0.7\pi x) - \cos(0.8\pi x) - \cos(\pi x) + \cos(1.5\pi x) + \cos(2\pi x)]. \quad (4.3.1)$$

Comparing Figs. 4.2 and 4.4, we can see that this gave a qualitatively similar distribution of aggregates (though on this occasion n approached unity by $t = 18$, at which point the simulation was stopped). Although in this case we found four, rather than three aggregates were formed, we note that the two aggregates on the right appear to be merging, as their centres move closer together over time. Once again, this is broadly in agreement with the linear stability analysis.

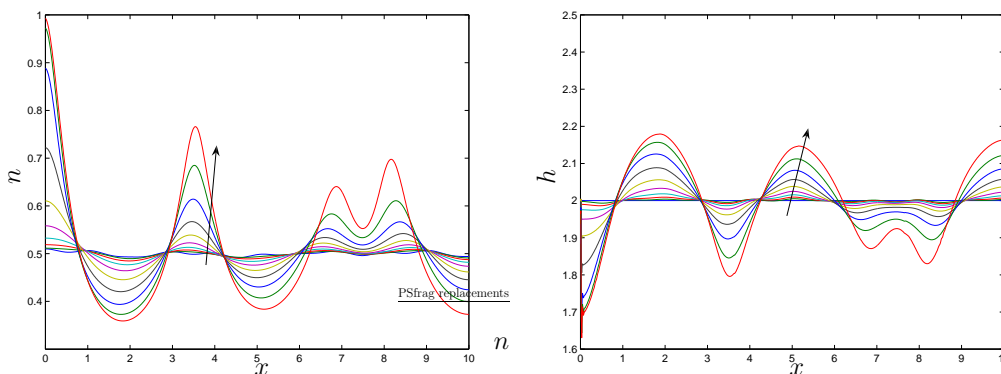


FIGURE 4.4: Numerical solution for n (left) and h (right) at $t = 0, 2 \dots 18$. Parameter values as for Fig. 4.2

We now repeat the simulation of Fig. 4.2 with $\hat{k}_2 = 50$, in order to consider the effect of increased cell-ECM adhesion on the aggregation process. In this case, we found n reached unity within one of the aggregates by $t = 28$. Comparing Figs. 4.2 and 4.5, we observe that the cell distributions are almost identical. This is in sharp contrast to the results of Chapter 2, where increased cell adhesion considerably reduced the size of the aggregates which formed. However, this result is unsurprising, as the wavenumber of the perturbation to which the system is most unstable is not influenced by \hat{k}_2 (see §4.2.1).

The cell velocity u_n is now much smaller ($O(10^{-3})$) as opposed to $O(10^{-2})$. By contrast, if the simulation is repeated with $\hat{k}_2 = 0.1$, then not only is there little effect on the formation of aggregates, but the difference in u_n from the $\hat{k}_2 = 1$ case is also small ($O(10^{-3})$ - results not shown). This suggests that in this regime cell migration is of less importance, and redistribution of cells is occurring mainly due to movement of the culture medium. Supporting this hypothesis, the variation in the layer height h is greater when $\hat{k}_2 = 50$ (see Fig. 4.5), consistent with culture medium being forced out of the developing aggregates, leading to an overall loss of volume in those regions (hence reduced layer height, and increased cell volume fraction n).

It is obvious from equation (3.5.32) that the cell-generated pressures represented by the Σ_n term can cause movement of the culture medium, even if there is no cell movement ($u_n = 0$). This is a result of our choice of scalings in §3.5: to maintain an overall pressure $p_T \sim O(1)$, there must be a large pressure in the culture medium to balance that generated by the cells. The challenge is to provide a physical interpretation of how the cells can (in response to the chemoattractant) generate an effective pressure in the culture medium which causes it to flow, whilst not moving a great deal themselves. We offer the following scenario as one possible explanation. Suppose we consider two nearby, initially spherical cells. Under the influence of the chemoattractant, they may change shape, deforming so that their cell membranes come into contact, and thus forcing out the culture medium originally in the region between them. The degree of movement of the cells' centre of mass may be relatively small; the essential feature is the change of shape. Such a scenario has obvious limitations. Firstly, the cells must be quite close together for this to occur. Secondly, the volume of water displaced in each interaction must be relatively small. This would suggest it is only really plausible as a mechanism for aggregation (if at all) at high cell seeding densities, where there are large numbers of cells in sufficient proximity. However, our supposition is at least

partly supported by the observations described in [96] (discussed in detail in Chapter 1), in which it was observed that hepatocytes frequently exhibited membrane extension, leading to cell-cell coupling.

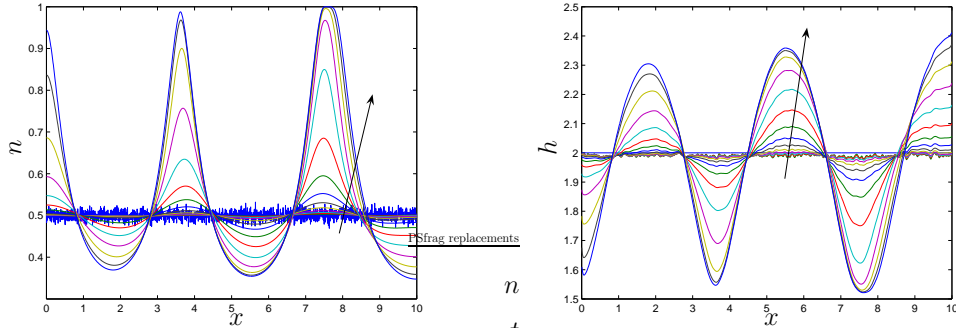


FIGURE 4.5: Numerical solution for n (left) and h (right) at $t = 0, 2 \dots 28$. Parameter values: $\hat{k}_2 = 50$, otherwise as for Fig. 4.2

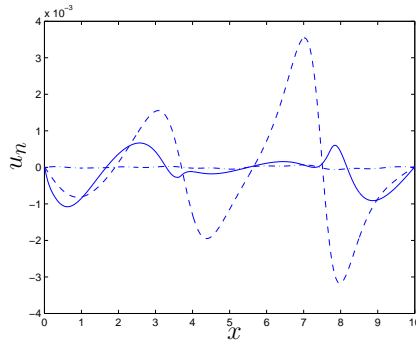


FIGURE 4.6: Numerical solution for u_n at $t = 2$ (dash-dot), $t = 18$ (dash) and $t = 28$ (solid). Parameter values as for Fig. 4.5

We now consider the effect of changing the cell seeding density. We repeat the simulation shown in Fig. 4.2, changing the mean of the distribution for $n(x, 0)$ from 0.5 to 0.4. Equation (4.2.18) then gives the most unstable wavenumber as $q_c \approx 0.9$, so we expect to see two aggregates (corresponding to the permissible wavenumber 0.3π); this prediction is confirmed by the results shown in Fig. 4.7. This contrasts with the results of Chapter 2, where

reduced cell seeding density did not significantly affect the number of aggregates formed (although the aggregates were smaller). Note that aggregate growth is much slower than in Fig. 4.2 (the amplitude of the variation in n is only $O(10^{-3})$ by $t = 40$) and the velocity of the cells is also reduced to $O(10^{-4})$.

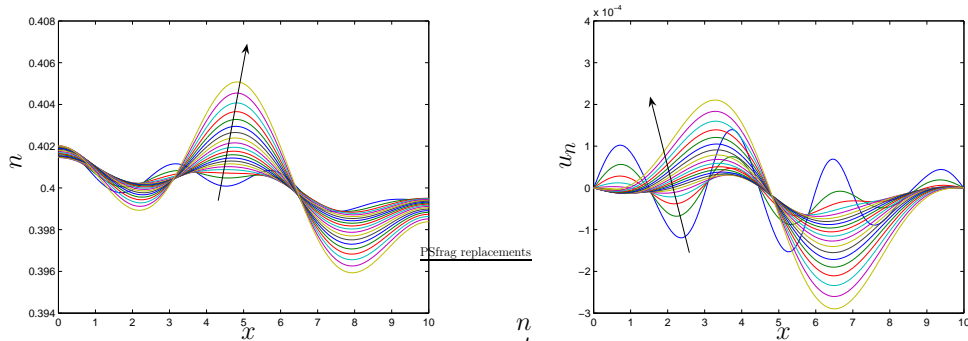


FIGURE 4.7: Numerical solution for n (left) and u_n (right). Results displayed at intervals of 2 time units from $t = 2$ to $t = 40$ (results at $t = 0$ omitted for clarity) - arrow indicates increasing time. Parameter values as for Fig. 4.2

We now investigate the effect of surface tension on the aggregation process. In the following simulations, we set $\Upsilon(n) = n$, so surface tension increases with the cell volume fraction. This is also the simplest form for Υ consistent with our comments in §3.3.3. To give a comparison of the rates of aggregation in each case, we set $n(x, 0) = 0.5 + 0.05 \cos(0.6\pi x)$ (so as to eliminate the possible effect of random variations in the normally-distributed initial condition on aggregation rates). When we compare simulations with $C = 0$ and $C = 0.5$ (other parameters as for Fig. 4.2), we observe that the effect of surface tension is to retard slightly the aggregation process (at $t = 20$, the maximum values of n are 0.93 and 0.90 respectively) - see Fig. 4.8.

A similar comparison for the layer height h is shown in Fig. 4.9 - although we have shown the output only at $t = 0$, $t = 10$ and $t = 20$ for the sake of clarity. In the absence of surface tension, movement of the culture medium out of the developing aggregates causes the interface to deform from its initially

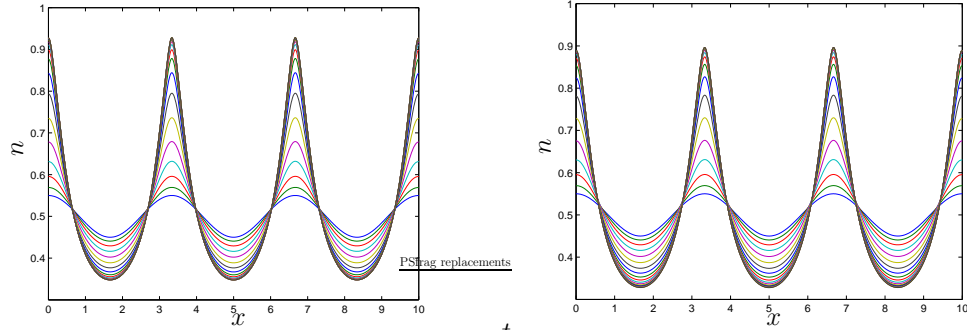


FIGURE 4.8: Numerical solution for n with $C = 0$ (left) and $C = 0.5$ (right) up to $t = 20$. Other parameter values as for Fig. 4.2

flat profile, as described above. The deformation increases as aggregation progresses (though, in fact the increase between $t = 10$ and $t = 20$ is quite small). When $C = 0.5$, we see that although there is an initial deformation of the interface as before, at later times surface tension acts to flatten the interface. This restricts movement of the culture medium out of the aggregates, which explains the retarding effect on aggregation.

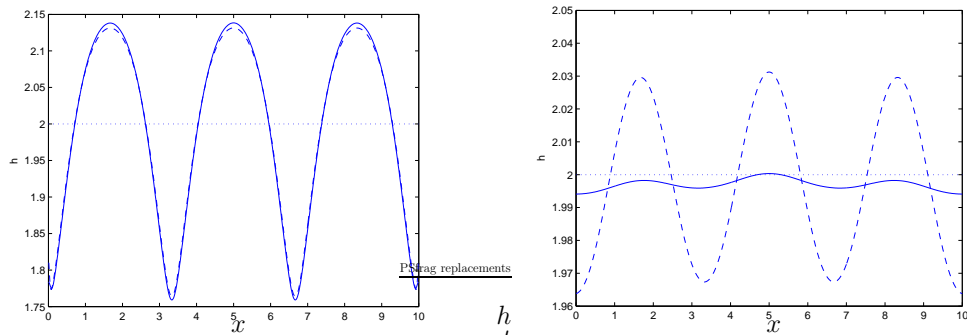


FIGURE 4.9: Numerical solution for h with $C = 0$ (left) and $C = 0.5$ (right) at $t = 0$ (dotted), $t = 10$ (dashed) and $t = 20$ (solid). Other parameter values as for Fig. 4.2

4.4 Numerical simulations - Lubrication regime

4.4.1 Numerical methods

The numerical simulations in this section were performed using a modified version of the code described in §4.3 (full details are given in Appendix C). The initial conditions for n , g , ϕ , ψ and h are used to determine the solutions at $t = 0$ for c and u_n . These are then used to update n , g , ϕ , ψ and h . Since equation (3.6.35) is now fourth-order in h , there is no longer any need to include a small diffusion term on the RHS, as in the previous regime. However, a small diffusion term is added to the RHS of (3.6.34) for the reasons discussed in §4.3. The code was validated in the manner previously described.

4.4.2 Numerical results

We begin by taking $\alpha = 1.4$, $\tau = 2.5$ and $\Upsilon(n) = n$, as in §4.3. Initial conditions are $\phi(x, 0) = \psi(x, 0) = 0$, $g(x, 0) = 1$, $h(x, 0) = 2$, and the value of $n(x, 0)$ at each grid point is normally distributed with mean 0.5 and standard deviation 0.01. We then set $\hat{\Gamma}_1 = \hat{k}_1 = \hat{k}_2 = C = \hat{\mu}_n = \hat{E} = 1$. In the resulting simulation, we observe the formation of three aggregates, as for the first simulation in §4.3.2. Throughout the domain $n < 1$ up to $t = 40$. The interface at $y = h$ is higher in the regions between aggregates, and lower in the aggregate regions. As discussed in §4.3.2, we believe this is due to culture medium being pushed out from between the cells as the aggregates form. The amplitude of the disturbances to the interface grow until about $t = 34$, and then begin to diminish due to surface tension forces, as cell movement decreases. Note that the simulations show that, overall, h moves downwards over time. This is an artefact of the numerical scheme, resulting in a small percentage mass loss over the period for which the simulation is run. Whilst we believe that this is

acceptable in the present context (in which we are mainly concerned with the qualitative behaviour of solutions), it would obviously be desirable to develop a more sophisticated code to eliminate this problem before undertaking a more in-depth investigation.

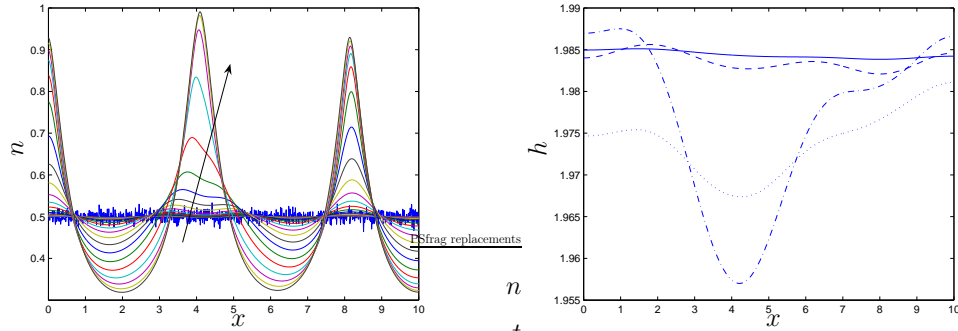


FIGURE 4.10: Left: numerical solution for n . Results displayed at intervals of 2 time units from $t = 0$ to $t = 40$ - arrow indicates increasing time. Right: numerical solution for h at $t = 10$ (solid), $t = 20$ (dashed), $t = 34$ (dash-dot) and $t = 40$ (dotted). Parameter values $\hat{\Gamma}_1 = \hat{k}_1 = \hat{k}_2 = C = \hat{\mu}_n = \hat{E} = 1$.

We can interpret ϕ as the component of ECM displacement arising from cell-ECM drag (see equation (3.6.7)) (whilst ψ is the displacement due to pressure gradients in the ECM - see equation (3.6.6)). We see that ϕ initially increases in the direction representing movement towards each aggregate, as the ECM is pulled along with the migrating cells. However, at later times, ϕ decreases, as cell speed u_n is reduced, and elastic forces act within the ECM to restore the undeformed configuration (Fig. 4.11).

By contrast, ψ represents displacements in the opposite direction to ϕ , though their amplitude is much smaller ($O(10^{-3})$). As a result, movements of the initially flat cell-ECM interface g are dominated by ϕ . As a result, g begins to increase within the forming aggregates, but at later times flattens as deformation decreases (see Fig. 4.12).

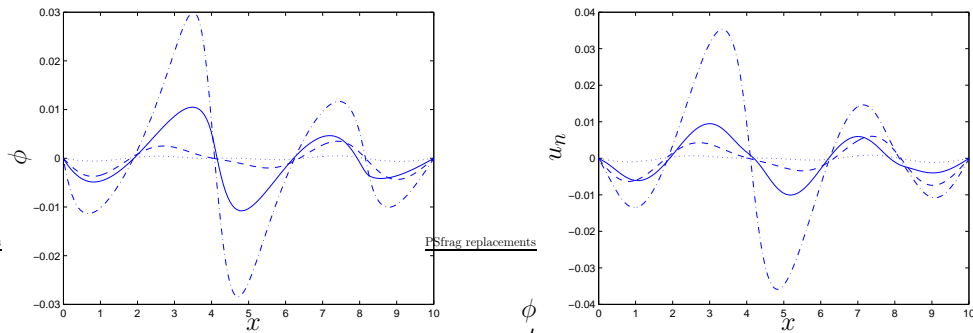


FIGURE 4.11: Numerical solution for ϕ (left) and u_n (right) at $t = 10$ (dotted), $t = 20$ (dashed), $t = 34$ (dash-dot) and $t = 40$ (solid). Parameter values as for Fig. 4.10 .

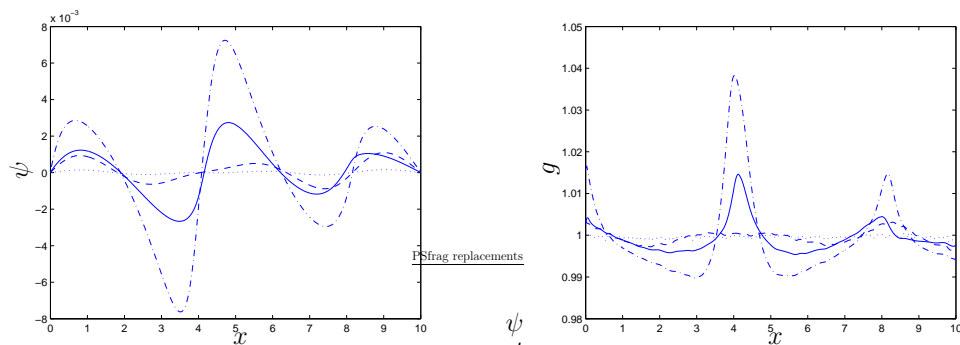


FIGURE 4.12: Numerical solution for ψ (left) and g (right) at $t = 10$ (dotted), $t = 20$ (dashed), $t = 34$ (dash-dot) and $t = 40$ (solid). Parameter values as for Fig. 4.10 .

We now investigate the effect of increasing cell-ECM adhesion, by increasing \hat{k}_2 from $\hat{k}_2 = 1$ to $\hat{k}_2 = 10$. We see that this results in a reduction in the rate of aggregation (compare the cell densities in Figs. 4.13 and 4.10). The solution for h is qualitatively similar to the previous case, with its height increasing in the regions between aggregates (results not shown). The expected reduction in cell velocity is apparent from contrasting Figs. 4.11 and 4.14, but there is no corresponding reduction in ϕ (ECM deformation due to cell-ECM drag), probably due to the compensating effect of stronger adhesion. (Note that the maximum values of u_n and ϕ are attained at $t = 36$ and $t = 38$ in

this case, with a decrease in amplitudes thereafter. The solutions at these times are not shown in Fig. 4.14 to facilitate comparison with Fig. 4.11.) As previously, the maximum amplitude of ψ is approximately 8×10^{-3} . Thus the position of the cell-ECM interface g depends mainly on ϕ , and is qualitatively similar to the previous simulation (results not shown).

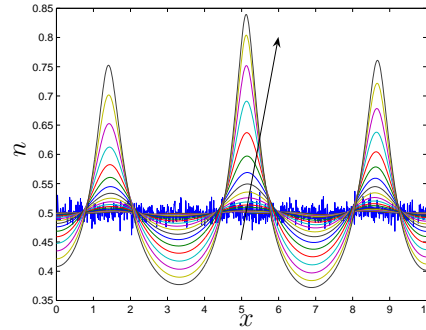


FIGURE 4.13: Numerical solution for n . Results displayed at intervals of 2 time units from $t = 0$ to $t = 40$ - arrow indicates increasing time. Parameter values: $\hat{k}_2 = 10$, other parameters as for Fig. 4.10.

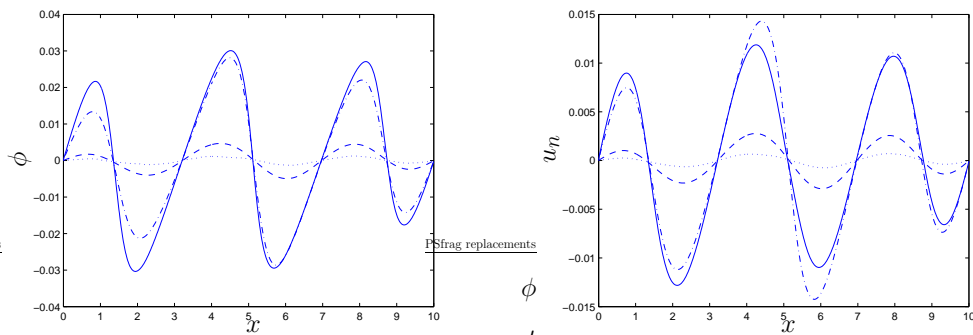


FIGURE 4.14: Numerical solution for ϕ (left) and u_n (right) at $t = 10$ (dotted), $t = 20$ (dashed), $t = 34$ (dash-dot) and $t = 40$ (solid). Parameter values: $\hat{k}_2 = 10$, other parameters as for Fig. 4.11.

We now consider the effect of reducing the cell seeding density, so the mean of the normal distribution for $n(x, 0)$ is set at 0.4 rather than 0.5, with other

parameters as for Fig. 4.10. This has a very noticeable effect, as only one aggregate is now formed (see Fig. 4.15). This fact, together with the much slower rate of aggregation is very similar to the equivalent case described in §4.3.2 (see Fig. 4.7).

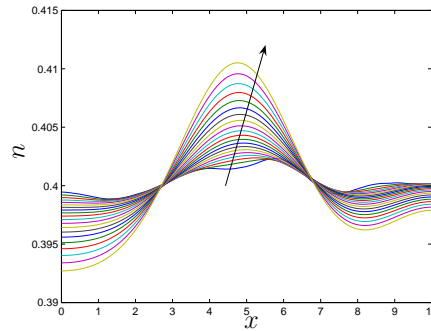


FIGURE 4.15: Numerical solution for n - effect of lower cell seeding density. Results displayed at intervals of 2 time units from $t = 2$ to $t = 40$ - arrow indicates increasing time (plot at $t = 0$ omitted for clarity). Parameter values as for Fig. 4.10.

In contrast to the extensional regime, surface tension does not appear to affect the rate of aggregation in this regime. We once again set $n(x, 0) = 0.5 + 0.05 \cos(0.6\pi x)$ (so as to eliminate the possible effect of random variations in the normally-distributed initial condition on aggregation rates), and compare simulations with $C = 0.1$, $C = 1$ and $C = 5$ (other parameter values being as for Fig. 4.10). The magnitude of the perturbation to h becomes smaller as the value of C is increased; when $C = 0.1$ the maximum amplitude of the perturbation is 0.02, whilst for $C = 5$ it is 4×10^{-4} . However, this variation is apparently too small to have any noticeable effect on the the results for n , u_n , g , ϕ and ψ (results not shown). Repeating the simulations with the normally-distributed initial conditions, we find that three aggregates are formed in each case, suggesting that surface tension also does not affect the most unstable wavenumber, at least over this range of values of C (results not

shown).

We now examine the effects of changing the ECM properties on the formation of aggregates. We first increased the viscosity of the ECM relative to that of the cells (*i.e.* by decreasing $\hat{\mu}_n$ from 1 to 0.1), leaving all other parameters as in Fig. 4.10. For some simulation runs this resulted in the formation of four aggregates rather than three, but in others only three aggregates were formed (as in Fig. 4.16), and we hence concluded that this was due to random variations in the initial conditions, rather than as a result of changing the ECM viscosity. (Supporting this, further simulations with $\hat{\mu}_n = 5$ and $\hat{\mu}_n = 0.01$ also resulted in the formation of three aggregates - results not shown.) The increased stiffness of the ECM results, as would be expected, in a significant reduction in ECM deformation; ϕ is now $O(10^{-3})$ at most and $\psi \sim O(10^{-4})$ (see Fig. 4.17). Hence the amplitude of the disturbance to g is $O(10^{-3})$ (results not shown). Similar results are obtained if we set $\hat{m}u_n = 1$, and decrease the ECM relaxation time, by increasing \hat{E} from 1 to 10 (results not shown). Changing the relaxation time of the ECM also did not appear to affect the number of aggregates formed.

Although the maximum values of n reached in Fig. 4.16 appear slightly less than those in Fig. 4.10, repeating the simulations with the sinusoidal initial conditions used above did not show any noticeable difference in the rate of aggregation between the cases $\hat{\mu}_n = 0.1$, $\hat{\mu}_n = 1$ and $\hat{\mu}_n = 5$ (results not shown).

4.5 Discussion

In this chapter, we have explored the behaviour of the two thin-film models of cell aggregation developed in Chapter 3. Our investigations suggest that

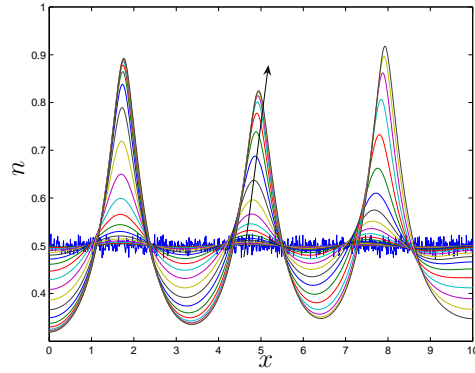


FIGURE 4.16: Numerical solution for n . Results displayed at intervals of 2 time units from $t = 0$ to $t = 40$ - arrow indicates increasing time. Parameter values: $\hat{\mu}_n = 0.1$, other parameters as for Fig. 4.10.

in both the extensional and lubrication regimes, the cell seeding density is an important factor influencing aggregate formation. Using linear stability analysis, we showed that in both regimes, the cell seeding density n_s must lie within certain limits for instability (aggregation) to occur. The precise values of these limits depend upon the decay rate of the chemoattractant α and the cells' sensitivity to it, τ , for our particular choice of additional pressure term Σ_n . This behaviour is in qualitative agreement with some of the experimental results reported by Peshwa *et al.* [93]. They found that when hepatocytes are seeded at densities lower than 3.1×10^4 cells cm^{-2} , no spheroids are formed. However, cells formed clumps for all seeding densities above this, although for densities above 8.4×10^4 cells cm^{-2} , the cells form multilayers, rather than spheroids. For the model developed in Chapter 2, aggregation was predicted for $n < n_c$ (*i.e.* there was no lower bound on the range of seeding densities for which instability could occur); however, if we had chosen a non-zero value for n_{min} , a lower bound would have been introduced.

Within the range of values for which instability occurs, cell seeding density influences the number of aggregates eventually formed. For the extensional

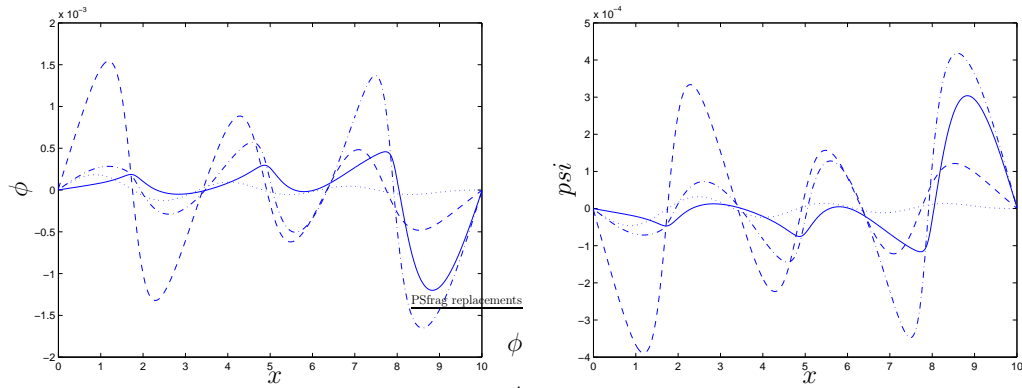


FIGURE 4.17: Numerical solution for ϕ (left) and ψ (right) at $t = 10$ (dotted), $t = 24$ (dashed), $t = 34$ (dash-dot) and $t = 40$ (solid). Parameter values as for Fig. 4.16.

regime, this value can easily be predicted from the linear stability analysis (see Fig. 4.1), and the prediction was found to agree with the results of the numerical simulations. In particular, we saw that reducing the cell seeding density from $n_0 = 0.5$ to $n_0 = 0.4$ resulted in a reduction in the number of aggregates formed (from three to two) in both regimes, and the rate of aggregation was considerably reduced. Due to conservation of mass, a reduction in the number of aggregates formed will tend to imply an increase in the size of the resulting aggregates (since the changes in total cell mass being considered here are quite small). By contrast, numerical simulations of the model in Chapter 2 suggested that reducing the cell seeding density did not affect the number of aggregates formed, or the rate of aggregation, but the size of the aggregates was reduced. Experimental results seem to suggest that decreased cell seeding density leads to the formation of smaller aggregates [122], which favours the predictions of the Chapter 2 model.

In both regimes increasing the cell-substrate adhesion coefficient \hat{k}_2 results in the expected reduction in the cells' speed. However, in contrast with the model of Chapter 2, the degree of cell-ECM adhesion has no effect on the number or size of the aggregates formed in either regime. In the extensional

regime the reduction in the cells' speed has, perhaps counter-intuitively, almost no effect on the formation of cell aggregates. This is because cell velocities are small in the extensional regime, and we believe it represents cell aggregation predominantly by the expulsion of culture medium from the aggregates, with negligible migration of the cells. The idea that the pressures generated by the cells can cause movement of the culture medium, whilst the cells themselves move very little appears paradoxical. We suggested that it may occur through cell membrane extension and cell-cell coupling. This interpretation is at least partly supported by experimental observations of hepatocytes [96], but since the same study also remarked that significant translations frequently occurred following cell-cell coupling, we consider it unlikely that this mechanism can be solely responsible for the formation of liver cell spheroids.

In the lubrication regime, increased cell-ECM adhesion does result in a decreased rate of aggregation, which is in line with experimental results showing that spheroid formation is inhibited on adhesive substrates [102]. This fact suggests the lubrication regime is the more relevant biologically. However, it may be appropriate to view the two regimes as representing two different stages in the formation of cell clusters. We might postulate that, immediately after the cells are seeded in the culture wells, there has not been sufficient time for them to develop strong cell-ECM or intercellular adhesions (hence we would expect \hat{k}_2 and C to be small, as in the extensional regime). Small clumps of cells might form as a result membrane extension by neighbouring cells. After a few hours in culture, cells have time to develop stronger adhesions to the ECM, and each other, and so the assumptions of lubrication regime (larger \hat{k}_2 and C , compared to the extensional regime) may then be more appropriate. Coupled pairs or small clumps of cells migrate, leading to the formation of larger aggregates. This scenario appears consistent with the findings of Powers *et al.* [96], who describe initial cell-cell contacts being made by membrane extension, with migration by more than one body length more common after

cell-cell contact had occurred. However, it is of course highly speculative, and lacks experimental verification.

The effect of varying the strength of surface tension appears rather limited. In both regimes, increasing surface tension reduced the amplitude of the disturbance to h , as would be expected. In the extensional regime, this appeared to slow aggregation slightly, probably due to impeding the flow of culture medium out of the aggregates. However, in the lubrication regime, there was no noticeable effect on the rate of aggregation for values of c between 0.1 and 5.

Deformations of the ECM are negligible in the extensional regime, which means that the physical properties of the ECM represented by $\hat{\mu}_n$ and \hat{E} are irrelevant. However, in the lubrication regime, coupling between the cells and the ECM is non-trivial. As the aggregates develop, the ECM is pulled into them by the migrating cells, causing the cell-ECM interface to increase in height slightly, under the aggregates. However, as we found in Chapter 2, changing the mechanical properties of the ECM has a negligible effect on the behaviour of the cells (although it does change the degree of deformation of the ECM). This is probably due to the fact that our model assumes that the forces generated by the cells (represented by Σ_n) and the degree of cell-ECM adhesion are independent of the properties and deformation of the ECM. In practice, the inter-relationship between cell-ECM adhesion, cell velocity and the mechanical properties of the ECM is likely to be very complex. Recent studies *e.g.* [23] have shown that cells can respond to the stiffness of the substrate to which they are adhered in various ways. Lo *et al* [61] reported a number of effects on the migration of 3T3 fibroblast cells. At low seeding densities, cells migrate preferentially towards stiff substrates, a behaviour they term ‘durotaxis’. Cells generate stronger traction forces on stiff, compared to soft substrates, and there are also differences in cell speed. Finally, movement of the cells can be directed by stretching the substrate; pushing the substrate

towards the leading edge of a migrating cell causes it to retract, and the cell reverses its direction of migration; when the substrate is pulled away from the trailing edge of the cell, a similar reversal occurs. The topography of the surface on which cells are seeded has also been shown to affect their migration behaviour [49], and thus changes in the ECM layer height, g , may also have an effect.

The main limitation of the modelling presented in this chapter is the lack of validation against experimental data. As a result, the model contains a number of speculative forms for the constitutive relations which describe *e.g.* the response of the cells to the chemoattractant and the interaction forces between the cells and the culture medium, and the cells and the ECM. Our aim was to try to use the model to gain some generic insights into the qualitative effects on cell aggregation of varying certain parameters. The two parameters which appear to have the greatest effect are the cell seeding density, and the cell-ECM adhesion strength, both of which can be manipulated relatively easily experimentally (the latter can be changed by surface modification of the ECM). In both regimes, cell seeding density affects whether aggregation occurs, the number of aggregates formed and their rate of formation. We would therefore suggest that quantitative experimental investigations of the effect of varying the cell seeding density and cell-ECM adhesion strength may prove to be valuable in helping to optimise the process of spheroid formation.

The thin-film limits we have considered in this chapter represent only a small region of the parameter space of the original two-dimensional model developed in Chapter 3. Simulations of the full 2D model would allow us to better understand the relevance of the regimes we have explored here (in which reductions to a one-dimensional form are possible) and the physical situations in which they may arise. Further extension of our work, to include simulations of the two-dimensional thin-film approximations of an underlying

three-dimensional model (along the lines of [53, 84]) would also be beneficial, as this represents more accurately the true geometry of the biological problem. This extension would almost certainly be required for quantitative validation of the model against experimental data. However, it would require a much more sophisticated numerical code, which is beyond the scope of this thesis.

Chapter 5

Non-local models for the interactions of hepatocytes and stellate cells

5.1 Introduction

In previous chapters, we have investigated the aggregation of a single population of hepatocytes and the influence of the extracellular matrix and culture medium on their behaviour. In this chapter, we focus on the interactions between hepatocytes and stellate cells *in vitro*. Recent experimental evidence has shown that when these two cell types are cultured together, cell aggregates form more rapidly, and remain functional for a longer period than when the hepatocytes are cultured alone [101, 102].

One explanation for the improved rate of aggregation is that it may be due to an enhanced chemotactic effect. Studies have shown that, when stimulated with hepatocyte-conditioned medium, stellate cells from rats produce hepato-

cyte growth factor (HGF) [111]. Furthermore, insulin-like growth factor-1, a component of the hepatocyte-conditioned medium, was able to produce this effect when administered in isolation. As discussed in Chapter 3, hepatocytes are known to respond chemotactically to HGF *in vitro* [113]. In a recent paper, Gentilini *et al.* reported that insulin-like growth factor-1 can produce a chemotactic response in human hepatic stellate cells placed in a modified Boyden chamber system [38]. Hence there may be a feedback loop between the two cell types: the hepatocytes produce insulin-like growth factor-1 which attracts the stellates, causing them to produce more HGF. This, in turn, acts on the hepatocytes as a chemoattractant, resulting in the formation of heterogeneous cell aggregates.

However, recent work in the Tissue Engineering Group at the University of Nottingham has suggested an alternative hypothesis [118]. Time-lapse video footage, taken during the aggregation process, shows the stellates extending long processes, which, when they contact an hepatocyte, appear to pull the cell into the nascent aggregate (Fig. 5.1). This leads to the hypothesis that it is the physical contact between the two cells types which promotes the formation of aggregates. It is possible that the retraction of these processes by the stellates is provoked by some chemical factor secreted by the hepatocytes, as mono-cultured stellates stimulated with hepatocyte-conditioned medium retracted their processes, whilst when the conditioned medium was absent, they did not. Note that stellates appear to have low motility in mono-culture, so we assume that they do not produce a chemoattractant which acts upon themselves. Furthermore, aggregates formed more slowly, and were less well defined, when the stellates were co-cultured with cells of the Hep G2 cell line (hepatocellular carcinoma cells), rather than hepatocytes, suggesting an interaction specific to these two particular cell types. However, the stellates exhibited the same contractile response to hepatocyte fragments as to whole cells, which might suggest the retraction of the processes is not wholly due to

the secretion of chemical factors by hepatocytes.

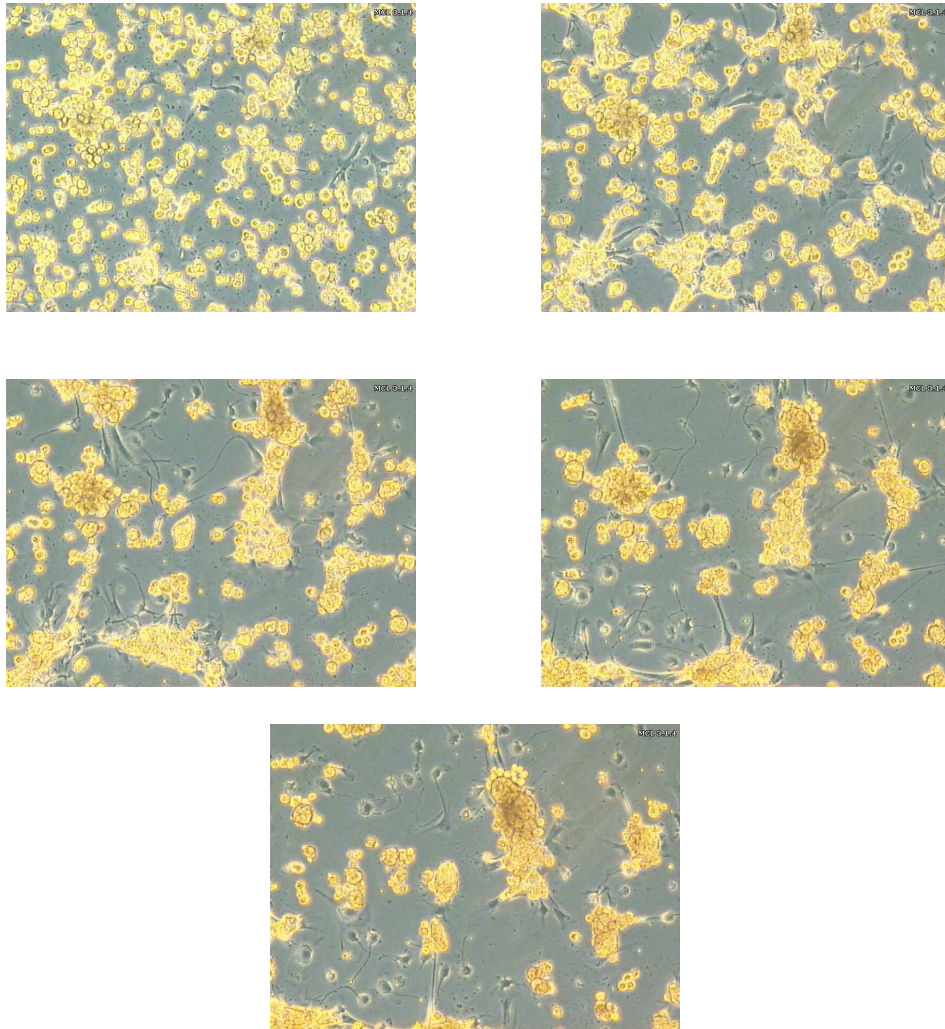


FIGURE 5.1: Snapshots from time-lapse video of an hepatocyte-stellate cell co-culture during aggregation. The hepatocytes appear yellow, and have a rounded morphology. Stellates appear grey, but their long cellular processes are clearly distinguishable. Total time elapsed: approx. 21 hours. (Images courtesy of Robert Thomas, Tissue Engineering Group. Similar images also appear in [118].)

The results of Thomas *et al.* [118] suggest that there is very little, or no attraction between stellate cells. Stellates cells in monoculture were found to have relatively low cell motility compared to those in co-culture over similar

period, and no aggregates were observed to form (see Fig. 5.2). Accordingly, we assume there is no stellate-stellate attraction throughout this chapter.

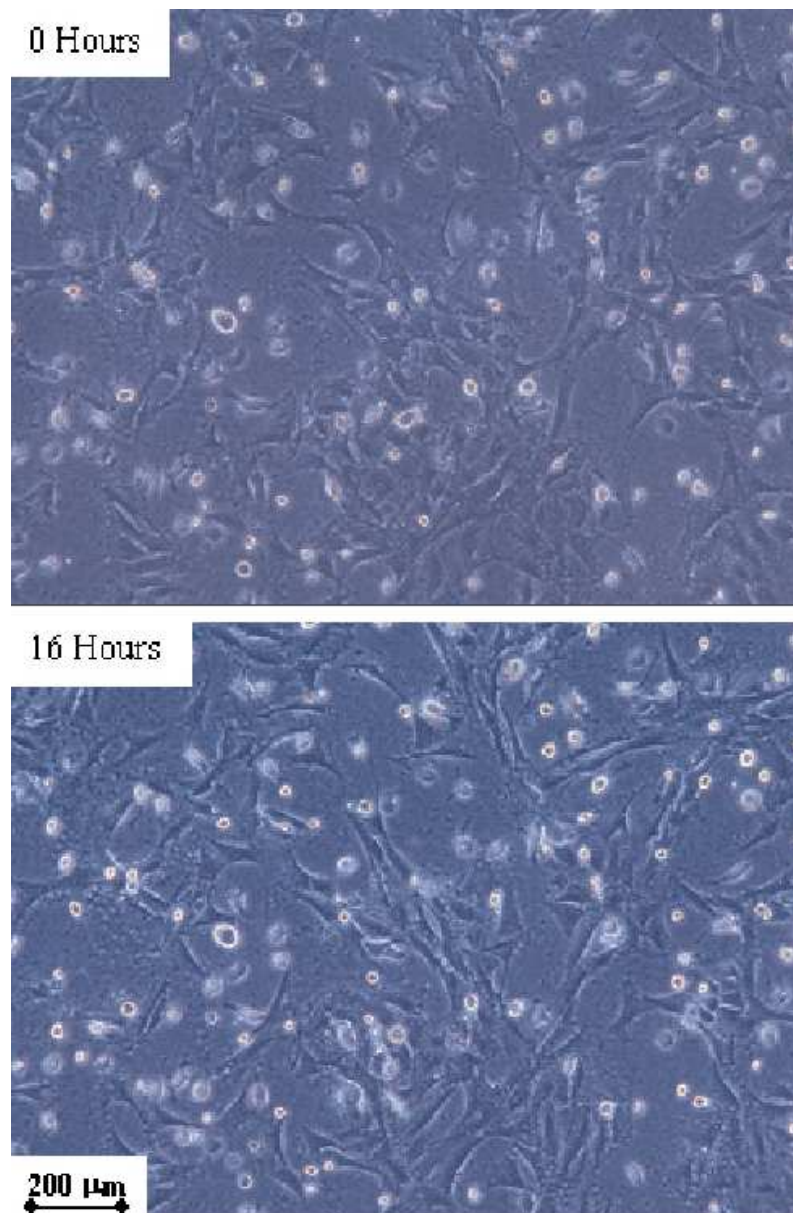


FIGURE 5.2: Stellate cells in monoculture (from [118]). Note there is little cell motility, especially compared with Fig. 5.1 over a similar timescale.

Whilst multiphase models, such as those considered in Chapters 2-4 provide one, physically-based, approach to describing the interactions between

cell populations, Painter and Sherratt [89] have extended the Keller-Segel type modelling framework to the case of two cell populations. An important feature of their model is that limitations of space mean that the random motion and chemotaxis coefficients for each cell type will depend upon the densities of both cell types. They specialise their model to the case of cell movements by chemotaxis, showing that a number of different patterns can be generated, depending upon the types of interaction assumed. The equilibrium solutions for a model of two cell populations subject to chemotaxis were also considered by Fasano *et al* [31], in the case where the random motility coefficients for the two cell populations are constants.

In this chapter, we investigate the two hypotheses of hepatocyte-stellate interactions described above, with the aim of generating experimentally testable predictions, which will allow tissue engineers to distinguish between the two possible mechanisms of aggregation. To do this, we develop a continuum model to describe the interactions between hepatocytes and stellate cells, which incorporates non-local effects explicitly through an integral term. This allows us to consider cell-cell interactions by direct physical contact, as well as by chemical signalling. Our approach will be, in some ways, more simplistic than that adopted in earlier chapters as we shall neglect the effect of the ECM and culture medium in order to focus specifically on cell-cell interactions. A further departure from the previous chapters is that the multiphase modelling framework is not used, and we instead develop our model along the lines described in §1.5.4. We begin in §5.2 by describing our modelling framework in general terms, extending previous work (which considered the case of a single population) to incorporate non-local interactions between the two cell populations in §5.3. We then customise this generic two-population formulation, as appropriate to the two hypotheses described above, in §5.4 and §5.5 respectively. The behaviour of the two models is then investigated using a combination of linear stability analysis (§5.6) and numerical simulations (§5.7) The chapter

concludes in §5.8 with a comparison of our model predictions and recent experimental results, and suggestions for further work.

5.2 Review of non-local modelling framework

Our approach builds on a model due to Mogilner and Edelstein-Keshet [73], which describes non-local interactions within a social aggregate (such as a swarm) consisting of a single type of organism, when inertial effects are negligible. The governing equation, which for simplicity is derived in a one dimensional geometry, takes the form

$$\frac{\partial C}{\partial t} + \frac{\partial}{\partial x}(vC) = D \frac{\partial^2 C}{\partial x^2}, \quad (5.2.1)$$

where C is the swarm density, D is the random motility coefficient, and v is the density-dependent velocity of the swarm, given by the convolution integral

$$v(x, t) = \int_{\Omega} K(x - y)C(y, t)dy. \quad (5.2.2)$$

Hence, the velocity of the swarm at a point x depends upon the density of individuals in a neighbourhood Ω surrounding x . The function K is called the kernel, and weights the effect of interactions according to distance (usually, interactions between nearby individuals are assumed to have greater effect). $K(x - y)$ is usually interpreted as being proportional to the force exerted on an individual at x by another at y [72]. (However, an explicit momentum balance is usually not written down in this type of model.) The model has been used to describe the aggregation behaviour of *Myxobacteria* [72], and similar models have been derived in an ecological context [10, 40] (see §1.5.4).

The choice of kernel function is key to determining the behaviour of the swarm; an even kernel gives rise to collective movement, whilst an odd kernel

describes aggregation in a swarm whose centre of mass is stationary [73]. When the kernel includes an even part, travelling wave solutions of the model can be found, provided the odd part of the kernel is sufficiently small [72, 73]. For a particular choice of odd kernel, the bifurcation structure of the model is studied in [72], revealing that both large scale aggregations (having wavenumbers close to zero) and periodic patterns may arise, depending on the parameters representing the strengths and ranges of attraction and repulsion. In the latter case, the onset of patterning close to bifurcation is studied using a weakly nonlinear analysis (in the former case, where the critical wavenumber is close to zero, the nonlinear analysis is not pursued, as it is non-trivial).

5.2.1 Relation to individual-based models

An alternative model for inter-individual interactions in a social aggregate is presented in [74]. In this paper, a Lagrangian (individual-based) approach is adopted, with each member of the swarm treated as a point mass whose movements are governed by the pairwise sum of its interactions with the other swarm members. The model is written as

$$\frac{d\mathbf{x}_i}{dt} = \sum_{i \neq j} \mathbf{F}(\mathbf{x}_i - \mathbf{x}_j), \quad (5.2.3)$$

where \mathbf{x}_i is the position of the i th member of the swarm, \mathbf{F} is the interaction force and $i, j = 1, 2, \dots, N$ (N being the number of members of the swarm). Note that, once again, inertial effects are assumed negligible, and the units are so chosen that the constant of proportionality (*i.e.* drag coefficient) is unity.

In a recent paper, Bodnar and Velazquez [11] have formally established that, in the one-dimensional case, models of the form (5.2.1) can be derived as macroscopic limits of Lagrangian models such as (5.2.3), provided the interaction force \mathbf{F} is of gradient type (*i.e.* $\mathbf{F} = -\nabla W$). The basic thrust of the argument is as follows. We define the velocity of the i th cell, v_i , from equation

(5.2.3), to be

$$v_i = -\frac{1}{N} \left(\sum_{i \neq j} W'(x_i - x_j) \right), \quad (5.2.4)$$

where we have inserted the factor $1/N$ for subsequent notational convenience, and assumed v_i remains finite as $N \rightarrow \infty$. Now, provided the lengthscale over which interactions take place (*i.e.* the lengthscale over which W undergoes $O(1)$ variations) is much greater than the typical distance between cells, we can approximate v_i by the following, as $N \rightarrow \infty$

$$v(x_i) = - \int_{\Omega} W'(x_i - y) C(y) dy, \quad (5.2.5)$$

where C is the swarm density, as in equation (5.2.1), and Ω is the domain in which $W'(x_i - y)$ is non-zero. Given that the density of the swarm obeys the equation

$$\frac{\partial C}{\partial t} + \frac{\partial}{\partial x}(vC) = 0, \quad (5.2.6)$$

we hence obtain

$$\frac{\partial C(x, t)}{\partial t} = \frac{\partial}{\partial x} \left(C(x, t) \int_{\Omega} W'(x - y) C(y, t) dy \right), \quad (5.2.7)$$

which is equivalent to equation (5.2.1) when $W' = -K$ and $D = 0$.

In the case of the potential W being repulsive, Bodnar and Velazquez show that the addition of ‘white noise’ terms ξ_i to the RHS of equation (5.2.3) gives rise, in the continuum limit, to a diffusion term on the RHS of equation (5.2.7) (making it equivalent to (5.2.1)) - although the diffusion coefficient may depend on C for certain choices of W .

The usefulness of this connection between the individual-based and continuum models is clear. From the interactions between a pair of cells, we can infer the correct form for the interaction kernel in the continuum model, subject to the assumptions about cell spacing and pairwise interactions stated above.

5.3 Model formulation

5.3.1 Modelling aims

We wish to explore two hypotheses regarding the interactions of hepatocytes and stellate cells. The first is that stellates and hepatocytes are attracted to each other by chemical signals; the second, that the attraction is due to the stellates extending processes, which physically contact the hepatocytes and pull them into the growing aggregates. In both hypotheses, we assume hepatocytes are attracted to other hepatocytes by a chemical signal (as in Chapter 3), and that cells repel each other if they come too close together (irrespective of cell type). For each hypothesis, we first use our models to predict the distribution of cells within aggregates for different parameter values. Current experimental research in the Tissue Engineering Group at Nottingham involves the examination of histological sections through fully formed spheroids to determine the distribution of the two cell types within the spheroid. Comparing these results with the model predictions can give us information about the relative strengths of hepatocyte-hepatocyte, hepatocyte-stellate and stellate-stellate interactions (*c.f.* the Steinberg hypothesis [112], as discussed in Chapter 1. The possibility of segregation of the two cell types within an aggregate due to chemical signals has also been shown recently by Painter and Sherratt [89].)

Once the relative strengths of the interactions between the two cells types have been established, we wish to predict the optimum seeding ratio of hepatocytes to stellate cells to achieve swift aggregate formation. Experimental research carried out by Riccalton-Banks [102] found that a 2:1 ratio of hepatocytes to stellates resulted in the formation of greater numbers of aggregates than did ratios of 5:1, 10:1, or hepatocyte-only cultures. However, using our models we can investigate other ratios, the 1:1 ratio being of particular interest, since the trend in the experiments appears to favour increasing the number of stellates.

5.3.2 Governing equations

We begin by extending the model of Mogilner and Edelstein-Keshet [73] to describe the non-local interactions between two cell populations. As in [73], for simplicity, we restrict attention to a one-dimensional geometry and neglect inertia. We also assume that both populations undergo a small amount of random motion.

We let $n(x, t)$ be the density of hepatocytes, and $m(x, t)$ the density of stellate cells. We propose governing equations for the densities of each species of the following form

$$\frac{\partial n}{\partial t} + \frac{\partial}{\partial x}(nv_n) = D_n^* \frac{\partial^2 n}{\partial x^2}, \quad (5.3.1)$$

$$\frac{\partial m}{\partial t} + \frac{\partial}{\partial x}(mv_m) = D_m^* \frac{\partial^2 m}{\partial x^2}, \quad (5.3.2)$$

where v_n and v_m are the advective velocities of the two species and D_n^* and D_m^* are the corresponding random motility coefficients. Note that asterisks are used henceforth to distinguish dimensional parameters from their (unasterisked) dimensionless equivalents.

The dependence of the velocities upon non-local effects are prescribed through the following convolution integral terms

$$v_n = K_{nm} * m + K_n * n = \int_{\Omega} (K_{nm}(x - \xi)m(\xi, t) + K_n(x - \xi)n(\xi, t)) d\xi, \quad (5.3.3)$$

$$v_m = K_{mn} * n + K_m * m = \int_{\Omega} (K_{mn}(x - \xi)n(\xi, t) + K_m(x - \xi)m(\xi, t)) d\xi, \quad (5.3.4)$$

where Ω is the domain within which interactions are assumed to take place.

In (5.3.3) and (5.3.4), the kernel functions describe the interactions between the different populations; K_{nm} represents the effect of stellates (m) on hepato-

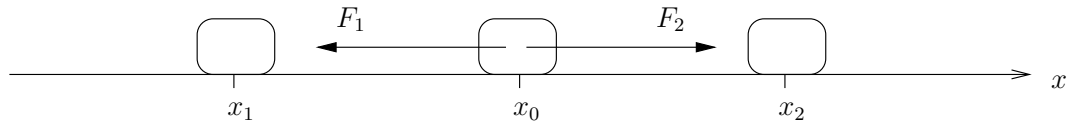


FIGURE 5.3: Forces F_1 and F_2 acting on a cell at x_0 due to attraction to cells at x_1 and x_2 respectively. When the cells are evenly spaced ($x_0 - x_1 = x_2 - x_0$), the magnitudes of the forces are equal ($F_1 = F_2$).

cytes (n); conversely, K_{mn} represents the effect of hepatocytes on stellates; K_n and K_m represent the interactions between members of the same population. The kernels are prescribed functions of the independent spatial variable, and must be odd functions of their argument because we expect individuals to the right of x to induce a velocity of the opposite sign (but equal magnitude) to that induced by individuals to the left of x (as illustrated in Fig. 5.3).

In Appendix D, we demonstrate that equations (5.3.1) and (5.3.2) can support the existence of travelling wave solutions in simple special cases. Similar analysis has been undertaken for one-species non-local models [10, 72, 73], but in those cases, the existence of the travelling waves relies on the kernel function being even (or having an even part) which represents some bias in the external environment causing collective ‘drift’ of the group [73]. In the case of the two-species model considered here, travelling wave solutions are possible even though all the kernel functions involved are assumed to be odd. Such models may be appropriate for describing the interactions of groupings of *e.g.* predators and prey. To our knowledge, travelling wave solutions are not possible for a one-species model with an odd kernel, and hence represent an emergent property of the system.

5.4 Hypothesis 1: Hepatocyte-stellate interactions through chemotaxis

In this section, we develop a model based on the hypothesis that the interactions between hepatocytes and stellate cells are mediated by diffusible chemicals. We use the familiar Keller-Segel framework to describe the cells' motion up chemical gradients, and discuss its relation to the non-local form for the cell velocities described above. We also use the non-local formulation to include the effect of space limitation (*i.e.* the fact that there is a maximum number of cells that can occupy a particular region of space).

As in Chapter 3, we assume that hepatocytes secrete a chemical (whose concentration is denoted by c_1) to which they are attracted; this causes their aggregation in the absence of the stellates. We assume that stellates are also attracted to this chemical. Stellates are assumed to produce a different chemical, possibly HGF, the concentration of which is denoted by c_2 . This is attractive to hepatocytes, but does not affect the stellates. We assume, as in [72], that the timescale for diffusion of both chemicals is short compared to that for cell movement, and hence that the quasi-steady approximation for the concentrations is valid. We thus obtain the following dimensional governing equations

$$\frac{\partial n}{\partial t} + \chi_1^* \frac{\partial}{\partial x} \left(n \frac{\partial c_1}{\partial x} \right) + \chi_2^* \frac{\partial}{\partial x} \left(n \frac{\partial c_2}{\partial x} \right) + \frac{\partial}{\partial x} (n K_R^* * (n + m)) = D_n^* \frac{\partial^2 n}{\partial x^2}, \quad (5.4.1a)$$

$$\frac{\partial m}{\partial t} + \phi^* \frac{\partial}{\partial x} \left(m \frac{\partial c_1}{\partial x} \right) + \frac{\partial}{\partial x} (m K_R^* * (n + m)) = D_m^* \frac{\partial^2 m}{\partial x^2}, \quad (5.4.1b)$$

$$D_1^* \frac{\partial^2 c_1}{\partial x^2} + \alpha_1^* n - \gamma_1^* c_1 = 0, \quad (5.4.1c)$$

$$D_2^* \frac{\partial^2 c_2}{\partial x^2} + \alpha_2^* m - \gamma_2^* c_2 = 0. \quad (5.4.1d)$$

Here, D_n^* and D_m^* are the random motility coefficients for the two cell types, whilst K_R^* is the repulsion kernel, which describes the fact that, when two cells come close enough to touch, they experience a repulsive force (see below). The

constants χ_1^* and χ_2^* represent the sensitivity of the hepatocytes to gradients of c_1 and c_2 , and ϕ^* similarly gives the sensitivity of the stellates to gradients of c_1 . We denote the diffusion coefficients of the two chemicals by D_1^* and D_2^* respectively. We assume they are produced at rates α_1^* and α_2^* , and decay with coefficients γ_1^* and γ_2^* . If we wish to identify c_2 with HGF, we note from [111] that we should make α_2^* dependent on the density of hepatocytes, n . However, for the sake of simplicity, we assume here that α_2^* is constant.

The repulsion kernel is assumed to take the form

$$K_R^*(x) = \begin{cases} R^* \left(\frac{r^*}{x} - 1 \right) & \text{if } 0 < x \leq r^*, \\ R^* \left(\frac{r^*}{x} + 1 \right) & \text{if } -r^* \leq x < 0, \\ 0 & \text{otherwise} \end{cases} \quad (5.4.2)$$

Thus, the repulsive force has a strength R^* , and is felt only when cells come within a range r^* of each other (measured as the distance between their centres). As the distance between the cells tends to zero, the repulsive force becomes arbitrarily large. A plot of the form of this function is given in Fig. 5.4. We refer to this repulsive interaction as ‘space-limitation’. Note that in this chapter, we assume the strength of repulsive interactions is always the same, no matter which types of cells are involved. This may not be true in practice, due to differences in cell size or strength of cell-substrate adhesion between the two cell types, but given the current limited state of the experimental data, we postpone such considerations for future work.

The effect of space-limitation is important for the following reason. If our hypothesis is correct, both stellates and other hepatocytes will be attracted towards hepatocyte aggregates. Without the repulsion terms included, the densities of both cell types will tend to sharp peaks with coincident centres. However, physically, we expect competition for space, which should prevent the density of an aggregate becoming very large, and may result in the segregation of the two cell types (with the most powerfully attracted cell types in

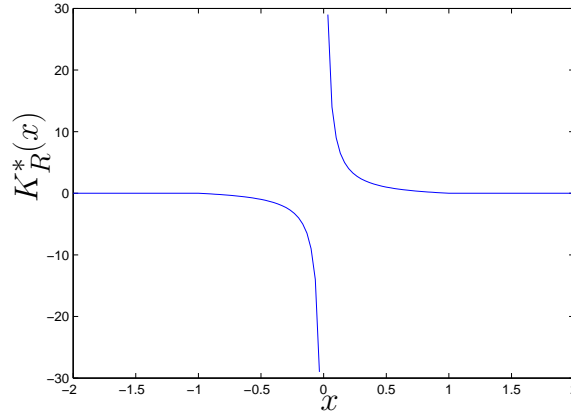


FIGURE 5.4: Repulsion kernel $K_R^*(x)$ (with $R^* = r^* = 1$).

proximity to each other and the other cells relegated to the margins) as in [89].

5.4.1 Boundary and initial conditions

We assume that the cell densities are symmetric about $x = 0$, and are spatially periodic functions, with period $2L$. The latter condition is essentially a mathematical artifice which causes the convolution integral terms to vanish at the edges of the domain, and thus the no flux conditions for the cells and chemoattractants at $x = -L, L$ then take their familiar forms. A possible, more physical, alternative to the assumption of periodicity would be to include repulsive effects between cells and the walls of the culture well, though we do not pursue such a formulation here, as we believe it would add unnecessary complication to the model. The boundary and initial conditions thus read

$$n(x, 0) = n_0(x), \tag{5.4.3}$$

$$m(x, 0) = m_0(x), \tag{5.4.4}$$

$$\frac{\partial n}{\partial x} \Big|_{x=-L} = \frac{\partial n}{\partial x} \Big|_{x=L} = 0, \tag{5.4.5}$$

$$\frac{\partial m}{\partial x} \Big|_{x=-L} = \frac{\partial m}{\partial x} \Big|_{x=L} = 0, \tag{5.4.6}$$

$$\left. \frac{\partial c_1}{\partial x} \right|_{x=-L} = \left. \frac{\partial c_1}{\partial x} \right|_{x=L} = 0, \quad \left. \frac{\partial c_2}{\partial x} \right|_{x=-L} = \left. \frac{\partial c_2}{\partial x} \right|_{x=L} = 0. \quad (5.4.7)$$

5.4.2 Nondimensionalisation

We now nondimensionalise our model (5.4.1) in the following manner

$$\tilde{x} = \frac{x}{\lambda}, \quad \tilde{t} = \frac{t}{T}, \quad \tilde{n} = \frac{n}{\bar{n}}, \quad \tilde{m} = \frac{m}{\bar{n}}, \quad \tilde{c}_1 = \frac{c_1 D_1^*}{\alpha_1^* \lambda^2 \bar{n}}, \quad \tilde{c}_2 = \frac{c_2 D_2^*}{\alpha_2^* \lambda^2 \bar{n}}. \quad (5.4.8)$$

Here, as in previous chapter, λ is the lengthscale over which cell aggregates form, T is the aggregation timescale (with λ and T to be determined) and \bar{n} is a typical overall cell seeding density. The dimensionless system is then (dropping tildes)

$$\frac{\partial n}{\partial t} + \chi_1 \frac{\partial}{\partial x} \left(n \frac{\partial c_1}{\partial x} \right) + \chi_2 \frac{\partial}{\partial x} \left(n \frac{\partial c_2}{\partial x} \right) + \frac{\partial}{\partial x} (n(K_R * (n + m))) = D_n \frac{\partial^2 n}{\partial x^2}, \quad (5.4.9a)$$

$$\frac{\partial m}{\partial t} + \phi \frac{\partial}{\partial x} \left(n \frac{\partial c_1}{\partial x} \right) + \frac{\partial}{\partial x} (m(K_R * (n + m))) = D_m \frac{\partial^2 m}{\partial x^2}, \quad (5.4.9b)$$

$$\frac{\partial^2 c_1}{\partial x^2} + n - \gamma_1 c_1 = 0, \quad (5.4.9c)$$

$$\frac{\partial^2 c_2}{\partial x^2} + m - \gamma_2 c_2 = 0. \quad (5.4.9d)$$

where we have introduced the following dimensionless parameters

$$\chi_1 = \frac{\chi_1^* \alpha_1^* \bar{n} T}{D_1^*}, \quad \chi_2 = \frac{\chi_2^* \alpha_2^* \bar{n} T}{D_2^*}, \quad \phi = \frac{\phi^* \alpha_1^* \bar{n} T}{D_1^*}, \quad D_n = \frac{D_n^* T}{\lambda^2}, \quad (5.4.10)$$

$$D_m = \frac{D_m^* T}{\lambda^2}, \quad \gamma_1 = \frac{\gamma_1^* \lambda^2}{D_1^*}, \quad \gamma_2 = \frac{\gamma_2^* \lambda^2}{D_2^*}, \quad r = \frac{r^*}{\lambda}, \quad R = R^* T \bar{n}. \quad (5.4.11)$$

χ_1 , χ_2 and ϕ thus represent the dimensionless strengths of the chemotaxis, D_n and D_m are ratios of the aggregation timescale to the timescale for random movement of the two cell types; γ_1 and γ_2 are the squares of the ratios of the aggregate lengthscale to the diffusion lengthscale of the two chemicals and R and r are the dimensionless strength and range of repulsion respectively. In the above equations K_R is the dimensionless repulsion kernel, defined as

$$K_R(x) = \begin{cases} R \left(\frac{r}{x} - 1 \right) & \text{if } 0 < x \leq r \\ R \left(\frac{r}{x} + 1 \right) & \text{if } -r \leq x < 0 \\ 0 & \text{otherwise} \end{cases} \quad (5.4.12)$$

The boundary conditions now become

$$\frac{\partial n}{\partial x} \Big|_{x=-\frac{1}{\epsilon}} = \frac{\partial n}{\partial x} \Big|_{x=\frac{1}{\epsilon}} = 0, \quad (5.4.13)$$

$$\frac{\partial m}{\partial x} \Big|_{x=-\frac{1}{\epsilon}} = \frac{\partial m}{\partial x} \Big|_{x=\frac{1}{\epsilon}} = 0, \quad (5.4.14)$$

$$\frac{\partial c_1}{\partial x} \Big|_{x=-\frac{1}{\epsilon}} = \frac{\partial c_1}{\partial x} \Big|_{x=\frac{1}{\epsilon}} = 0, \quad \frac{\partial c_2}{\partial x} \Big|_{x=-\frac{1}{\epsilon}} = \frac{\partial c_2}{\partial x} \Big|_{x=\frac{1}{\epsilon}} = 0, \quad (5.4.15)$$

where $\epsilon = \lambda/L$, and the period of n and m is now $2/\epsilon$.

We note here that it is possible to solve for c_1 and c_2 in terms of n and m using Green's functions. The method is demonstrated in [57] for a domain of infinite spatial extent, which gives

$$c_1(x) = \frac{1}{2\sqrt{\gamma_1}} \int_{-\infty}^{\infty} n(y) \exp(-\sqrt{\gamma_1}|x-y|) dy, \quad (5.4.16)$$

$$c_2(x) = \frac{1}{2\sqrt{\gamma_2}} \int_{-\infty}^{\infty} m(y) \exp(-\sqrt{\gamma_2}|x-y|) dy. \quad (5.4.17)$$

Given our assumption of the periodicity of n and m , we could extend them to an infinite spatial domain and use the above approach without introducing any error. We exploit this fact to simplify our linear stability analysis in §5.6.

5.5 Hypothesis 2: Hepatocyte-stellate interactions through direct physical contact

We now formulate a model based on our second hypotheses: that hepatocyte-stellate interactions occur through direct physical contact. Hepatocytes are again assumed to exert attractive forces on other hepatocytes due to chemotaxis. However, from the time lapse video, it appears that stellate cells exert attractive forces on hepatocytes if the latter come within range of their processes. The hepatocyte-stellate and stellate-hepatocyte interaction forces are thus of the same form. For simplicity, we shall assume they are also of the

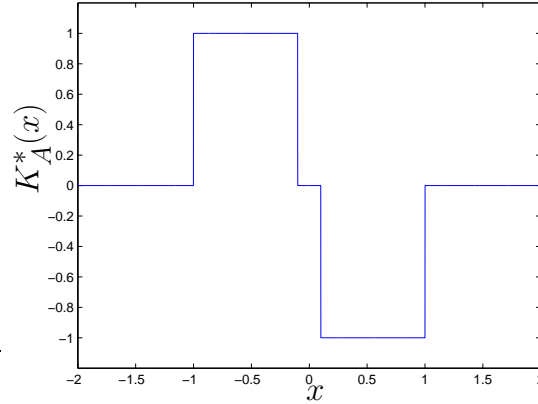


FIGURE 5.5: Hepatocyte-stellate attraction kernel $K_A^*(x)$ (with $A_2^* = a_2^* = 1, r^* = 0.1$).

same magnitude, and hence write $K_{mn} = K_{nm}$. (This assumption neglects the possibility that one of the cell types may be larger or more strongly adherent to the ECM than the other. However, it is consistent with our earlier assumption concerning the strength of the repulsive force.) We assume that the force on the hepatocytes due to the cellular processes of the stellates is constant, provided that the two cells are sufficiently close for contact to occur, but separated by sufficient distance that the two cells do not repel each other. For simplicity, we have ignored the potential dependence of the force on a chemical signal derived from the hepatocytes, as there is currently no data as to the form of such a dependence. We hence assume the following decomposition for our kernel function

$$K_{nm}(x) = K_R^*(x) + K_A^*(x) \tag{5.5.1}$$

where:

$$K_A^*(x) = \begin{cases} -A_2^* & \text{if } r^* \leq x \leq a_2^*, \\ A_2^* & \text{if } -a_2^* \leq x \leq -r^*, \\ 0 & \text{otherwise.} \end{cases} \tag{5.5.2}$$

The function K_A^* is plotted in Fig. 5.5. The constant A_2^* represents the strength of the attraction, whilst a_2^* is the average length of a stellate cellular process

(hence representing the typical range of attraction) and r^* is the range of repulsion, as defined earlier.

As before, we assume that the hepatocyte-hepatocyte interaction force is due to a chemoattractant, and that stellates are not attracted to other stellates. The governing equations thus take the following dimensional form

$$\frac{\partial n}{\partial t} + \chi_1^* \frac{\partial}{\partial x} \left(n \frac{\partial c_1}{\partial x} \right) + \frac{\partial}{\partial x} (n(K_R * n + K_{nm} * m)) = D_n^* \frac{\partial^2 n}{\partial x^2}, \quad (5.5.3a)$$

$$\frac{\partial m}{\partial t} + \frac{\partial}{\partial x} (m(K_R * m + K_{mn} * n)) = D_m^* \frac{\partial^2 m}{\partial x^2}, \quad (5.5.3b)$$

$$D_1^* \frac{\partial^2 c_1}{\partial x^2} + \alpha_1^* n - \gamma_1^* c_1 = 0, \quad (5.5.3c)$$

The boundary and initial conditions are as in equations (5.4.3)-(5.4.7), with the exception that c_2 no longer appears in our system of equations.

5.5.1 Nondimensionalisation

We now render the governing equations dimensionless, using the scalings stated in equation (5.4.8). The governing equations then become

$$\frac{\partial n}{\partial t} + \chi_1 \frac{\partial}{\partial x} \left(n \frac{\partial c_1}{\partial x} \right) + \frac{\partial}{\partial x} (n(K_R * n + K_{nm} * m)) = D_n \frac{\partial^2 n}{\partial x^2}, \quad (5.5.4a)$$

$$\frac{\partial m}{\partial t} + \frac{\partial}{\partial x} (m(K_R * m + K_{mn} * n)) = D_m \frac{\partial^2 m}{\partial x^2}, \quad (5.5.4b)$$

$$\frac{\partial^2 c_1}{\partial x^2} + n - \gamma_1 c_1 = 0, \quad (5.5.4c)$$

where the kernel functions now take their dimensionless form, and the dimensionless parameters and K_R are the same as those specified in equations (5.4.10)-(5.4.12), with the following additions

$$A_2 = A_2^* T \bar{n}, \quad a_2 = \frac{a_2^*}{\lambda}, \quad (5.5.5)$$

$$K_{nm}(x) = K_R(x) + \begin{cases} -A_2 & \text{if } r \leq x \leq a_2, \\ A_2 & \text{if } -a_2 \leq x \leq -r, \\ 0 & \text{otherwise,} \end{cases} \quad (5.5.6)$$

$$K_{mn} = K_{nm}. \quad (5.5.7)$$

The boundary conditions are specified as in (5.4.13)-(5.4.15), once again with the exception that c_2 no longer appears in our system of equations.

5.6 Linear stability analysis

We now examine the linear stability of our two models to determine the parameter regimes in which we may expect to see aggregation. We take the limit of a large domain ($\epsilon \rightarrow 0$) so that we can exploit the Green's function solutions for c_1 and c_2 (given in equations (5.4.16) and (5.4.17)) to include the chemotaxis terms within the non-local framework [72]. We then need only consider the stability of the dimensionless version of the non-local model (5.3.1)-(5.3.2), with the appropriate kernel functions for each model (which are modified to include the chemotaxis terms where appropriate - *e.g.* see equation (5.6.14)). This provides some simplification of notation in the analysis.

We consider the spatially homogeneous steady state, $n = n_0$, $m = m_0$ which approximates the conditions immediately after the cells are seeded in the culture wells, and introduce small perturbations of the form

$$n = n_0 + \hat{n}(x, t), \quad m = m_0 + \hat{m}(x, t), \quad (5.6.1)$$

where $|\hat{n}|, |\hat{m}| \ll 1$. We substitute these forms into the governing equations, (5.3.1) and (5.3.2), and linearise to obtain

$$\frac{\partial \hat{n}}{\partial t} = D_n \frac{\partial^2 \hat{n}}{\partial x^2} - n_0 \frac{\partial}{\partial x} (K_{nm} * \hat{m} + K_n * \hat{n}), \quad (5.6.2)$$

$$\frac{\partial \hat{m}}{\partial t} = D_m \frac{\partial^2 \hat{m}}{\partial x^2} - m_0 \frac{\partial}{\partial x} (K_{mn} * \hat{n} + K_m * \hat{m}). \quad (5.6.3)$$

We remark that terms containing convolutions with constant densities, *e.g.* $K_{nm} * m_0$ vanish, since the kernels are assumed to be odd.

We now set

$$\hat{n} = n_1 e^{(iqx + \omega t)}, \quad \hat{m} = m_1 e^{(iqx + \omega t)}, \quad (5.6.4)$$

where q and ω are, respectively, the wavenumber and growth rate of the perturbation, and $|n_1|, |m_1| \ll 1$. We note that, including the forms of the perturbations assumed in (5.6.4), the convolution terms give *e.g.*

$$\begin{aligned} K_n * \hat{n} &= n_1 \int_{-\infty}^{\infty} K_n(x-y) e^{(iqy + \omega t)} dy \\ &= n_1 e^{(iqx + \omega t)} \int_{-\infty}^{\infty} K_n(\zeta) e^{-iq\zeta} d\zeta \\ &= n_1 e^{(iqx + \omega t)} \tilde{K}_n(q). \end{aligned} \quad (5.6.5)$$

where henceforth tildes denote Fourier transforms, so that

$$\tilde{f}(q) = \int_{-\infty}^{\infty} f(x) e^{-iqx} dx. \quad (5.6.6)$$

Substituting (5.6.4) into equations (5.6.2) and (5.6.2), we hence obtain

$$n_1 \omega = -D_n q^2 n_1 - iqn_0 (m_1 \tilde{K}_{nm}(q) + n_1 \tilde{K}_n(q)), \quad (5.6.7)$$

$$m_1 \omega = -D_m q^2 m_1 - iqm_0 (n_1 \tilde{K}_{mn}(q) + m_1 \tilde{K}_m(q)), \quad (5.6.8)$$

We remark that since the kernels are odd, their Fourier transforms are purely imaginary.

We can re-write equations (5.6.7) and (5.6.8) in the form

$$\mathbf{J}(n_1, m_1) = 0, \quad (5.6.9)$$

where \mathbf{J} is the matrix:

$$\mathbf{J} = \begin{pmatrix} \omega + D_n q^2 + iqn_0 \tilde{K}_n & iqn_0 \tilde{K}_{nm} \\ iqm_0 \tilde{K}_{mn} & \omega + D_m q^2 + iqm_0 \tilde{K}_m \end{pmatrix} \quad (5.6.10)$$

For nontrivial solutions, $(n_1, m_1) \neq \mathbf{0}$, and we require $\det(\mathbf{J}) = 0$. This leads to a quadratic dispersion relation of the form

$$\omega^2(q) + B(q)\omega + C(q) = 0, \quad (5.6.11)$$

where

$$B(q) = q^2(D_n + D_m) + iq(n_0\tilde{K}_n + m_0\tilde{K}_m), \quad (5.6.12)$$

$$C(q) = (D_nq^2 + iqn_0\tilde{K}_n)(D_mq^2 + iqm_0\tilde{K}_m) + q^2n_0m_0\tilde{K}_{nm}\tilde{K}_{mn}. \quad (5.6.13)$$

We now analyse the dispersion relation for the two models derived above.

5.6.1 Model 1: Chemotaxis

We incorporate the chemotaxis terms in the convolution integrals by exploiting the Green's function solutions for c_1 and c_2 . This gives rise to additional terms in the kernel functions, which are now given by

$$K_n(x) = -\text{sign}(x)\frac{\chi_1}{2}\exp\left(-\frac{|x|}{a_n}\right) + K_R(x), \quad (5.6.14)$$

$$K_{nm}(x) = -\text{sign}(x)\frac{\chi_2}{2}\exp\left(-\frac{|x|}{a}\right) + K_R(x), \quad (5.6.15)$$

$$K_{mn}(x) = -\text{sign}(x)\frac{\phi}{2}\exp\left(-\frac{|x|}{a_n}\right) + K_R(x), \quad (5.6.16)$$

$$K_m(x) = K_R(x), \quad (5.6.17)$$

where:

$$a_n = \frac{1}{\sqrt{\gamma_1}}, \quad a = \frac{1}{\sqrt{\gamma_2}}. \quad (5.6.18)$$

Hence, a_n and a represent the ranges of attraction over which the chemicals c_1 and c_2 act, relative to the aggregation lengthscale λ .

The Fourier transforms of the above are given by

$$\tilde{K}_n(x) = \frac{iq\chi_1a_n^2}{a_n^2q^2 + 1} - 2iRr\Psi(qr), \quad (5.6.19a)$$

$$\tilde{K}_m(x) = -2iRr\Psi(qr), \quad (5.6.19b)$$

$$\tilde{K}_{nm}(x) = \frac{iq\chi_2a^2}{a^2q^2 + 1} - 2iRr\Psi(qr), \quad (5.6.19c)$$

$$\tilde{K}_{mn}(x) = \frac{iq\phi a_n^2}{a_n^2q^2 + 1} - 2iRr\Psi(qr), \quad (5.6.19d)$$

The function Ψ denotes the Fourier transform of the repulsion kernel (5.4.12) and is defined as

$$\Psi(x) = Si(x) + \frac{1}{x}(\cos x - 1), \quad (5.6.20)$$

where $Si(x)$ is the sine integral [1]

$$Si(x) = \int_0^x \frac{\sin t}{t} dt. \quad (5.6.21)$$

For simplicity, we first consider the case $R = 0$, so repulsion effects vanish. The coefficients in dispersion relation (5.6.11) then become

$$B(q) = q^2 \left(D_n + D_m - \frac{n_0 \chi_1 a_n^2}{a_n^2 q^2 + 1} \right), \quad (5.6.22)$$

$$C(q) = q^4 D_m \left(D_n - \frac{n_0 \chi_1 a_n^2}{a_n^2 q^2 + 1} \right) - \frac{q^4 n_0 m_0 \chi_2 \phi a_n^2 a^2}{(a_n^2 q^2 + 1)(a^2 q^2 + 1)}. \quad (5.6.23)$$

A sufficient condition for instability to occur is $C < 0$. This implies

$$D_m \left(D_n - \frac{n_0 \chi_1 a_n^2}{a_n^2 q^2 + 1} \right) < \frac{n_0 m_0 \chi_2 \phi a_n^2 a^2}{(a_n^2 q^2 + 1)(a^2 q^2 + 1)}. \quad (5.6.24)$$

An interpretation of this relation is that, in order for instability to arise, random motion of the two cell populations (characterised by D_n and D_m), which tends to spread the cells uniformly over the domain, must be dominated by chemotaxis. As $q \rightarrow \infty$, the RHS of inequality (5.6.24) tends to zero, so the model is linearly stable to perturbations of very high wavenumber. We remark that $\omega(0) = 0$, and that the LHS of equation (5.6.24) is minimised, and the RHS maximised, for $q = 0$ (with other parameters regarded as fixed). This implies that instability will occur for a finite range of wavenumbers $0 < q^2 < q_{max}^2$, where q_{max}^2 is the positive root of

$$q^4 D_n D_m a_n^2 a^2 + q^2 D_m (D_n a_n^2 + D_n a^2 - n_0 \chi_1 a_n^2 a^2) + D_n D_m - n_0 D_m \chi_1 a_n^2 - n_0 m_0 \chi_2 \phi a_n^2 a^2 = 0. \quad (5.6.25)$$

When there is no hepatocyte-hepatocyte attraction ($\chi_1 = 0$), it is easy to determine the way in which the cell seeding densities n_0 and m_0 can affect whether or not instability occurs. We assume that $n_0 + m_0 \leq 1$, and regard

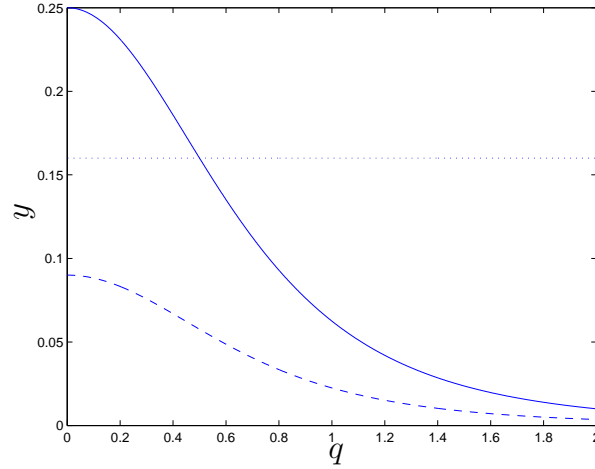


FIGURE 5.6: An illustration of the inequality (5.6.24), with $\chi_1 = 0$, $D_n = D_m = 0.4$, $\chi_2 = \phi = a_n = a = 1$. The dotted line ($y = D_n D_m = 0.16$) represents the LHS. The RHS, with $m_0 = 1 - n_0$, (*i.e.* $y = \frac{n_0(1-n_0)}{(q^2+1)(q^2+1)}$) is plotted for $n_0 = 0.5$ (solid) and $n_0 = 0.1$ (dashed). Hence, when $n_0 = 0.5$, instability occurs for $0 < q < q_{max}$, with $q_{max} \approx 0.5$, whilst for $n_0 = 0.1$, the system is linearly stable.

the parameters D_n , D_m , a_n , a , χ_2 and ϕ as fixed, since these are intrinsic to the cells (and hence difficult to control experimentally). Instability is then most likely to occur when $n_0 = m_0 = 1/2$ (*i.e.* instability may occur for this cell seeding ratio, but not for others, for given parameter values), since this maximises the term on the RHS of (5.6.24). This is illustrated in Fig. 5.6. Hence, in this case, aggregates are most likely to form if the cells are seeded at a 1:1 hepatocyte to stellate ratio, at the maximum possible seeding density.

We remark that while, in general, the case $B < 0 < C$ could give rise to instability, in practice it cannot occur in this model for the following reason. If $B < 0$, then

$$\frac{n_0 \chi_1 a_n^2}{a_n^2 q^2 + 1} > D_n + D_m \geq D_n, \quad (5.6.26)$$

which in turn implies that the first term of equation (5.6.23) is non-positive,

and hence we cannot have $C > 0$. Thus, equation (5.6.24) is both a necessary and sufficient condition for instability to occur.

We now consider the more general case where $R \neq 0$, in which case the sufficient condition for instability, $C < 0$, becomes

$$\begin{aligned} & (q^2 D_m + 2qm_0 Rr \Psi(qr)) \left(q^2 D_n + 2qn_0 Rr \Psi(qr) - \frac{q^2 n_0 \chi_1 a_n^2}{a_n^2 q^2 + 1} \right) \\ & < q^2 n_0 m_0 \left(\frac{q \chi_2 a^2}{a^2 q^2 + 1} - 2Rr \Psi(qr) \right) \left(\frac{q \phi a_n^2}{a_n^2 q^2 + 1} - 2Rr \Psi(qr) \right). \end{aligned} \quad (5.6.27)$$

We now note the following features. Firstly, when $\chi_1 = \chi_2 = \phi = 0$ (*i.e.* there are no attractive interactions), we have $C > 0$ and $B > 0$, so the uniform steady state is stable. Secondly, for non-negligible attractions, as $q \rightarrow \infty$, we always have B and C becoming positive, since the χ_1 , χ_2 and ϕ terms remain $O(1)$, whilst other terms are at least $O(q)$ (since $\Psi(qr) \rightarrow \pi/2$ as $q \rightarrow \infty$ -see [1]). Hence the model remains stable to perturbations of very high wavenumber. Thirdly, for $q \ll 1$, $\Psi(qr)$ tends to $qr(1-r)$; the condition (5.6.27) then reads

$$\begin{aligned} & (D_m + 2m_0 Rr(1-r)) (D_n + 2n_0 Rr(1-r) - n_0 \chi_1 a_n^2) < \\ & n_0 m_0 (\chi_2 a^2 - 2Rr(1-r)) (\phi a_n^2 - 2Rr(1-r)). \end{aligned} \quad (5.6.28)$$

Once again, we must now consider the case $B < 0$, $C > 0$, which represents an alternative sufficient condition for instability. Writing out C in full we have

$$\begin{aligned} C = & (q^2 D_m + 2qm_0 Rr \Psi(qr)) \left(q^2 D_n + 2qn_0 Rr \Psi(qr) - \frac{q^2 n_0 \chi_1 a_n^2}{a_n^2 q^2 + 1} \right) - \\ & q^2 n_0 m_0 \left(\frac{q \chi_2 a^2}{a^2 q^2 + 1} - 2Rr \Psi(qr) \right) \left(\frac{q \phi a_n^2}{a_n^2 q^2 + 1} - 2Rr \Psi(qr) \right). \end{aligned} \quad (5.6.29)$$

Firstly, we note that since $\Psi(x)$ is an odd function of its argument, C is an odd function of q (and hence it suffices to consider positive q). Secondly, $\Psi(0) = 0$; and, since $\Psi'(x) = (1 - \cos(x))/x^2 \geq 0$, it follows that $\Psi(x) > 0$ for $x > 0$. We can then say that, since $B < 0$, the second bracket of the first term above

is negative. Hence, for $C > 0$ it is necessary that the second term be negative - *i.e.*

$$\left(\frac{q\chi_2 a^2}{a^2 q^2 + 1} - 2Rr\Psi(qr) \right) \left(\frac{q\phi a_n^2}{a_n^2 q^2 + 1} - 2Rr\Psi(qr) \right) < 0, \quad (5.6.30)$$

i.e. we require the net hepatocyte-stellate interaction to be repulsive, with the stellate-hepatocyte interaction attractive, or *vice versa*. This type of behaviour is not the same as that considered in Appendix D, in which the heterogeneous attraction-repulsion relationship between the two species leads to travelling wave solutions. In that case there is no growth of the instability (the initial form of groupings of each species persists, they merely undergo a spatial translation). By contrast, to observe the type of behaviour considered here it is essential that one of the species is attracted to itself, otherwise we cannot satisfy the condition $B < 0$.

5.6.2 Model 2: Physical contact

Once again, we begin by considering the simpler case, in which $R = 0$. The Fourier transform of the hepatocyte-stellate interaction kernel, \tilde{K}_{nm} , is then given by

$$\begin{aligned} \tilde{K}_{nm} &= -2i\mathfrak{F}_s(K_{nm}) = -2i \int_0^\infty K_{nm}(x) \sin(qx) dx \\ &= 2i \int_r^{a_2} A_2 \sin(qx) dx \\ &= 2i \frac{A_2}{q} (\cos(qr) - \cos(qa_2)). \end{aligned}$$

The Fourier transform of K_n is given by equation (5.6.19b).

Upon substituting these forms into the dispersion relation (5.6.11), we find the coefficients are given by

$$B(q) = q^2 \left(D_n + D_m - \frac{n_0\chi_1 a_n^2}{a_n^2 q^2 + 1} \right), \quad (5.6.31)$$

$$C(q) = q^4 D_m \left(D_n - \frac{n_0\chi_1 a_n^2}{a_n^2 q^2 + 1} \right) - 4n_0 m_0 A_2^2 (\cos(qr) - \cos(qa_2))^2. \quad (5.6.32)$$

By the same reasoning used in §5.6.1, a necessary and sufficient condition for instability is that $C < 0$, and hence

$$q^4 D_m \left(D_n - \frac{n_0 \chi_1 a_n^2}{a_n^2 q^2 + 1} \right) < 4 n_0 m_0 A_2^2 (\cos(qr) - \cos(qa_2))^2. \quad (5.6.33)$$

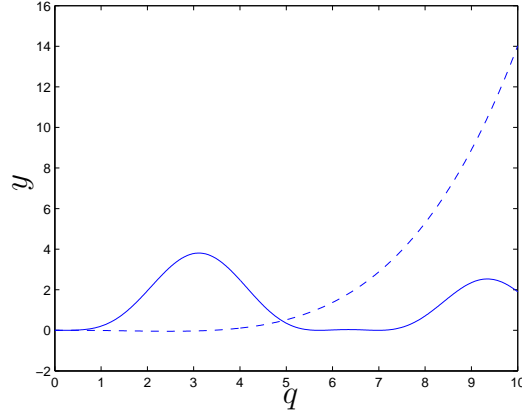


FIGURE 5.7: An illustration of the inequality (5.6.33), with $n_0 = m_0 = 0.5$, $D_n = D_m = 0.04$, $\chi_1 = A_2 = a_2 = 1$, $r = 0.1$. The dotted line ($y = 0.04q^4(0.04 - 1/2(q^2 + 1))$) represents the LHS, the solid line ($y = (\cos(0.1q) - \cos(q))^2$) the RHS. Hence instability occur for these parameter values for $0 < q < q_{max}$, with $q_{max} \approx 5$.

For the purposes of illustration, the above inequality is plotted in Fig. 5.7 for a particular choice of parameter values. We observe once again, that the model is linearly stable to perturbation of large wavenumber ($q \rightarrow \infty$), as in this limit the first term of equation (5.6.32) dominates, and so the inequality (5.6.33) cannot hold. Using the same reasoning as for Model 1, when there is no hepatocyte-hepatocyte attraction ($\chi_1 = 0$), instability is most likely to occur if the cells are seeded in a 1:1 ratio (*i.e.* $n_0 = m_0 = 1/2$).

For small wavenumbers ($q \ll 1$), we can expand the cosine terms as a power series, and equation (5.6.33) is modified to

$$D_m (D_n - n_0 \chi_1 a_n^2) < n_0 m_0 A_2^2 (a_2^2 - r^2)^2. \quad (5.6.34)$$

Hence instability is more likely to occur if the ranges of attraction a and a_n are increased or the range of repulsion r decreased.

Now considering the more general case, $R \neq 0$, we obtain

$$B(q) = q^2 \left(D_n + D_m - \frac{n_0 \chi_1 a_n^2}{a_n^2 q^2 + 1} + 2q(n_0 + m_0) R r \Psi(qr) \right), \quad (5.6.35)$$

$$C(q) = (q^2 D_m + 2q m_0 R r \Psi(qr)) \left(q^2 D_n + 2q n_0 R r \Psi(qr) - \frac{q^2 n_0 \chi_1 a_n^2}{a_n^2 q^2 + 1} \right) - 4q^2 n_0 m_0 \left(\frac{A_2}{q} (\cos(qr) - \cos(qa_2)) - R r \Psi(qr) \right)^2. \quad (5.6.36)$$

For instability, we require either $C < 0$ or $B < 0$ and $C > 0$. The first condition can once again simply be interpreted as stating that attractive interactions must be strong enough to overcome diffusion and now also repulsion. The second condition cannot occur in this model, since $B < 0$ implies the first term of C is negative, and hence $C < 0$.

5.7 Numerical simulations

5.7.1 Numerical methods

The numerical simulations in this chapter were, once again, performed using MATLAB. For Model 1, we begin by calculating the chemical concentrations c_1 and c_2 , given the initial conditions for n and m , from equations (5.4.9c) and (5.4.9d) using matrix inversion. (For Model 2, we need solve only for c_1 using (5.5.4c).) We then calculate the convolution terms (*i.e.* those terms involving K_R and K_A), using the trapezium rule. We thus obtain the overall velocities (V_n and V_m) for the two cell types, which include contributions from chemotaxis and non-local terms - *e.g.* for Model 1 (5.4.9), we have

$$V_n = \chi_1 \frac{\partial c_1}{\partial x} + \chi_2 \frac{\partial c_2}{\partial x} + K_R * (n + m), \quad (5.7.1)$$

$$V_m = \phi \frac{\partial c_1}{\partial x} + K_R * (n + m). \quad (5.7.2)$$

The conservation equations for each cell type are then written in terms of these velocities - *e.g.* equation (5.4.9a) becomes

$$\frac{\partial n}{\partial t} + \frac{\partial}{\partial x}(nV_n) = D_n \frac{\partial^2 n}{\partial x^2}. \quad (5.7.3)$$

These equations allow us to update the cell densities, using the explicit up-winding routine described in detail in Chapter 2. The velocities are then, in turn, updated, and the process repeated until the desired end time is reached.

The code for the convolution integrals was validated by checking that it correctly calculated the convolution of the kernel functions with prescribed profiles for n and m . Similar verification was carried out on the solutions for the chemical concentrations, and the standard grid refinement checks were made. Mass conservation for the two cell species is verified at each time-point, and was found not to exceed 3% for the simulations shown here.

5.7.2 Model 1

For the simulations in this section, we adopt a timestep $\Delta t = 0.0001$, with 1000 grid points in the domain, taken to be $[-10, 10]$ (except for Figs. 5.8 and 5.9 which required 2000 grid points to obtain acceptable resolution). We assume that the cells undergo relatively little random motion, and hence set $D_n = D_m = 0.001$. Repulsion is assumed to be strong and short-ranged, and so we set $R = 100$, $r = 0.1$. The diffusion lengthscale for c_1 must set the lengthscale of the aggregates, λ in the absence of stellates; we assume that the diffusion lengthscale of c_2 is similar, and hence set $\gamma_1 = \gamma_2 = 1$. Our initial conditions are $n_0 = 0.5 + 0.05 \cos(\pi x/5)$, with $m_0 = 0.5 + 0.05 \cos(\pi x/10)$, so the stellates are most densely seeded in the centre of the domain. The chemotactic affinities of the cells determine the aggregation timescale, T . We assume that the interactions between hepatocytes are stronger than those between hepatocytes and stellates and hence set $\chi_1 = 5$, $\chi_2 = 1$, $\phi = 1$. The

results show that the hepatocytes form a core within the aggregates, which is flanked by stellates (see Fig. 5.8). The total cell density ($n + m$) is shown in Fig. 5.9. It was not possible to run this simulation for longer times, as the gradients of m become large close to the core of the aggregates (increasing the number of grid points improves the resolution, at the expense of considerably increasing the time taken to run a simulation - as we felt our results adequately illustrated the cell distribution within the developing aggregate, we did not pursue this issue further) .

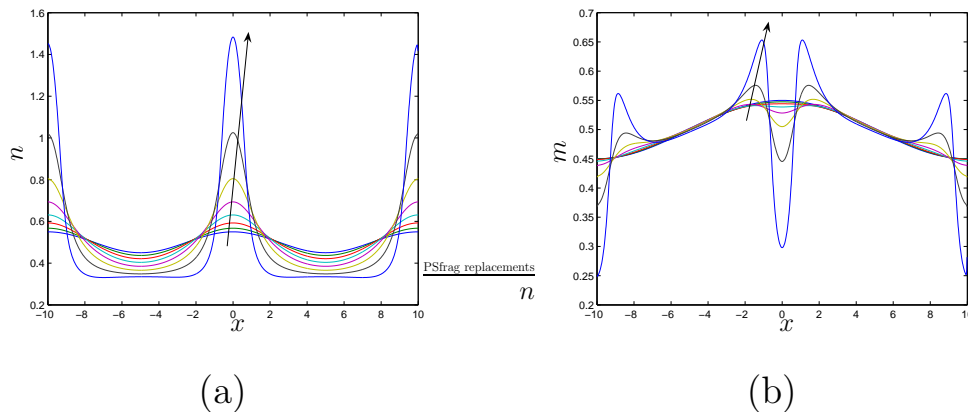


FIGURE 5.8: Numerical solution for cell densities: (a) n ; (b) m at intervals of 0.5 time units, between $t = 0$ and $t = 3.5$ (arrow indicates increasing time). Parameter values: $\chi_1 = 5$, $\chi_2 = 1$, $\phi = 1$, $R = 100$, $r = 0.1$, $\gamma_1 = \gamma_2 = 1$, $D_n = D_m = 0.001$.

Keeping the same initial conditions, we now assume that it is the hepatocyte-stellate attraction that is strongest, and so set $\chi_1 = 1$, $\chi_2 = 5$, $\phi = 5$. We now observe that both cell types are mixed together within the aggregates - there is no segregation into a core of hepatocytes and an outer layer of stellates as previously (compare Figs. 5.10 and 5.8). The overall distribution of cell density has the same profile as that of the two cell types individually (Fig. 5.11). Comparing our results with experimental observations (see §5.8), we believe that it is most likely that the hepatocyte-stellate attraction is strongest in

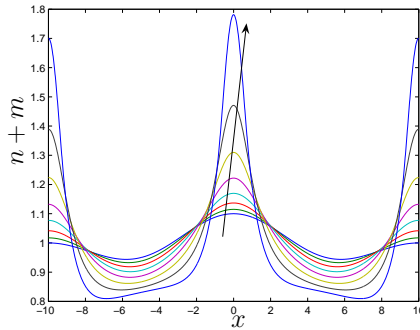


FIGURE 5.9: Numerical solution for total cell density $n + m$ at intervals of 0.5 time units, between $t = 0$ and $t = 3.5$ (arrow indicates increasing time). Parameters as for Fig. 5.8.

practice, and we therefore now fix these values of χ_1 , χ_2 and ϕ , and look at the influence of other factors on the aggregation process.

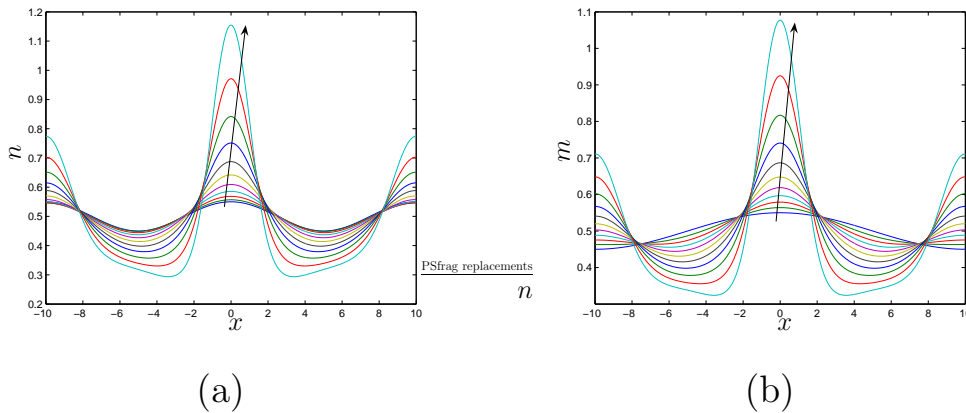


FIGURE 5.10: Numerical solution for cell densities: (a) n ; (b) m at intervals of 0.5 time units, between $t = 0$ and $t = 5$ (arrow indicates increasing time). Parameter values: $\chi_1 = 1$, $\chi_2 = 5$, $\phi = 5$, other parameters as for Fig. 5.8.

We now repeat the simulation described above, with the new initial conditions $n_0 = 2/3 + 0.05 \cos(\pi x/5)$, with $m_0 = 1/3 + 0.05 \cos(\pi x/10)$, so the hepatocyte to stellate ratio is now approximately 2:1, instead of 1:1 as previously. We then compare Figs. 5.11 and 5.13, and note that at $t = 5$, the overall

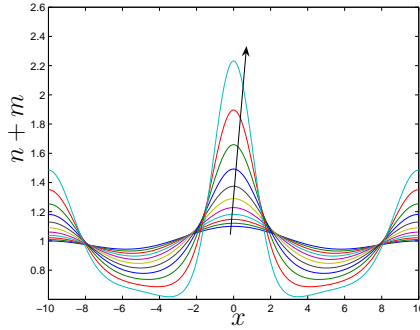


FIGURE 5.11: Numerical solution for total cell density $n + m$ at intervals of 0.5 time units, between $t = 0$ and $t = 5$ (arrow indicates increasing time). Parameters as for Fig. 5.10

cell density ($n + m$) within the aggregates is greater for the 1:1 ratio (taking a maximum value of 2.2) compared to the 2:1 ratio (where the maximum value is 2.0). This suggests the aggregation is proceeding more quickly, and that it is thus more advantageous to seed hepatocytes and stellates in a 1:1 than a 2:1 ratio to promote aggregate formation. This is because a 1:1 ratio tends to maximise the amount of contact between the two cell types which have the strongest attraction. However, comparing Figs. 5.10 and 5.12, we note that at the same time point, the maximum density of hepatocytes in the aggregates is greater for the 2:1 ratio, whilst for stellates, the maximum density is greater for the 1:1 ratio. This reflects the relative abundance of the two cell types upon seeding. If factors other than the speed of aggregate formation need to be taken into account experimentally, such as functionality of the engineered tissue (since most of the functions of the liver are performed by hepatocytes), it may thus not be optimal to seed the cells in a 1:1 ratio. We discuss this issue more fully in §5.8.

We now consider the effect of changing relative decay rates of the two chemoattractants, so we set $\gamma_2 = 0.5$, keeping all other parameters the same. This effectively means the stellate-hepatocyte attraction range is a factor of

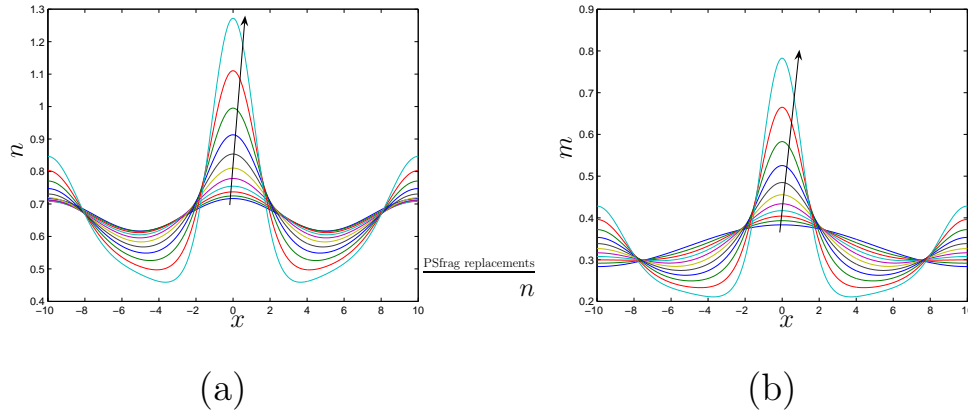


FIGURE 5.12: Numerical solution for cell densities: (a) n ; (b) m at intervals of 0.5 time units, between $t = 0$ and $t = 5$ (arrow indicates increasing time). Hepatocyte:stellate seeding ratio of 2:1; parameters as for Fig. 5.10.

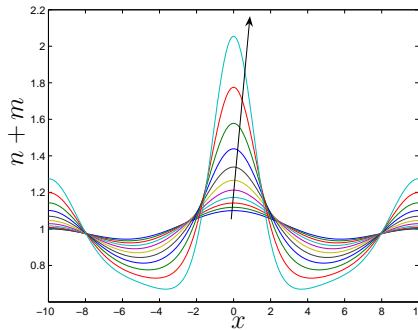


FIGURE 5.13: Numerical solution for total cell density $n + m$ at intervals of 0.5 time units, between $t = 0$ and $t = 5$ (arrow indicates increasing time). Parameters as for Fig. 5.12

$\sqrt{2}$ greater than that between hepatocytes. We notice, comparing Fig. 5.14 with Fig. 5.10, that this gives rise to taller peaks in the distributions of both cell types. This is because the growing aggregates now influence more distant cells.

Repeating the above with $\gamma_2 = 2$ (*i.e.* reducing the range of hepatocyte-stellate attraction compared to that between hepatocytes) we find the converse effect (see Fig. 5.16) - the peaks in the cell distributions are now less

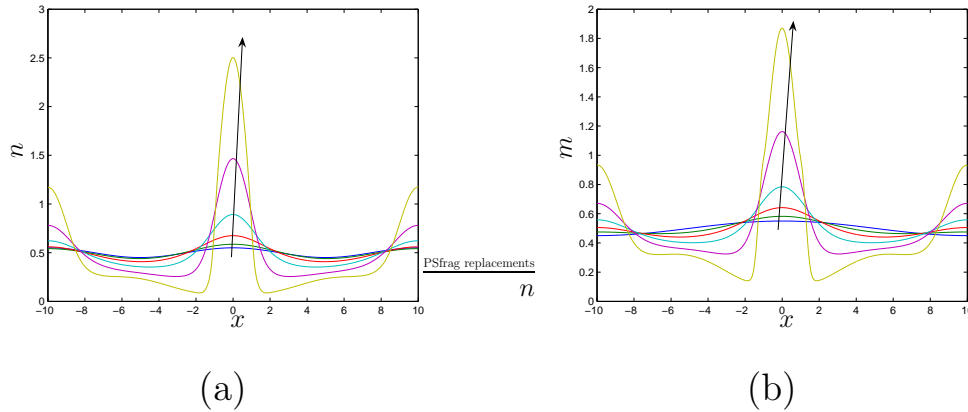


FIGURE 5.14: Numerical solution for cell densities: (a) n ; (b) m at unit time intervals, between $t = 0$ and $t = 5$ (arrow indicates increasing time). $\gamma_2 = 0.5$, other parameters as for Fig. 5.10

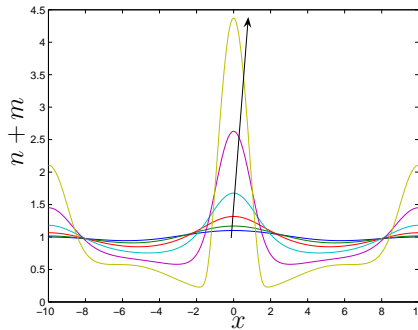


FIGURE 5.15: Numerical solution for total cell density $n + m$ at unit time intervals, between $t = 0$ and $t = 5$ (arrow indicates increasing time). Parameters as for Fig. 5.14

pronounced, since the growing aggregates' effective influence only extends to nearby cells.

5.7.3 Model 2

We now repeat the above investigations for the second model, in which the hepatocyte-stellate interaction is assumed to be via physical contact. The simulations in this section again use a timestep $dt = 0.0001$, but to obtain

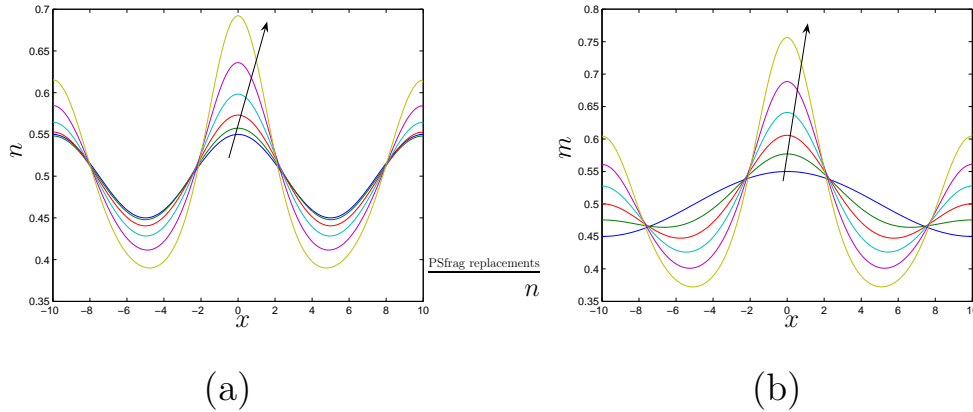


FIGURE 5.16: Numerical solution for cell densities: (a) n ; (b) m at unit time intervals, between $t = 0$ and $t = 5$ (arrow indicates increasing time). $\gamma_2 = 2$, other parameters as for Fig. 5.10.

acceptably smooth, well resolved solutions we now use 2000 grid points and set $D_n = D_m = 0.1$. We begin by setting $\chi_1 = 5$, $A_2 = a_2 = \alpha = 1$, with initial conditions and other parameter values as for the simulations in Fig. 5.8. Since the hepatocyte-hepatocyte attraction is now strongest, we again observe the segregation of the two cell types within the aggregates, with hepatocytes in the centre and stellates at the edges, as for Model 1. The results are shown in Figs. 5.17 and 5.18.

If we now reverse the relative strengths of the two interactions, setting $A_2 = 5$, $\chi_1 = 1$, we then observe a uniform mix of the two cell types within aggregates, again as for Model 1 (see Fig. 5.19). An obvious difference here is that in this case there are a larger number of smaller aggregates.

Taking the same parameter values as above, we now seed the cells in a 2:1 hepatocyte:stellate ratio as in Fig. 5.12. The result is again the same as for Model 1, that the overall cell density within the aggregates is higher when the 1:1 seeding ratio is used, as opposed to the 2:1 ratio (the maximum densities reached in the two cases being 4.5 and 4.3 respectively - see Figs. 5.20 and

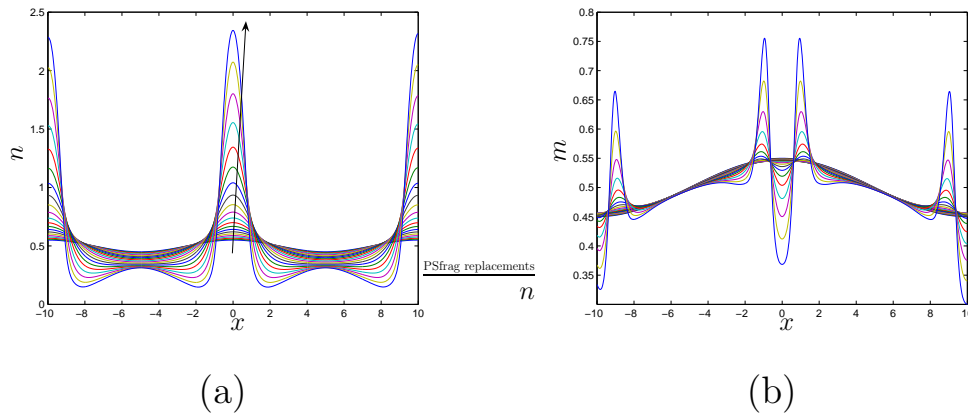


FIGURE 5.17: Numerical solution for cell densities: (a) n ; (b) m at intervals of 0.25 time units, between $t = 0$ and $t = 5$ (arrow indicates increasing time). Parameters: $D_n = D_m = 0.1$, $R = 100$, $r = 0.1$, $\gamma_1 = 1$, $A_2 = a_2 = 1$, $\chi_1 = 5$.

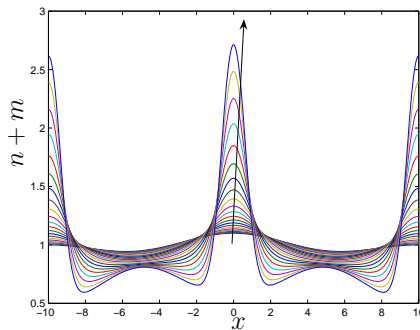


FIGURE 5.18: Numerical solution for total cell density $n + m$ at intervals of 0.25 time units, between $t = 0$ and $t = 5$ (arrow indicates increasing time). Parameter values as for Fig. 5.17.

5.22). In this model the maximum value of n reached is also greater for the 1:1 ratio (the values begin 2.3 and 2.2 for the 1:1 and 2:1 ratios respectively), despite the greater relative abundance of hepatocytes in the case of the 2:1 ratio, contrasting with the case for Model 1. However, for the stellates, the maximum of m is greatest in the 1:1 case, as we would expect from the relative abundances of the two cell types (see Fig. 5.23). As for Model 1, we believe that the 1:1 seeding ratio increases the rate of aggregation because it tends to

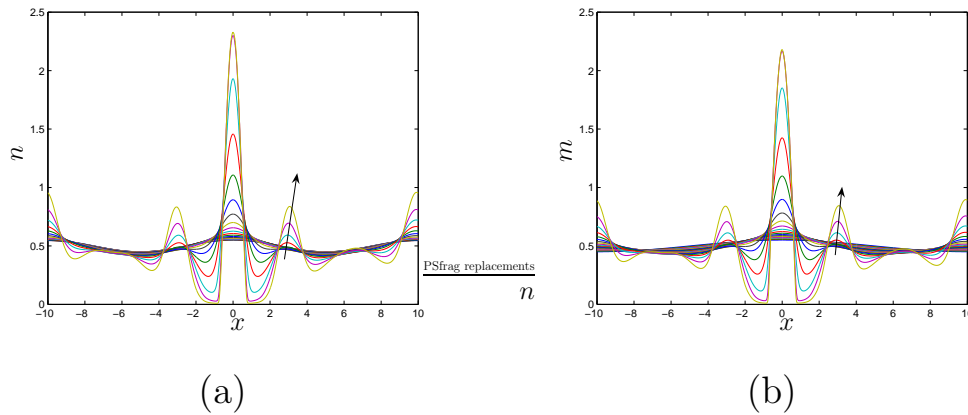


FIGURE 5.19: Numerical solution for cell densities: (a) n ; (b) m at intervals of 0.15 time units from $t = 0$ to $t = 3$ (arrow indicates increasing time). Parameter values: $A_2 = 5$, $\chi_1 = 1$ (other parameters as for Fig. 5.17).

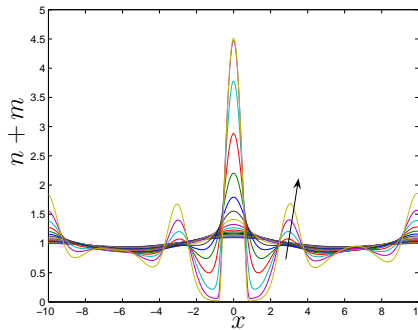


FIGURE 5.20: Numerical solution for total cell density $n + m$, at intervals of 0.15 time units from $t = 0$ to $t = 3$ (arrow indicates increasing time). Parameters as for Fig. 5.19.

maximise the degree of contact between the cell types which are most powerfully attracted to each other.

We now increase the range of attraction so that $a_2 = 2$. By comparison with Fig. 5.19, we see from Fig. 5.23 that this results in a smaller number of aggregates, in which the cell density is higher. As for Model 1, this is because the growing aggregates can now pull in more distant cells.

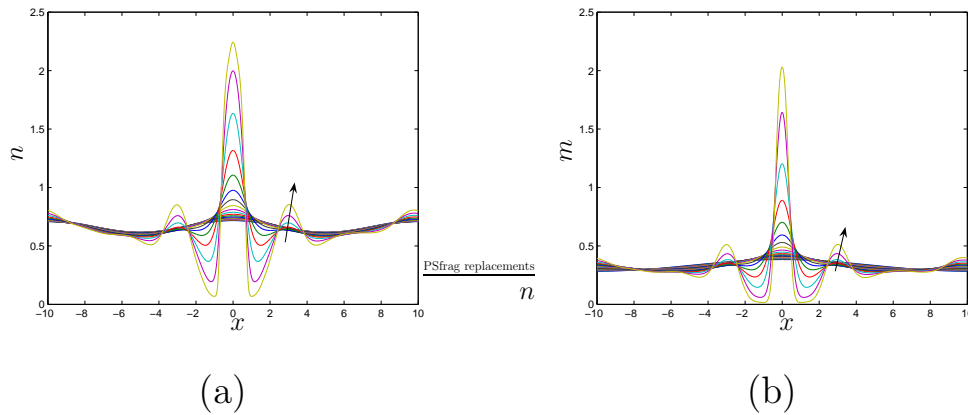


FIGURE 5.21: Numerical solution for cell densities: (a) n ; (b) m , at intervals of 0.15 time units from $t = 0$ to $t = 3$ (arrow indicates increasing time). Cell seeding ratio of 2:1; parameters as for Fig. 5.19.

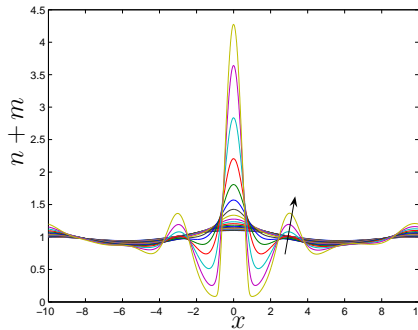


FIGURE 5.22: Numerical solution for total cell density $n + m$, at intervals of 0.15 time units from $t = 0$ to $t = 3$ (arrow indicates increasing time). Parameters as for Fig. 5.21.

By contrast, when we reduce the range of attraction so $a_2 = 0.5$, aggregation no longer takes place (results not shown). Quite simply, the range of the stellate cells' processes is too small to be able to counter the spreading effects of cell-cell repulsion and random movement.

In summary, our numerical results suggest that when the hepatocyte-stellate attraction is stronger than the hepatocyte-hepatocyte attraction (which, from experimental observations, we believe to be most likely - see §5.8), it may

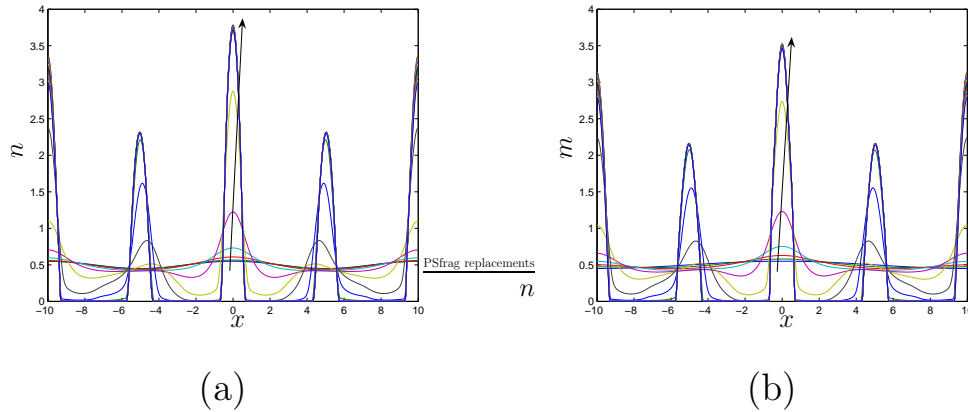


FIGURE 5.23: Numerical solution for cell densities: (a) n ; (b) m at intervals of 0.15 time units from $t = 0$ to $t = 3$ (arrow indicates increasing time). $a_2 = 2$, other parameters as for Fig. 5.19.

be advantageous to seed the two cell types in a 1:1 ratio to promote swift aggregation. This is true for both mechanisms hypothesised for the hepatocyte-stellate interaction - *i.e.* chemical (Model 1) or physical (Model 2). Of lesser significance (due to the fact that it cannot be modified experimentally) is the fact that a longer range of attraction gives rise to denser aggregates. Conversely, if attraction is too short ranged, aggregation may not take place.

5.8 Discussion

In this chapter, we have derived new non-local models for the interactions between hepatocytes and stellate cells, extending an earlier one-species model by Mogilner and Edelstein-Keshet [74]. Two hypotheses were investigated: in the first, stellates and hepatocytes were attracted to each other by chemical signals; in the second, the attraction was assumed to be due to the stellates putting out processes, which physically contacted the hepatocytes. In both hypotheses, hepatocytes were attracted to other hepatocytes by a chemical signal (as in Chapter 3), and the effects of space limitation were incorporated through the non-local repulsion terms.

Under both hypotheses, we found that the final distribution of the cells within the aggregates depended upon the relative strength of the attraction between hepatocytes and stellates. When this was weaker than the attraction hepatocytes have for each other, aggregates had a core consisting of hepatocytes, with stellates relegated to the edges of the cluster. Conversely, when the hepatocyte-stellate attraction was the strongest, the two cell types were evenly mixed within the aggregates. These results are in agreement with those of Painter and Sherratt [89], who studied the interactions of two cell populations using a Keller-Segel type model, where the diffusion and chemotaxis coefficients were functions of the cell densities (this allowed the effect of space limitation to be included by making the coefficients vanish at a critical cell density). A limitation of their model was that it only considered the situation in which one of the two cell populations produced a chemoattractant.

Our results also echo those of the Steinberg hypothesis (or differential adhesion hypothesis (DAH) - see Chapter 1), where the distribution of cells in aggregates depends upon the relative strengths of the adhesions formed between cells of each type [112]. Steinberg postulated the existence of a ‘free energy’ function; cells can reduce their free energy by the formation of adhesions, and the arrangement of the cells in an aggregate then corresponds to a minimum of the free energy of the system. His predictions have recently been validated experimentally, using detailed measurements of cadherin (a cell adhesion molecule) levels [34]. A continuum model of this phenomenon has recently been put forward by Armstrong *et al* [5]. They applied a non-local framework similar to that used in this chapter, with the non-local terms modelling adhesion forces. However, we also note that both our Model 1 and the model of Painter and Sherratt [89] display similar cell sorting, based on the cells having different affinities for chemoattractants, together with space limitation. This suggests that it may be of interest to explore (both experimen-

tally and through modelling) the relationship between the relative adhesion strengths and chemotactic affinities of two cell types, and their distribution within aggregates.

There was no obvious qualitative feature which differentiated the results of Model 1 from those of Model 2, since although Model 2 tended to produce smaller aggregates in our simulations, similar results could occur for Model 1 if we used different initial conditions or parameter values, so we are not able to suggest an experimental observation which would distinguish between the mechanisms of aggregation hypothesised here. However, the evidence of the time-lapse video does seem to suggest quite clearly that physical contact between the cells is an important factor, and our results agree with the assertion in Thomas *et al* [118] that aggregation need not involve cross talk between the two cell types (*i.e.* physical contact alone can account for aggregation). Chemical signalling of the type hypothesised in Model 1 cannot be ruled out though, and also provides a possible explanation. In practice, it is probable that both mechanisms contribute to the formation of aggregates.

One of the main aims in this chapter was to compare the predictions of our models with experimental results, particularly in relation to the distribution of hepatocytes and stellates within spheroids. This type of data has recently become available thanks to experiments carried out in the Tissue Engineering Group at the University of Nottingham. Figure 5.24 shows the location of the stellate cells (stained green) within five different aggregates. Comparison of these images with our theoretical results leads us to believe that the hepatocyte-stellate attraction is the strongest. The bottom left image is perhaps the most supportive of this conclusion, as we can see traces of the green stain in most areas of the spheroid, although perhaps most concentrated at the lower edge. In the upper three images, we see stellates located both at the centre and the edges of the aggregates, whilst the lower right image shows

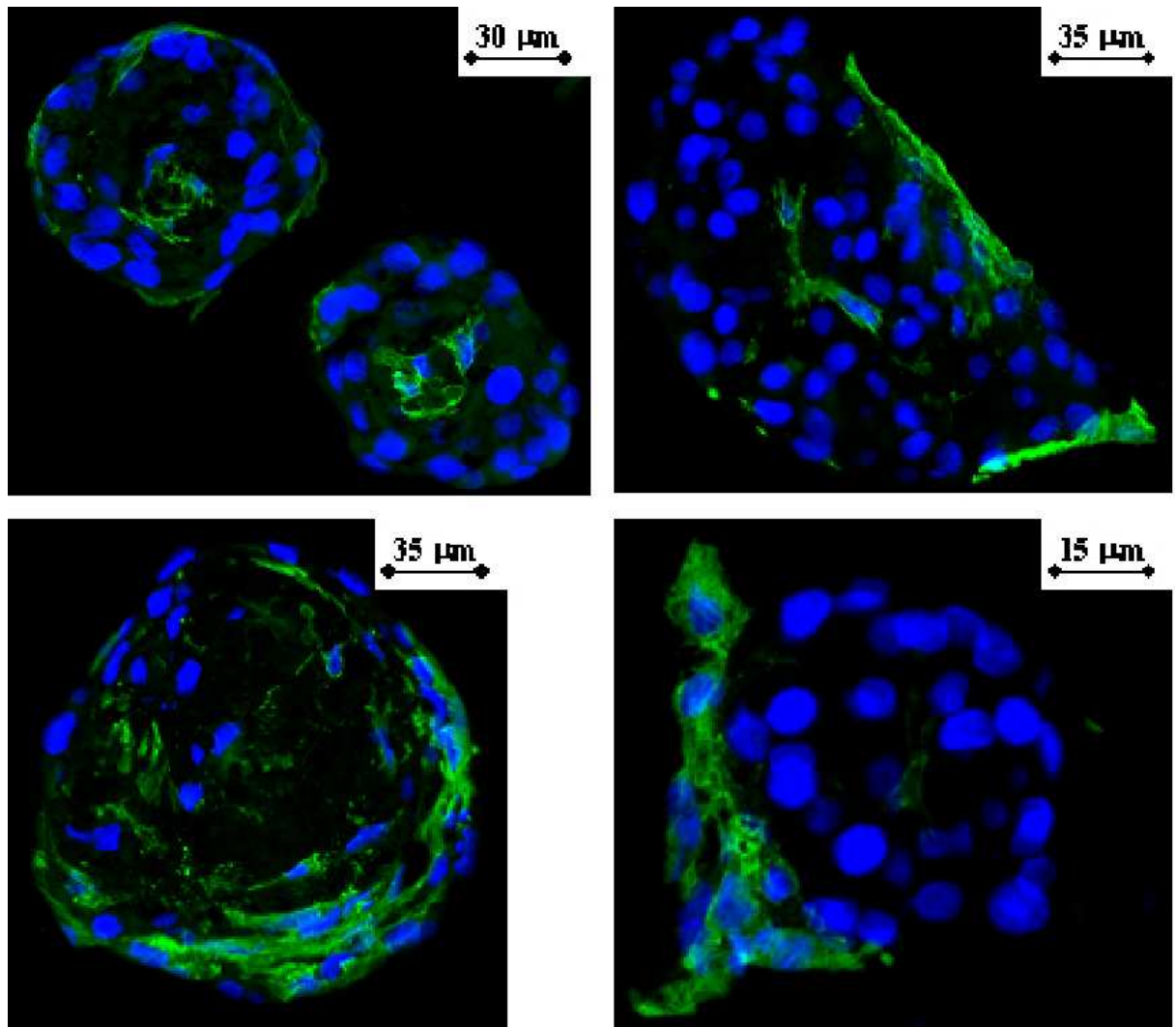


FIGURE 5.24: Sections through hepatocyte-stellate cell spheroids (from [118]). Stellate cells appear green.

stellates located just at the left-hand edge. Hence, although the experimental evidence does not entirely agree with either of the theoretical scenarios we have considered (*i.e.* either hepatocytes and stellates intermixing, or hepatocytes in the centre of aggregates and stellates on the edge), we believe it is most likely that hepatocyte-stellate interactions are the strongest, and that the discrepancies may be explained by the fact that our model is continuous, whilst the real cells are discrete, and so we could not expect a completely even intermixing of the two types. The fact that stellate cells are found both at the

centre *and* edges of aggregates [118] appears to rule out the possibility that the hepatocyte-hepatocyte interaction is strongest.

Intuitively, we would expect the hepatocyte-stellate interaction to be strongest, as there would otherwise be little reason to add the stellates (replacing them with more hepatocytes would have a greater effect). Our results suggest the optimal ratio of the seeding densities of the two cell types to promote swift aggregation is 1:1, since this maximises the amount of contact between the cells which attract each other most strongly. However, we remark that in the liver *in vivo* the ratio is approximately 20:1, and thus if considerations other than promoting swift aggregation are taken into account (*e.g.* optimising the functionality of the spheroids produced) there may be good reasons to opt for a higher ratio. At present, there is little experimental evidence on how the numbers of stellates within a spheroid affects its functionality or viability, although Riccalton-Banks has compared the functionality of hepatocyte-only and hepatocyte-stellate (2:1 ratio) spheroids [102]. She found that the co-cultured spheroids remained functional (in terms of albumin secretion and cytochrome P-450 enzyme activity) for nearly two months, compared to just over one month for the hepatocyte-only spheroids. This suggests that the presence of the stellate cells has, in fact, a positive impact on the functionality of the engineered tissue, and we thus recommend that the efficacy of culturing hepatocytes and stellates in a 1:1 ratio be tested experimentally.

The work presented here has been preliminary in nature and we have explored only a small region of each model's parameter space, corresponding to the types of behaviour we thought most applicable to the aggregation of hepatocytes and stellate cells. Further investigation of the behaviour of the model would be interesting mathematically, and might also yield further biological insights into the interactions of two cell populations. However, such work requires a more sophisticated numerical code - ideally one which is less computa-

tionally expensive, facilitating simulations to longer times whilst maintaining adequate resolution.

The results we have obtained here are only qualitative, and a great deal of further experimental data is required before the model predictions could be relied on quantitatively. In particular, the correct functional forms for the kernel functions describing the interactions between cells need to be determined. This could be done by measuring the forces acting between two cells, and utilising the connection between the individual cell- and continuum-level descriptions discussed in §5.2.1. Another interesting approach would be to compare the results of our continuum model with those of an individual-based model along the lines of that described in [74]. The latter might provide better agreement with the experimental results, as we suggested above.

The most obvious improvement to the model would be to extend it to more physically realistic two- and three-dimensional geometries and determine the types of patterns which may arise in such cases. We might incorporate the effects of cell adhesion to the ECM, as we have done in Chapters 2 and 3. More generally, for two species non-local models of the type introduced here, there is considerable scope for profitable future study, as interest in modelling the interactions between cell populations is increasing. Furthermore, in ecology, the interactions of two groups of different species (*e.g.* predators and prey) might be described using such a formulation. A more complete description of types of possible travelling wave solutions to the model might be of relevance in the latter context. Of more abstract mathematical interest, questions concerning the proof of existence and uniqueness of the solutions remain open.

Chapter 6

Discussion

The formation of clusters of liver cells takes place during the early stages of spheroid formation, which, in turn, appears key to the growth of viable, functional liver tissue in the laboratory. In this thesis, we have used mathematical modelling to gain insight into the factors which may prevent or hinder the aggregation process. This work provides a starting point for future experimental and theoretical studies, which may ultimately enable tissue engineers to optimise their culture technique.

In the first part of the thesis, we considered the aggregation of a single cell population, plated on a layer of viscoelastic ECM. We developed models in Chapters 2 and 3 based on the principles of the mechanochemical theory of Murray [76], although our models were formulated using a different mathematical framework. We adopted a two-phase, mixture theory approach, which coupled the motion of the cells with that of the surrounding culture medium, which was not included in previous models. Another significant difference was that we derived the velocities of the cells, culture medium and ECM from momentum balances, whereas in [76], only the ECM velocity is determined in this way, the cell velocity being prescribed in terms of the other dependent variables.

The two-phase approach has a number of advantages over the formulation presented in [76]. The first is that, since n represents the volume fraction of cells, rather than the number density, there is a constraint that $n \leq 1$, so the effect of space limitation is automatically included. This is not the case for *e.g.* the standard form of the Keller-Segel model (where the diffusion and chemotaxis coefficients are constants), in which the cell density n can become very large. The second is that the mixture theory framework can accommodate an arbitrary number of phases in a consistent manner (see *e.g.* [59]). This is likely to become of greater significance in the future, as interest in understanding the interactions between different cell populations, and between cells and other materials (such as artificial scaffolds) increases. However, there are also a number of disadvantages to using this framework. The most obvious is that, by including a momentum balance on the cells, we increase the size of the system of model equations by at least one, compared to Murray's formulation. There is also the need to introduce constitutive relations, both for the stress tensors for each phase, and the interaction forces between them. The choices made for these constitutive relations are essentially arbitrary, in that they are not derived in a rational manner from 'microscopic' equations (as is the case in homogenisation theory - see Chapter 1). A strong justification for a particular choice of constitutive law can hence only be made by comparing the model predictions with quantitative experimental data. However, we remark that the models of Murray and co-workers [76] also introduce a number of constitutive laws (for stress tensors, ECM 'tethering' force, and the cell flux) and so this feature is not unique to our modelling approach, though our exposition perhaps gives greater prominence to the number of such assumptions made.

The model developed in Chapter 2 assumed a one-dimensional geometry, and prescribed the extra pressure generated by the cells in response to their

surroundings as a function of the cell volume fraction n (*i.e.* $\Sigma_n = \Sigma_n(n)$). As a result of the simplified geometry adopted, cell-ECM drag was included as a body force acting on the cells, when, physically, it should be included as a boundary condition at the interface between the ECM and the cell / culture medium mixture. Using linear stability analysis, we determined that, for our choice of function for Σ_n , aggregates would form when the cell seeding density was less than a critical value ($n_0 < n_c$). Numerical simulations showed the aggregates to have sharply defined boundaries and a constant cell density in the interior, which is qualitatively consistent with experimental observations. Reducing the cell seeding density appeared to reduce the size (but not the number) of aggregates, again in line with experimental observations [122]. Increasing cell-ECM or cell-culture medium drag resulted in the formation of smaller aggregates, but the properties of the ECM (viscosity and Young's modulus) had negligible effect.

In Chapter 3, the model developed in Chapter 2 was extended to a more realistic 2D geometry (representing a vertical section through the culture well), and chemotaxis was included by making Σ_n dependent on the concentration c of a chemical secreted by the cells. An interesting feature of the model is the fact that the diffusion and chemotaxis coefficients (which are usually assumed to be independent constants in the Keller-Segel model) are then related to Σ_n . We identified two scaling regimes (which we termed 'extensional' and 'lubrication') in which we could exploit the thin geometry of the problem to reduce the model equations to one-dimensional form at leading order. The two reduced models were then investigated, using a combination of linear stability analysis and numerical simulations, in Chapter 4. We showed that aggregation will occur in both models, provided the cell seeding density lies between upper and lower bounds. The cell seeding density appeared to have a much greater effect in these models compared to Chapter 2, since it affected the number and size of aggregates formed, and also their rate of growth. In the extensional regime,

the degree of cell-ECM adhesion had little effect on the aggregation process; this appears to be because, in this regime, aggregation occurs mainly by the expulsion of culture medium from between the cells, without significant cell migration. However, in the lubrication regime, increased cell-ECM adhesion did slow the formation of aggregates.

As in Chapter 2, the viscosity and Young's modulus of the ECM had little noticeable effect on aggregation in the lubrication regime. This is probably because we assumed there was no inter-relationship between the cell-generated stresses (represented by Σ_n), the degree of cell-ECM adhesion and the mechanical properties of the substrate. However, recent studies *e.g.* [23] have shown that cells can respond to the stiffness of the substrate to which they are adhered in various ways. Lo *et al* [61] reported a number of effects on the migration of 3T3 fibroblast cells. At low seeding densities, cells migrate preferentially towards stiff substrates, a behaviour they term 'durotaxis'. Cells generate stronger traction forces on stiff, compared to soft substrates, and there are also differences in cell speed. Finally, movement of the cells can be directed by stretching the substrate; pushing the substrate towards the leading edge of a migrating cell causes it to retract, and the cell reverses its direction of migration; when the substrate is pulled away from the trailing edge of the cell, a similar reversal occurs. This latter fact suggests that Σ_n should include dependence on the displacement of the ECM. However, to our knowledge, mathematical models of these substrate-related phenomena have not yet been formulated.

The overall results from our modelling in Chapters 2-4 thus suggest that the two most important factors influencing aggregation are the cell seeding density and the degree of cell-ECM adhesion. The models do not agree on the effect of changing these factors, which provides a means for assessing which of them is most appropriate, by comparing their predictions with experimen-

tal results. Unfortunately, the current lack of quantitative experimental data means that at present it is not entirely clear which scenario is most realistic. However, given that the models we have developed in Chapters 2-4 make unrealistic assumptions concerning the geometry of the culture well, it is probable that they will need to be extended to more biologically relevant geometries - *e.g.* 2D (representing a plan view of the culture well) or 3D - before such validation could be undertaken. It is hence probably most sensible to view them as providing a starting point for future modelling work.

In Chapter 5, we turned to the problem of modelling the interactions of hepatocytes and stellate cells in co-culture. We considered two hypotheses: firstly, that chemical signalling takes place between two cell populations, leading to an improved rate of aggregation due to an enhanced chemotactic effect; secondly, that the hepatocytes and stellates interact through direct physical contact, the stellates putting out long, tentacle-like cellular processes, which pull hepatocytes into the growing aggregates. In this case, we adopted a modelling framework based on a one-population non-local model by Mogilner and Edelstein-Keshet [73], which we extended to the case of two interacting populations. Chemotaxis was also included (using the standard Keller-Segel type formulation) but the ECM and culture medium were neglected, so as to focus on cell-cell interactions. Under each hypothesis, we determined how the relative strengths of hepatocyte-hepatocyte and hepatocyte-stellate interactions affected the distribution of the two cell types within the aggregates. In both cases, we found that when the hepatocyte-stellate interaction was the stronger, the two cell types were evenly distributed within the aggregates; when the hepatocyte-hepatocyte interaction was the stronger, the hepatocytes formed a ‘core’, with the stellates relegated to the edges. Our model predictions were then compared with images of sections through spheroids produced experimentally, which suggested that the hepatocyte-stellate interaction was the stronger in practice. Given this information, we then looked at the effect

of changing the seeding ratios of the two cell types on the rate of aggregation. Our results suggested a 1:1 ratio of hepatocytes to stellates ought to be best for promoting swift aggregate formation, as it tends to maximise the degree of contact between cells which attract each other most strongly. Our prediction is in line with the experimental results of Riccalton-Banks, who reported that a 2:1 ratio of hepatocytes to stellates led to swifter spheroid formation than ratios of 5:1, 10:1 and 20:1 [102].

Once again, the main limitation of our model is the assumption of an unrealistic geometry. In order to validate the predictions quantitatively against experiment, we believe it would be necessary to consider at least a two-dimensional geometry, representing a plan view of the culture well, such as was considered in [5]. A weakness of the work presented in Chapter 5 is the use of an unsophisticated numerical method for producing simulations. Although our results were sufficient to determine the distribution of cells within aggregates as they developed, which was the main aim of the study, it was not been possible to run simulations for long times, as it would be very computationally expensive to obtain reasonable resolution. In their study of a similar non-local model, Armstrong *et al* [5] used a finite volume method which was capable of running to much longer times. They found that aggregates begin to merge at long times.

Our results concerning the distribution of the two cell types within the aggregates echo those of the Steinberg hypothesis (see Chapter 1), which predicts the cell distribution based on the relative strengths of the adhesions between cells of different types. Indeed, a continuum model based on the Steinberg hypothesis has recently been put forward, in which the cell adhesion forces are modelled using a non-local framework similar to the one we presented in Chapter 5 [5]. However, our model has shown that the same cell distributions may arise as a result of the two cell types having different affinities for

chemoattractants, together with space limitation. The effect was also found by Painter and Sherratt [89], who employed a slightly different model in which space limitation is included by having the diffusion and chemotaxis coefficients vanish when the cell densities reach a sufficiently high value. This suggests an interesting question: Can cell adhesion forces and chemotaxis interact to produce cell distribution patterns in tissues which could not be predicted by either mechanism alone? We could investigate this possibility theoretically by combining the two models we developed in Chapter 5, and extending them to a more biologically relevant 2- or 3D geometry.

The models we have presented here have all been macroscopic, continuum models, which by their nature omit the detail of processes taking place at individual-cell or subcellular scales. As both computing power and our knowledge of the pathways by which individual cells sense and respond to external cues (such as chemical gradients, or substrate displacements) increase, it may become feasible to undertake very detailed multi-scale computations, including both cell and subcellular scale processes. This type of modelling approach is currently still in its infancy, but an example is provided by a recent model of vascular tumour growth [3] in which PDEs for nutrient (oxygen) and angiogenic factor (VEGF) distributions are coupled to a cellular automaton model for the cell distribution (cells may proliferate, filling empty space, or die creating a void) which is in turn coupled to ODE models for sub-cellular processes (the cell cycle). In the context of cell movement by chemotaxis, it may be possible to extend recent agent-based models of cell proliferation and movement in a monolayer [130] to include the distribution of chemoattractant, and the sub-cellular processes by which chemical gradients are sensed and acted upon. Whilst such models would make the fullest possible use of experimental data and offer the potential to recreate biological systems in great detail, they represent a huge increase in complexity compared to the continuum models considered here, and will be extremely difficult to analyse.

Appendix A

Diffusion in a multiphase mixture

In this appendix, we present a derivation of the volume-averaged equations describing the diffusion of a passive solute through a multi-phase material, using the indicator function approach adopted by Drew (amongst others) [26].

A.1 Basic notions

We assume there are N different phases, or components of the mixture under consideration, and introduce an indicator function for each phase, defined as

$$I_{\beta}(\mathbf{x}, t) = \begin{cases} 1 & \text{if } \mathbf{x} \text{ is in phase } \beta \text{ at time } t \\ 0 & \text{otherwise,} \end{cases} \quad (\text{A.1.1})$$

where $\beta = 1 \dots N$.

We then associate with every point in space an averaging volume, V_A . This averaging volume must be both large enough to give rise to well-behaved averages, and small enough to accurately represent the variations in the quantities of interest. It has been shown that the averaging procedure yields meaningful results provided that the characteristic lengths: d (distance over which

variations in exact quantities occur), l (characteristic length for the averaging procedure), L (characteristic length for the process) obey $d \ll l \ll L$ [135]. The volume average of the exact microscopic field $f(\mathbf{x}, t)$ is hence defined as

$$\langle f \rangle(\mathbf{x}, t) = \frac{1}{V_A} \int_{V_A} f dV. \quad (\text{A.1.2})$$

We now define the volume fraction ϕ_β of phase β to be

$$\phi_\beta(\mathbf{x}, t) = \langle I_\beta \rangle. \quad (\text{A.1.3})$$

Using the above, we define the ‘phase-weighted’ or ‘phasic average’ [26] of an exact field f in phase β (denoted by \bar{f}_β) to be

$$\bar{f}_\beta = \frac{\langle I_\beta f \rangle}{\phi_\beta}, \quad (\text{A.1.4})$$

so that $\langle f \rangle = \sum_\beta \phi_\beta \bar{f}_\beta$.

A.2 Reaction-diffusion equation for a solute in an mixture

We assume that the exact concentration of the solute is $C(\mathbf{x}, t)$. It diffuses with constant diffusivity, $D = I_\beta D_\beta$ and decays at the constant rate, $\alpha = I_\beta \alpha_\beta$ in each phase of the material. The exact governing equation is hence

$$\frac{\partial C}{\partial t} + \nabla \cdot (\mathbf{u}C) = \nabla \cdot (D\nabla C) - \alpha C. \quad (\text{A.2.1})$$

Multiplying this equation by the indicator function I_β , we obtain

$$\begin{aligned} \frac{\partial}{\partial t}(I_\beta C) - C \frac{\partial I_\beta}{\partial t} + \nabla \cdot (I_\beta \mathbf{u}C) - \mathbf{u}C \nabla I_\beta \\ = \nabla \cdot (I_\beta D_\beta \nabla C) - D_\beta \nabla C \cdot \nabla I_\beta - I_\beta \alpha_\beta C, \end{aligned} \quad (\text{A.2.2})$$

where we have used the fact that $I_\beta^2 = I_\beta$.

From the definition of I_β , we observe that ∇I_β acts rather like a Dirac δ -function, picking out the interfaces between phases. It can be shown [26] that

$$\frac{\partial I_\beta}{\partial t} + \mathbf{u}_i \cdot \nabla I_\beta = 0 \quad (\text{A.2.3})$$

where \mathbf{u}_i is the velocity of the interface. We note that when there is no interchange of mass between phases, as is the case for the models of Chapters 2-4, then the second and fourth terms of the LHS of equation (A.2.2) cancel. Upon making this assumption and integrating equation (A.2.2) over the averaging volume, we then obtain

$$\begin{aligned} \frac{\partial}{\partial t} \langle I_\beta C \rangle + \nabla \cdot \langle I_\beta \mathbf{u} C \rangle \\ = \nabla \cdot \langle I_\beta D_\beta \nabla C \rangle - \langle D_\beta \nabla C \cdot \nabla I_\beta \rangle - \langle \alpha_\beta I_\beta C \rangle. \end{aligned} \quad (\text{A.2.4})$$

Noting that the quantities D_β and α_β are constants in each phase and using the definition (A.1.4) yields

$$\begin{aligned} \frac{\partial}{\partial t} (\phi_\beta \bar{C}_\beta) + \nabla \cdot \langle I_\beta \mathbf{u} C \rangle \\ = D_\beta \nabla \cdot (\phi_\beta \nabla \bar{C}_\beta) - \langle D_\beta \nabla C \cdot \nabla I_\beta \rangle - \alpha_\beta \phi_\beta \bar{C}_\beta. \end{aligned} \quad (\text{A.2.5})$$

where the first term on the RHS derives from $D_\beta \nabla \cdot \langle I_\beta \nabla C \rangle$. The term which follows it may be interpreted as an interfacial diffusive flux, whilst the second term on the LHS of equation (A.2.5) is the averaged convective flux. The form of the latter two terms is not immediately obvious from the definitions of averaged quantities given earlier, and we hence require constitutive laws for them in terms of the quantities \bar{C}_β and $\bar{\mathbf{u}}_\beta$.

In Chapter 3, we propose a very simple form for the advective flux, taking it to be given by $\phi_\beta \mathbf{u}_\beta \bar{C}_\beta$, in common with the form chosen by Roose *et*

al [105], Cogan and Keener [21] and Byrne and Owen [16] (although we subsequently discard the terms on the LHS of equation (A.2.5)). Our form of the diffusion term in equation (A.2.5) also agrees with that of [21], but differs from those used in [16, 105]; we believe these differences may be ascribed to differences of interpretation, as to which terms represent diffusive fluxes, and which interfacial or advective fluxes.

Appendix B

ECM equations in the extensional regime

In this appendix, we present the solution of the ECM equations in the extensional regime described in Chapter 3. In fact, in this regime it turns out that there is no $O(1)$ deformation of the ECM, and for $\hat{k}_2 \sim O(1)$, $u_{n0} \equiv 0$. This is not obvious from the form of the governing equations, and so we give the calculation here.

B.1 ECM equations

We seek solutions of the governing equations (3.3.4), (3.3.48) and (3.3.49) in the form of regular power series expansions in the small parameter η^2 , so that

$$U = U_0 + \eta^2 U_1 + \dots \quad V = V_0 + \eta^2 V_1 + \dots \quad P = P_0 + \eta^2 P_1 + \dots$$

Now, assuming that $\hat{\mu}_n \sim O(1)$, at leading order equation (3.3.48) gives

$$\frac{\partial^2}{\partial y^2} \left(\frac{\partial U_0}{\partial t} \right) + \hat{E} \frac{\partial^2 U_0}{\partial y^2} = 0, \quad (\text{B.1.1})$$

We seek a solution of equation (B.1.1) of the form

$$U_0(x, y, t) = r(x, t) + ys(x, t). \quad (\text{B.1.2})$$

From (3.3.8) we see that $U_0 = 0$ on $y = 0$ so that $r(x, t) \equiv 0$. Since equation (3.3.51) gives $U_0(0, y, t) = U_0(1/\epsilon, y, t) = 0$, s obeys the following boundary conditions

$$s(0, t) = s\left(\frac{1}{\epsilon}, t\right) = 0. \quad (\text{B.1.3})$$

By conservation of mass (3.3.4), we observe that

$$\frac{\partial V_0}{\partial y} = -y \frac{\partial s}{\partial x}. \quad (\text{B.1.4})$$

Integrating, and imposing $V_0 = 0$ on $y = 0$, (equation (3.3.8)) we determine that

$$V_0 = \frac{-y^2}{2} \frac{\partial s}{\partial x}. \quad (\text{B.1.5})$$

At $O(1)$, equation (3.3.49) gives

$$-\hat{\mu}_n \frac{\partial P_0}{\partial y} + \frac{\partial^2}{\partial y^2} \left(\frac{\partial V_0}{\partial t} + \hat{E} V_0 \right) = 0. \quad (\text{B.1.6})$$

Substituting for U_0 and V_0 in terms of s , we obtain

$$\frac{\partial P_0}{\partial y} = -\frac{1}{\hat{\mu}_n} \frac{\partial}{\partial x} \left(\frac{\partial s}{\partial t} + \hat{E} s \right). \quad (\text{B.1.7})$$

Integration thus gives

$$P_0 = F(x, t) - \frac{y}{\hat{\mu}_n} \frac{\partial}{\partial x} \left(\frac{\partial s}{\partial t} + \hat{E} s \right), \quad (\text{B.1.8})$$

where $F(x, t)$ will be determined below by imposing the normal stress boundary condition at $y = g_0$ (see equation (B.1.13)).

Taking $\hat{k}_2 \sim O(1)$ for the moment, the tangential stress boundary conditions (3.3.55) and (3.3.70) now give

$$\left(\frac{\partial s}{\partial t} + \hat{E} s \right) = n_0 \frac{\partial u_{n0}}{\partial y} = \hat{\mu}_n \hat{k}_2 n_0 \left(u_{n0} - g_0 \frac{\partial s}{\partial t} \right) \quad \text{on } y = g_0. \quad (\text{B.1.9})$$

Since (in §3.5) we have applied (3.5.10) on $y = h_0$, and thereby established that u_{n0} is independent of y in this regime, we see from the first part of equation (B.1.9) that

$$\frac{\partial s}{\partial t} + \hat{E} s = 0, \quad (\text{B.1.10})$$

(the above clearly also applies when $\hat{k}_2 \sim O(\eta^2)$). On integrating, and applying the initial condition, we thus obtain the trivial solution $s \equiv 0$. Hence $U_0 = V_0 = 0$, and on integrating (3.3.13) and applying (3.3.58) we further obtain $g_0 \equiv 1$.

The second part of equation (B.1.9) implies that

$$u_{n0} = g_0 \frac{\partial s}{\partial t}, \quad (\text{B.1.11})$$

and therefore $u_{n0} \equiv 0$. (Note that u_{n0} would be undetermined for $\hat{k}_2 \sim O(\eta^2)$ - hence the need to consider higher-order terms to determine u_{n0} in §3.5.)

It only remains to determine the pressure P_0 , for which we require the normal stress boundary condition (3.3.54), which at leading order gives

$$\begin{aligned} -\hat{\mu}_n P_0 + 2 \frac{\partial}{\partial y} \left(\frac{\partial V_0}{\partial t} + \hat{E} V_0 \right) - \frac{\partial}{\partial y} \left(\frac{\partial U_0}{\partial t} + \hat{E} U_0 \right) \frac{\partial g_0}{\partial x} \\ = \hat{\mu}_n \left(-p_{T0} + 2n_0 \frac{\partial v_{n0}}{\partial y} - n_0 \frac{\partial g_0}{\partial x} \frac{\partial u_{n0}}{\partial y} \right) \quad \text{on } y = g_0. \end{aligned} \quad (\text{B.1.12})$$

Substituting for U_0 , V_0 and g_0 from above, and using (3.5.14) and (3.5.23) we find

$$F(x, t) = - \left(C\Upsilon(n_0) \frac{\partial^2 h_0}{\partial x^2} \right). \quad (\text{B.1.13})$$

However, as we have seen, this pressure is not sufficient to generate an $O(1)$ displacement of the ECM, and so at leading order the ECM can be taken as rigid in this regime.

Appendix C

Numerical schemes for the thin-film models

In this Appendix, we give details of the numerical schemes used to produce the simulations of the thin film models, which are presented in Chapter 4. Throughout, we use the notation

$$f(j\Delta x, i\Delta t) = f_j^i,$$

where Δx is the spatial step size and Δt is the timestep.

C.1 Extensional regime

The governing equations are discretised as follows. Equation (4.2.1):

$$\begin{aligned} \frac{n_j^{i+1} - n_j^i}{\Delta t} + \frac{u_{nj}^i}{\Delta x} \begin{cases} (n_{j+1}^{i+1} - n_j^{i+1}) & \text{if } u_{nj}^i < 0, \\ (n_j^{i+1} - n_{j-1}^{i+1}) & \text{if } u_{nj}^i \geq 0, \end{cases} \\ - \frac{\hat{\Gamma}_1 n_j^i}{(\Delta x)^2 \hat{k}_1 (h_j^i - 1)} \left[\mathcal{Q}_{j+\frac{1}{2}}^i (\Sigma_{nj+1}^i n_{j+1}^{i+1} - \Sigma_{nj}^i n_j^{i+1}) - \mathcal{Q}_{j-\frac{1}{2}}^i (\Sigma_{nj}^i n_j^{i+1} - \Sigma_{nj-1}^i n_{j-1}^{i+1}) \right] = 0, \end{aligned} \tag{C.1.1}$$

where

$$\mathcal{Q}_j^i = \frac{(h_j^i - 1)(1 - n_j^i)}{n_j^i}, \quad \text{and} \quad \mathcal{Q}_{j+\frac{1}{2}}^i = \frac{\mathcal{Q}_{j+1}^i + \mathcal{Q}_j^i}{2}. \quad (\text{C.1.2})$$

Equation (4.2.2):

$$\begin{aligned} & \frac{4}{(\Delta x)^2} \left[\mathcal{R}_{j+\frac{1}{2}}^i (u_{nj+1}^{i+1} - u_{nj}^{i+1}) - \mathcal{R}_{j-\frac{1}{2}}^i (u_{nj}^{i+1} - u_{nj-1}^{i+1}) \right] \\ & + \frac{2\hat{\Gamma}_1}{\hat{k}_1(\Delta x)^2} \left[n_{j+\frac{1}{2}}^i (\mathcal{S}_{j+1}^i - \mathcal{S}_j^i) - n_{j-\frac{1}{2}}^i (\mathcal{S}_j^i - \mathcal{S}_{j-1}^i) \right] \\ & = \hat{k}_2 n_j^i u_{nj}^{i+1} - C \frac{(h_j^i - 1)}{2\Delta x} [\Upsilon_{j+1}^i \mathcal{H}_{j+1}^i - \Upsilon_{j-1}^i \mathcal{H}_{j-1}^i], \end{aligned} \quad (\text{C.1.3})$$

where

$$\mathcal{R}_j^i = (h_j^i - 1)n_j^i, \quad \mathcal{H}_j^i = \frac{h_{j+1}^i - 2h_j^i + h_{j-1}^i}{(\Delta x)^2}, \quad (\text{C.1.4})$$

$$\mathcal{S}_j^i = \frac{(h_j^i - 1)(1 - n_j^i)}{2n_j^i(\Delta x)} (n_{j+1}^i \Sigma_{nj+1}^i - n_{j-1}^i \Sigma_{nj-1}^i). \quad (\text{C.1.5})$$

Equation (4.2.3):

$$\begin{aligned} & \frac{h_j^{i+1} - h_j^i}{\Delta t} + \frac{1}{\Delta x} \begin{cases} (u_{hj+1}^i h_{j+1}^{i+1} - u_{hj}^i h_j^{i+1}) \text{ if } u_{hj}^i < 0, \\ (u_{hj}^i h_j^{i+1} - u_{hj-1}^i h_{j-1}^{i+1}) \text{ if } u_{hj}^i \geq 0, \end{cases} \\ & = \frac{u_{hj+1}^i - u_{hj-1}^i}{2\Delta x} + D \frac{(h_{j+1}^{i+1} - 2h_j^{i+1} + h_{j-1}^{i+1})}{(\Delta x)^2}, \end{aligned} \quad (\text{C.1.6})$$

where:

$$u_{hj}^i = u_{nj}^i + \frac{\hat{\Gamma}_1(1 - n_j^i)}{2(\Delta x)\hat{k}_1 n_j^i} (n_{j+1}^i \Sigma_{nj+1}^i - n_{j-1}^i \Sigma_{nj-1}^i) \quad (\text{C.1.7})$$

and D is the small diffusion coefficient (see Chapter 4 for details).

Equation (4.2.4):

$$\begin{aligned} & \frac{1}{(\Delta x)^2 (h_j^i - 1)} \left[\mathcal{T}_{j+\frac{1}{2}}^i (c_{j+1}^{i+1} - c_j^{i+1}) - \mathcal{T}_{j-\frac{1}{2}}^i (c_j^{i+1} - c_{j-1}^{i+1}) \right] \\ & - \alpha(1 - n_j^i) c_j^{i+1} + n_j^i (1 - n_j^i) = 0, \end{aligned} \quad (\text{C.1.8})$$

where $\mathcal{T}_j^i = (h_j^i - 1)(1 - n_j^i)$.

C.2 Lubrication regime

In this regime, the governing equations are discretised in the following way.

Equation (4.2.19)

$$\frac{\phi_j^{i+1} - \phi_j^i}{\Delta t} + \hat{E}\phi_j^{i+1} = \frac{\hat{\mu}_n C h_j^i}{2\Delta x} [\Upsilon_{j+1}^i \mathcal{H}_{j+1}^i - \Upsilon_{j-1}^i \mathcal{H}_{j-1}^i]. \quad (\text{C.2.1})$$

where \mathcal{H}_j^i is given in equation (C.1.4).

Equation (4.2.20):

$$\frac{\psi_j^{i+1} - \psi_j^i}{\Delta t} + \hat{E}\psi_j^{i+1} = -\frac{\hat{\mu}_n C}{4\Delta x} [\Upsilon_{j+1}^i \mathcal{H}_{j+1}^i - \Upsilon_{j-1}^i \mathcal{H}_{j-1}^i]. \quad (\text{C.2.2})$$

Equation (4.2.21):

$$\begin{aligned} & \frac{n_j^{i+1} - n_j^i}{\Delta t} + \frac{\bar{u}_{nj}^i}{\Delta x} \begin{cases} (n_{j+1}^{i+1} - n_j^{i+1}) & \text{if } \bar{u}_{nj}^i < 0, \\ (n_j^{i+1} - n_{j-1}^{i+1}) & \text{if } \bar{u}_{nj}^i \geq 0, \end{cases} \\ & - \frac{\hat{\Gamma}_1 n_j^i}{(\Delta x)^2 \hat{k}_1 (h_j^i - g_j^i)} \left[\mathcal{A}_{j+\frac{1}{2}}^i (\Sigma_{nj+1}^i n_{j+1}^{i+1} - \Sigma_{nj}^i n_j^{i+1}) - \mathcal{A}_{j-\frac{1}{2}}^i (\Sigma_{nj}^i n_j^{i+1} - \Sigma_{nj-1}^i n_{j-1}^{i+1}) \right] \\ & = \frac{C n_j^i}{(\Delta x)^2 \hat{k}_1 (h_j^i - g_j^i)} \left[\mathcal{A}_{j+\frac{1}{2}}^i (\Upsilon_{j+1}^i \mathcal{H}_{j+1}^i - \Upsilon_j^i \mathcal{H}_j^i) - \mathcal{A}_{j-\frac{1}{2}}^i (\Upsilon_j^i \mathcal{H}_j^i - \Upsilon_{j-1}^i \mathcal{H}_{j-1}^i) \right], \end{aligned} \quad (\text{C.2.3})$$

where:

$$\mathcal{A}_j^i = \frac{(h_j^i - g_j^i)(1 - n_j^i)}{n_j^i}. \quad (\text{C.2.4})$$

Equation (4.2.22):

$$\begin{aligned} & \frac{g_j^{i+1} - g_j^i}{\Delta t} + \frac{1}{\Delta x} \begin{cases} (u_{gj+1}^i g_{j+1}^{i+1} - u_{gj}^i g_j^{i+1}) & \text{if } u_{gj}^i < 0, \\ (u_{gj}^i g_j^{i+1} - u_{gj-1}^i g_{j-1}^{i+1}) & \text{if } u_{gj}^i \geq 0, \end{cases} \\ & = D \frac{(g_{j+1}^{i+1} - 2g_j^{i+1} + g_{j-1}^{i+1})}{(\Delta x)^2}, \end{aligned} \quad (\text{C.2.5})$$

where we have eliminated time derivatives of ϕ and ψ using equations (4.2.19)

and (4.2.20) to obtain:

$$\begin{aligned} u_{gj}^i &= -\frac{\hat{E} g_j^i \phi_j^i}{2} - \frac{\hat{E} g_j^{i2} \psi_j^i}{3} \\ & \quad + \left(\frac{h_j^i g_j^i}{2} - \frac{g_j^{i2}}{6} \right) \frac{\hat{\mu}_n C}{2\Delta x} [\Upsilon_{j+1}^i \mathcal{H}_{j+1}^i - \Upsilon_{j-1}^i \mathcal{H}_{j-1}^i], \end{aligned} \quad (\text{C.2.6})$$

and D is, once again, the small diffusion coefficient.

Equation (4.2.23):

$$\begin{aligned} & \frac{h_j^{i+1} - h_j^i}{\Delta t} + \frac{1}{\Delta x} \begin{cases} (\mathcal{U}_{j+1}^i h_{j+1}^{i+1} - \mathcal{U}_j^i h_j^{i+1}) \text{ if } \mathcal{U}_j^i < 0, \\ (\mathcal{U}_j^i h_j^{i+1} - \mathcal{U}_{j-1}^i h_{j-1}^{i+1}) \text{ if } \mathcal{U}_j^i \geq 0, \end{cases} \\ & + \frac{1}{(\Delta x)^4} \left[\mathcal{B}_{j+\frac{1}{2}}^i (\Upsilon_{j+1}^i [h_{j+2}^{i+1} - 2h_{j+1}^{i+1} + h_j^{i+1}] - \Upsilon_j^i [h_{j+1}^{i+1} - 2h_j^{i+1} + h_{j-1}^{i+1}]) \right. \\ & \quad \left. - \mathcal{B}_{j-\frac{1}{2}}^i (\Upsilon_j^i [h_{j+1}^{i+1} - 2h_j^{i+1} + h_j^{i-1}] - \Upsilon_{j-1}^i [h_j^{i+1} - 2h_{j-1}^{i+1} + h_{j-2}^{i+1}]) \right] \\ & = \frac{\mathcal{G}_{j+1}^i - \mathcal{G}_{j-1}^i}{2\Delta x}, \quad (\text{C.2.7}) \end{aligned}$$

where we have used equations (4.2.19), (4.2.20), (4.2.22) and (4.2.24) to ensure all the fourth-order surface tension terms appear explicitly above. The quantities \mathcal{B}_j^i , \mathcal{U}_j^i and \mathcal{G}_j^i are given by:

$$\begin{aligned} \mathcal{B}_j^i &= \frac{C(h_j^i - g_j^i)(1 - n_j^i)}{\hat{k}_1 n_j^i} + \frac{C(h_j^i - g_j^i)^2}{n_j^i} \left(\frac{1}{\hat{k}_2} + \frac{(h_j^i - g_j^i)}{3} \right) \\ & \quad + \hat{\mu}_n C(h_j^i - g_j^i) \left(h_j^i g_j^i - \frac{g_j^{i2}}{2} \right) + \frac{1}{2} \hat{\mu}_n C h_j^i g_j^{i2} - \frac{1}{6} \hat{\mu}_n C g_j^{i3}, \quad (\text{C.2.8}) \end{aligned}$$

$$\mathcal{U}_j^i = -\hat{E} g_j^i \phi_j^i - \hat{E} g_j^{i2} \psi_j^i + \frac{\hat{\Gamma}_1(1 - n_j^i)}{2(\Delta x) \hat{k}_1 n_j^i} [n_{j+1}^i \Sigma_{n_{j+1}}^i - n_{j-1}^i \Sigma_{n_{j-1}}^i] \quad (\text{C.2.9})$$

$$\mathcal{G}_j^i = g_j^i \mathcal{U} + \frac{1}{2} \hat{E} g_j^{i2} \phi_j^i + \frac{1}{3} \hat{E} g_j^{i3} \psi_j^i. \quad (\text{C.2.10})$$

Equation (4.2.24):

$$\begin{aligned} \bar{u}_{nj}^i &= \left[\hat{\mu}_n C g_j^i h_j^i - \frac{\hat{\mu}_n C g_j^{i2}}{2} + \frac{C(h_j^i - g_j^i)}{n_j^i} \left(\frac{1}{\hat{k}_2} + \frac{(h_j^i - g_j^i)}{3} \right) \right] \left[\frac{\Upsilon_{j+1}^i \mathcal{H}_{j+1}^i - \Upsilon_{j-1}^i \mathcal{H}_{j-1}^i}{2\Delta x} \right] \\ & \quad - \hat{E}(g_j^i \phi_j^i + g_j^{i2} \psi_j^i), \quad (\text{C.2.11}) \end{aligned}$$

(where we have again eliminated time derivatives of ϕ and ψ using equations (4.2.19) and (4.2.20)).

Equation (4.2.25):

$$\begin{aligned} & \frac{1}{(\Delta x)^2 (h_j^i - g_j^i)} \left[\mathcal{K}_{j+\frac{1}{2}}^i (c_{j+1}^{i+1} - c_j^{i+1}) - \mathcal{K}_{j-\frac{1}{2}}^i (c_j^{i+1} - c_{j-1}^{i+1}) \right] \\ & \quad - \alpha(1 - n_j^i) c_j^{i+1} + n_j^i (1 - n_j^i) = 0, \quad (\text{C.2.12}) \end{aligned}$$

where $\mathcal{K}_j^i = (h_j^i - g_j^i)(1 - n_j^i)$.

Appendix D

Travelling wave solutions of the two-species non-local model

In this appendix, we demonstrate that equations (5.3.1) and (5.3.2) can support the existence of travelling wave solutions in simple special cases. Similar analysis has been undertaken for one-species non-local models [10, 72, 73], but in those cases, the existence of the travelling waves relies on the kernel function being even (or having an even part) which represents some bias in the external environment causing collective ‘drift’ of the group [73]. In the case of the two-species model considered here, travelling wave solutions are possible even though all the kernel functions involved are assumed to be odd. Such models may be appropriate for describing the interactions of groupings of *e.g.* predators and prey. To our knowledge, such solutions are not possible for a one-species model with an odd kernel, and hence represent an emergent property of the system.

We consider the highly simplified case in which there is no random motion and cells have no net interaction with others of the same population - *i.e.* $D_n^* = D_m^* = K_n = K_m \equiv 0$. We introduce the travelling wave co-ordinate $z = x - vt$,

where v is the (constant) travelling wave velocity, and assume the existence of solutions of the following form

$$n = NH_L(z - d), \quad m = MH_L(z), \quad (\text{D.0.1})$$

where

$$H_L(x) = \begin{cases} 1 & \text{if } 0 \leq x \leq L \\ 0 & \text{otherwise} \end{cases}$$

These solutions represent two compact groups of length, L - one of each species - with uniform densities N and M respectively. At $t = 0$, the n species occupy the region $d \leq x \leq d + L$, whilst the m species occupy $0 \leq x \leq L$. Substituting into equations (5.3.1) and (5.3.2) gives

$$-vn' + (n(K_{nm} * m))' = 0, \quad (\text{D.0.2})$$

$$-vm' + (m(K_{mn} * n))' = 0, \quad (\text{D.0.3})$$

where primes denote a derivative with respect to z . The kernel functions are assumed to take the form

$$K_{nm}(x) = \begin{cases} A \text{sign}(x) & \text{if } -r \leq x \leq r \\ 0 & \text{otherwise} \end{cases}$$

with $K_{mn} = -\alpha K_{nm}$. Thus, the n species ('prey') is repelled by m ('predators') within a distance r of them, whilst predators (m) are attracted to prey (n).

Noting that $v_n = K_{nm} * m$ is defined only in the region $d \leq z \leq d + L$, the convolution term in equation (D.0.2) gives

$$v_n = M \int_0^L K_{nm}(z - y) dy \quad (\text{D.0.4})$$

$$= AM \int_{\max(0, z-r)}^{\min(L, z+r)} \text{sign} z - y dy. \quad (\text{D.0.5})$$

We assume that $r > d + L$ (*i.e.* all the prey are within the sensing range of the predators), then, given the restrictions on z stated above, the limits on

the integral will be 0 and L . For $d > L$ (which is necessary to ensure that the two groups of cells do not overlap), we find $\text{sign}(z - y) = 1$ for $d \leq z \leq d + L$, and so

$$v_n = AML. \quad (\text{D.0.6})$$

Similarly, v_m which is defined on the region $0 \leq z \leq L$ is given by

$$v_m = N \int_d^{d+L} K_{mn}(z - y) dy \quad (\text{D.0.7})$$

$$= -\alpha AN \int_{\max(d, z-r)}^{\min(d+L, z+r)} \text{sign} z - y dy. \quad (\text{D.0.8})$$

Assuming, as before, the restrictions $r > d + L$ and $d > L$, we find that

$$v_m = \alpha ANL \quad (\text{D.0.9})$$

Returning to our travelling wave equations (D.0.2) and (D.0.3), it is thus clear that we require

$$M = \alpha N, \quad (\text{D.0.10})$$

and the travelling wave velocity is

$$v = \alpha NAL. \quad (\text{D.0.11})$$

The above analysis describes the case of a ‘fruitless chase’ between a group of predators and a group of prey. As the two species move with the same velocity, the prey are never caught. Of course, this is an excessively simplified example, since we have chosen particularly simple forms for the interaction kernels, ignored interactions between members of the same species and further assumed that the two groups are the same size.

References

- [1] M. Abramowitz and I. A. Stegun, editors. *Handbook of Mathematical Functions*. Dover, 9th printing edition, 1970.
- [2] S. F. Abu-Absi, J. R. Friend, L. K. Hansen, and W. S. Hu. Structural polarity and functional bile canaliculi in rat hepatocyte spheroids. *Exp. Cell Res.*, 274:56–67, 2002.
- [3] T. Alarcon, H. M. Byrne, and P. K. Maini. A multiple scale model for tumour growth. *Multiscale Modelling and Simulation*, 3:440–475, 2005.
- [4] J. W. Allen and S. N. Bhatia. Formation of steady state oxygen gradients in vitro - Application to liver zonation. *Biotech. Bioeng.*, 82(3):253–262, 2003.
- [5] N. J. Armstrong, K. J. Painter, and J. A. Sherratt. A continuum approach to modelling cell-cell adhesion. *J. Theor. Biol.*, in press, 2006.
- [6] P. B. Armstrong. Cell sorting out: the self assembly of tissues *in vitro*. *Critical Reviews in Biochemistry and Molecular Biology*, 24(2):119–149, 1989.
- [7] P. Babak, K. G. Magnusson, and S. Sigurdsson. Dynamics of group formation in collective motion of organisms. *Math. Med. Biol.*, 21:269–292, 2004.
- [8] P. Bedossa and V. Paradis. Liver extracellular matrix in health and disease. *J. Pathol.*, 200:504–515, 2003.

- [9] R. N. Bhandari, L. A. Riccalton, A. L. Lewis, J. R. Fry, A. H. Hammond, S. J. B. Tendler, and K. M. Shakesheff. Liver tissue engineering: A role for co-culture systems in modifying hepatocyte function and viability. *Tissue Eng.*, 7:345–357, 1997.
- [10] J. Billingham. Dynamics of a strongly non-local reaction-diffusion population model. *Nonlinearity*, 17:313–346, 2004.
- [11] M. Bodnar and J. J. L. Velazquez. Derivation of macroscopic equations for individual cell-based models: A formal approach. *Mathematical Methods in the Applied Sciences*, 28:1757–1779, 2005.
- [12] C. J. W. Breward, H. M. Byrne, and C. E. Lewis. The role of cell-cell interactions in a two-phase model for avascular tumour growth. *J. Math. Biol.*, 45 (2):125–152, 2002.
- [13] R. Burridge and J. B. Keller. Poroelasticity equations derived from microstructure. *J. Acoustic Soc. Am.*, 70(4):1140–1146, 1981.
- [14] H. M. Byrne and M. A. J. Chaplain. The importance of constitutive equations in mechanochemical models of pattern formation. *Appl. Math. Lett.*, 9 (6):85–90, 1996.
- [15] H. M. Byrne, J. R. King, D. L. S. McElwain, and L. Preziosi. A two-phase model of solid tumour growth. *Appl. Math. Lett.*, 16(4):567–573, 2003.
- [16] H. M. Byrne and M. R. Owen. A new interpretation of the Keller-Segel model based on multiphase modelling. *J. Math. Biol.*, 49(6):604–626, 2004.
- [17] H. M. Byrne and L. Preziosi. Modelling solid tumour growth using the theory of mixtures. *Math. Med. Biol.*, 20:341–366, 2003.
- [18] S. H. Cartmell, J. Dobson, S. B. Verschueren, and A. J. El Haj. Development of magnetic particle techniques for long-term culture of bone

- cells with intermittent mechanical activation. *IEEE Transactions on Nanobioscience*, 1(2):92–97, 2002.
- [19] Compressed Mortality File (CDC WONDER On-line Database - <http://wonder.cdc.gov>), Accessed 12 May 2003.
- [20] C. Chen, J. Chueh, H. Tseng, H. Huang, and S. Lee. Preparation and characterisation of biodegradable PLA polymeric blends. *Biomaterials*, 24:1167–1173, 2003.
- [21] N. G. Cogan and J. P. Keener. The role of biofilm matrix in structural development. *Math. Med. Biol.*, 21:147–166, 2004.
- [22] S. C. Cowin. How is a tissue built? *J. Biomech. Eng.*, 122:553–569, 2000.
- [23] D. E. Discher, P. Janmey, and Y. Wang. Tissue cells feel and respond to the stiffness of their substrata. *Science*, 310:1139–1143, 2005.
- [24] Y. Dolak and C. Schmeiser. The Keller-Segel model with logistic sensitivity function and small diffusivity. *SIAM J. Appl. Math.*, 66(1):286–308, 2005.
- [25] D. A. Drew. Averaged field equations for two-phase media. *Stud. Appl. Math.*, 2:133–166, 1971.
- [26] D. A. Drew. Mathematical modelling of two-phase flow. *Ann. Rev. Fluid Mech.*, 15:261–291, 1983.
- [27] D. A. Drew and L. A. Segel. Averaged equations for two-phase flows. *Stud. Appl. Math.*, 3:205–231, 1971.
- [28] M. Dvir-Ginzberg, I. Gamlieli-Bonshtein, R. Agbaria, and S. Cohen. Liver tissue engineering within alginate scaffolds: effects of cell-seeding density on hepatocyte viability, morphology and function. *Tissue Eng.*, 9 (4):757–766, 2003.

- [29] A.C. Eringen. *Mechanics of Continua*. John Wiley & Sons, London, 1967.
- [30] G. B. Ermentrout and L. Edelstein-Keshet. Cellular automata approaches to biological modelling. *J. Theor. Biol.*, 160 (1):97–133, 1993.
- [31] A. Fasano, A. Mancini, and M. Primicerio. Equilibrium of two populations subject to chemotaxis. *Mathematical Models and Methods in Applied Sciences*, 4:503–533, 2004.
- [32] N. Fausto, A. D. Laird, and E. M. Webber. Role of growth factors and cytokines in hepatic regeneration. *FASEB*, 9:1527–1536, 1995.
- [33] G. Forgacs, R. A. Foty, Y. Shafrir, and M. S. Steinberg. Viscoelastic properties of living embryonic tissues: a quantitative study. *Biophys. J.*, 74:2227–2234, 1998.
- [34] R. A. Foty and M. S. Steinberg. The differential adhesion hypothesis: a direct evaluation. *Developmental Biology*, 278:255–263, 2005.
- [35] A. C. Fowler. *Mathematical Models in the Applied Sciences*. Cambridge University Press, Cambridge, 1997.
- [36] S. J. Franks and J. R. King. Interactions between a uniformly proliferating tumour and its surroundings: uniform material properties. *Math. Med. Biol.*, 20, 2003.
- [37] Y. Fujii, K. Nakazawa, and K. Funatsu. Intensive promotion of spheroid formation by soluble factors in a hepatocyte-conditioned medium. *J. Biomater. Sci. Polym. Ed.*, 11 (7):731–745, 2000.
- [38] A. Gentilini, F. Marra, P. Gentilini, and M. Pinzani. Phosphatidylinositol-3 kinase and extracellular signal-regulated kinase mediate the chemotactic and mitogenic effects of insulin-like growth factor-1 in human hepatic stellate cells. *J. Hepatology*, 32:227–234, 2000.

- [39] R. Glicklis, J. C. Merchuk, and S. Cohen. Modelling mass transfer in hepatocyte spheroids via cell viability, spheroid size and hepatocellular functions. *Biotechnology and Bioengineering*, 86(6):672–680, 2004.
- [40] S. A. Gourley, M. A. J. Chaplain, and F. A. Davidson. Spatio-temporal pattern formation in a non-local reaction-diffusion equation. *Dynamical Systems*, 16(2):173–192, 2001.
- [41] M. E. Gracheva and H. G. Othmer. A continuum model of motility in ameboid cells. *Bull. Math. Biol.*, 66:167–193, 2004.
- [42] A. Grief and G. Richardson. Magnetic bioreactors. In *Proceedings of the Second Mathematics in Medicine Study Group*, pages 71–83. University of Nottingham, 2001.
- [43] P. A. Gunatillake and R. Adhikari. Biodegradable synthetic polymers for tissue engineering. *Eur. Cell. Mater.*, 5:1–16, 2003.
- [44] P. D. Howell. *Extensional thin layer flows*. PhD thesis, University of Oxford, 1994.
- [45] P. D. Howell. Models for thin viscous sheets. *Eur. J. Appl. Math.*, 7:321–343, 1996.
- [46] J. D. Humphrey. Continuum biomechanics of soft biological tissues. *Proc. R. Soc. Lond. A*, 459:3–46, 2003.
- [47] T. L. Jackson and H. M. Byrne. A mechanical model of tumour encapsulation and transcapsular spread. *Math. Biosci.*, 180:307–328, 2002.
- [48] H. O. Jauregui. *Principles of Tissue Engineering (Second Edition)*, chapter 39 : Liver, pages 541–551. Academic Press, 2000.
- [49] J. Kaiser, A. Reinmann, and A. Bruinink. The effect of topographic characteristics on cell migration velocity. *Biomaterials*, 27:5230–5241, 2006.

- [50] J. P. Keener and J. Sneyd. *Mathematical physiology*. Springer, 1998.
- [51] E. F. Keller and L. A. Segel. Initiation of slime mold aggregation viewed as an instability. *J. Theor. Biol.*, 26:399–415, 1970.
- [52] E. F. Keller and L. A. Segel. Model for chemotaxis. *J. Theor. Biol.*, 30:225–234, 1971.
- [53] J. R. King and J. M. Oliver. Thin-film modelling of poroviscous free surface flows. *Euro. J. Appl. Math.*, 16:519–553, 2005.
- [54] R. Langer and D. A. Tirrell. Designing biomaterials for biology and medicine. *Nature*, 428:487–492, 2004.
- [55] P. G. Layer, A. Robitzki, A. Rothermel, and E. Willbold. Of layers and spheres; the reaggregate approach in tissue engineering. *Trends in Neurosciences*, 25(3):131–134, 2002.
- [56] E. L. LeCluyse, P. L. Bullock, and A. Parkinson. Strategies for restoration and maintenance of normal hepatic structure and function in long-term cultures of rat hepatocytes. *Adv. Drug Deliv. Rev.*, 22:133–186, 1996.
- [57] C. T. Lee, M. F. Hoopes, J. Diehl, W. Gilliland, G. Huxel, E. V. Leaver, K. McCann, J. Umbanhowar, and A. Mogilner. Non-local concepts and models in biology. *J. Theor. Biol.*, 210:201–219, 2001.
- [58] K. W. Lee, S. K. Lee, J. W. Joh, S. J. Kim, B. B. Lee, K. W. Kim, and K. U. Lee. Influence of pancreatic islets on spheroid formation and functions of hepatocytes in hepatocyte-pancreatic islet spheroid culture. *Tissue Eng.*, 10:965–77, 2004.
- [59] G. Lemon, J. King, H. Byrne, O. Jensen, and K. Shakesheff. Multiphase modelling of tissue growth using the theory of mixtures. *J. Math. Biol.*, submitted:1–39, 2005.

- [60] F. Lin, C. M-C. Nguyen, S-J. Wang, W. Saadi, S. P. Gross, and N. L. Jeon. Effective neutrophil chemotaxis is strongly influenced by mean IL-8 concentration. *Biochem. Biophys. Res. Commun.*, 319:576–581, 2004.
- [61] C. Lo, H. Wang, M. Dembo, and Y. Wang. Cell movement is guided by the rigidity of the substrata. *Biophys. J.*, 79:144–152, 2000.
- [62] S. R. Lubkin and T. Jackson. Multiphase mechanics of capsule formation in tumours. *J. Biomech. Eng.*, 124:237–243, 2002.
- [63] M. Luca, A. Chavez-Ross, L. Edelstein-Keshet, and A. Mogilner. Chemotactic signalling, microglia and Alzheimer’s disease senile plaques: Is there a connection? *Bull. Math. Biol.*, 65:693–730, 2003.
- [64] P.K. Maini and J. D. Murray. A nonlinear analysis of a mechanical model for biological pattern formation. *SIAM J. Appl. Math.*, 48(5):1064–1072, 1988.
- [65] M. Massoudi. Constitutive relations for the interaction force in multi-component particulate flows. *Int. J. Nonlinear Mech.*, 38:313–336, 2003.
- [66] G.K. Michalopoulos and M. C. DeFrances. Liver regeneration. *Science*, 276:60–66, 1997.
- [67] W. W. Minuth, K. Schumacher, R. Strehl, and S. Kloth. Physiological and cell biological aspects of perfusion culture technique employed to generate differentiated tissues for long term biomaterial testing and tissue engineering. *J. Biomater. Sci. Polymer Edn.*, 11(5):495–522, 2000.
- [68] W. W. Minuth, P. Steiner, R. Strehl, K. Schumacher, U. de Vries, and S. Kloth. Modulation of cell differentiation in perfusion culture. *Experimental Nephrology*, 7:394–406, 1999.
- [69] T. Mitaka. The current status of primary hepatocyte culture. *Int. J. Exp. Pathol.*, 79:393–409, 1998.

- [70] P. V. Moghe, F. Berthiaume, R. M. Ezzell, M. Toner, R. G. Tompkins, and M. L. Yarmush. Culture matrix configuration and composition in the maintenance of hepatocyte polarity and function. *Biomaterials*, 17:373–385, 1996.
- [71] P. V. Moghe, R. N. Cogger, M. Toner, and M. L. Yarmush. Cell-cell interactions are essential for maintenance of hepatocyte function in collagen gel but not on matrigel. *Biotechnol. Bioeng.*, 56 (6):706–710, 1997.
- [72] A. Mogilner. *Modelling spatio-angular patterns in cell biology*. PhD thesis, University of British Columbia, Vancouver, Canada, 1995.
- [73] A. Mogilner and L. Edelstein-Keshet. A non-local model for a swarm. *J. Math. Biol.*, 38:534–570, 1999.
- [74] A. Mogilner, L. Edelstein-Keshet, L. Bent, and A. Spiros. Mutual interactions, potentials and individual distance in a social aggregation. *J. Math. Biol.*, 47:353–389, 2003.
- [75] K.W. Morton and D.F. Mayers. *Numerical solution of partial differential equations : an introduction*. Cambridge University Press, Cambridge, 1994.
- [76] J. D. Murray. *Mathematical Biology*. Springer-Verlag, New York, 2nd edition, 1993.
- [77] J. D. Murray. On the mechanochemical theory of biological pattern formation with application to vasculogenesis. *C. R. Biologies*, 326:239–252, 2003.
- [78] J. D. Murray and G. F. Oster. Generation of biological pattern and form. *IMA J. Math. Appl. Med. Biol.*, 1:51–75, 1984.
- [79] T. G. Myers. Thin films with high surface tension. *SIAM Review*, 40(3):441–462, 1998.

- [80] H. Nagai, K. Terada, G. Watanabe, Y. Ueno, N. Aiba, T. Shibuya, M. Kawagoe, T. Kameda, M. Sato, H. Senoo, and T. Sugiyama. Differentiation of liver epithelial (stem-like) cells into hepatocytes induced by coculture with hepatic stellate cells. *Biochem. Biophys. Res. Commun.*, 293:1420–1425, 2002.
- [81] P. Namy, J. Ohayon, and P. Tracqui. Critical conditions for pattern formation and *in vitro* tubulogenesis driven by cellular traction fields. *J. Theor. Biol.*, 227:103–120, 2004.
- [82] N. A. N'Dri, W. Shyy, and R. Tran-Son-Tay. Computational modelling of cell adhesion and movement using a continuum-kinetics approach. *Biophys. J.*, 85:2273–2286, 2003.
- [83] Liver activity. UK transplant activity 2001, UK Transplant - NHS, 2001.
- [84] J. M. Oliver, J. R. King, K. J. McKinlay, D. M. Grant, C. A. Scotchford, J. V. Wood, and P. D. Brown. Thin film theories for two-phase reactive flow models of active cell motion. *Math. Med. Biol.*, 22:53–98, 2005.
- [85] G. F. Oster, J. D. Murray, and A. K. Harris. Mechanical aspects of mesenchymal morphogenesis. *J. Embryol. Exp. Morph.*, 78:83–125, 1983.
- [86] H. G. Othmer and A. Stevens. Aggregation, blowup and collapse: The ABC's of taxis in reinforced random walks. *SIAM J. Appl. Math.*, 57(4):1044–1081, 1997.
- [87] M. R. Owen, H. M. Byrne, and C. E. Lewis. Mathematical modelling of the use of macrophages as vehicles for drug-delivery to hypoxic tumour sites. *J. Theor. Biol.*, 226:377–391, 2004.
- [88] M. R. Owen and M. A. Lewis. The mechanics of lung tissue under high-frequency ventilation. *SIAM J. Appl. Math.*, 61(5):1731–1761, 2001.
- [89] K. J. Painter and J. A. Sherratt. Modelling movement of interacting cell populations. *J. Theor. Biol.*, 225:327–339, 2003.

- [90] E. Palsson. A three-dimensional model of cell movement in multicellular systems. *Future Generation Computer Systems*, 17(835-852), 2001.
- [91] E. Palsson and H. G. Othmer. A model for individual and collective cell movement in *Dictyostelium discoideum*. *PNAS*, 97(19):10448–10453, 2000.
- [92] B. Perthame. Pde models for chemotactic movements: parabolic, hyperbolic and kinetic. *Preprint*, 1:1–28, 2004.
- [93] M. V. Peshwa, F. J. Wu, B. D. Follstad, F. B. Cerra, and W. Hu. Kinetics of hepatocyte spheroid formation. *Biotechnol. Prog.*, 10:460–466, 1994.
- [94] M. V. Peshwa, F. J. Wu, H. L. Sharp, F. B. Cerra, and W. Hu. Mechanistic of formation and ultrastructural evaluation of hepatocyte spheroids. *In Vitro Cell Dev. Biol.*, 32:197–203, 1996.
- [95] M. J. Powers, K. Domansky, M. R. Kaazempur-Mofrad, A. Kalezi, A. Capitano, A. Upadhyaya, P. Kurzawski, K. E. Wacka, D. B. Stolz, R. Kamm, and L. G. Griffith. A microfabricated array bioreactor for perfused 3D liver culture. *Biotechnol. Bioeng.*, 78(3):257–269, 2002.
- [96] M. J. Powers and L. Griffith-Cima. Motility behaviour of hepatocytes on extracellular matrix substrata during aggregation. *Biotechnology and Bioengineering*, 50:392–403, 1996.
- [97] M. J. Powers, R. E. Rodriguez, and L. G. Griffith. Cell-substratum adhesion strength as a determinant of hepatocyte aggregate morphology. *Biotechnology and Bioengineering*, 53:415–426, 1997.
- [98] L. Preziosi and S. Astanin. Modelling the formation of capillaries. In A. Quarteroni, editor, *Integration of Complex Systems in Biomedicine*, chapter 4. Springer, 2005.
- [99] N. M. Ribe. A general theory for the dynamics of thin viscous sheets. *J. Fluid Mech.*, 457:255–283, 2002.

- [100] L. Riccalton-Banks. Tissue engineering: The science of spare parts. *Wellcome Trust / New Scientist Millennial essay competition*, (runner up), 2001.
- [101] L. Riccalton-Banks, C. Liew, R. Bhandari, J. Fry, and K. Shakesheff. Long-term culture of functional liver tissue: Three-dimensional coculture of primary hepatocytes and stellate cells. *Tissue Eng.*, 9(3):401–409, 2003.
- [102] L. A. Riccalton-Banks. *Maintenance of Primary Rat Hepatocytes in vitro Using Co-culture Techniques*. PhD thesis, University of Nottingham, 2002.
- [103] L. Richert, D. Binda, G. Hamilton, C. Viollon-Abadie, E. Alexandre, D. Bigot-Lasserre, R. Bars, P. Coassolo, and E. LeCluyse. Evaluation of the effect of culture configuration on morphology, survival time, antioxidant status and metabolic capacities of cultured rat hepatocytes. *Toxicol. In Vitro*, 16:89–99, 2002.
- [104] M. V. Risbud and M. Sittinger. Tissue engineering: advances in *in vitro* cartilage generation. *Trends in Biotechnology*, 20(8):351–356, 2002.
- [105] T. Roose, P. A. Netti, L. L. Munn, Y. Boucher, and R. K. Jain. Solid stress generated by spheroid growth estimated using a linear poroelasticity model. *Microvascular Research*, 66:204–212, 2003.
- [106] J. Rozga. Hepatocyte proliferation in health and in liver failure. *Medical Science Monitor*, 8 (2):RA32 – RA38, 2002.
- [107] K. L. Schmeichel and M. J. Bissel. Modelling tissue-specific signalling and organ function in three dimensions. *J. Cell Science*, 116:2377–2388, 2003.

- [108] C. Selden, M. Khalil, and H. J. F. Hodgson. What keeps hepatocytes on the straight and narrow? Maintaining differentiated liver function. *Gut*, 44:443–446, 1999.
- [109] C. E. Semino, J. R. Merok, G. G. Crane, G. Panagiotakos, and S. Zhang. Functional differentiation of hepatocyte-like spheroid structures from putative liver progenitor cells in three-dimensional peptide scaffolds. *Differentiation*, 71:262–270, 2003.
- [110] E. J. Semler, C. S. Ranucci, and P. V. Moghe. Mechanochemical manipulation of hepatocyte aggregation can selectively induce or repress liver-specific function. *Biotechnol. Bioeng.*, 69 (4):359–369, 2000.
- [111] S. Skrtic, V. Wallenius, S. Ekberg, A. Brenzel, A. M. Gressner, and J. Jansson. Hepatocyte-stimulated expression of hepatocyte growth factor (hgf) in cultured rat hepatic cells. *J. Hepatology*, 30:115–124, 1999.
- [112] M. S. Steinberg. Reconstruction of tissues by dissociated cells. *Science*, 141(3579):401–408, 1963.
- [113] D. B. Stolz and G. K. Michalopoulos. Synergistic enhancement of EGF, but not HGF, stimulated hepatocyte motility by TGF- β 1 *in vitro*. *J. Cell. Physiol.*, 170:57–68, 1997.
- [114] R. Strehl, K. Schumacher, U. de Vries, and W. W. Minuth. Proliferating cells versus differentiated cells in tissue engineering. *Tissue Eng.*, 8(1):37–42, 2002.
- [115] E. A. Swabb, J. Wei, and P. M. Gullino. Diffusion and convection in normal and neoplastic tissues. *Cancer Res.*, 34:2814–2822, 1974.
- [116] K. R. Swanson, E. C. Alvord, and J. D. Murray. Quantifying efficacy of chemotherapy of brain tumours with homogeneous and heterogeneous drug delivery. *Acta Biotheoretica*, 50(4):223–237, 2002.

- [117] S. Terada, M. Sato, A. Sevy, and J. P. Vacanti. Tissue engineering in the twenty-first century. *Yonsei Medical Journal*, 41(6):685–691, 2000.
- [118] R. J. Thomas, A. Bennett, B. Thomson, and K. M. Shakesheff. Hepatic stellate cells on poly(DL-lactic acid) surfaces control the formation of 3D hepatocyte co-culture aggregates *in vitro*. *Euro. Cell. Mater.*, 11:16–26, 2006.
- [119] R. J. Thomas, R. Bhandari, D. A. Barrett, , A. J. Bennett, J. R. Fry, D. Powe, B. J. Thomson, and K. M. Shakesheff. The effect of three-dimensional co-culture of hepatocytes and hepatic stellate cells on key hepatocyte functions *in vitro*. *Cells Tissues Organs*, 181(2):67–79, 2005.
- [120] T. W. Thomas and P. A. DiMilla. Spreading and motility of human glioblastoma cells on sheets of silicone rubber depend on substratum compliance. *Med. Biol. Eng. Comput.*, 38:360–370, 2000.
- [121] D. W. Thompson. *On Growth and Form*. Cambridge University Press, 2nd edition, 1942.
- [122] J. Z. Tong, S. Sarrazin, D. Cassio, F. Gauthier, and F. Alvarez. Application of spheroid culture to human hepatocytes and maintenance of their differentiation. *Biology of the Cell*, 81:77–81, 1994.
- [123] R. T. Tranquillo and J. D. Murray. Mechanistic model of wound contraction. *J. Surg. Res.*, 55:233–247, 1993.
- [124] A. M. Turing. The chemical basis of morphogenesis. *Phil. Trans. Roy. Soc. B*, 237:37–72, 1952.
- [125] B. Vasiev and C. J. Weijer. Modelling chemotactic cell sorting during *dictyostelium discoideum* mound formation. *Biophys. J.*, 76:595–605, 1999.
- [126] B. Vasiev and C. J. Weijer. Modelling of *Dictyostelium discoideum* slug migration. *J. Theor. Biol.*, 223:347–359, 2003.

- [127] D. Velegol and F. Lanni. Cell traction forces on soft biomaterials. I Microrheology of type I collagen gels. *Biophys. J.*, 81:1786–1792, 2001.
- [128] C. Verdier. Rheological properties of living materials: From cells to tissues. *J. Theor. Med.*, 5(2):67–91, 2003.
- [129] G. Vunjak-Novakovic, I. Martin, B. Obradovic, S. Treppo, A. J. Grodzinsky, R. Langer, and L. E. Freed. Bioreactor cultivation conditions modulate the composition and mechanical properties of tissue engineered cartilage. *J. Orthopaedic Research*, 17(1):130–138, 1999.
- [130] D. C. Walker, J. Southgate, G. Hill, M. Holcombe, D. R. Hose, S. M. Wood, S. Mac Neil, and R. H. Smallwood. The Epitheliome: Agent-based modelling of the social behaviour of cells. *Biosystems*, 76(1-3):89–100, 2004.
- [131] S. L. Waters, L. J. Cummings, K. M. Shakesheff, and F. R. A. J. Rose. Tissue growth in a rotating bioreactor. part i: Mechanical stability. *Math. Med. Biol.*, in press.
- [132] S. J. Weekley. *Particle dynamics in liquid-line lung airways*. PhD thesis, University of Nottingham, UK, 2004.
- [133] M. J. Whitaker, R. A. Quirk, S. M. Howdle, and K. M. Shakesheff. Growth factor release from tissue engineering scaffolds. *J. Pharm. Pharmacol.*, 53(11):1427–1437, 2001.
- [134] M.J. Whitaker. *Supercritical Fluid Processing of Polymers, Proteins and Cells for Tissue Engineering Applications*. PhD thesis, University of Nottingham, 2003.
- [135] S. Whitaker. The transport equations for multi-phase systems. *Chem. Eng. Sci.*, 28:139–147, 1973.
- [136] T. P. Witelski. Shocks in nonlinear diffusion. *Appl. Math. Lett.*, 8(5):27–32, 1995.

- [137] L. J. Worobetz, R. J. Hilsden, E. A. Shaffer, J. B. Simon, P. Paré, V. G. Bain, M. Ma, F. Wong, L. Blendis, P. Adams, J. Heathcote, S. S. Lee, L. B. Lilly, A. W. Hemming, and G. A. Levy. *First Principles of Gastroenterology*, chapter 14 : Liver, pages 462–557. Online edition (<http://gastroresource.com>). Accessed 1 October, 2002.
- [138] R. J. Zdrahala and I. J. Zdrahala. *In vivo* tissue engineering: Part I. Concept genesis and guidelines for its realisation. *J. Biomaterials Applications*, 14:192–209, 1999.
- [139] A. Zimmermann. Liver regeneration: the emergence of new pathways. *Medical Science Monitor*, 8 (3):RA53 – RA63, 2002.